

**Optimization of dynamic transfer function
analysis for impedance spectroscopy and
intensity-modulated photo spectroscopy for
application to non-stationary and distributed
electrochemical systems**

**The Faculty of Engineering at the
University of Erlangen-Nuremberg
To obtain the degree**

DOCTOR-ENGINEER

Submitted by

Mr. Dipl. Chem. Karl-Albrecht Schiller

Erlangen - 2012

**Approved as a dissertation by
of the Technical Faculty of the
University of Erlangen-Nuremberg**

Date of submission: 16.03.2012

Day of the promotion: 06.08.2012

Dean: Prof. Dr.-Ing. Marion Merklein

Rapporteur: Prof. Dr. Patrik Schmuki,
Prof. Dr. Günter Grampp

Summary

Electrode and cell impedance measurements are established methods for investigating electrochemical processes. Kinetic data is usually determined by analyzing the impedance spectra. This can provide useful information for the application. Examples include the corrosion rate of materials or the details of processes that determine the efficiency of fuel and photovoltaic cells.

The present work is mainly concerned with the more advanced development of these measuring methods with regard to the evaluation procedures (dynamic transfer function analysis, TFA) and the extension to optical excitation of light-sensitive systems (intensity-modulated photospectroscopy, IMPS).

The author has carried out this work over a long period of time alongside his work as head of research and managing director of Zahner-Messtechnik, Kronach. In many cases, application examples are presented for the developments, which were mostly carried out in cooperation with universities and research institutes. The Institute of Materials Science at the Friedrich-Alexander University of Erlangen-Nuremberg with the Chair of Corrosion and Surface Technology LKO, which also supervises the work, has played a major role here.

Due to the selected problems the author was confronted with, the investigations presented are wide-ranging. This includes work on the verification, correction and evaluation of measured transfer functions, the time dependence of quasi-stationary systems and the modeling of photoelectrochemical systems, e.g., solar cells.

The result of the first topic mentioned can be an estimation of the measurement uncertainty of TFA data and thus the significance and error range of electrochemical parameters obtained (e.g., the charge transfer resistance or diffusion resistance of an electrode).

The temporal variation of real electrochemical systems during the recording of spectra can be a serious experimental problem, since drift collides with a basic requirement for TFA, i.e., stationarity during the measurement time.

The well-known Kramers-Kronig transformation theoretically allows for recognizing measurement errors that are attributable to the loss of causality due to temporal drift. However, it can be considered a challenging task to calculate this. In contrast, the logarithmic Hilbert transform for two poles, ZHIT, formulated by the author and now widely used, has proven itself in practical applications due to its uncomplicated numerical methods and its insensitivity to the limited frequency range of experimental data.

Despite drift, TFA data can be evaluated quite accurately if it is possible to calculate defined spectra from successive spectra by interpolation to fixed points in time. Examples of applications for ZHIT and interpolation include the transient systems such as iron in an electrolyte containing CO₂, the gradual carbon monoxide poisoning of a fuel cell, the flooding of a fuel cell cathode by reaction water, or the swelling behavior of organic coatings.

The understanding of devices for electrochemical power generation such as batteries, fuel cells or modern solar cells often requires special knowledge of the dynamic properties of "distributed" systems, e.g., porous structures and inhomogeneous dielectrics, as well as the determination of the causes of their relaxation behavior. Therefore, it seemed appropriate to address these phenomena here.

For the little-known relaxation behavior of the temperature of electrochemical systems such as in fuel cells or batteries as a result of the heat due to the current, model investigations were carried out on temperature-dependent resistors. As a result, the theoretical formulation of the general relaxation impedance is presented and discussed together with the experimental results.

The modeling of electrode impedances using electrically equivalent networks ("equivalent circuit diagrams") has become widely accepted. If photoelectrically active objects such as solar cells are to be described in a modular and dynamic way, instead of carrying out individual analytical calculations for each application as was previously the case, this can be achieved by introducing a localized photocurrent source as a network component.

For this purpose, the author describes his approach towards a technical realization. A special fitting strategy ("TRIFIT" algorithm) allows the joint model fitting of experimental data of the transfer function triplet of impedance, dynamic photocurrent and dynamic photovoltage, obtained from measurements in the same system state of the object. Compared to the measurement of individual spectra, e.g., only the impedance, this approach improves the ratio

of the number of observables to the number of free parameters and the models approach uniqueness.

In this regard, the author carried out experimental investigations on dye-sensitized solar cells based on TiO₂ nanotubes and on tantalum oxide films on tantalum. For the photoanode side of the dye-sensitized solar cell, the model published by a Danish working group ("Bay & West") of distributed photocurrent generation in the active, porous material was confirmed using the TRIFIT algorithm.

In addition, the dynamic efficiency, determined from the time constants of the charge carrier behavior (diffusion or lifetime) of photocurrent and voltage spectra of various samples of thin-film dye solar cells in cooperation with colleagues from the LKO, could be assigned to the various manufacturing parameters and sensitization dye contents of the TiO₂ nanotubes.

The dynamic behavior of the tantalum oxide films could be modeled over wide ranges of electrolytic production by anodic oxidation for the measured data triplets by a simple electrical equivalent circuit diagram. It essentially contains the photocurrent source and a model of the oxide for the different regions with p-, intrinsic and n-conductivity ("PIN" model), as presented in the chapter on inhomogeneous dielectrics.

The reliable measurement of dynamic photocurrent and photovoltage spectra IMPS and IMVS places high expectations on the measuring equipment. Uncalibrated or poorly reproducible light intensity, non-linearity of the light modulation and frequency-dependent artifacts make the interpretation of the experimental results considerably more difficult. The "Controlled Intensity Modulated Photo Spectroscopy" CIMPS is described, a development of the author which significantly improves the accuracy of the photo-electrochemical transfer function measurement compared to the use of current-controlled LEDs as a light source, which is otherwise often found in the literature.

Abstract

In the evaluation of electrochemical processes, it is popular to measure the electrical impedance of electrodes and cells. Kinetic knowledge, obtainable from the impedance spectra, can be used to extract application-relevant information. Examples are for instance the corrosion rate of materials or process details determining the efficiency of fuel cells or photovoltaic cells.

This work aims on the improvement of the impedance related techniques with emphasis on the analysis procedure (Dynamic Transfer Analysis TFA). Moreover, it is proposed to widen the TFA tools for the application on photo-sensitive objects (Intensity Modulated Photo Spectroscopy IMPS).

The author performed this work beside his profession as manager and head of research in his company Zahner-Messtechnik in Germany, Kronach. For many cases, application examples for the developed procedures are presented. Usually, they grew in cooperation with universities and external research institutes. Hereby, the leading role was performed by the Department of Materials Science of the Friedrich-Alexander University, Germany, Erlangen, with the chair for surface science and corrosion LKO as a mentor of this work.

In analogy to the requests brought to the author from the cooperation partners, the studies are diverse, comprising tasks of verification, recovery and analysis of measured transfer function data, the time dependency of quasi-steady state systems as well as the modeling of photo-electrical systems such as solar cells.

Procedures for the estimation of the reliability of experimental TFA data, the determination of the significance and uncertainty of electrochemical parameters (e.g., the electrode polarization resistance or the characteristic values of the diffusion involved), evaluated by the TFA can be considered results of this work.

The temporal change of an electrochemical system during the recording time of a spectrum may be a serious experimental obstacle, as drift collides with one of the basic requirements for any TFA, which is the stationarity during the measurement time.

Theoretically, the well-known Kramers-Kronig-Transform allows for the detection of parasitic errors caused by the loss of causality due to temporal change, but its computation is questionable. The Logarithmic Hilbert Transform for Two-Poles, referred to as ZHIT, was developed by the author and asserts itself in practice for its uncomplicated numerics and its ruggedness against the limited frequency range of experimental data.

Even TFA-data affected by time-drift may be analyzed in a comparably accurate manner. For this, several spectra have to be acquired sequentially and data sets belonging to certain points in time need to be calculated by means of a temporal interpolation. This is demonstrated alongside the ZHIT on non-steady-state systems like corroding Iron in an electrolyte which contains CO₂, a fuel cell which is gradually poisoned by carbon monoxide present in the fuel gas, another fuel cell, where the cathode is flooded by reaction water and organic protective coatings on metal under water uptake.

The insight into devices for the electrochemical energy conversion like batteries and fuel cells, or into modern solar cells often requires the knowledge of the dynamic properties of distributed systems, as represented by porous structures and non-homogeneous dielectrics, and of their characteristic relaxation behavior. It appeared appropriate to address such phenomena in this work.

The temperature relaxation behavior of electrochemical objects like fuel cells or batteries under the influence of electrical current heat is not so commonly known. Therefore, exemplary studies on temperature dependent resistors were performed in this work. As an outcome, the theoretical formulation of the "General Relaxation Impedance" will be presented and discussed together with the experimental results.

It is a well-established practice to model the impedance of electrodes by means of electrical equivalent circuits. In contrast, accurate modeling of photo-electrical active objects like solar cells is usually done by individual analytical computations. If one wants to transcribe the modular way of equivalent circuit analysis also to dynamic photo-electric transfer functions, one may introduce a localized photocurrent source as a network component.

The author describes his technical realization in an analysis program. A special fitting feature of this program is the so called "TRIFIT-algorithm". It allows the joint best model fit of the three types of experimental data from impedance, dynamic photocurrent- and photo voltage efficiency spectra, which were acquired all from the same system state of the object under test. Compared to the analysis of the isolated spectra, like it is popular in EIS, the relation between the number of known observables and the number of free parameters is increased. This leads to a model close to definiteness with less ambiguity.

Experiments in this field were performed by the author on dye-sensitized solar cells "DSSC" based on TiO_2 -nanotubes and on Tantalum oxide films created by anodic oxidation of Tantalum metal. By means of the TRIFIT-algorithm the "Bay-West"-model of a porous distributed photocurrent generation, published by a Danish group, could be verified for the photo-anode of the DSSC.

Besides this, in cooperation with colleagues from the LKO institute several samples of thin film solar cells were examined. Their charge carrier time constants for diffusion and recombination, evaluated as dynamic efficiency from photocurrent- and photo voltage spectra, could be assigned to the parameters of synthesis and the content of sensitizing dye of the samples.

The experimental impedance-, dynamic photocurrent- and photo voltage efficiency spectra of the Tantalum oxide films could be modelled over a wide range of preparation parameters of the anodic oxidation by means of a simple electrical equivalence circuit. It is primarily composed of the photocurrent source, which is embedded in the model of the oxide, containing three characteristic conduction areas with p-, intrinsic- and n-conductivity. This "PIN-model" is presented in the chapter about inhomogeneous dielectrics.

For the determination of reliable dynamic photo-voltage and photocurrent spectra, an instrumentation of high-quality standard is necessary. Poor reproducibility or missing calibration of the used light intensity, non-linearity of the light modulation and frequency dependent artefacts have a negative effect on the interpretation of the experimental results. A development of the author, the "Controlled Intensity Modulated Photo Spectroscopy" CIMPS is able to enhance the accuracy of photo-electrochemical transfer function measurements significantly, compared to the literature common usage of current controlled LED as light source. The CIMPS principle will be outlined here, too.

Foreword

The history of this work is somewhat unusual. It began in 1978 at the Institute of Physical and Electrochemistry in Erlangen, when Prof. Herrmann Göhr offered me the opportunity to do my doctorate with him on the subject of "Modern electrocatalysts" after I had completed my diploma thesis. When, in the late stages of my work, I was faced with the choice of taking the plunge into self-employment or staying at the institute and completing my doctorate, I seized the opportunity to found a company. Unfortunately, the commercial success that ensued meant that I had to put many personal goals on hold, including completing my doctorate.

In the many years that followed, Prof. Göhr, with whom I had a warm personal relationship, and former colleagues, above all Dr. Franz Richter, Prof. Rüdiger Kaus and Dr. Norbert Wagner, repeatedly encouraged me to pick up the thread again. I also received encouragement from Prof. Waldfried Plieth, Dr. Ursula Rammelt, Prof. Florian Mansfeld, Prof. Klaus Jüttner and many other like-minded people. I owe my breakthrough to Prof. Patrik Schmuki, who, after a few months of academic collaboration, offered me the chance to work with him as a doctoral supervisor and to make another attempt at his institute.

Table of contents

1 Introduction, motivation and problem definition.....	11
2 The dynamic transfer function analysis TFA.....	13
3 Optimization of the signal evaluation for the TFA.....	17
3.1 Verification, correction and evaluation of measured transfer functions.....	17
3.1.1 Estimation of the measurement uncertainty of TFA data during the recording of experimental spectra.....	17
3.1.2 Estimating the accuracy of parameters obtained from the TFA, taking measurement uncertainty into account.....	23
3.1.2.1 Significance of the elements in models for transfer functions.....	24
3.1.2.2 Smoothing and interpolation routine for measurement data.....	26
3.1.2.3 Consideration of the uncertainty of the sampling points in the Fitt process to estimate the overall uncertainty of the parameters determined in Fitt.....	27
3.1.3 Effects of the time dependency of systems examined with the TFA and their treatment.....	29
3.1.3.1 "On-Line" drift compensation.....	29
3.1.3.2 Temporal interpolation of spectra.....	30
3.1.3.3 Development of the logarithmic Hilbert transformation for two poles "ZHIT".....	31
3.1.3.4 Verification and approximate correction of time dependencies in experimental spectra using ZHIT.....	36
3.1.4 Application of the tools for identifying and handling time dependencies on selected systems with limited stability.....	38
3.1.4.1 Investigations of metallic corrosion.....	38
3.1.4.2 Drift effects in the fuel cell: Influence of CO poisoning of the anode and the disturbed water balance of the cathode on the impedance of a PEM fuel cell.....	41
3.1.4.3 Investigation of the swelling behavior of some organic coatings on metals.....	45
3.1.5 Concluding remarks on dealing with temporal drift in dynamic transfer functions.....	46
4 Extended library for impedance models.....	48
4.1 The impedance of porous electrodes.....	48
4.2 The impedance of inhomogeneous dielectrics.....	52
4.2.1 The impedance of cover layers with conductivity gradients.....	54
4.2.1.1 The Young-Göhr impedance.....	56
4.2.1.2 The application of the Young-Göhr impedance in the Mott-Schottky analysis.....	59
4.2.1.3 The impedance of dielectrics with power law conductivity curve based on A. I. Sotnikov.....	63
4.2.1.4 The PIN model.....	64
4.3 The behavior of the impedance under the influence of the test variables voltage and current on the system parameters.....	67
4.3.1 Faraday impedance of systems with temporal relaxation of the effective rate of the transmission reaction.....	68
4.3.2 The influence of current heat on the impedance of systems with significantly temperature-dependent conductivity.....	70
4.3.3 The general relaxation impedance.....	77
5 Modeling photo-electrochemical transfer functions.....	79
5.1 Program implementation.....	82
5.1.1 Stack-oriented calculation rule.....	82

5.2 Models	86
5.2.1 The extended photocurrent source	87
5.2.2 The porous dye-sensitized solar cell model according to L. Bay and K. West.....	88
6 Optimization and fit of transfer function triplets	91
6.1 Fitt procedure for impedance spectra (Complex Non Linear Least Squares "CNLS" fit)	92
6.2 "TRIFIT" procedure	94
7 Experimental applications of photo-electrochemical TFA	96
7.1 Optimization of measurement technology for intensity-modulated photospectroscopy	96
7.1.1 Principle of the traditional measurement technique for IMPS / IMVS known from the literature	96
7.1.2 The principle of intensity control: "Controlled Intensity Modulated Photo Spectroscopy" CIMPS.....	98
7.2 Dynamic measurements on a dye-sensitized solar cell based on TiO₂ nanotubes... 99	
7.2.1 Experimental	100
7.2.2 Modeling of a TiO ₂ nanotube photo anode according to L. Bay and K. West	104
7.2.3 Discussion of the results achievable with the model according to L. Bay and K. West	105
7.3 Physical and dynamic measurements on tantalum oxide films	107
7.3.1 Preparing the samples and setting up the electrochemical experiments	107
7.3.2 Electrochemical and photo-electrochemical measurement campaign on the tantalum oxide film	109
7.3.3 Physical measurements on the tantalum oxide film.....	109
7.4 Discussion and evaluation of the measurement results on the tantalum oxide film	109
8 Appendix	118
8.1 List of multiple formula characters	118
8.2 List of frequently used abbreviations	120
8.3 Linear Kramers-Kronig transformation via FFT and IFFT in the -s-plane	121
8.4 Examples of the user-defined calculation of an impedance element	123
8.4.1 Source code of the Landes-Hahn temperature relaxation impedance	124
8.4.2 Source code of the 1st order temperature relaxation impedance.....	124
8.4.3 Source code of the general relaxation impedance	124
8.5 Derivation of the general relaxation impedance	124
8.6 The equivalence between the impedance of a porous electrode according to L. Bay and K. West and according to H. Göhr	128
8.7 Conversion of the specific photoelectric transfer function according to L. Bay and K. West for non-specific quantities with elimination of linearly dependent, redundant parameters	131
9 Bibliography	133

1 Introduction, motivation and problem definition

The world is determined on all scales by the flow of time, which manifests itself in the flow of energy. This controls the development of the universe as well as our personal destiny. The constant flow of energy from the high-quality reservoir of low entropy towards higher entropy favors the formation of structures through self-organization and, at the extreme, leads to life. The competition of time-dependent processes determines the direction in which physical reality moves.

Due to the great importance of time dependencies, natural science strives to develop effective experimental and theoretical tools. We have the pioneers Pierre-Simon Laplace and Jean-Baptiste-Joseph Fourier to thank for the realization that complicated interwoven processes in time are easier to understand in the mathematical space of periodic processes, the "frequency domain". This is the starting point of the dynamic transfer function analysis "TFA". In recent decades, TFA has established itself as a valuable tool in many areas of science and technology. In electrochemistry, it is in the form of impedance spectroscopy EIS, which describes the dynamic behavior of electrical voltage on and current through a measured object. It is ideally suited to investigating the mechanisms and kinetics of electrochemical processes, e.g., in fuel cells. The analog transfer functions of photo-electrically active systems between light intensity and voltage IMVS, or light intensity and current IMPS, can provide deep insights into the nature of photo-electrochemical processes and have become particularly important for the development of new types of solar cells.

A high level of significance in the interpretation of the measured transfer functions TF is achieved by simulating the dynamic behavior of the object under investigation in a suitable physical model and comparing the model calculation with the measurement results.

The method most frequently used in EIS adapts "equivalent circuit diagrams" to the measured transfer functions through simulation and iterative optimization. It requires knowledge of the impedance behavior of the processes taking effect in the measurement objects and their interactions.

This behavior is generally known for the basic electrochemical processes in many cases and is part of common evaluation programs. However, the widely used simple models can sometimes only imperfectly reproduce the impedance spectra observed in practice.

One aim of the work presented was to equip a calculation program developed within this framework with impedance models known from the literature and additionally developed in-house in such a universal way that a high degree of coverage of the cases relevant in practice is achieved.

In the event that the investigated transfer functions still contain components that were not provided for in the library of impedance models, a special compiler should enable the simple integration of any algorithms and rules defined by the user for the calculation of impedances.

Similar to the EIS, the calculation program should support the quantitative evaluation of IMPS and IMVS data by providing corresponding models.

The successful application of the dynamic transfer function analysis TFA naturally requires more than just sufficient support for modeling. Practical applicability is subject to certain requirements regarding the physical behavior of the measurement objects themselves and the boundary conditions of the measurement method. Strictly speaking, some of the requirements of TFA, such as compliance with stability, linearity and periodicity, contradict the behavior of real objects and the practical feasibility within a reasonable finite amount of time.

A further aim of the work was therefore to minimize the effects of this systematic control violation during the measurement by improving the measurement data acquisition and also to obtain reliability parameters.

Newly developed methods were to be used to check the measurement data during analysis for violations due to temporal changes in stability and causality rules and deviations from the required behavior for two-pole impedances. A reliable criterion for estimating measurement errors was to be obtained from the unwanted noise component in the response signal that occurs directly during the TF measurement.

The desire to improve the methodology of TFA arose from problems that came up when applying the techniques already available to systems under investigation. A simulation and optimization

program that could be used as universally as possible had become necessary in order to be able to model porous systems of fuel cell and battery electrodes realistically enough. The oxide layers and films on metals, which were also investigated as part of the work, required the implementation of a series of new models that could take into account conductivity gradients and dielectric relaxation processes within the layers. Partial surface blocking, such as occurred during active-passive transitions at corroding electrodes and CO poisoning of polymer membrane fuel cell anodes, could be understood by implementing a model for surface relaxation.

The processes of corrosion and poisoning of fuel cells are also exemplary for systems with implicit instationarity. In such systems, their properties change significantly within the TF measurement time. This provided the motivation to develop drift detection and correction methods and triggered the desire to be able to generally determine the reliability of TF measurement data directly during the measurement as a measurement uncertainty.

IMPS and IMVS measurements were required for the photo-electrochemical investigation of tantalum oxide layers. The same technique was used for investigations on dye-sensitized solar cell anodes made of nano porous and nanotubular titanium dioxide. In order to avoid the systematic scale and phase errors that are unavoidable with the traditional IMPS and IMVS technique and to enable long-term stable, calibrated TF measurements at modulated light intensity, the known technique had to be extended accordingly.

The combination of the results from EIS, IMPS and IMVS measurements, determined on a single test object, is particularly promising, as it allows ambiguities in the models of the individual methods to be eliminated. For this purpose, the simulation and optimization program had to be enabled to simulate the data of all three transfer function types using a common model and at the same time be able to fit a common error minimum.

2 The dynamic transfer function analysis TFA

The dynamic transfer function analysis TFA is an established method that is often used in EIS, for example, and its basics can certainly be assumed to be known. In view of the chapters on plausibility checks for experimental TF data and the discussion of the less popular photoelectric TF, it nevertheless seems useful to briefly describe the basics of TFA in connection with EIS, IMVS and IMPS.

If a real physical system S is investigated, its behavior should be sufficiently described by a not too large set of n measurable properties E_i such as concentration, pressure, temperature, voltage, current (Figure 1). Since each property can be dependent on the other properties, an extensive set of functions f of many properties may be required for a sufficient description:

$$E_i = f(E_1, E_2, \dots, E_{i-1}, E_{i+1}, \dots, E_{n-1}, E_n) \quad (1)$$

When investigating such systems, for example using thermodynamic or electrical methods, it is advantageous to focus on pairs of individual dependencies a , such as:

$$E_2 = a(E_1) \quad (2)$$

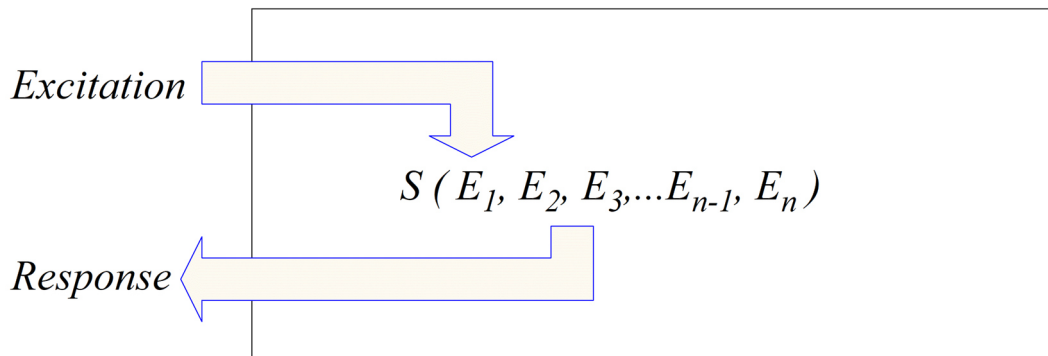


Figure 1: Schematic of a physical system S , which can be characterized by the properties E_i . Two selected properties E_1 and E_2 form a transfer function pair as in Eq. (2)

The electrical voltage U_I on an object as a function of the current I flowing through the object forms such a representative pair, as well as the photovoltage U_P as a function of the light intensity P , and the photocurrent I_P as a function of the light intensity P in photoelectrically active systems, Eq. 3.

$$U_I = a_{UI}(I), \quad U_P = a_{UP}(P), \quad I_P = a_{IP}(P) \quad (3)$$

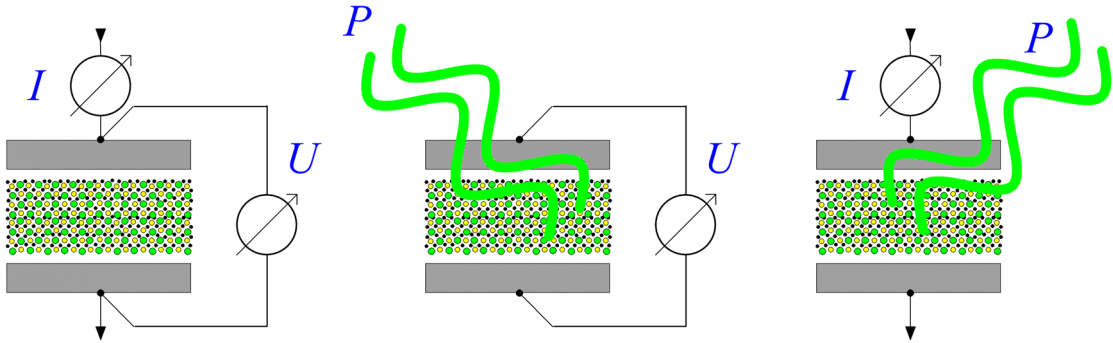


Figure 2: Basic schemes of the TF measurements discussed in this paper. Left: Space element filled with matter with electrically contacted ends. The total voltage U is measured at the taps and the current I through the taps. Center and right: Measurement of photovoltage and photocurrent as a function of the light intensity P on a photo-electrically active object.

The transfer function $a_{2,1}$ is determined by specifically changing only the property E_1 of the properties E_i and observing the property E_2 . (In the following, the "test function" E_1 is labeled with the index f for "force" and the "response function" E_2 with the index r for "response")¹.

In the time-independent limiting case, the stationary versions of the current-voltage curve, light intensity-voltage characteristic and light intensity-current characteristic of an object are found for the systems in Eq. 3. If the current-voltage curve is not only time-independent, but also linear and passive², Ohm's law Eq. 4 follows with the resistance R :

$$U = a(I) = R \cdot I, \quad R = const \quad (4)$$

The intensity photocurrent characteristic Eq. 3 of an ideal photodiode at zero or negative bias voltage behaves similarly with the photocurrent efficiency η :

$$I_p = \eta \cdot P, \quad \eta = const \quad (5)$$

In order to be able to describe the non-linear, active case, which is much more common in physical practice, the definition of resistance can be extended to the "differential resistance" R_{diff} Eq. 6 and assign one to each point of any continuous current-voltage curve.

The same applies to the photovoltage and photocurrent efficiencies Eq. 7, 8 η_{diff} of a photoactive electrochemical object such as the oxide anode of a dye-sensitized solar cell (DSSC).

¹ For certain pairs of properties, such as voltage on an object and current through this object, or force on a point of a deformable object and the path of this point during deformation, the excitation and response variables are localized "at the same point of attack", so to speak. In the chapter on the verification of measurement data, the special aspects of such "two poles" must be discussed in more detail. There it is shown that their TFs are subject to stricter rules than, for example, the TFs of "four poles". Such less restricted TFs can be imagined on the basis of the TF force-displacement if the deformation-force-displacement example discussed above is compared with the behavior of the pedal force and brake shoe displacement of a servo brake in a vehicle.

In some systems, such as two-terminal systems, the role of the excitation and response functions can easily be interchanged experimentally to arrive at the inverse TF. This applies quite practically to the EIS, where impedance and the inverse function admittance can be determined both potentiostatically (the voltage is specified as the "excitation function") and galvanostatically (the current is specified as the "excitation function"). With the IMPS and the IMVS, as in the example of the servo brake, the interchangeability is not given.

² An electrochemical system is called electrically passive if its current-voltage curve includes the zero point (as with ohmic resistance), in contrast to an "active" battery, for example.

$$R_{diff}(U, I) = \frac{dU}{dI} \quad (6)$$

$$\eta_{U,diff}(U, P) = \frac{dU}{dP} \quad (7)$$

$$\eta_{I,diff}(I, P) = \frac{dI}{dP} \quad (8)$$

If we move from the stationary limiting case to a description that includes time dependence, we must take into account that the response function E_r no longer depends only on the respective instantaneous value of the excitation function E_f at time t_1 , but also on its previous history $t \leq t_1$ Eq. 9.

$$E_r = f[E_f(t \leq t_1)] \quad (9)$$

Such physical objects with "memory" are usually described by time-dependent differential equations as in Eq. 10.

$$E_r = a_0 + a_1 \cdot E_f + a_2 \cdot \frac{dE_f}{dt} + a_3 \cdot \frac{d^2 E_f}{dt^2} + a_4 \cdot \frac{d^3 E_f}{dt^3} + \dots \quad (10)$$

For the coupled systems frequently used in electrochemistry, the treatment of the associated non-linear differential equation systems in the time domain is hardly practicable. However, the analysis can be simplified considerably in three steps. In the first step, the stationary part of Eq. 11 is separated by considering the system at a specific bias.

$$E_{bias} = a_0 + a_1 \cdot E_f \quad E_r = E_{bias} + E_t \quad (11)$$

In the second step, the resulting time-dependent remainder E_t Eq. 12 is examined for very small changes dE_f of the excitation function and the higher-order terms can therefore be neglected.

$$E_t = a_2 \cdot \frac{dE_f}{dt} \quad (12)$$

In the last step, the three-way relationship between excitation function - response function - time is simplified by restricting it to a sinusoidal progression of the excitation function in time (Eq. 13) with the amplitude A , the periodicity factor $e^{j\omega t}$, the imaginary unit j , the angular frequency ω and the phase shift φ , which is formally equivalent to applying the Laplace transformation using the operator $s = j \cdot \omega$

$$E_t = A \cdot e^{j\omega t} \quad (13)$$

Stable systems respond to sufficiently small, sinusoidal excitations Eq. 14 also sinusoidal Eq. 15 with a phase shift φ that is generally different from zero. This makes it possible to use the quotient of the sinusoidal response function divided by the sinusoidal excitation function to obtain a characteristic time-independent, generally complex variable, the "dynamic" transfer function H^* in Eq. 16.

$$E_{if} = A_f \cdot e^{j\omega t} \quad (14)$$

$$E_{ir} = A_r \cdot e^{j(\omega t + \varphi)} \quad (15)$$

H^* describes the behavior of a physical system with the transfer function modulus $|H|$ and the phase shift φ much more conveniently, since the differential and integral equations necessary for the description in the time domain are simplified to algebraic relationships in the frequency domain.

$$H^*(\omega) = \frac{A_r \cdot e^{j(\omega t + \varphi)}}{A_f \cdot e^{j\omega t}} = |H| \cdot e^{j\varphi} \quad (16)$$

The impedance Z^* Eq. 17 is the type of dynamic TF most commonly used in this work. In an electrochemical system, partial impedances can be assigned to components and sub-processes that are characteristic of chemical and kinetic parameters, mechanisms and electrode topology. The partial impedances (hereinafter referred to as "impedance elements") generally differ in their frequency behavior, so that they can be identified and finally determined within the properties of the overall network due to the manageable linking rules in the frequency domain.

$$Z^*(\omega) = \frac{U_0 \cdot e^{j(\omega t + \varphi)}}{I_0 \cdot e^{j\omega t}} = |Z| \cdot e^{j\varphi} \quad (17)$$

This is the basis for the widespread practice of evaluating EIS data using simulation and fitting programs for electrical equivalences ("equivalent circuit diagrams"). Although the same considerations apply to the dynamic TF IMPS and IMVS Eq. 18, 19 of photo-electrically active systems, the evaluation of their complete electrical equivalences is not very popular. Due to the lack of convenient calculation tools, it is usually limited to the determination of a characteristic frequency or time constant.

$$\eta_{IMPS}^*(\omega) = \frac{A_I \cdot e^{j(\omega t + \varphi)}}{A_P \cdot e^{j\omega t}} = |\eta_{IMPS}| \cdot e^{j\varphi} \quad (18)$$

$$\eta_{IMVS}^*(\omega) = \frac{A_U \cdot e^{j(\omega t + \varphi)}}{A_P \cdot e^{j\omega t}} = |\eta_{IMVS}| \cdot e^{j\varphi} \quad (19)$$

In summary, it can be said that the behavior of real, stable systems with small deflections in the time domain can be unambiguously converted into their behavior in the frequency domain (and vice versa) using the Laplace transformation. The Laplace transform can therefore be used, for example, to deduce the corresponding impedance spectrum from the time laws for voltage and current of an object. On the other hand, it can be concluded from the Fourier transformation that the restriction to sinusoidal time functions is of a purely formal nature, as the behavior of any time function can be inferred if the frequency spectrum is completely known.

As will be explained later, the "sine wave methods" nevertheless have decisive advantages in the practical application of dynamic TFA, as in impedance spectroscopy, compared to "multispectral" methods that use arbitrary test time functions. Especially when it comes to the effect and identification of measurement errors, the direct physical application of purely sinusoidal excitations proves to be superior to the multispectral approach.

3 Optimization of signal evaluation for the TFA

3.1 Verification, correction and evaluation of measured transfer functions

Measured transfer functions such as the EIS are usually evaluated by applying physical models. The underlying processes must be identified and the numerical values of their characteristic parameters determined. The reliability of the determined results is decisive for the benefit of this procedure. In particular, accuracy estimates of the parameter values from model calculations and Fit procedures are required. Knowledge of the uncertainty of the measured values is the fundamental prerequisite for consistent error estimation. Finally, the accuracy of the determined parameters can be estimated examining the error propagation via modeling and Fit procedures. However, the individual error of the measured values is not the only contribution to the overall uncertainty. There is also the question of the extent to which the measured transfer function can be attributed exclusively to the object of interest. The influence of the measurement setup on the measurement result is often underestimated and the contributions of parasitic effects on the transfer function are not recognized. In EIS, these are, for example, the stray capacitance and inductance of connection lines, the magnetic coupling between current-carrying and voltage-measuring lines ("mutual induction") [108], [109] or the internal resistance of reference electrodes [110], [109]. Similar to oversimplified model assumptions in the analysis, the errors caused by artefacts can be minimized by careful measurement setup and consideration in an appropriately extended model.

The effects of inadequate model concepts are therefore not the subject of the following section. Instead, the first section explains the procedure developed in this thesis for determining a reliability criterion during the ongoing measurement. The second section explains how the measurement uncertainties determined can be used to estimate the accuracy of the parameters found by modeling and the Fit procedure.

To ensure that the mathematical simplification strategy discussed in Chapter 2 can be applied, the measurement technique and the object of investigation must ensure compliance with linearity, stability, periodicity and causality, which goes hand in hand with the applicability of the Kramers-Kronig transformation "KKT" [67], [68], [69], [70]. Violations of linearity, stability and periodicity are reflected in the measurement uncertainty, as shown in the first section of this chapter. Causality in the sense of KKT does not mean the universal cause-effect relationship, but the relationship between a unique system state of the object under investigation and its measured transfer function. If the system changes noticeably during the measurement period, this causality is violated. Many processes investigated by means of transfer function analysis are subject to such temporal drift, as in the field of corrosion or battery research. The third part of this chapter therefore presents the strategies developed in the course of the work on how drift can be detected and its effects minimized during measurement and evaluation.

3.1.1 Estimation of the measurement uncertainty of TFA data during the recording of experimental spectra

When recording spectra, measured data is assigned to discrete frequencies. This assignment cannot be carried out with arbitrary precision, as spectrally pure frequencies are not available in a finite measurement time. This can be visualized using the example of the correlation between the frequency bandwidth Eq. 20 of an atomic emission line Δ_ω and the state lifetime τ .

$$\Delta_\omega = \frac{1}{\tau} \tag{20}$$

For any type of transfer function analysis, it is also generally the case that a frequency uncertainty must be attributed to the discrete examination frequencies, which is proportional to the inverse measurement duration. Therefore, even a perfect measuring instrument according to Eq. 20 can only be attributed a limited frequency accuracy. During a real measurement, further disturbances occur in addition to the disturbances according to Eq. 20. In general, the problem can be formulated as limited frequency selectivity (LFS) as follows: With TFA, unwanted interference ("noise") occurs in addition to the desired signal response, which is

inevitably also recorded due to the LFS. The signal-to-noise ratio (S/N) can therefore be used as a measure of the quality of a measurement.

In order to determine the S/N, it is necessary to be able to identify desired and undesired components in the response signal. This is possible with the method realized in the work [111]. It uses a sinusoidal signal ("monochromatic") excitation. The response signal is acquired with high oversampling [75] and subject of a complete frequency analysis ("Monochromatic Oversampling Method" MOS) (Figure 3). Using MOS, the transfer function can be calculated from the quotient of the fundamental waves, while the higher-order components ("harmonics") can be clearly assigned to unwanted interference.

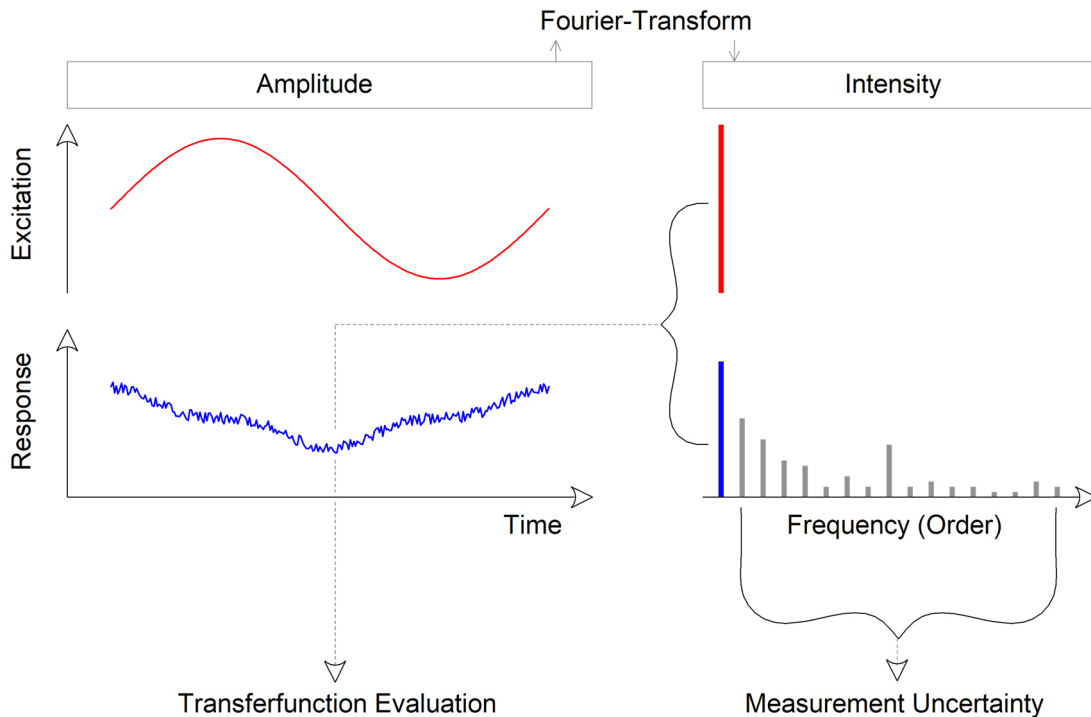


Figure 3: Functional diagram of the TFA based on the method of monochromatic oversampling MOS. The excitation function (red) is sinusoidal and periodic. The response function (system response, blue), which is also periodic, can be distorted by disturbances (non-linearity, noise). After the Fourier transform, the TF can be determined from the quotient of the fundamental waves. The frequency components of higher harmonic order (gray) can be used to estimate the measurement error.

However, the extent to which harmonics interfere with the measurement result for the TFA cannot be indicated by simply determining the S/N. Instead, the harmonic component must be weighted in a special way, as the following explanations will show.

In Figure 4 an undisturbed response signal is shown symbolically together with an interference signal of three and a half times the frequency. Due to the fractional period duration ratio, positive and negative deflections of the interference signal do not completely cancel each other out on average over time. Due to the finite measurement time, the mathematical evaluation method can only detect precisely frequency components that are multiples of the signal frequency ("harmonics")³ The interference signal contaminates the result for the fundamental wave. The TFA determined from the quotient of the fundamental waves is inevitably distorted by such leakage. If one compares Figure 4 with the ratios shown in Figure 5 it can be seen that as the frequency of the interfering signal increases, the interfering component loses influence due to the shorter period.

³ The continuous Fourier integral cannot be used directly for frequency analysis of experimental data because the experimentally unobservable period from zero to infinity is mapped to a continuous (infinitely high) frequency resolution. Only a finite number of discrete measurement samples can be determined in a finite observation interval τ ("measurement window"). Experimentally, the most effective method is uniform sampling in successive measurement windows with subsequent discrete Fourier transformation. This leads to discrete frequencies at intervals of $1/\tau$, the "harmonics".

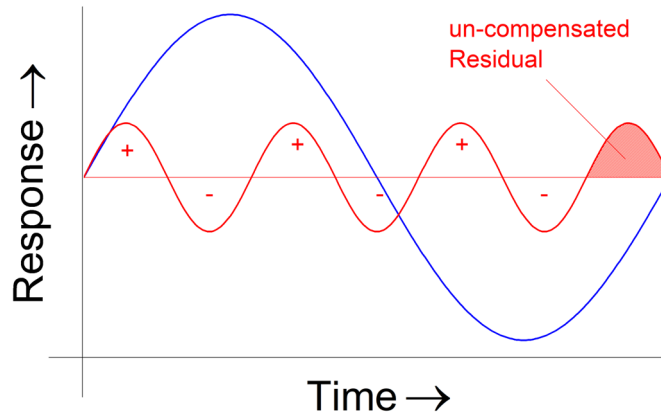


Figure 4: Schematic of a response signal (blue) together with a disturbance of 3.5 times the frequency of the wanted signal (red). The shaded area (a positive half-wave of the interference signal) symbolizes the portion of the signal integral that does not average out within the period of the measurement signal.

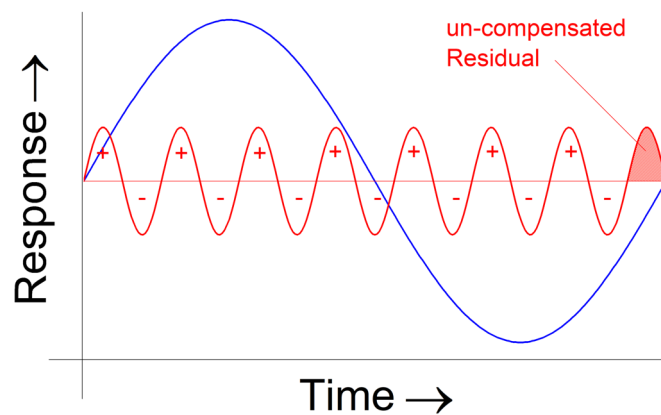


Figure 5: Schematic of a response signal (blue) together with a disturbance of 7.5 times the frequency of the wanted signal (red). The portion of the interference signal integral that does not average out within the period duration of the measurement signal is smaller than at 3.5 times the frequency due to the shorter period duration.

Furthermore, a comparison with Figure 6 shows that with a "suitable" period duration, the interfering components balance each other out perfectly. To summarize, it can be said that the influence of interfering signals decreases with increasing frequency compared to the wanted signal. It disappears when the frequency of the interfering signal is an integer multiple n of the wanted frequency f . In the frequency plane, exactly one line for the interfering frequency then appears next to the frequency line of the fundamental wave. In contrast, the interference effect is maximum at frequencies $f \cdot (n+0.5)$. In this case, the frequency analysis results in two additional lines of approximately equal intensity next to the fundamental wave, which correspond to frequencies of $f \cdot n$ and $f \cdot (n+1)$.

This means that contaminating harmonics, which impair the measurement accuracy, are always accompanied by adjacent lines. Conversely, "isolated" harmonics without adjacent lines do not contribute to measurement errors.

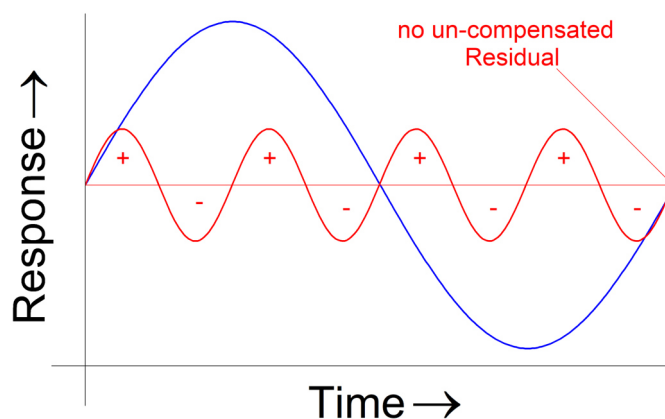


Figure 6: Schematic of a response signal (blue) together with a disturbance of 4 times the frequency of the wanted signal (red). The portion of the interference signal integral that does not average out within the period of the measurement signal disappears at interference frequencies that are integer multiples of the fundamental frequency.

Unfortunately, even the best electronics cannot prevent the excitation signal from containing unwanted interference components ("distortion factor"), especially at the power limit of a potentiostat at high currents and high frequencies. This must be taken into account when assessing the interference in the response signal. Obviously, the greater the intensity of the interference in relation to the useful signal, the more effective it is. Finally, this leads to a strategy ("Weighted Harmonics Autocorrelation" WHA) for assessing the effect of interference frequencies that appear as harmonics in the response signal spectrum:

1. Determine the intensity-frequency spectra of the excitation and response signal.
2. Calculate the transfer function from the quotient of the fundamental wave intensities.
3. Weight the harmonic intensities with the reciprocal of their frequency.
4. Divide the harmonics by the intensity of the fundamental wave.
5. Consider harmonic components that already appear in the excitation signal.
6. Carry out an autocorrelation of the weighted harmonics.
7. The autocorrelation amplitude for the line spacing 1 is the desired indicator for the measurement uncertainty.

As explained above, the composition of a signal mixture cannot be measured with arbitrary accuracy in a finite time, but it is easy to calculate how a measurement result for a known signal mixture is distorted by the limited measurement time. To do this, a time section (e.g., one period) of the superposition of a sinusoidal useful signal with a variable proportion of interference signal is simulated and subjected to Fourier analysis. The ratio of the useful signal intensity used in the simulation and the result of the Fourier analysis for the fundamental wave indicates the deviation to be expected in the experiment. At the same time, the autocorrelation amplitude for the line spacing 1 can be calculated from the WHA. The comparison of both values can be used to calibrate the WHA.

For the final method, the WHA was normalized so that its measurement uncertainty specification corresponds to the observed error in the presence of stochastic disturbances (white noise). The method was tested by simulation and control experiments for its suitability for other types of interference. The simulation in Figure 7 shows the comparison of the actual deviation and the deviation estimated with the WHA for the case of a sinusoidal interference signal of variable frequency.

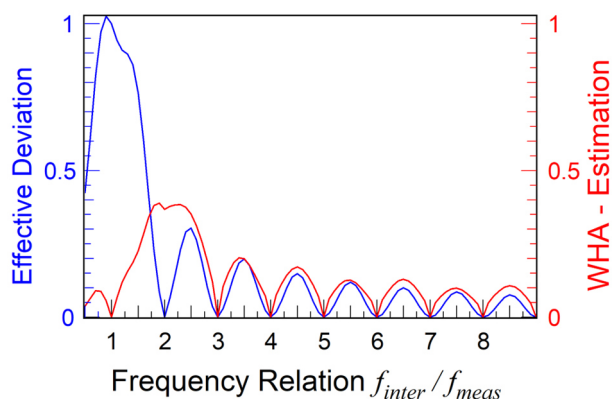


Figure 7: Test of the WHA method for sinusoidal interference signals f_{inter} by simulation. Comparison of the actual deviation caused (blue) and the measurement uncertainty predicted by the WHA method (red).

For interference frequencies greater than twice the measurement frequency, the estimate and the deviation actually observed approximately coincide. As expected from the above considerations, the influence of the interference decreases with increasing frequency. It is locally maximum at frequency multiples $f \cdot (n+0.5)$ and disappears at integer multiples of frequencies $f \cdot n$. Deviating from this, there is a noticeable discrepancy for interference frequencies close to the useful frequency. In principle, the time required for an accurate measurement approaches infinity if the interfering frequency approaches the useful frequency arbitrarily. Unfortunately, the WHA cannot provide a reliable error estimate under these circumstances.

In order to test the influence of external interference caused by bandwidth-limited noise ("pink noise") and by individual frequencies such as the mains frequency in practice, an electrical model ("equivalent circuit diagram" ESB) representative of a moderately complicated electrode reaction was set up for the control experiment (Figure 9) and measured in a potentiostatic arrangement under optimum conditions. Alternatively, an interference signal from a function generator could be fed into the measuring circuit for the reference electrode (Figure 8).

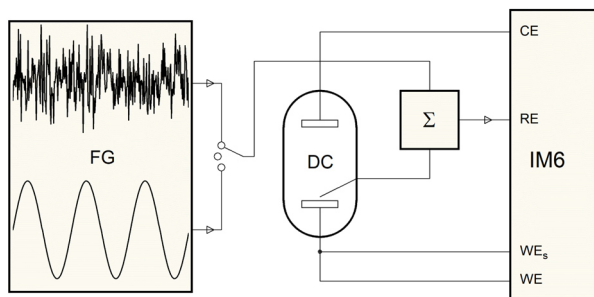


Figure 8: Test setup for measuring the influence of noise limited in the frequency bandwidth and single frequency interference on the accuracy of impedance measurements. FG: Function generator for injecting pink noise or sinusoidal interference. DC: Electrode model (dummy cell DC). Σ : Summing circuit. WE, RE, CE: Working, reference and counter electrode connection of the test cell to the impedance measuring system.

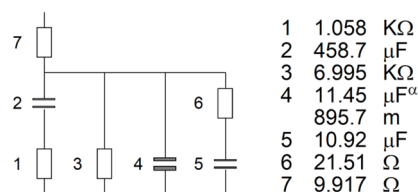


Figure 9: Detailed circuit diagram of the test object shown in Figure 8 sketched test setup. Symbolic meaning of the circuit elements: 1, 2: hindered adsorption. 3 Charge transfer resistance. 4 Double-layer capacitance. 5, 6: Further hindered adsorption. 7: Electrolyte resistance.

Figure 10 and Figure 11 show that for both types of external disturbances the error estimation with the WHA is in acceptable agreement with the actual observed scatter.

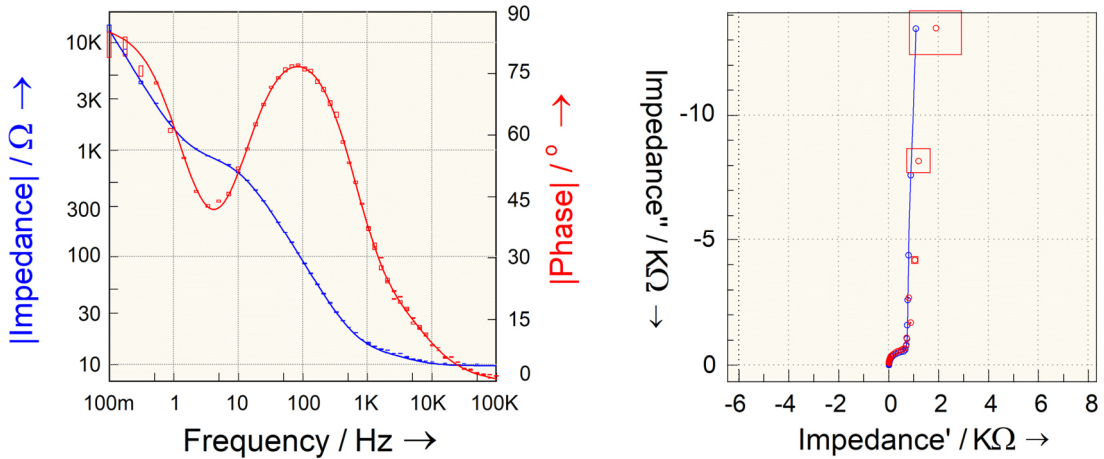


Figure 10: Bode (left) and Nyquist (right) diagrams of the control measurement according to Figure 8 on the influence of pink noise on the measurement accuracy of impedance spectra. The solid lines (blue and red for impedance magnitude and phase on the left, blue for the complex impedance on the right) are measured without superimposed interference. The sample point symbols indicate the measurement points under superimposed interference. The error bars or error squares around the perturbed measured values indicate the uncertainty estimated using the WHA.

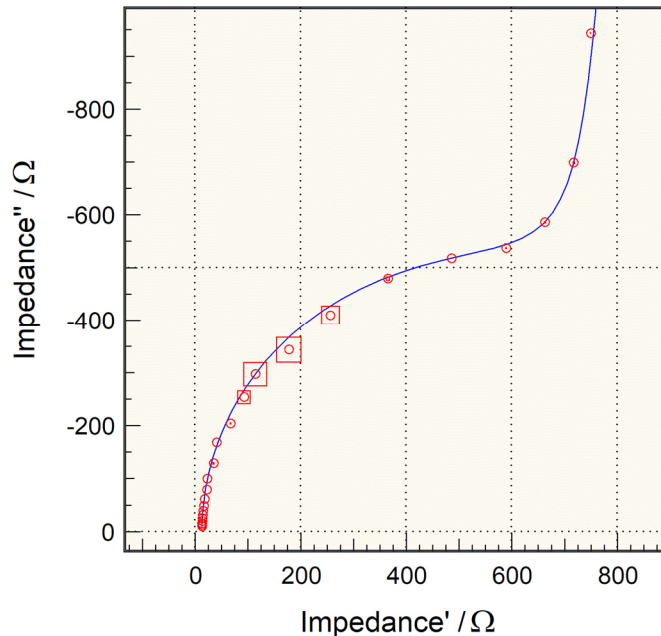


Figure 11: Nyquist diagram of the control measurement according to Figure 8 on the influence of single-frequency interference on the measurement accuracy of impedance spectra. The blue solid line for the complex impedance is measured without superimposed interference in the frequency range between 1Hz and 1KHz. The circle symbols indicate the measurement sample points under superimposed interference of 100Hz. The error squares around the perturbed measured values indicate the uncertainty estimated using the WHA.

In addition to external interference acting on the device under test DUT, harmonics generated by the non-linearity of the DUT itself can also affect the accuracy of the TFA. An anti-parallel circuit of two semiconductor diodes (power Schottky contact diodes, hot carrier diodes) was set up as a measurement object for a suitable control experiment. The current-voltage characteristic of such a combination corresponds to the Butler-Volmer curve of a symmetrical electrode reaction. A polarization current of $10\mu\text{A}$ was simulated by galvanostatic loading. The measurement of the comparative impedance spectrum with the highest possible accuracy was carried out with an amplitude of only 1mV in order to avoid the occurrence of non-linearities. A further measurement with an intentionally high amplitude of 20mV shows characteristic deviations that can be attributed to the occurrence of harmonics due to the non-linearity. Figure

12 shows that a useful error estimate can also be made for this type of disturbance using the WHA.

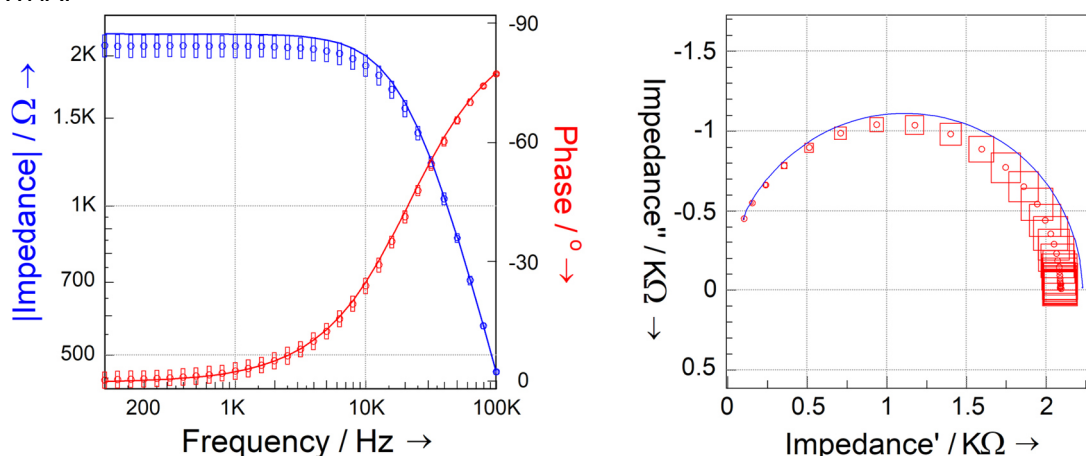


Figure 12: Bode (left) and Nyquist (right) diagrams of a control measurement on the influence of non-linearity with Butler-Volmer characteristics. The solid lines (blue and red for impedance magnitude and phase on the left, blue for the complex impedance on the right) are measured at an optimally small amplitude of 1mV. The sample point symbols indicate the measurement points when the amplitude is too high with 20mV. The error bars or error squares around the disturbed measured values show the uncertainty estimated using the WHA.

3.1.2 Estimation of the accuracy of parameters obtained from the TFA, taking into account the measurement uncertainty

The path from measurement to interpretation and evaluation of the data is usually aimed at determining the numerical values of the parameters, characteristic of the processes under investigation. In individual cases, the measurement uncertainty can be used to draw direct conclusions about the accuracy of the parameters achieved. When determining conductance and capacitance from the measured impedance for conductivity, capacitance or Mott-Schottky measurements, for example, it is sufficient to convert the measurement accuracy of the impedance to the uncertainty of the real and imaginary parts of the admittance.

In most cases, however, the relationship between measurement and result uncertainty is much less clear. The following considerations are also not intended to address the strategy sometimes used to extract parameter values from the geometric properties of measured transfer functions in special graphical representations such as the Nyquist diagram of impedance from the diameter of semicircles, axis intersections, etc. parameter values.

The most promising approach is based on a physical model of the system under investigation. An electrical equivalence ("equivalent circuit diagram") is created from the model, with the help of which it is possible to reproduce the measured transfer function in principle. By iterative comparison with the measured data and adjustment of the model parameters of the electrical model, an attempt is made to harmonize the model calculation with the measured data. At the end of this simulation and fitting process, the desired numerical values of the characteristic parameters are available as parameters of the adapted model.

With real objects, you will always have to accept a certain degree of imperfection in the modeling, also in order to limit the number of free variables. For this reason, and because of the uncertainty of the measurement data itself, the model calculation will never be in perfect agreement with the measured data set after the fit. Both contributions, fit and measurement errors, contribute to the overall uncertainty of the determined parameters. Due to the large number of possible models and their often non-linear properties, an analytical solution for error propagation appears neither reasonable nor feasible. In this work, an approximate determination of the total uncertainty was therefore attempted, which is based on plausible assumptions [112]. This includes the determination of significance, i.e., the assessment of the "importance" of elements of the model within the overall network. This is the subject of the following section 3.1.2.1.

The individual uncertainty of the measurement data should be taken into account in the Fit process. However, it often makes sense not to use the original measurement data. In order to

avoid excessive measurement times, the time required during the measurement for low frequency ranges is usually limited by reducing the number of frequency sample points. However, the physical information content of a transfer function is on average evenly distributed over all frequencies, since fast and slow processes contribute equally to the TF. In order to fit a model to a data set without overestimating certain frequency ranges, a uniform density of sampling points over the logarithm of the frequency is therefore desirable. As part of the work, a smoothing method was developed for processing the original measurement data, which should fulfill the following tasks:

1. Provision of interpolated sample points of the transfer function as a supplement to the original data, e.g., in logarithmic-equal frequency spacing.
2. Attenuation of the effect of local disturbances ("spikes").
3. Provision of the 1st and 2nd derivative of the transfer function according to the logarithm of the frequency.
4. Mapping of the uncertainty of the original measuring points to the interpolated sampling points.

In section 3.1.2.2 the interpolation procedure is explained.

In the last section 3.1.2.3 of this chapter is explained, how the individual uncertainties of the sampling points selected for the fit are included in the total error of the determined parameters.

3.1.2.1 Significance of elements in models for transfer functions

The concept of significance can be generally applied in TFA, e.g., also in IMPS/IMVS. Since the concept of significance can be easily justified in EIS, it will be explained using the example of an impedance model for an electrode reaction in which both the charge transfer reaction rate constant and the transport of reactants jointly determine the rate. The electrical equivalent circuit diagram shows Figure 13.

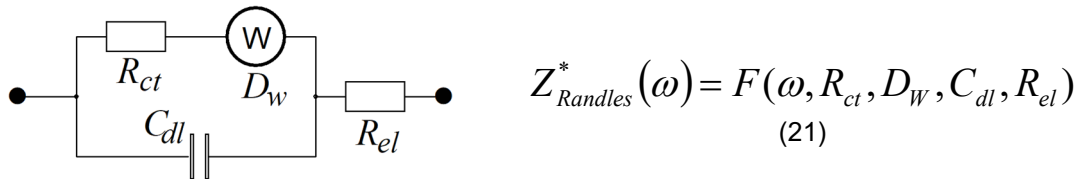


Figure 13: Equivalent circuit diagram ("Randles circuit") of an electrode reaction with diffusion hindrance with the parameters R_{ct} : charge transfer resistance, D_w : Diffusion impedance ("Special Warburg" impedance), C_{dl} : Double layer capacitance and R_{el} : Electrolyte resistance.

When looking at the influence of the parameters P of the various elements i in the model, it is noticeable that the elements contribute a particularly large amount to the total impedance Z in certain frequency ranges. For the limiting case of very high frequencies f , for example, the electrolyte resistance R_{el} is the sole determining factor, as the impedance of the residual network approaches zero due to the vanishing impedance of the double-layer capacitance.

In order to quantify the influence of a parameter value P_i via its relative contribution to the impedance, the significance S , Eq. 22 was defined.

$$S_i(f) = \frac{d|Z(f)| \cdot P_i}{dP_i \cdot |Z(f)|} = \frac{d|Z(f)|}{|Z(f)|} \cdot \frac{dP_i}{P_i} \quad (22)$$

In Figure 14 this is shown using the example of a Randles model, in which the course of the significances S_i of the parameters P_i is plotted against the frequency f .

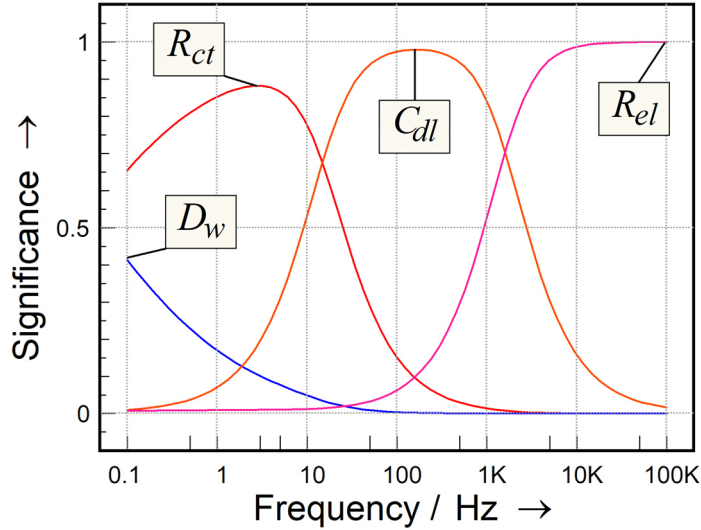


Figure 14: Significance curve (the relative contribution to the total impedance) of the elements of an electrode according to the Randles model (Figure 13) over the frequency. The frequencies at which the influence of a parameter becomes maximum are marked accordingly.

The characteristic significance S_{max} for the parameter is determined at the frequency of its maximum influence f_{max} . For impedance elements whose numerical parameter values are linearly related to the impedance, such as resistance and capacitance, the significance is a maximum of one, e.g., for R_{el} in Figure 14 at 100KHz. Since, as can be seen from the example of a "constant phase" element CPE, Eq. 23, parameters can also appear exponentially in the impedance, significances considerably greater than one can also occur.

$$Z_{CPE} = \frac{1}{(j \cdot \omega \cdot Q)^\alpha} \quad (23)$$

j = imaginary unit, ω = angular frequency, Q = loss capacitance, α = CPE exponent

The significance can be used to estimate the relevance of a parameter in the model. Impedance elements with significance values well below 1% may be dispensable. In the automatic fit routine ("complex non-linear least squares fit" CNLS), the significance can be used to control the feed parameters so that elements with lower significance are varied more in order to save computing time. The following consideration is used to estimate the parameter uncertainty: In general, a residual deviation $\Delta|Z_{fit}|$ at the frequency f_{max} remains at the end of a Fit procedure due to the fundamental incompleteness of the model, even with arbitrarily high measurement accuracy. If the parameter dominates here with a significance close to one, the parameter uncertainty $\Delta|P|$ corresponds approximately to the residual deviation $\Delta|Z_{fit}|$. Since the residual deviation can be attributed solely to the parameter under consideration in the worst case, even if the significance is smaller, $\Delta|Z_{fit}|$ must be weighted with the reciprocal of the significance (Eq. 24).

$$\Delta|P| \approx \frac{\Delta|Z_{fit}|}{S} \quad (24)$$

3.1.2.2 Smoothing and interpolation routine for measurement data.

The smoothing function mentioned at the beginning of chapter 3.1.2 should be continuous and at least twice differentiable.

$$Z_{Smooth} = \sum_{i=0}^d \left(a_i \cdot x^i \right) \quad (25)$$

For this purpose, the entire data set of the measured spectrum is entered into a second to fourth order d polynomial calculation with the coefficients a_i according to the logarithm x of the frequency for each interpolation point (Eq. 25) Z_{Smooth} of the interpolated curve. The measurement points are weighted using a Gaussian function of selectable width, which is maximum at the frequency location x of the interpolation point (Figure 15). In addition, the measurement uncertainty known from the "Weighted Harmonics Autocorrelation" WHA is taken into account. In addition, the measurement uncertainties of the data set are averaged for each individual interpolation point with its Gaussian weighting. In this way, an interpolated uncertainty is also assigned to each interpolated sample point Z_{Smooth} .

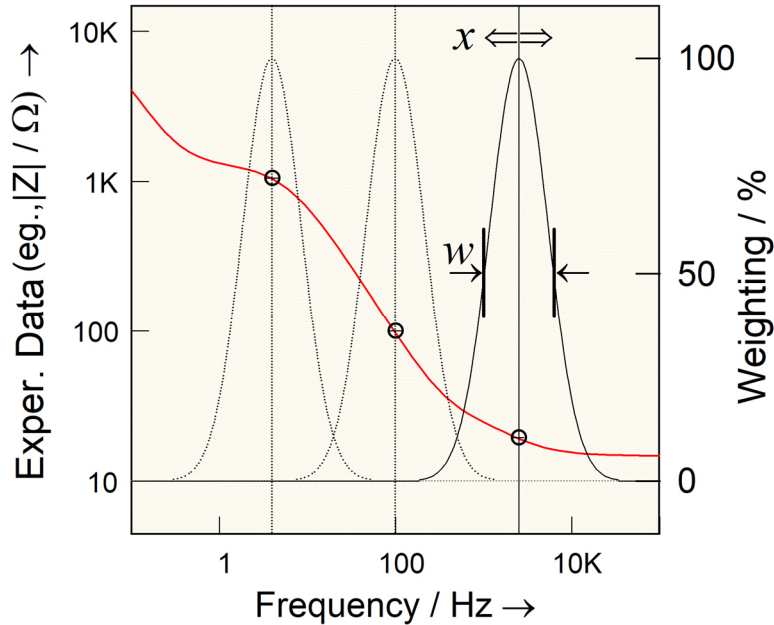


Figure 15: Creation of the local polynomials for calculating the sampling points (in the example at three different frequencies) of a smoothing function for a TF measurement data set. For each sampling point at frequency x , the entire data set is used, weighted with an individual Gaussian function of constant half-width w , but adjusted in the frequency position.

3.1.2.3 Consideration of the uncertainty of the sampling points in the Fitting process to estimate the overall uncertainty of the parameters determined in Fit

In 3.1.2.1 it was shown how the residual deviation $\Delta|Z_{fit}|$ after the Fit procedure between model calculation and measurement data can be used to estimate the accuracy of the determined parameter values $\Delta|P|$, neglecting the measurement uncertainty (Eq. 24). If the uncertainty of the data used for the Fit procedure $\Delta|Z_{sample}|$ is added absolutely to the residual deviation, the strategy according to Eq. 24 can finally be used to estimate the total uncertainty $\Delta|P_{tot}|$ of the results (Eq. 26).

$$\Delta|P_{tot}| \approx \frac{\Delta|Z_{fit}| + \Delta|Z_{sample}|}{S} \quad (26)$$

The measurement uncertainty or the interpolated uncertainty must then be entered as the uncertainty $\Delta|Z_{sample}|$, depending on whether the original data or interpolated data is used for the fit.

Figure 16 shows the complete process of parameter determination from the measurement data schematically. Either the original measurement data or the logarithmic-equidistant interpolated sampling points from the smoothed data can be used as a reference for the Fit procedure. In the third path shown, the ZHIT transform is calculated from the smoothed curve as a reference in order to approximately free the experimental measurement data from the artifacts caused by temporal drift. This procedure is explained in the following chapter. In the first case, the uncertainties of the experimental TF found by means of the WHA are used to estimate the accuracy of the model parameters; in the other cases, the interpolated uncertainties of the synthesized sampling points are used for this purpose.

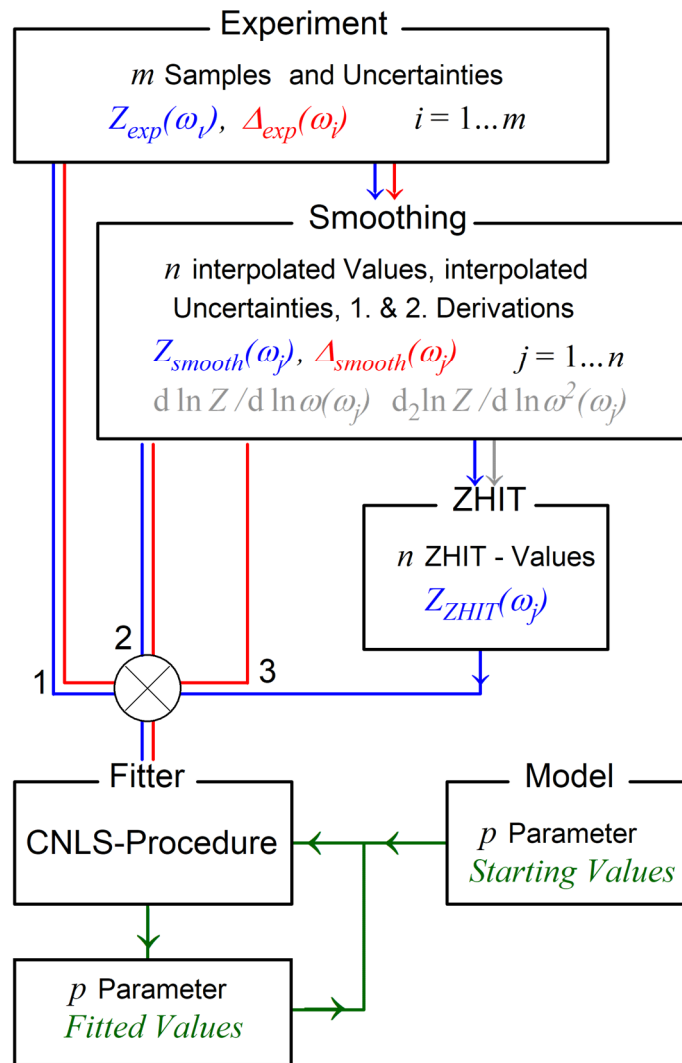


Figure 16: Flow chart for the determination of physical parameters from the TF. The left branch (1) shows the use of the original measurement data for the model-fitting process, the middle branch (2) shows the use of the smoothed curve. The values of the absolute impedance of the reference grid points in the right-hand branch (3) are calculated from the smoothed curve using the ZHIT method, see the following section.

3.1.3 Effects of the time dependency of systems examined with the TFA and their treatment

An almost ubiquitous problem in the practical application of TFA is that the objects under investigation are not arbitrarily stable over time. Striking examples of this are the impedance of electrodes under the influence of corrosion or of batteries under load.

If an object of the TFA changes noticeably during the measurement, the measured values determined at individual frequency sampling points no longer belong to a single, coherent spectrum. Instead, each sample represents a section of a sequence of different spectra, each of which belongs to a slightly different state of the system at different times.

The measurement result determined under such conditions does not fulfill the criteria for the spectrum of a clearly defined causal system Eq. 9. This means that one of the above-mentioned prerequisites for the applicability of dynamic TFA is not fulfilled. In practice, this means that such a spectrum cannot be represented directly with regular models for the TF. The usual procedure for evaluation using model simulation and fitting then fails. However, depending on the time scale of the drift and the time of detection, its effects can be successfully countered at different levels.

However, if the temporal drift is strong enough for strong changes to take effect at low frequencies within individual recorded periods of the measurement frequency, it makes not much sense to record in this frequency range.

The prerequisite for TFA is the extraction of the dynamic-periodic component of the system response. In stationary systems, a constant component (bias) can be subtracted from the response signal for this purpose. If the bias is not constant, a linear change over time can be approximately assumed if the drift is small. This can be visualized, for example, by the slowly decreasing measurement voltage of a battery with a constant current load. In the first section 3.1.3.1 of this chapter the "On-Line Drift Compensation" method is described, developed in the course of the work, which noticeably reduces the distortion of the TF due to drift during the recording of the measurement data.

If the drift is even weaker, it becomes apparent only when comparing consecutively measured spectra that the system under investigation has already changed over time during the recording. In section 3.1.3.2 a method is described that calculates spectra that are approximately free of drift from spectra series by interpolation over time. The method according to H. Göhr was already published in German language in 1979 [82], [85], but published also in 1984 e.g. by Z. Stoykov and B. Savova-Stoykov [84]. Because it contributes to the comprehensive treatment of time-dependent TF in the program package, it is characterized in this paper.

In section 3.1.3.3 finally, the significance and application of ZHIT in the identification and treatment of time dependencies is explained.

3.1.3.1 "On-line" drift compensation

With a temporally unstable test object, even without a superimposed excitation function, you can observe how the response function changes over time. If you carry out a frequency analysis on such a system response in a necessarily limited time interval, you will observe frequency components that differ from zero. If the change over time is approximately linear, the frequency spectrum of the Fourier transform corresponds to a sawtooth function (Figure 17) [107]. If the change is not too large compared to the desired response function, the drift can be determined from the shift of successive periods, e.g., by linear regression. Instead of a constant bias value, a bias that changes linearly over the measurement window can be subtracted to determine the dynamic-periodic system response. This allows the distortion of individual measurement points measured at low frequencies to be suppressed relatively effectively (Figure 18) [92].

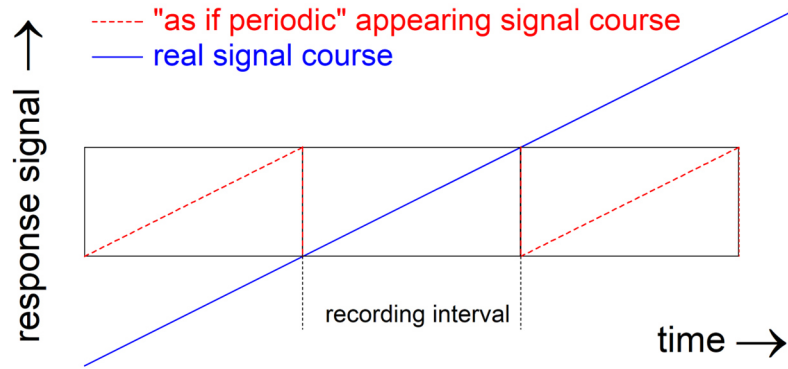


Figure 17: A temporal section of a linearly changing signal (blue) is perceived by the discrete Fourier transform as if it were periodic (red, dashed). The resulting spectrum therefore corresponds to the spectrum of a sawtooth signal.

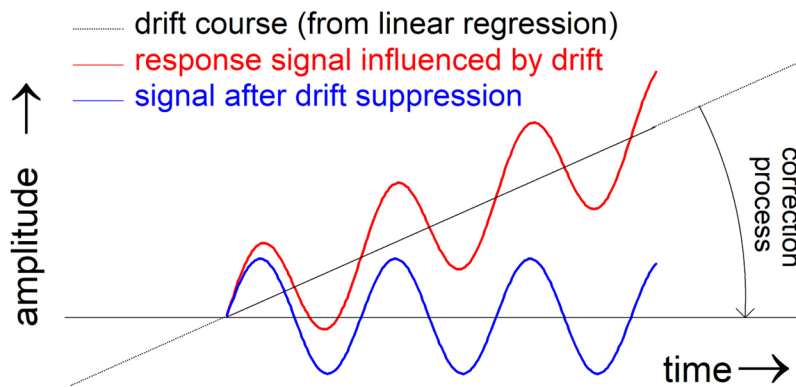


Figure 18: Separation of the periodic system response for a system that changes linearly in time during the measurement interval for a frequency sample point.

The corresponding routines were integrated into the measurement data acquisition software during the course of the work.

3.1.3.2 Temporal interpolation of spectra

From the experimental examples described later here, it can be concluded that TFA can still be successful even with moderately rapidly changing systems. The bundle of measures necessary for reliable results includes the temporal interpolation of spectrum series.

When investigating corrosion processes or taking measurements on batteries, you are prepared for the drift of the measurement objects. In this case, the most sensible way to organize the TFA is to record a series of spectra over time. During the recording of each spectrum, a certain change in the system state will have to be accepted. From the course of the transfer function at a certain frequency over time, which can be calculated from successive spectra, TF spectra can be calculated by suitable interpolation, each of which belongs to a certain, fixed time. The interpolated spectra appear to have been recorded in a snapshot-like manner in a short period of time. Figure 19 [92] outlines the principle using the example of impedance spectra.

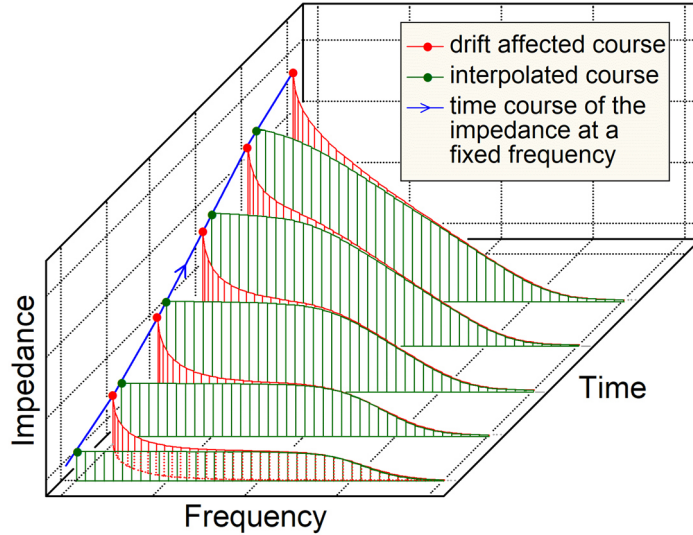


Figure 19: Sketch of the interpolation method according to H. Göhr and F. Richter for determining "snapshot-like" impedance spectra (green) from spectrum series over time. At low frequencies (left), the original spectra (red) appear increasingly distorted over time.

The synthetic interpolation points between the data of the actually measured spectra generally result from a mathematical interpolation operation along the course of the components, which cannot take into account the inherent relationship via the Hilbert transformation between real part and imaginary part, as it exists for causal functions (see following section). Therefore, even with strictly causal original spectra, the occurrence of more or less strong causality errors in the interpolated spectra must always be expected. To compensate for this unavoidable residual error, the interpolation procedure is combined with the ZHIT procedure described in the following two sections.

3.1.3.3 Development of the logarithmic Hilbert transformation for two-pole "ZHIT"

A method that indicates the loss of causality in experimental spectra caused by temporal drift is of great benefit, as explained above.

In principle, this should be possible using the Kramers-Kronig transformation, because dynamic transfer functions H of causal systems are not arbitrary complex functions of frequency ω . Instead, the real component $\text{Re}\{\}$ - and the imaginary component $\text{Im}\{\}$ are linked via the Kramers-Kronig relationship (Eq. 27, 28). It was developed independently and almost simultaneously at the beginning of the 20th century by H.A. Kramers and R.L. de Kronig [67], [68], [69]. Accordingly, the following applies:

$$\text{Re}\{H(\omega_0)\} = \text{Re}\{H(0)\} - \frac{2}{\pi} PV \int_0^{\infty} \frac{\omega \text{Im}\{H(\omega)\}}{\omega^2 - \omega_0^2} d\omega \quad (27)$$

$$\text{Im}\{H(\omega_0)\} = \frac{2}{\pi} \omega_0 PV \int_0^{\infty} \frac{\text{Re}\{H(\omega)\}}{\omega^2 - \omega_0^2} d\omega \quad (28)$$

Here, PV ("Principal Value") means that the following integral is to be understood as the principal value integral excluding the pole at $\omega = \omega_0$.

Eq. 27 and 28 state that if the course of one component of the transfer function H is known in the entire frequency range from $\omega = 0$ to ∞ , the value of the other component at the point ω_0 can be determined via the principal value integral.

Because a deviation between the calculated and the measured curve according to Eq. 27 and 28 should indicate a violation of the causality condition, techniques based on Eq. 27 and 28

have been proposed many times and for a long time to check experimental EIS data [73]. An overview of this topic can be found in P. Agarwal and M. Orazem [74].

Unfortunately, there are some problems when applying the linear Kramers-Kronig transform "LKK" to experimental data. A serious limitation becomes apparent from the integration limits for the frequency in Eq. 27 and 28: The LKK requires knowledge of the transfer function even in the non-experimentally accessible range up to frequency zero and infinity. Interpolation techniques beyond the frequency limits of the experiment are necessary in order to be able to calculate the LKK approximately.

Another problem is the calculation of a principal value integral. With conventional numerical integration, the summation of differences of very large numbers leads to large errors.

For test purposes, a tried and tested algorithm for the numerical calculation of the LKK was integrated into the evaluation program as part of the present work. This was based on a proposal by R. Unbehauen [66].

The method avoids the direct calculation of Eq. 27 and 28. Instead, the experimental spectrum is transferred to the complex stability plane (s-plane). In this metric, a Fourier transformation with subsequent conjugation and inverse transformation leads directly to the KK transform of the input component.

This method, which is described in more detail in the appendix, has the property that neither a principal value integral nor explicit curves for frequencies towards zero and infinity have to be interpolated by applying the Discrete Fourier Transform DFT.

In practical application, however, the method presented reveals the same weaknesses of all methods based on the direct LKK: The calculated curves show increasing uncertainties in the range of the frequency limits of the experiment. Particularly at the lower end of the frequency range, where the agreement between the experimental and the theoretical curve should indicate causality and thus temporal stability, this calls into question the usefulness of such methods in general.

Figure 20 shows the practical effects of this problem. The impedance spectrum of a simple model (right) was calculated in a limited frequency range and subjected to the procedure developed for experimental data. Although the output spectrum is trivially perfectly causal, the LKK shows significant deviations at both the high and low frequency ends of the band.

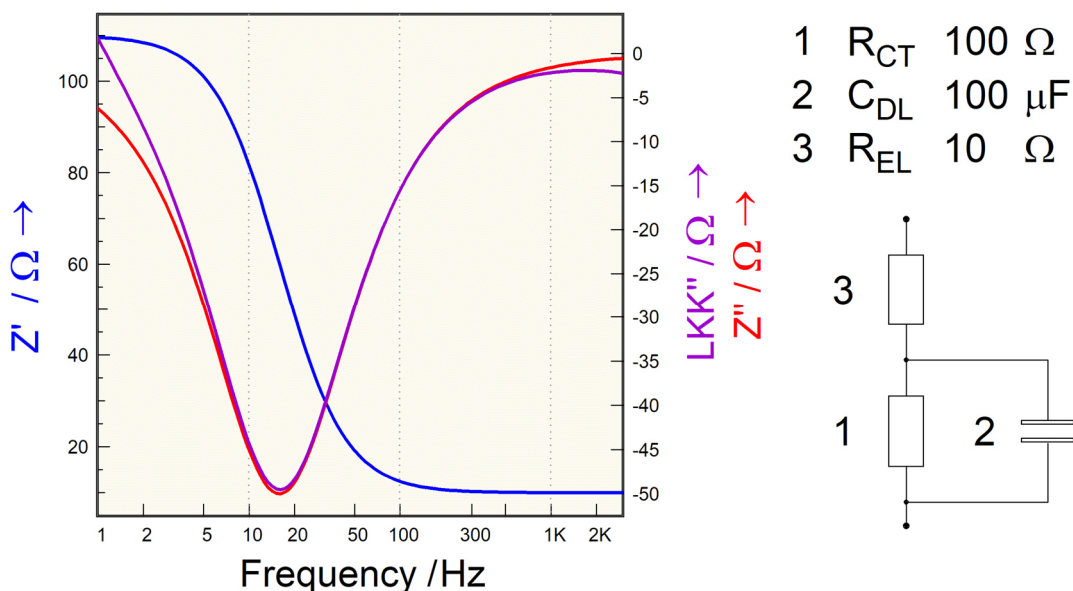


Figure 20: Result of the LKK procedure (left) according to [66], applied to a simulated EIS spectrum of the model shown on the right. The curve of the imaginary part (violet) calculated from the real part (blue) shows clear deviations from the model (red) near the frequency limits.

In the course of the work, a long-known observation finally led to a more helpful solution compared to the LKK procedure.

If you look at impedance spectra in the logarithmic representation (Bode diagram), the course of the phase angle is similar to the course of the 1st derivative of the logarithm of the impedance magnitude. This is no coincidence and was already described in 1945 in a fundamental work by H. W. Bode [71] for special cases. In the author's former working group, H. Göhr proved in 1977

[72] by means of the LKK that for impedance elements whose spectra are characterized by a phase angle that is constant over the frequency, Eq. 29, the relationships in Eq. 30 apply exactly.

$$H(j\omega) = C \cdot (j\omega)^\alpha \quad (29)$$

$$\alpha = \frac{2}{\pi} \cdot \varphi, \quad \alpha = \frac{d \ln |H(\omega)|}{d \ln \omega} \quad (30)$$

The simple Eq. 30 is certainly unsuitable for checking the quality of impedance spectra in general, as it is only valid for systems with a constant phase angle. On the other hand, as can be seen from Figure 21, the more pronounced the phase change with the frequency $d\varphi / d \ln \omega$ is, the greater are the deviations from Eq. 30 in the general case. Therefore, the author assumed that in the general case a useful approximation for quality tests of measurements can be found by extending Eq. 30 by a correction term proportional to the derivative of the phase angle $d\varphi / d \ln \omega$ (Eq. 31).

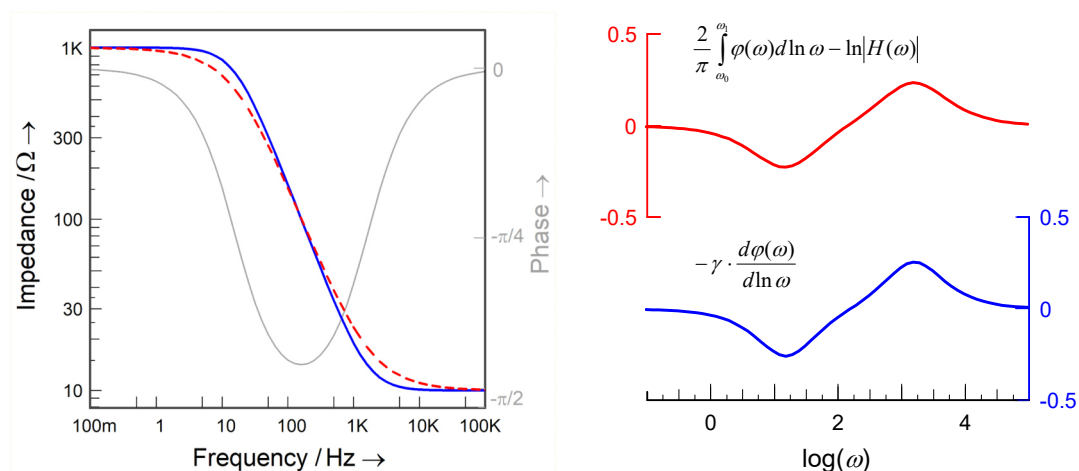


Figure 21 Left: Comparison of the impedance modulus curve (blue) with the anti-derivative function (red, dashed) of the phase angle curve (gray) of a Randles circuit. On the right, the deviation of the anti-derivative function from the impedance (red) and the derivative $d\varphi / d \ln \omega$ of the phase angle curve, multiplied by $-\gamma$ from Eq. 31 (blue) are shown.

$$\ln |H(\omega_0)| \approx \text{const.} + \frac{2}{\pi} \int_{\omega_0}^{\omega_1} \varphi(\omega) d \ln \omega + \gamma \cdot \frac{d\varphi(\omega)}{d \ln \omega} \quad (31)$$

Investigations of a large number of experimental and simulated impedance spectra by the author revealed that the proportionality factor γ in Eq. 31 is approximately constant and, irrespective of the system under investigation, $\gamma \approx -0.52$ [81].

The relationship Eq. 31 was included by the author in the program for the analysis of EIS data "SIM" and proved to be a reliable quality test for experimental EIS data.

Attempts to find out more about the nature of γ were initially unsuccessful. Only W. Ehm, at the author's request, succeeded in 1998 in mathematically deriving the nature of γ from the Kramers-Kronig relationship. This proof with error analysis for Eq. 31 by W. Ehm is available on the Internet [77]. In the following, only the way (according to R. Kaus, [79]) will be made plausible.

The starting point is the Kramers-Kronig relationship, applied to the logarithm of the transfer function (equivalent to the Bode diagram) Eq. 31 and 33. This relationship is referred to below as the logarithmic Hilbert transform "LHIT" to distinguish it from the linear Kramers-Kronig relationship LKK [76].

$$\ln|H(\omega_0)| - \ln|H(0)| = -\frac{2}{\pi} \omega_0^2 \cdot PV \int_0^{\infty} \frac{\varphi(\omega)}{\omega(\omega^2 - \omega_0^2)} d\omega \quad (32)$$

$$\varphi(\omega_0) = \frac{2}{\pi} \omega_0 PV \int_0^{\infty} \frac{\ln|H(\omega)|}{\omega^2 - \omega_0^2} d\omega \quad (33)$$

A comparison of the ZHIT expression Eq. 31 with the LHIT expression Eq. 31 provides the following expression for the correction term in Eq. 31 extended by $\pi/2$, as abbreviated in Eq. 34 with $\Delta(\omega_0)$, Eq. 34a.

$$\Delta(\omega_0) = \frac{\pi}{2} \cdot \gamma \frac{d\varphi(\omega)}{d \ln(\omega)} \quad (34)$$

$$\begin{aligned} (a) \quad \Delta(\omega_0) &= \frac{\pi}{2} (\ln|H(\omega_0)| - \ln|H(0)|) - \int_0^{\omega_0} \varphi(\omega) d \ln \omega \\ (b) \quad &= -\int_0^{\infty} \frac{\omega_0^2 \varphi(\omega)}{\omega(\omega^2 - \omega_0^2)} d\omega - \int_0^{\omega_0} \varphi(\omega) \frac{d\omega}{\omega} \\ (c) \quad &= -\int_0^{\omega_0} \left(\frac{\omega_0^2}{\omega^2 - \omega_0^2} + 1 \right) \varphi(\omega) \frac{d\omega}{\omega} - \int_{\omega_0}^{\infty} \frac{\omega_0^2}{\omega^2 - \omega_0^2} \varphi(\omega) \frac{d\omega}{\omega} \\ (d) \quad &= -\int_0^{\omega_0} \frac{\omega^2}{\omega^2 - \omega_0^2} \varphi(\omega) \frac{d\omega}{\omega} - \int_0^{\omega_0} \frac{\omega_0^2}{\omega_0^4 / \omega^2 - \omega_0^2} \varphi(\omega_0^2 / \omega) \frac{d\omega}{\omega} \\ (e) \quad &= + \int_0^{\omega_0} \left(\varphi\left(\omega_0 \frac{\omega_0}{\omega}\right) - \varphi\left(\omega_0 \frac{\omega}{\omega_0}\right) \right) \frac{\omega}{\omega^2 - \omega_0^2} d\omega, \end{aligned} \quad (35)$$

If the notation is shortened slightly by omitting the principal value symbol and substituting (from Eq. 34 to 34) ω_0^2/ω by ω , the expression Eq. 34 can be derived. Eq. 34 corresponds to a mean value of weighted differences of φ .

Since the weight $\omega / (\omega^2 - \omega_0^2)$ only contributes to $\Delta(\omega_0)$ in the vicinity of ω_0 because of the pole at $\omega = \omega_0$, where ω_0/ω is also close to its reciprocal ω/ω_0 and close to one, the phase differences can be replaced approximately with good accuracy by derivatives of the phase according to $\ln \omega$. Eq. 36 is then obtained.

$$\Delta(\omega_0) = \sum_{k=1}^{\infty} \int_0^{\omega_0} \frac{\varphi_k(\omega_0)}{k!} \left(\left(\ln \frac{\omega_0}{\omega} \right)^k - \left(\ln \frac{\omega}{\omega_0} \right)^k \right) \frac{\omega}{\omega^2 - \omega_0^2} d\omega = \sum_{k=1}^{\infty} a_k \frac{\varphi_k(\omega_0)}{k!} \quad (36)$$

For even k , the coefficients a_k disappear and the coefficients are given by Eq. 37.

$$a_k = 2 \int_0^{\omega_0} \left(\ln \frac{\omega_0}{\omega} \right)^k \frac{\omega}{\omega^2 - \omega_0^2} d\omega = 2 \int_0^1 \left(\ln r^{-1} \right)^k \frac{r}{r^2 - 1} dr, \quad r = \frac{\omega}{\omega_0} \quad (37)$$

$$\int_0^{\infty} \frac{x^{s-1}}{e^x - 1} dx = \Gamma(s) \zeta(s) \quad (38)$$

Substituting r in Eq. 37 by $e^{-x/2}$ one can use Eq. 38 and Eq. 37 can be integrated. In Eq. 38, $\Gamma(s)=(s-1)!$ is the gamma function. It result for the coefficients the rule $a_k = -2^{-k} \zeta(k+1) k!$.

$$\gamma_k = \frac{2}{\pi} \frac{a_k}{k!} = -\frac{2}{\pi} \zeta(k+1) \cdot 2^{-k} \quad \text{for odd } k, k \geq 1. \quad (39)$$

Thus, the ZHIT relationship can finally be expressed as an approximation of n th order A as in Eq. 40. Here, the φ_k mean the k th derivatives $d^k \varphi$ to $d \ln \omega^k$.

$$A_n(\omega_0) = \frac{2}{\pi} \int_0^{\omega_0} \varphi(\omega) d \ln \omega + \sum_{1 \leq k \leq n, k \text{ odd}} \gamma_k \cdot \varphi_k(\omega_0) \quad (40)$$

$$\text{with } \varphi_k(\omega_0) = \frac{d^k \varphi(\omega)}{(d \ln \omega)^k} \quad \text{bei } \omega = \omega_0.$$

If we break the approximation Eq. 40 at $k=1$, the second coefficient of the Riemann zeta function multiplied by $2/\pi$ is obtained for γ_1 . This value of $-\pi / 6$ corresponds approximately to the empirically determined value of -0.52 and finally confirms the ZHIT approximation:

$$\gamma \approx -\pi / 6 \quad (41)$$

When analyzing TF such as impedance spectra, the application of the ZHIT offers a number of advantages compared to the LKK-based methods. The ZHIT can be calculated quickly and completely unproblematically by numerical integration, whereby the correction term proportional to γ can be derived from the smoothing function described in chapter 3.1.2.2. It is also practical that even a rough inspection of the Bode diagram of a TF by visual inspection provides indications of problems if the approximately valid relationship between phase and amplitude curve according to Eq. 30 in the form of derivative and anti-derivative function is grossly violated. However, the most important property of the ZHIT is its local applicability: amplitude and phase response are related to each other via the ZHIT, which is already valid for a limited section of the frequency bandwidth.

Another advantage of the ZHIT can be traced back to its origin in the LHIT equations 31 and 33: Equations 42 and 43 for the components of a complex transfer function Eq. 16 stand for the popular graphical representations Nyquist and Bode diagram, respectively. While the Kramers-Kronig relationship Eq. 27, 28 can be applied to the linear representation Eq. 42, the logarithm Eq. 43 must be used for its counterpart LHIT.

$$H(j\omega) = R(\omega) + j \cdot X(\omega) \quad (42)$$

$$\ln\{H(j\omega)\} = \ln|H(j\omega)| + j \cdot \varphi(\omega) \quad (43)$$

In contrast to the LKK on Eq. 42, the LHIT relationships Eq. 31 and 33 assigned to Eq. 43 are no longer applicable to all transfer functions fulfilling the LKK. In other words, the LKK is more generally applicable, while the applicability of the LHIT imposes stronger restrictions on the analyzed systems. The restrictions are triggered by the logarithmic operator, for which singularities in the transfer functions under consideration must be excluded: If such transfer functions are plotted in the complex s -plane, no zeros may occur in the positive half-plane [71]. This is equivalent to the exclusion of all-pass contributions⁴ to the transfer function. Regular EIS,

⁴ Frequency pass filters such as high pass, low pass and band pass characterize the influence of the frequency on the transmission factor (gain) of a TF. A high pass, for example, means constant gain at high frequencies but decreasing gain at low frequencies. The all-pass filter plays a special role in that it indicates constant gain across all frequencies. Like the other pass types, however, it allows phase shifts between the excitation and response signals. A TF that contains all-pass contributions can be broken down into the components TF_{\min} (without all-passes) + TF_{all} (sum of all-passes). TF_{\min} shows the same gain curve as TF and is called "minimum phase TF", as *all* solely phase-shifting components have disappeared. The most prominent representative of an all-pass filter is the transmission line: an ideal transmission line has

IMPS and IMVS DUTs do not contain all-passes, such as transmission paths with dead times. They are minimum phase systems or, like the impedance, two-pole systems and allow the application of LHIT. The ZHIT based on the LHIT can therefore be used to detect deviations from the minimum phase system behavior and identify them as measurement errors. However, this class of measurement errors cannot be recognized by the LKK, since all-passes such as transmission lines are LKK-transformable because they are causal. Frequent measurement errors, such as those that occur when measuring small impedances at high frequencies, caused by a transformer effect between the current-carrying and the voltage-measuring lines (so-called mutual induction) are therefore recognized by the ZHIT, but not by the LKK. Examples from EIS measurement practice on batteries and fuel cells can be found in [80] and [108]. The functional principle of causality verification and correction is explained in the following chapter.

3.1.3.4 Verification and approximate correction of time dependencies in experimental spectra using ZHIT

Figure 22 shows the effects of temporal drift on the impedance spectrum of a simple electrode reaction in a simulation. It was assumed that the charge transfer resistance decreases with time, as is observed in practice, e.g., during heating. The deviations from the drift-free case in the low frequency range can be clearly seen in the impedance modulus curve.

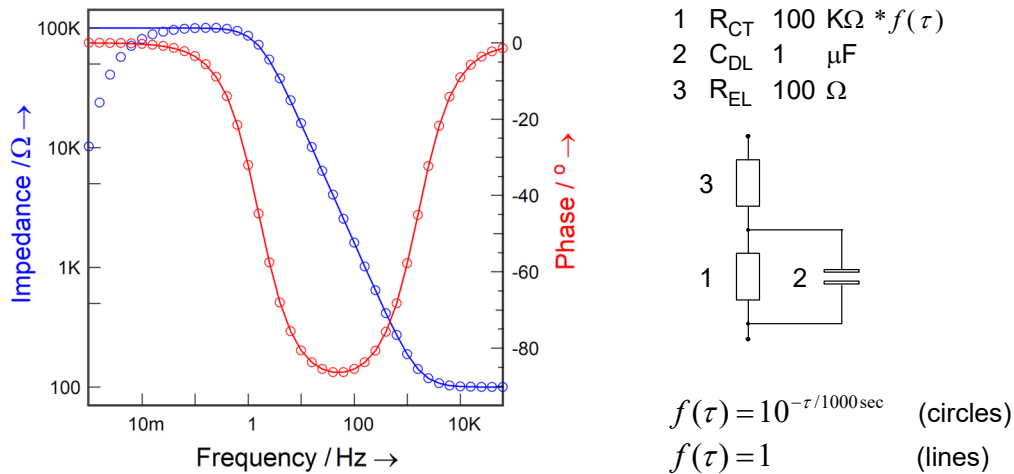


Figure 22 left: Bode diagrams of the impedance model shown on the right (simplified Randles circuit with charge transfer resistance R_{CT} , double-layer capacitance C_{DL} and electrolyte resistance R_{EL}). The solid lines show the curve without time drift, the circle symbols show the curve with simulated drift of the charge transfer resistance. The drift at the lower frequency end is clearly visible, emphasized by the increase in measuring time with the period duration $\tau = 1/f$.

If one examines the time-dependent spectrum from Figure 22 by calculating the corresponding absolute impedance curve from the phase response of the simulated experiment using ZHIT, Eq. 31, the deviation from the "experimental" impedance modulus curve at low frequencies indicates strong temporal changes in the system under investigation during the recording of the spectrum (Figure 23).

a frequency-independent amplitude of one. The finite transmission time results in a phase shift proportional to the frequency.

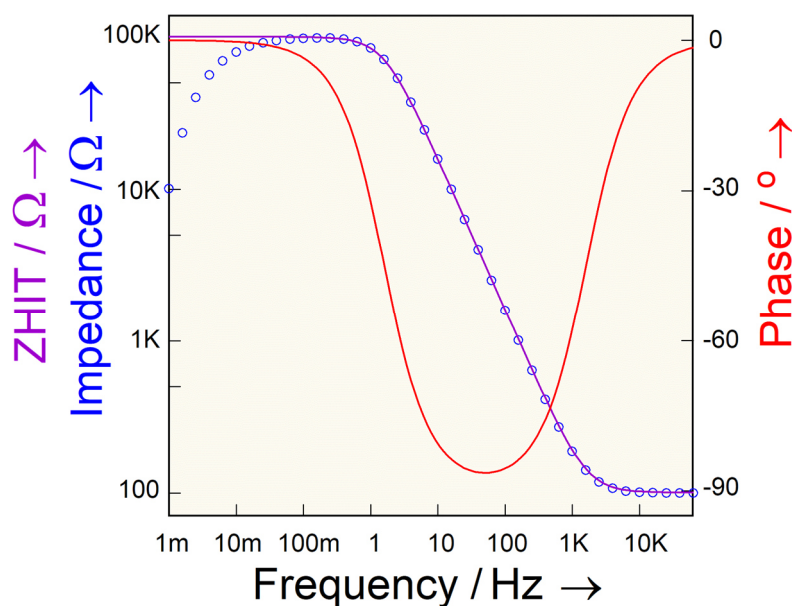


Figure 23: Comparison between the impedance spectrum of a simulated experiment (red: phase response, blue circles: impedance curve) under temporal drift according to the model of Figure 22 with the impedance curve calculated from the phase response using the ZHIT (violet, solid curve).

Systematic deviations of the ZHIT from the experimental impedance curve at high frequencies are generally due to parasitic all-pass contributions to the TF. With increasing frequency, unwanted reactance such as stray capacitance and leakage inductance of the measurement setup and leads contribute more and more to the impedance. Most experimenters are aware of this fact, although the causes are often still misunderstood. One example of this is the "coupling effect", which, triggered by internal resistance and the stray capacitance of the reference electrode in the traditional three-electrode cell setup, is interpreted as lead inductance due to its inductive appearance [110]. However, the presence of stray reactance does not represent a violation of causality or minimum phase system behavior and is therefore consistent with LKK, LHIT and ZHIT. If existing stray reactance in the TFA are taken into account, the affected TFs can be modeled without any problems. Parasitic all-pass contributions due to mutual induction [108], however, like temporal drift, lead to spectra that can no longer be understood with regular TF models. If errors at high frequencies are detected with the ZHIT, it may still be possible to achieve improvements by optimizing the measurement setup and suppressing mutual induction through magnetic compensation. However, if significant all-pass interference remains in the spectrum, evaluation in the high frequency range should be abandoned. The detection of drift influences at low frequencies is less problematic. Already in Figure 22 it is clear that drift has a significant effect on the impedance modulus curve, while the phase curve appears to be barely affected. What is shown in Figure 22 was deliberately emphasized by the choice of parameters for clarification, is a general property of transfer functions. Normalization by the complex logarithm operator leads to a separation of the characteristics of the dominant TF element into real and imaginary parts (Eq. 44): While the real part describes the parameter value range of the element, the imaginary part defines its character.

$$\ln Z = \ln|Z| + j\varphi, \quad \text{Re} = \ln|Z|, \quad \text{Im} = \varphi \quad (44)$$

In Figure 22 this is shown by the fact that the real part - i.e., the numerical value of the charge transfer resistance and thus the absolute impedance - changes up to a factor of ten, while its "character" as a resistor, determined by its phase angle of zero, remains unchanged. In general, individual elements dominate most of the frequency space in each TF, while transitions in dominance from one element to another are only of local significance. Therefore, one can generally conclude for transfer functions: If some determining parameters in a system are subject to temporal drift, the course of the phase angle in the TF is less affected by A-causality than the course of the amplitude modulus. Conversely, this can be used to justify a strategy for approximately freeing measured spectra from drift: The theoretical amplitude modulus response is calculated from the experimentally measured phase using the ZHIT. This is used for further evaluation instead of the experimental amplitude curve, which is falsified by the drift. This

procedure corresponds to the path to the TFA of Figure 16 on the right and usually works quite well: in the example, no difference can be seen between the impedance curve of the drift-free system (blue, solid curve in Figure 22) and the impedance curve calculated from the system under drift using the ZHIT (purple, solid curve in Figure 23).

3.1.4 Application of tools for the identification and treatment of time dependencies on selected systems with limited stability

Among experienced members of the "impedance community" there is widespread agreement on the assessment of the problem of non-steady-state for impedance spectroscopy. One can summarize in a simplified way: Drift processes should occur on a significantly slower scale than the time required to measure a spectrum. Nevertheless, there is still a certain amount of uncertainty among some scientists. This can go so far that impedance measurements on variable systems are rejected across the board, even though, trivially, there can be no absolute stability in nature.

As shown above, disturbances can be objectively identified and quantified through time dependency. In addition, a catalog of methods is available that can be used to minimize the effects of these disturbances, which extends the range of application of TFA. This is illustrated by the following examples.

3.1.4.1 Investigations into metallic corrosion

Due to the great economic damage caused to people worldwide by the corrosion of metals - estimates range up to 4% of the production volume of industrialized countries - there is lively research activity in this field all over the world.

The processes involved in the corrosion of metals can generally be traced back to the electrochemical reactions at the electrolyte-metal phase boundary, where metal dissolution or deposition occurs, for example.

Corrosion is a prime example of a time-dependent process. If the chemical turnover breaks down into individual events that are discontinuous in time, the only direct electrochemical quantification method available is the measurement of electrochemical noise [102].

If the corrosion attack is rather homogeneous, or if the individual events in the integral electrical measured variables blur approximately to the continuum, traditional methods of electrochemistry can be used successfully. The aim here is usually to determine the polarization resistance R_p , as this can be used to directly estimate a material loss [3], [4].

Many corroding systems have reaction paths that are too complicated to reliably determine R_p from DC polarization curves. Therefore, the measurement and analysis of impedance spectra is often preferred [5], [6], [7].

A process that progresses over time naturally also leads to changes over time in the characteristic variables, such as the R_p . In order to be able to make reliable statements nevertheless, the author considers it advisable to use the methods described in chapter 3.1 above for the identification and treatment of time dependencies in corrosion research.

The following example is one of the first "tests" of the strategy developed by the author.

As part of Ute Ruhrberg's doctoral thesis, impedance measurements were carried out on steels in an acidic medium in the presence of various corrosive and inhibiting agents at the Dechema Institute in Frankfurt [104]. Since many spectra could not be evaluated immediately due to significant temporal drift, the method described in 3.1.3.4 was used to successfully model the data. A typical example is shown in Figure 24. This shows the impedance spectrum of the steel Fe Mn₃₈₆ in a chloride-containing solution in the presence of CO₂ in the cathodic potential range around 0.5V against SHE.

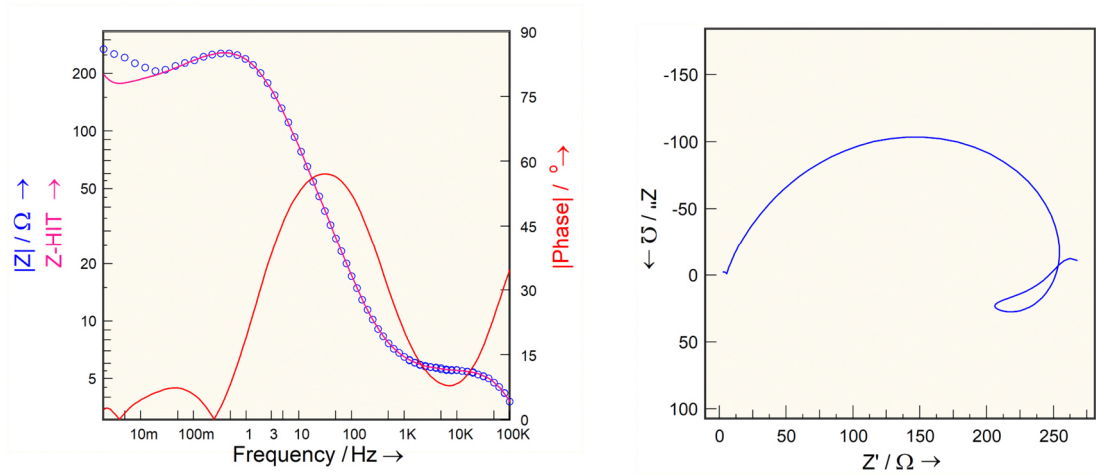


Figure 24: Impedance spectrum of an Fe Mn₃₈₆ steel in an aqueous, chloride-containing solution in the presence of CO₂. In addition to the experimental impedance magnitude (blue circles) and phase (red curve), the Bode diagram on the left also shows the ZHIT transform (purple curve), which differs significantly from the experimental impedance magnitude due to the strong time change at low frequencies. This area can be seen as a "loop" in the Nyquist diagram on the right.

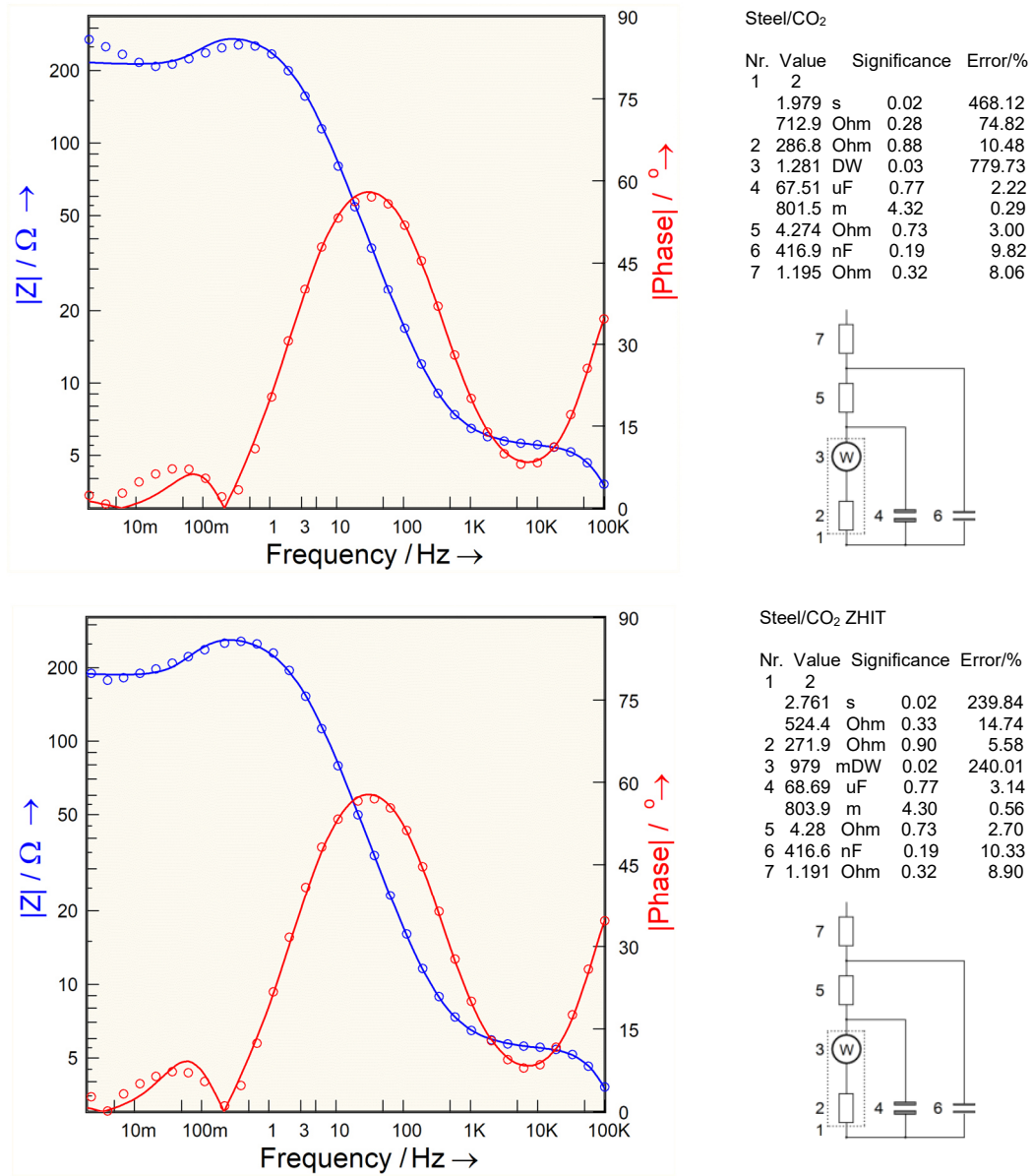


Figure 25: Simulation (solid curves) of the impedance spectrum of an FeMn₃₈₆ steel in an aqueous, chloride-containing solution in the presence of CO₂. The blue circles at the top correspond to experimental sample points, at the bottom to the ZHIT transform from the phase (red circles). The qualitatively better fit at the bottom is also shown by the uncertainty of the determined parameter tables, which is reduced by an average factor of about 3.

While the original data could not be modeled with sufficient accuracy due to the clearly visible drift in the low frequency range, this was possible after applying the ZHIT correction (Figure 25). The significance of the surface relaxation impedance used in the model (impedance element 1) will be discussed in a later chapter.

3.1.4.2 Drift effects in the fuel cell: Influence of CO poisoning of the anode and the disturbed water balance of the cathode on the impedance of a PEM fuel cell

Systems for electrochemical power generation such as batteries and fuel cells [87] are subject to drift over time. The properties of batteries trivially change quite quickly - after all, a rechargeable battery constantly passes through many different spatial distributions of electrical charge and concentration of electro-active masses in its normal operating cycle between charging and discharging.

Especially in the field of fuel cells, impedance spectroscopy has established itself as a standard investigation method [86], [88]. This is due to its fundamental ability to provide a wealth of specific information in situ, i.e., during active operation, using only the existing electrical connections. Ideally, the relevant loss contributions can be identified and assigned from this, thus creating the conditions for further optimization [89].

Unlike with batteries, stationarity can be aimed for with fuel cells - the supply of fuel and oxidizing agent should be stoichiometrically equivalent to the current draw. Drift therefore appears to be significant mainly in the form of degradation.

In practice, however, there are other changes whose time scale may well fall within the typical times of spectrum recording. These include, for example, the reaction of the cell to changes in the electrical load, the resulting fluctuating fuel and oxidant consumption and the transient processes of temperature, pressure and concentration to new steady-state values.

The shortage of educts, the accumulation of products and the poisoning caused by the accumulation of undesirable components of the fuel can have particularly dramatic effects [90]. If one wishes to rely on the data obtained, it seems advisable to use the methods described in chapter 3.1 to estimate the influence of the drift effects on the parameters and to minimize them if necessary. This procedure is illustrated below by two examples that were created with the author's assistance in the course of this work.

The catalytic reforming of hydrocarbons and alcohols to produce hydrogen for use in fuel cells produces a considerable amount of carbon monoxide CO. Some types of fuel cells, such as high-temperature solid oxide fuel cells (SOFCs), can capture CO in the fuel gas via the so-called shift reaction [91] with almost no problems. However, the high stability of the binding of CO during adsorption on the platinum of anode catalysts in low-temperature polymer electrolyte membrane (PEM) fuel cells or polymer electrolyte fuel cells (PEFC) poses a major problem for such cells. Even a low concentration of CO in the ppm range leads to significant inactivation of the anode for hydrogen oxidation due to accumulation over time. Only when the cell voltage falls below a value at which the anode potential rises above the oxidation potential of the CO can the anode be freed from CO again. More precise knowledge of the CO adsorption-oxidation mechanism could contribute to the development of CO-tolerant systems.

Another critical aspect of PEFC concerns the cathode: the protons produced during the oxidation of hydrogen at the anode take water molecules with them as they migrate through the polymer membrane. Together with the abundant water produced at the cathode at high currents due to oxygen reduction, there is a risk that the surface area at the active three-phase boundary will decrease due to flooding: The cathode "drowns" if the water is not effectively removed.

Under the direction of N. Wagner, investigations of the time-dependent impedance of PEFC under the influence of aimed CO poisoning were therefore carried out at DLR Stuttgart, [93] and with targeted blocking of the reaction water removal [92] were carried out. Both experiments produce strongly time-dependent impedance spectra that cannot be meaningfully evaluated without taking the drift behavior into account. The author was involved in the processing and evaluation of the spectra. In this section, only the effect of the drift treatment methods will be shown. More detailed information on modeling will be provided in the sections on porous systems and relaxation impedance.

A 23cm² -PEFC single cell was used in the CO experiment. A galvanostatic controlled load of 5A, corresponding to 217mA/cm² should ensure a stable, stationary behavior of the cathode. For this purpose, the oxygen was circulated with an eightfold stoichiometric excess of the gas flow in relation to the load current. In contrast to the cathode, the anode was operated in a "short circuit" without circulation of the fuel gas. After equilibrium adjustment under pure hydrogen, 100ppm CO was abruptly added to the fuel gas. Impedance spectra were recorded continuously during the measurement campaign. Each spectrum from 30 KHz to 0.05 Hz lasted about 20 min, so that noticeable changes in the system state could already be expected within the measurement time of a single spectrum.

After the start of poisoning, the dominant impedance changed from the cathode to the anode: While the hydrogen electrode only made a small contribution to the total impedance at the beginning, its Faraday impedance increased so strongly with increasing poisoning that the spectra were largely dominated by the relaxation impedance after approx. one hour [93]. Together with the double-layer capacitance of the anode, the relaxation impedance forms a slightly damped resonant circuit, which leads to the spectra shown in Figure 26 as almost perfect sequence of nearly circular Nyquist diagrams.

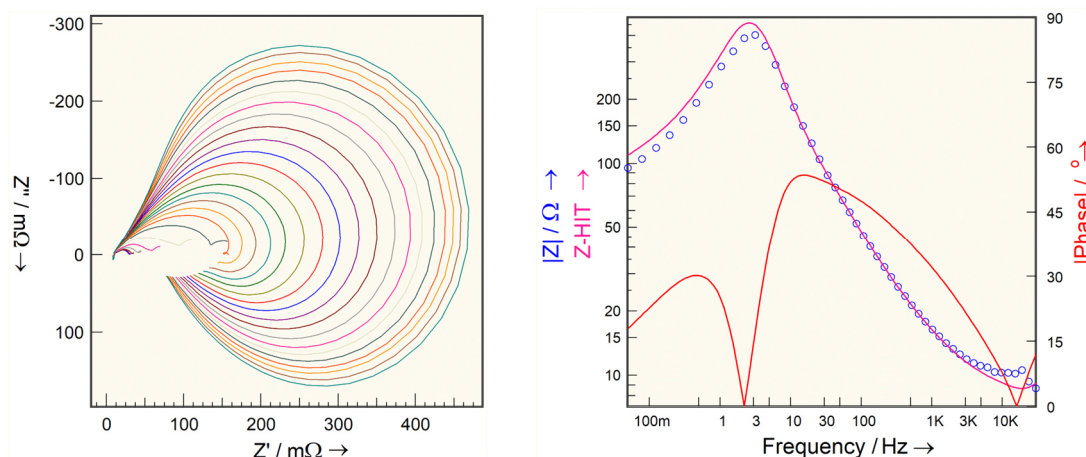


Figure 26: Nyquist diagrams of the impedance of a 23cm^2 -PECF single cell at $217\text{mA}/\text{cm}^2$ in chronological order after the start of aimed poisoning of the anode with 100ppm carbon monoxide in the hydrogen fuel gas (left). The two semicircles of cathode impedance and anode diffusion impedance, which are still resolvable at the beginning, become blurred with increasing proportion of the anode relaxation impedance, which shows an inductive character. The ZHIT conformity test of a selected measurement (approx. 3 h after CO application, cell voltage 0.244V) is shown on the right (the blue circles correspond to the experimental sample points of the impedance modulus).

From Figure 26 on the right, it is clear that the measurements are also subject to a clear time variation within the spectra: At lower frequencies, there is a significant difference between the impedance magnitude curve reconstructed from the ZHIT and the measured sample points. The slight deviations that are also visible at high frequencies are due to mutual induction components that could not be perfectly compensated for due to the given geometry of the fuel cell.

Apart from the first measurements, which were carried out in nearly stationary operation with pure hydrogen, the attempt to fit the original data with the model described below led to inadequate results. Therefore, the spectra series was analyzed using the model described in 3.1.3.2 into a series that was approximately free of drift. Residual deviations from causality were corrected according to the procedure described at the end of 3.1.3.4 explained at the end of 3.1.3.4. A comparison of the fit quality without and with drift correction applied shows Figure 27 using a spectrum measured a good three hours after the CO application as an example.

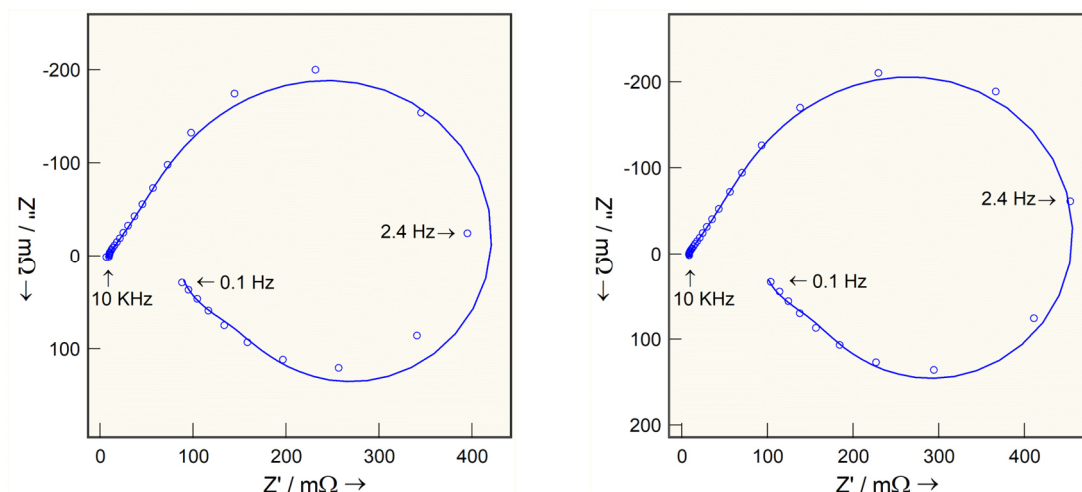


Figure 27: Simulation and fit (solid curves) of the impedance (circles) of a 23cm^2 -PECF single cell at $217\text{mA}/\text{cm}^2$ approx. 3h after the start of CO addition. The (smoothed) original data were used on the left, the data after time interpolation and ZHIT correction on the right.

In the investigation of blocked water transport in the second experiment, a fuel cell of the same design as described above was used. However, a significantly lower current density of $87\text{mA}/\text{cm}^2$ was imposed on it in order to avoid the occurrence of significant contributions of the H_2 diffusion to the impedance of the anode. This facilitated the evaluation, as the anode impedance, which was of less interest in this experiment, could be represented by a greatly simplified model, which could also be assumed to be relatively constant over the entire measurement time. More detailed information about the modeling is provided in the chapter on porous systems. Here, as in the case of CO poisoning, the focus will be on the aspects of drift over time.

Similar to above, but with reversed roles between anode and cathode, the anode side was operated with a surplus of moistened hydrogen circulating with the gas flow, while the cathode was abruptly cut off from the stationary state in order to provoke flooding by reaction water. Impedance spectra in the frequency range between 10mHz and 10KHz were recorded periodically over the entire measurement campaign of approx. eight hours. As can be seen from Figure 28 the impedance changed dramatically during the measurement period. This is particularly noticeable at the low-frequency end: here the impedance value increased by a factor of 20 from around $50\text{m}\Omega$ at the beginning to almost 1Ω at the end of the measurement period.

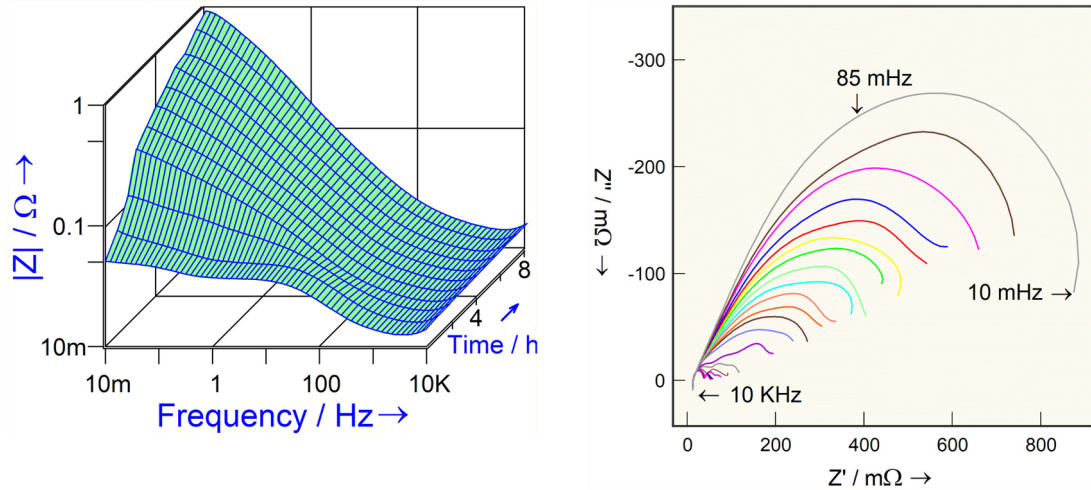


Figure 28 left: Time course of the impedance modulus spectra over eight hours of a PEFC in short-circuit operation of the cathode under a constant current load of 87mA/cm² (every 2nd measurement shown). Especially in the low-frequency range, the impedance increases dramatically with increasing flooding by transport and reaction water. This can also be seen in the Nyquist diagram of all measurements on the right.

The influence of the various drift reduction stages on the quality of the model calculation is shown in Figure 29 clearly. While deviations of up to around 15% remain after the fitting to the raw data, these disappear almost completely when the drift correction is fully utilized. The influence of the automatic online drift correction, present during the measurement is not shown. Based on experience during the development period, without this correction additional errors in the order of a further 20% at the lowest frequencies would have to be expected. It should be noted, however, that after ZHIT correction the error, as shown in Figure 29 on the right at 10KHz, can also increase locally:

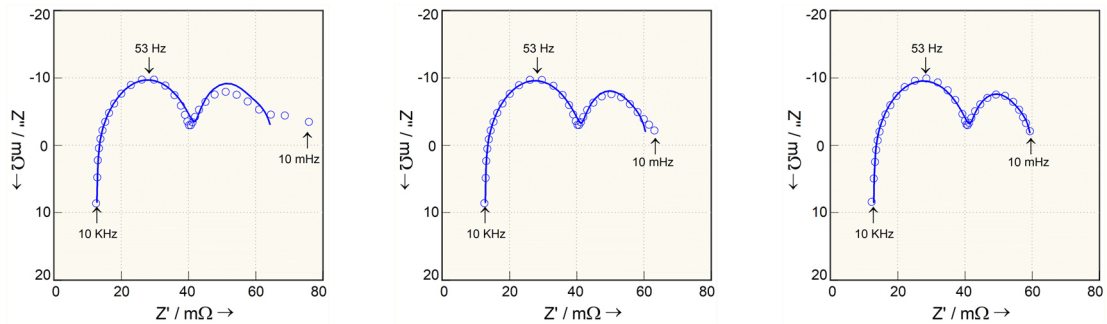


Figure 29: Selected spectrum (50 min after closing the gas outlet) from the impedance spectrum series over eight hours of a PEFC in short-circuit operation of the cathode under a constant current load of 87mA/cm². The selected measurement points are shown as circles, the model calculation after fitting as solid curves. Left: Fit to the raw data (online drift correction only). Center: Fit to the time-interpolated data. Right: Adjustment to the temporally interpolated data plus correction using ZHIT.

The successful application of ZHIT correction at low frequencies is based on the plausible assumption of a higher stability of the phase angle with respect to temporal changes, as explained above. However, this is precisely not the case with errors similar to an all-pass filter due to mutual induction at high frequencies. Conversely, the transmission ratio is more stable here. W. Ehm has also tried to find a generally valid proof for the inverse function of the ZHIT - i.e., the determination of the phase angle curve from the curve of the absolute impedance [78]. A corresponding transformation exists, but was found to be unsuitable for practical application due to its tendency to oscillate [78]. It is therefore generally recommended to minimize deviations in the high-frequency range by optimally setting up the experiment and to limit the frequency range to be interpreted accordingly if all-pass errors remain. However, the inverse ZHIT is used in the program developed by the author to calculate the phase response from the Fourier transform of step functions, such as those used in high-current interrupt measurements,

e.g., on fuel cells [126]. Here, due to the uncertainty of the trigger time, the phase angle information of the transform in the high-frequency part is practically useless, so that a back calculation of the phase from the transmission factor is necessary if switch-off measurements in frequency domain are to be evaluated as impedance spectra. Here, however, the - unstable - solution of W. Ehm is not used, but a phase angle estimate is iteratively adapted to this by comparing ZHIT and the impedance curve.

3.1.4.3 Investigation of the swelling behavior of some organic coatings on metals

The water absorption of organic anti-corrosion coatings after immersion in an electrolyte is a process whose time dependence can fall within the scale of typical impedance measurements. If such processes are to be followed by impedance spectroscopy, the use of ZHIT is recommended for checking and possibly correcting the experimental data.

In the following example [131] of impedance spectra potentially affected by drift, it was shown in a group with the author that post-processing of the experimental data is not absolutely necessary. In these investigations, the effects of temporal drift within the individual spectra were sufficiently small compared to the accuracy achievable on such systems.

In the underlying experiments, six commercially available barrier coatings on steel sheets (area of 4.5 cm²) were examined by impedance spectroscopy immediately after immersion in an aqueous, 0.5M KCl solution at 18 ± 1 °C (duration up to 2 days). In the measuring cell, a 3-electrode arrangement with 2.5 cm² Pt foil was used as a counter electrode. It took about 20 minutes to record a single spectrum in the frequency range of 20mHz - 100KHz.

The water absorption of organic coatings is a typically time-dependent process. Dramatic changes could therefore also be observed over the entire measurement period. However, small deviations from the sufficiently stable behavior from the perspective of the quasi-stationary EIS technique were only detected during the recording of the first spectra within the spectra. For this reason, the data was not corrected using ZHIT during further evaluation.

The illustrations in this section were taken from the source material of the original works.

The following graphic Figure 30 compares the impedance measurement results of two samples that are quite different in terms of water absorption.

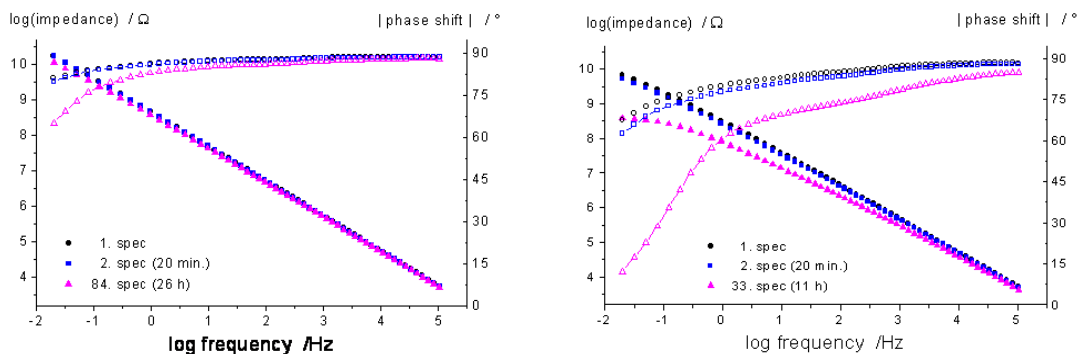


Figure 30: Impedance spectra series over time (Bode diagrams) of two different coating systems with low (left) and high (right) water absorption. The first two spectra after immersion and the last measured spectrum of the series are shown.

Since the measurement time required to determine a sample point in an impedance spectrum is highest at the lowest frequency, potential drift generally has the maximum effect there. In the following Figure 31 below shows the deviation between the impedance reconstructed without drift using ZHIT and the measured impedance at the point of lowest frequency for the respective measurement series for the coating systems shown above.

For impedance measurements on highly insulating barrier layer systems, a typical measurement error in the order of one to a few percent must be accepted due to the very small current measurement values. In Figure 31 it can be seen that for both coating systems, the additional error in the measurement caused by drift becomes comparably small even at the most severely affected support point after the first spectra.

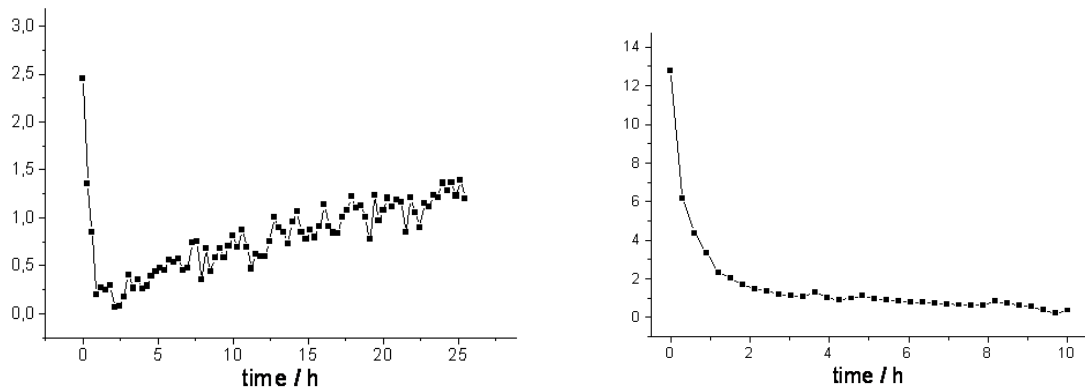


Figure 31: Course of the relative deviation between the impedance reconstructed according to ZHIT and the (smoothed) original data in percent at the point of greatest deviation (lowest frequency, 20 mHz) for two different coating systems with low (left) and high (right) water absorption.

The Young-Göhr model of a dielectric with a conductivity gradient, described in detail in section 4.2.1.1, is appropriate for the evaluation of the swelling behavior of organic coatings.

Various dielectric relaxation mechanisms are also proposed in the literature for modeling the dynamic behavior of barrier coatings [132], [133], [134], [135], [136]. The starting point of the considerations used there is usually the idea of dipoles arranged in the material in a (in reality irregular) lattice, which, coupled to neighbors, relax via "defect hopping" and the discharge spreads over the material in this way, the "Continuous Time Random Walk" CTRW.

However, the process, which can be seen as analogous to a first-order chemical reaction, leads to a behavior of the impedance that is similar to the phenomenon of a "hanging phase angle" towards low frequencies that is often observed in paint systems (see Figure 30 right), unlike the Young-Göhr model, cannot be correctly reproduced [137].

The author's colleague W. Strunz therefore developed the modified dielectric relaxation model "Continuous Time Random Walk 2nd Order" CTRW2 under the assumption that the relaxation takes place via an intermediate step and provided a numerical solution for the impedance calculation [131].

Both the Young-Göhr model [138] and the CTRW2 model [139] led to consistent results for the parameters that describe the water absorption over time.

The CTRW2 model was integrated into the SIM analysis program by means of a user-programmable impedance element, the "USER element". In contrast to the other freely programmable impedance elements discussed in this paper, some of whose source code can also be found in the appendix, section 8.4, the actual impedance calculation for CTRW2 is carried out in a separate program independent of SIM. In such a case, the USER element only provides the interface to the external program. In this way, the concept of the USER element also allows impedance models generated in other environments, such as Matlab®, to be used from SIM.

3.1.5 Concluding remarks on dealing with temporal drift in dynamic transfer functions

These examples of successful investigations on time-varying systems could give the impression that drift is an important but fundamentally solvable problem in TFA. This is already wrong because of the boundary conditions for the mathematical tools on which TFA is based. Attempts have been made to [83], [94] to extend the Fourier transform to time-varying systems. This or similar approaches have never achieved practical significance, probably because the drift characteristics of the investigated systems must be known before the TFA. The requirement therefore remains that the system drift may only have a significant effect on a larger time scale than the respective measurement window.

An interesting aspect of the drift control methods presented above is the temporal reference of the interpolated or ZHIT-treated spectra. While the interpolation method can be configured accordingly (the default time of the resulting "snapshots" is set to the mean measurement time of the original spectra), no clearly defined recording time is determined for the ZHIT "snapshot". It results approximately from the time at which more than 80% of the logarithmically weighted frequency lines are recorded in the passage from high to low frequencies. The exact time depends on the setting parameters of the frequency resolution.

It is repeatedly suggested that the drift problem should be tackled at its roots and that faster measurement methods based on multispectral test functions should be used instead of sine excitation. However, a closer analysis shows that this does not really improve the situation:

1. Any reduction in measurement time is always associated with a proportional reduction in information density, i.e., with correspondingly reduced accuracy and frequency resolution. This can already be concluded from Eq. 20. Moreover, as early as 1992, a fundamental paper [95] mathematically proved that in the case of TFA on non-linear systems affected by a finite proportion of interfering signals, such as the EIS, multispectral methods must be even slower than the sine wave method, provided that the information density remains the same.
2. Multispectral methods "pack" the frequency components of the test signal into multiples (harmonics) of the fundamental frequency, which results from the reciprocal measurement time. If this measurement time is compared with the sum of the measurement times of a sequentially performed sine wave measurement of the same frequency content, there is only a modest time advantage of e.g., less than a factor of 3, despite the loss of accuracy, if (as is usually the case in order not to worsen the signal-to-noise ratio too much) around ten harmonics are excited. In no way can a dramatic time effort reduction in the order of magnitudes be achieved.
3. In principle, the harmonic frequency distribution excites precisely those frequency lines that arise even without excitation due to non-linearity, interference signals or - particularly critical - due to time drift (see also Figure 17 and [107]). This means that distortions, which could be easily detected with sine wave excitation and used as an accuracy indicator as described above, are immediately processed as a source of error in the system response.
4. In order to circumvent the restrictions under point 3, a multispectral method called "ORP" [96] is often propagated. Here, in addition to the fundamental frequency f_g , only the odd harmonics $3f_g, 5f_g, 7f_g, \dots$ are excited, so that in principle it is possible to detect unwanted components. However, an even more modest time advantage is achieved, e.g., by a factor of two for ten harmonics. In return, the large distance of a factor of three between the frequency sample points at the lower frequency end, which is almost intolerable in the EIS, is accepted.

In practice, it has been shown that the loss of accuracy is even more dramatic, e.g., due to the inability to perform automatic amplitude adjustment by range switching over many orders of magnitude when moving from high to low frequencies, as is the case with the sine wave method. As information on the measuring range is only available after the measuring time for the lowest frequency has elapsed, automatic range switching can even result in a multiple of the total measuring time compared to single frequency excitation.

It is therefore not surprising that "new" procedures for saving time in TFA keep appearing in the literature in periods of a few years [97], [98], [99], [100], [101], but the citation soon died down again without any particular resonance.

Multispectral excitation certainly has a useful application potential - not, as the protagonists of the method usually recommend, to save "expensive" measurement time of many minutes or hours, but to make comparatively fast processes in the seconds range accessible to impedance analysis at all. In this case, it is not the - very short - period duration of the measurement frequency that determines the measurement time in the single frequency method, but the much longer time required for online signal analysis and data management. In order to exploit this potential, it is necessary to combine multiple sequential multispectral excitation and immediate data storage with subsequent offline analysis.

4 Extended library for impedance models

The following chapter introduces the impedance models as used, for example, for the interpretation of the data presented in chapter 3.1.4 and other systems with pore character, inhomogeneous dielectric and relaxation of the charge transfer reaction rate that are still to be discussed. The pore model according to H. Göhr was developed by the author with the help of J. Söllner [13] into a basic algorithm and soon afterwards implemented by the author as an assembler program in order to minimize the computing time corresponding to the mathematical effort. The model for the relaxation impedance was developed by H. Göhr with the participation of the author, who also implemented it in assembly language. The models for inhomogeneous dielectrics are based on different preliminary work, which is discussed in the relevant sections.

4.1 The impedance of porous electrodes

From pacemakers to batteries - in many technical applications of electrodes, the aim is to minimize power loss by reducing the overvoltage at the electrochemically active interface. In general, the current-carrying capacity of electrodes increases with their surface area. In order to improve the efficiency of a two-phase ion conductor-electron conductor system with the same volume, attempts are made to increase the surface area, e.g., by roughening the metal and / or porous penetration with the electrolyte. The impedance of the electrode can serve as a measure of success - it is inversely proportional to the electrode area - a low impedance therefore usually also means high efficiency.

If you look at early publications [10], [15], [16], [11], [12] on such systems, one finds related but mostly very specialized approaches to describe their impedance. It is noticeable that the attempt to support the most precise possible descriptions of the pore geometry comes at the expense of a flexible modeling of the processes inside the distributed electrochemical double layer. The impedance model for the "homogeneous pore system" according to H. Göhr [13] from 1983 pursues the opposite strategy: The description of the pore geometry is simplified to such an extent that no restrictions need to be accepted for modeling the double layer processes compared to the situation at smooth electrodes. The Göhr model is based on the assumption of uniform, cylindrical pores. The total impedance results from the multiple parallel connection of typical individual pores ("homogeneous pore system", see also Figure 32). Within the pores, the proportions of the various processes that contribute to the impedance of the electroactive surface are assumed to be independent of location.

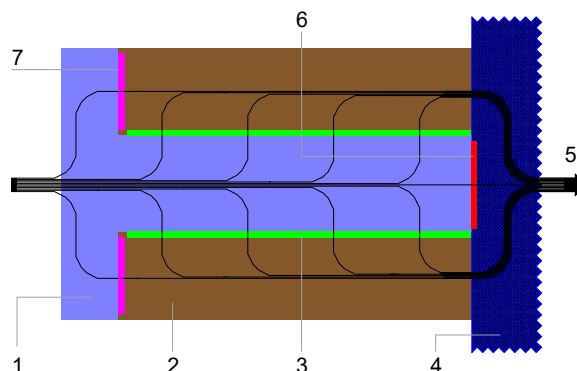


Figure 32: Current paths (5, black) in the single pore with electrolyte (1, light blue), end face impedance Z_e (7, violet), electron-conducting pore walls (2, brown), electrochemically active inner pore surface Z_q (3, green), impedance of the pore bottom Z_m (6, red) and the electrode (4, dark blue).

The analytical expression Eq. 45 obtained by H. Göhr with the abbreviations Eq. 46 to 53

$$Z = Z_{||} + Z^* \cdot \frac{1 + 2p \cdot s \left(\sqrt{(1-T^2)} - 1 \right) + T(p^2 q_m + s^2 q_e)}{T(1 + q_e q_m) + q_e + q_m} \quad (45)$$

$$Z^* = \sqrt{(Z_p + Z_s)} \cdot Z_q \quad (46)$$

$$Z_{||} = Z_p \cdot Z_s / (Z_p + Z_s) \quad (47)$$

$$q_e = Z^* / Z_e \quad (48)$$

$$q_m = Z^* / Z_m \quad (49)$$

$$p = Z_p / (Z_p + Z_s) \quad (50)$$

$$s = Z_s / (Z_p + Z_s) \quad (51)$$

$$\nu = \sqrt{(Z_p + Z_s) / Z_q} \quad (52)$$

$$T = \tanh(\nu) \quad (53)$$

contains beside

- the integral impedance Z_p of the ion-conducting electrolyte in the pores
- the integral impedance Z_s of the electronically conductive matrix
- the integral electrochemical interface impedance Z_q of the pore inner walls

the possibly different integral impedances Z_e of the electrolyte-side end face and the pore bottom Z_m .

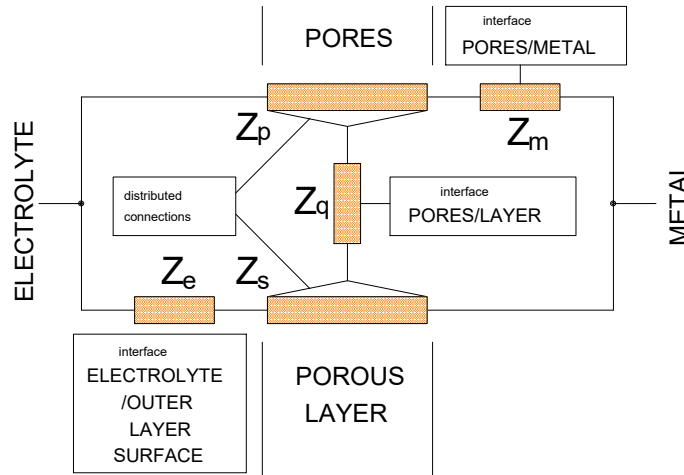


Figure 33: Symbolic circuit diagram of the Göhr homogeneous pore system (from [17]).

In Figure 33 the integral partial impedances are graphically illustrated in Eq. 45.

The partial impedances Z_q , Z_e and Z_m can be freely constructed in the created calculation program from the library elements or user-defined impedance expressions. Since the calculation of the Göhr pore impedance can be applied recursively, these partial impedances may in turn contain pore systems. To simplify the input procedure for the user, the partial impedances Z_p and Z_s assigned to the electrolyte and the matrix are assumed to be purely Ohmic.

On the surface, the clearly defined specifications of the homogeneous, cylindrical pore system appear to be a severe limitation for the applicability to real systems. Studies by other authors [18], [23], [20], [21], [22], however, show a broader range of application of the Göhr model.

If we consider the simple case⁵ of an ion-conducting phase II (e.g., pores filled with electrolyte) in an electron-conducting phase I (e.g., a metallic matrix) under the restrictive conditions

⁵ The equally important case of electrodes with porous cover layers, such as those found in passive aluminum, cannot be described using a two-phase model. It is better to model such cover layers using one or more stacked, partially insulating phases. The porosity or the penetration of electrolyte is reflected in their dielectric losses and leakage resistances.

- Negligible resistance for the conduction in phase I
- electrochemical activity only inside the pores on the side walls ($Z_e, Z_m \rightarrow \infty$)

then, after simplifying Eq. 45 accordingly, we find an expression that corresponds to the expression previously given by K. Mund [16] for the total impedance of a chain conductor ("Transmission Line Model" TLM) according to Figure 34. This results in the expression Eq. 54.

$$Z = \sqrt{Z_p \cdot Z_q} \cdot \sqrt{\coth\left(\frac{Z_p}{Z_q}\right)} \quad (54)$$

The agreement can be seen from the comparison of Figure 33 with Figure 34 of the underlying networks. Eq. 54 and Figure 34 reflect in many cases the impedance behavior of macropore systems with a granular structure, although there are no dedicated cylindrical pores.

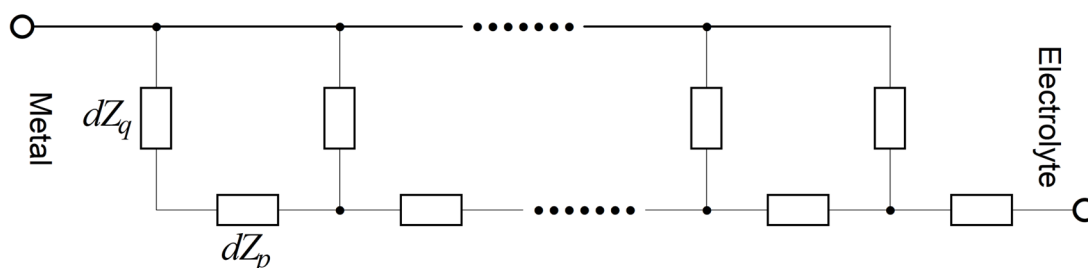


Figure 34: Chain conductor model ("Transmission Line Model" TLM) with the incremental partial impedances dZ_p of the line resistance (e.g., of the electrolyte, phase II) and dZ_q of the electrochemically active surface.

A broader applicability of Göhr's model thus results from its traceability to the traditional chain conductor, which, as A. Hahn and H. Landes describe for the case of an SOFC cathode, can be generalized as the impedance of a system of two interpenetrating spatial areas of different conductivity mechanisms [14]. This is illustrated in Figure 35.

The figure also shows that the gas-filled pores of the cathode material do not contribute to the impedance and are not explicitly included in the model.

The generally good agreement between modeled and experimentally measured impedance is due to the uniformity in the electrochemically effective volume of the macropore systems investigated. Conversely, no information about the pore geometry can be obtained by applying this model. The results represent mean values over a quasi-homogeneous, possibly granular system in which the impedances of the pore bottom and front surface Z_m and Z_e are of no significance.

A strength of the Göhr model compared to the TLM model lies in the free definability of the partial impedances Z_q , Z_e and Z_m . In particular, the impedance Z_q of the electrochemically active interface should only be simplified to double-layer capacitance and charge transfer resistance in special cases. However, such a case is described by A. Hahn in his dissertation [18].

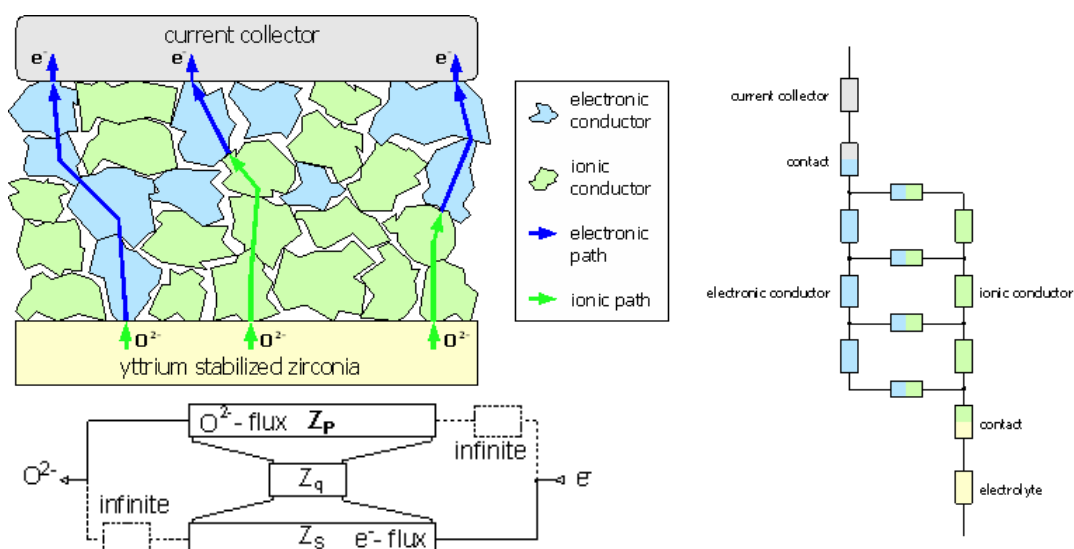


Figure 35: Application of the TLM model (right) to the mixed conductivity structure (left) of an SOFC cathode (taken from [24]). The figure below shows the assignment of the components to the Gohr model of the porous electrode (Figure 33).

However, as in the report by Mund [16], it is necessary to model the diffusion processes taking place in the microporous system as a substructure of the grains of the solid body of an electrode, as shown there. F. Richter [19] showed the recursive application of Gohr's model. He was able to successfully model the cathode of a tubular high-temperature fuel cell SOFC by inserting a further pore system as the interface impedance Z_q of a superordinate chain conductor.

When current flows through the interfacial impedance Z_q , however, a weakness of the Gohr model becomes apparent: Due to the voltage drop in the electrolyte over the pore length, the potential effective for different increments dZ_q of the interfacial impedance Z_q in the pore varies greatly. The overvoltage and thus the transfer current decreases approximately exponentially over the pore length. The increments dZ_q differ significantly and the assumption of homogeneity is inadmissible. According to [20], the impedance expressions of such inhomogeneous pore systems do not lead to closed solutions, similar to certain cases with the inhomogeneous dielectrics discussed in the following section.

At first glance, it is surprising that even with current flow, PEFC low-temperature fuel cells, for example, can be reproduced well with the Gohr model (Figure 36). However, due to the turnover concentrated at the pore mouth, the increments dZ_q of the interface impedance there have a much smaller impedance value than the increments deep inside the pore and therefore dominate the total impedance. The pore therefore appears effectively shortened by the current flow. The influence of porosity on the appearance of the total impedance decreases, which explains the good modeling results that can be achieved with the Gohr model even with large current flow variation.

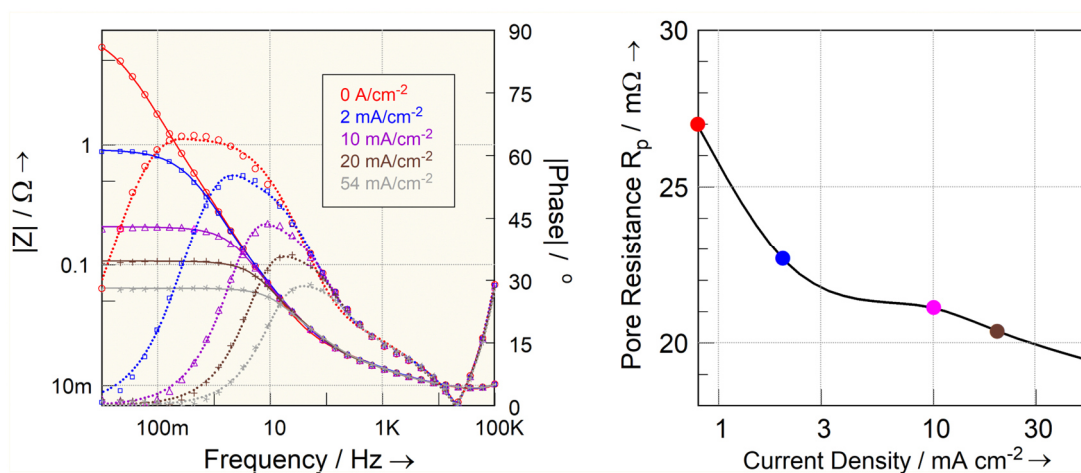


Figure 36: Impedance spectra series from [127] (Bode diagrams on the left) of a fuel cell at various loads (PEFC at 80 °C, $p_{O_2} = p_{H_2} = 2$ bar, Nafion-117 membrane, 4 mg Pt/cm²). The symbols correspond to the measured data, the curves (dotted: phase response) to the model simulation based on the Göhr pore model. The figure on the right shows the determined course of the pore resistance R_p over the current density.

At higher current densities, the apparent shortening effect of the pore is superimposed by the depletion of the effective number of pores: the reaction water on the cathode side (which dominates the impedance) "floods" many pores, so that the effective pore resistance (which is calculated from the parallel connection of all pores according to the Göhr model) increases again. At very high current densities > 150 mA/cm², the curve of Z_p over the current density (in Figure 36 no longer shown on the right) reverses again.

4.2 The impedance of inhomogeneous dielectrics

The last section dealt with how the spatial distribution of electroactive surfaces can cause the interaction of reactance and ohmic contributions to the electrode impedance to no longer lead to clearly defined individual time constants. Instead, distribution functions of time constants are observed that are not only characteristic of the processes, but also of the respective distribution geometry.

In the early days of impedance spectroscopy, interpretation problems were encountered with impedance contributions whose capacitive character dominated, but which were accompanied by a constant ohmic component over the observable frequency range. Such impedances behave approximately like capacitances, but the ohmic contribution causes characteristic small deviations: Instead of a phase shift of $-\pi/2$ (-90°), one observes a slightly smaller amount of phase angle, e.g. -89° , which is (approximately) frequency-independent, in contrast to the behavior of a combination of resistance and capacitance (RC element). The impedance transfer function Eq. 23 of such a (special) constant-phase element CPE follows the general relationships Eq. 29 and 30 with the restriction to exponents $\alpha > -1$ in the vicinity $\alpha \approx -1$.

Figure 37 shows the comparison of the impedance of capacitance and "loss capacitance" CPE.

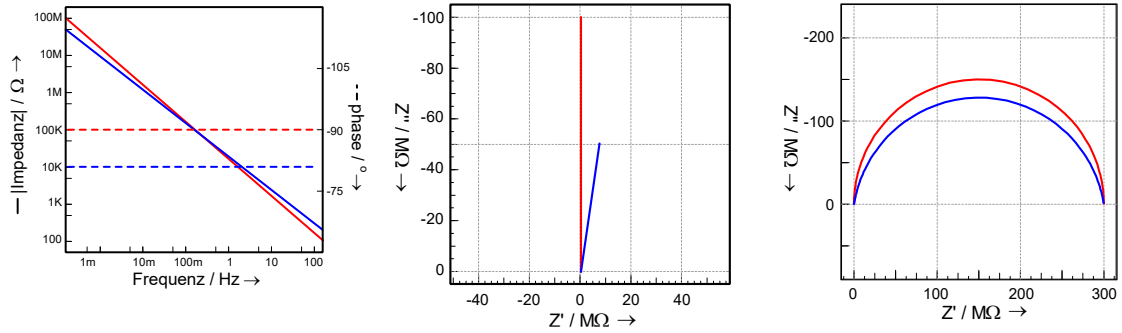


Figure 37: Comparison of the impedance curve of capacitance (red) and capacitance loss CPE (blue): Bode diagram (left) and Nyquist diagram (center). The Nyquist diagram on the right shows the impedance curve of a resistor-capacitor parallel circuit (red semicircle, RC element) in comparison with the combination resistor-CPE (blue, compressed semicircle).

Previously mostly recognized as an artifact, the frequent appearance of such CPE in the impedance spectroscopy of electrochemical systems is now widely accepted, although not always fully understood. Usually, the occurrence of CPE behavior in the double layer capacitance of metallic electrodes is associated with surface roughness: When measuring an electrode at an equipotential surface in the electrolyte, which is assumed to be flat, the different surface areas of a rough electrode are at different distances from the measurement equipotential plane due to the height profile. Each element of the double layer capacitance is connected with its locally different electrolyte resistance element to its RC element, so that the parallel connection to the total impedance of the electrode can no longer be summarized to a common, discrete time constant. Instead, a distribution function of time constants must be calculated. Quantitatively, however, it can be seen that the distribution effect for a structure as shown in Figure 38 only acts in the frequency transition range between the ohmic behavior of the electrolyte and the frequency range determined by the double-layer capacitance. CPE-like behavior, which is characterized by an approximately constant phase angle slightly different from $-\pi/2$ over a moderately large frequency range, does not occur. The resulting impedance spectra are similar to the spectra observed on smooth electrodes with an inhomogeneous field distribution, e.g., due to an unfavorable geometry of the counter electrode.

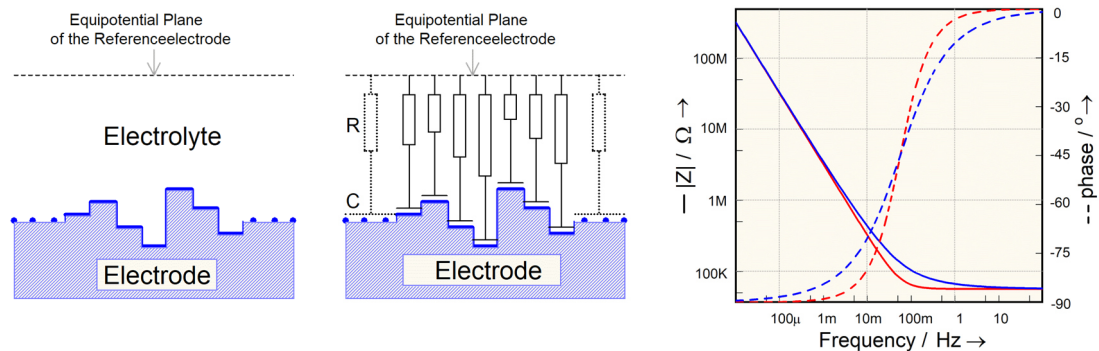


Figure 38: Simple model of a rough electrode in the electrolyte (left). The coupling of the double layer capacitance of different surface areas via different electrolyte resistances (center) leads to deviations (right: blue curves) from the impedance spectrum of a discrete time constant (right: red curves). The inhomogeneous electric field between the counter electrode and a smooth working electrode has a similar effect if the geometry is not perfectly planar.

As the cause of the CPE behavior of rough electrodes was therefore proposed in the 1980s a fractal geometry of the roughness [56], [57], [58]. A relationship between the fractal dimension d_F of the rough surface and the CPE exponent α has also been established (Eq. 55), but its validity has been questioned in current discussions [65] again.

$$\alpha = \frac{1}{d_F - 1} \quad (55)$$

CPE behavior has also been repeatedly observed with very smooth electrodes. Therefore, distribution mechanisms that do not require surface roughness have also been discussed. T. Pajkossy and D. M. Kolb [60], [61] have found, for example, that the activation energy for partial charge transfer in adsorption processes on polycrystalline electrodes can depend strongly on the orientation of the micro crystallites. For the average impedance of such an adsorption process, there is no discrete time constant of adsorption resistance and adsorption capacity - similar to rough electrodes for electrolyte resistance and double layer capacity. Instead, CPE-like behavior is found.

Loss capacitances do not only occur on electrodes in connection with double layer and adsorption capacitance. If the electrodes are protected from direct electrochemical attack by passive layers or polymers (lacquers) on the metals, the impedance is essentially determined by the properties of the covering layer. In the case of a corrosion protection layer, a simple relationship can often be found between its impedance behavior and the quality of the protection. Since a perfect hydrophobic polymer usually behaves like a perfect dielectric, all disturbances due to impurities, pores, cracks, delamination etc. contribute to characteristic deviations from the ideal capacitor behavior. Weaknesses in the coating usually show up in the impedance spectrum as an ohmic parallel branch to the layer capacitance. If the proportion of faults is too small to be detected in the low-frequency spectrum within a reasonable measurement time, electrochemical stress (cathodic polarization) can often be used to provoke growth of the damage and detect it in subsequent impedance spectra. This has given rise to the "AC-DC-AC" method [128], [129], [130], which is occasionally used in the food and packaging industry as a quality test for coatings.

The impedance spectra of passive layers and swellable coatings have a clearly different phenomenology from the spectra of hydrophobic polymers. Instead of showing visible resistance components only in the presence of defects in the low-frequency impedance spectrum, CPE-like behavior can be observed over a large frequency range, deviating from the ideal dielectric, even in the case of largely pore-free layers. The following section deals with the causes of such "dielectric losses" in passive layers, which are suspected in the gradient of a partial conductivity of the dielectrics [125].

4.2.1 The impedance of surface layers with conductivity gradients

It was suspected early that local differences in the stoichiometry of transition metal oxides can also lead to conductivity gradients within their oxide layers on the metals in the electrolyte (Figure 39). L. Young [113] postulated for the n-type oxide of niobium an exponentially decreasing conductivity $\sigma(x)$ from the metal towards the solution due to the decreasing stoichiometric excess of metal, which is observable closer to the electrolyte.

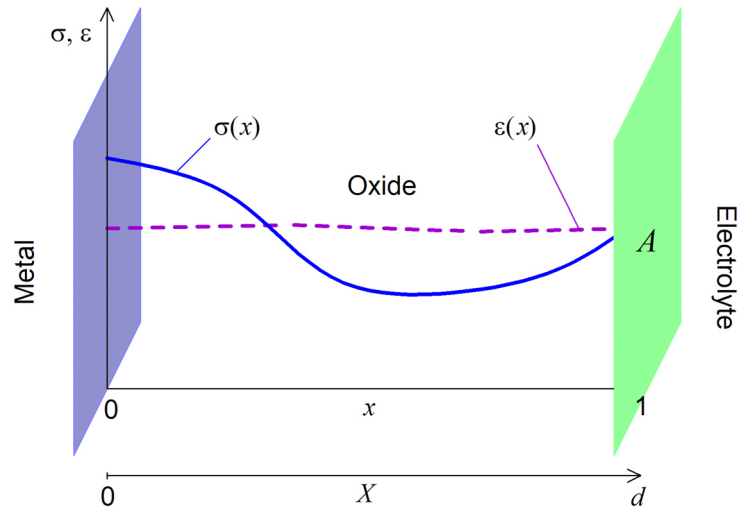


Figure 39: Surface layer with thickness d and area A on a metal in solution with locally different conductivity $\sigma(x)$ and dielectric constant $\varepsilon(x)$ as a function of the relative (normalized to the thickness) location $x = X/d$, $0 \leq x \leq 1$ perpendicular to the layer plane.

Sotnikov et al. [119] proposed a conductivity curve according to a power law, but without explicitly specifying formation mechanisms. For the oxide of tantalum, Scholte, Van Geel [120] and Sasaki [121] postulated a sequence of semiconducting phases with p-type conduction due to excess oxygen on the electrolyte side, low intrinsic conductivity in the main part of the oxide layer with balanced stoichiometry and n-type conduction due to excess metal directly in front of the metallic part of the electrode. The dielectric constant of the top layer material can also vary locally. Due to its small range of values compared to the variability of the conductivity of many orders of magnitude, the course of the dielectric constant generally does not need to be taken into account as shown in Eq. 57.

The impedance of such layers can therefore be modeled by dividing the dielectric into n sufficiently thin layers, within which the change in conductivity $d\sigma/dx$ can be neglected (Figure 40). Each sub-layer can thus be represented by a parallel RC element consisting of location-dependent resistance and constant capacitance. The total impedance results from the series connection of the elements (Eq. 56) by means of numerical integration. In special cases, direct mathematical integration is also possible.

$$Z_S = \frac{d}{A} \cdot \sum_{i=1}^n \frac{\Delta x_i}{\sigma_i + j\omega\varepsilon_0\varepsilon_i} \quad (56)$$

$$Z_S = \frac{d}{A} \cdot \int_0^1 \frac{dx}{\sigma(x) + j\omega\varepsilon_0\varepsilon(x)} \quad (57)$$

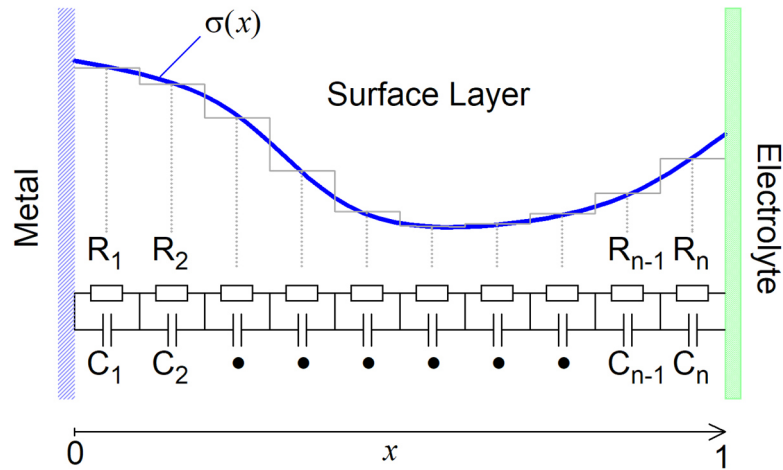


Figure 40: Division of a dielectric with a significant conductivity gradient into sufficiently thin layers with a negligible gradient, which can be represented by RC elements.

The frequency behavior of the impedance of the layers with conductivity profiles deviating from homogeneity is characterized by the fact that CPE-like behavior can be observed in a more or less wide range. The limit value for high frequencies always tends towards the dielectric capacitance⁶ and at low frequencies the impedance changes to the DC resistance, which results from the sum of all partial layer resistances.

4.2.1.1 The Young-Göhr impedance

The exponential conductivity curve proposed by Young σ_x (Eq. 58, Figure 41) is special in that the impedance calculation does not use numerical approximation and the total impedance Z_{YG} of such a layer (Eq. 59) can be expressed in closed mathematical form. This was demonstrated in the working group of H. Göhr as part of Norbert Müller's dissertation [122]. The corresponding model was therefore implemented directly in the library of the impedance simulation program SIM of the author's company.

$$\sigma_x = \sigma_0 \cdot e^{-\frac{x}{\delta}} \tag{58}$$

σ_0 = conductivity at location $x=0$ ($0 \leq x \leq 1$), δ = relative penetration depth of conductivity ($0 < \delta < 1$).

⁶ The dielectric capacitance corresponds to the capacitance of the space element that would be observed without the presence of ohmic conductivity. Since the AC conductivity of a capacitance increases with frequency, while the ohmic conductivity remains constant, the latter becomes negligible at high frequencies. The same applies to capacitive conductivity at low frequencies.

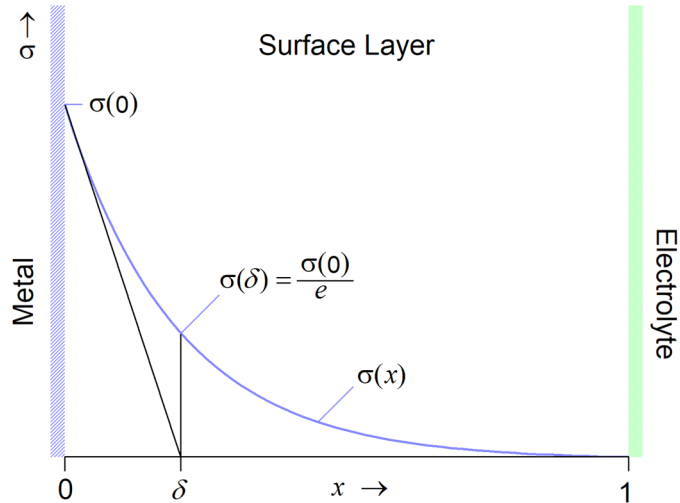


Figure 41: Conductivity profile according to Young within a cover layer. The impedance can be calculated by introducing the dielectric capacitance C_{YG} , the relative penetration depth δ and the RC time constant τ at the location $x=0$ using the formula (Eq. 59) according to Müller and Göhr.

$$Z_{YG} = \frac{\delta}{j\omega \cdot C_{YG}} \cdot \ln \left[\frac{1 + j\omega\tau \cdot e^{\frac{1}{\delta}}}{1 + j\omega\tau} \right] \quad (59)$$

With C_{YG} = dielectric capacitance, τ = RC time constant at location $x=0$, δ = relative penetration depth of the conductivity

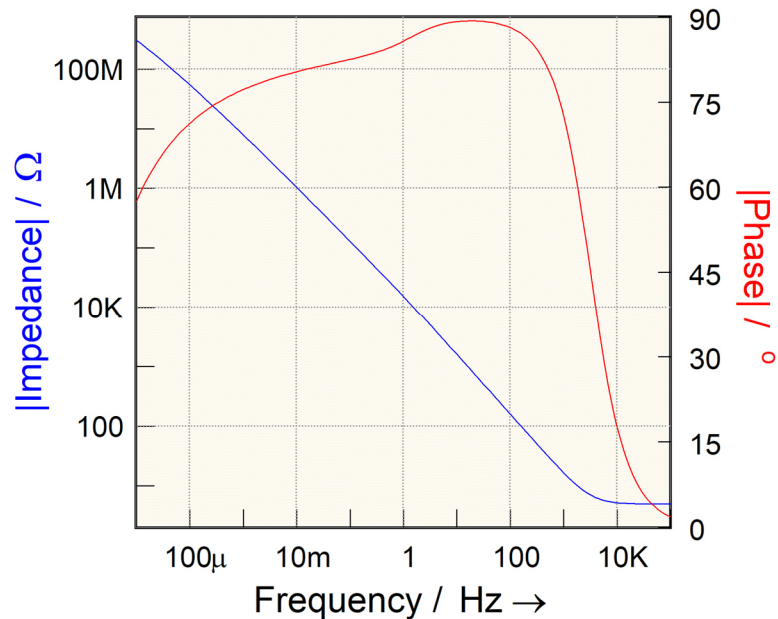


Figure 42: Bode diagram of the impedance curve of a typical Young-Göhr impedance Z_{YG} with the parameters $C_{YG} = 10\mu\text{F}$, $\tau = 0.1\text{s}$, $\delta = 0.07$ in series connection with an electrolytic resistor $R_{EL} = 5\Omega$.

The YG impedance model has been successfully applied, for example, to passive layers of titanium [122], [123], Zircalloy [124] and iron [123]. In addition, the swelling of water-based as well as solvent-based paints can cause conductivity profiles similar to the Young model due to the penetration of ions from the electrolyte. Therefore, such systems can also be described well with the YG impedance model [140]. An alternative model, which is based on the idea of discrete events of dielectric relaxation, has already been described in section 3.1.4.3.

The frequency response of the YG impedance differs within a certain frequency band (in Figure 42 approximately 100Hz to 10KHz) only slightly from the frequency response of a CPE element.

When measuring coatings on real objects, the observable, capacitively dominated frequency range is sometimes too small to reliably distinguish the YG impedance from the appearance of the CPE element. In this case, simplified modelling with a CPE element as an approximation for the YG impedance is useful, as this at least allows the relative penetration depth δ of the conductivity profile to be determined. According to Eq. 60, δ can be calculated very simply because it is linked to the exponent α of Eq. 29 of a CPE element. This means that the swelling of protective layers on metals in the electrolyte can already be quantitatively monitored with sufficient accuracy [123].

$$\alpha \approx 1 - \delta \tag{60}$$

α = Exponent of the constant phase element, δ = Relative penetration depth of the conductivity in the YG model

According to N. Müller, the approximation Eq. 60 is fulfilled for $\delta \ll 1$ and $\delta \ll \ln(\omega \cdot \tau)$ [122].

4.2.1.2 The use of the Young-Göhr impedance in Mott-Schottky analysis

Semiconducting oxide layers [53], [54], [55] such as the electron-conducting oxide film on titanium form a "space charge zone" in contact with an electrolyte of different Fermi level to equalize the phase boundary. Due to the usually high conductivity of the electrolyte relative to the semiconductor, the dominant part of this double layer is not in the electrolyte as a Helmholtz layer, but within the semiconducting phase. In the region of the space charge zone, the valence and conduction bands of the semiconductor are deformed (Figure 43).

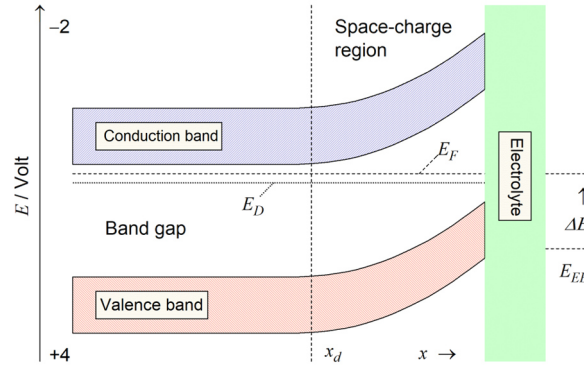


Figure 43: Band scheme of an n-type semiconductor on the electrochemical potential scale in contact with an electrolyte with the dominant redox potential E_{EE} of the solid/electrolyte system. In the example, E_{EE} is more anodic than the Fermi level E_F inside the pure semiconductor. The space charge zone (here a depletion zone) begins at the location x_d with a parabolic shape of the potential curve up to a bend $\Delta E = E_{EE} - E_F$ at the phase boundary.

If the redox potential E_{EE} of the electrode (in the example of titanium in an aqueous medium, it is the formation potential of the oxide) of an n-type semiconductor is more anodic⁷ than the Fermi level E_F inside the semiconductor before contact, a band bending of the magnitude $\Delta E = E_{EE} - E_F$ and a depletion zone of electrons with maximum depletion at the phase boundary occurs. In general, the Poisson equation describes the spatial dependence of the potential ϕ on the spatial dependence of a charge carrier concentration. In the case under consideration, the charge is made up of the sum of the positive charges of all n_b donors and all electron charges e_0 in the conduction band, which are electrically compensated, apart from a small potential-dependent component in the depletion zone. The Poisson equation can then be expressed as in Eq. 61 (notation according to [9]):

$$\frac{d^2\phi}{dx^2} = -\frac{n_b}{\varepsilon \cdot \varepsilon_0} \left(1 - e^{\frac{e_0 \cdot \phi}{kT}} \right) \quad (61)$$

For the depletion layer, if the exponential term dependent on the potential in Eq. 61 can be neglected, a quadratic course of the field strength results. The electron concentration then decreases with assumed Boltzmann statistics from the location x_d of the start within the depletion zone (Figure 43) in the direction of the phase boundary. The depletion zone is therefore regarded as a kind of barrier layer and according to the Mott-Schottky relationship Eq. 62 the capacitance C_{SC} is assigned to it.

The position of the Fermi level E_F within the band gap of the semiconductor and the majority charge carrier concentration n_b should be calculated according to Eq. 62 can therefore be determined by measuring the dependence of the capacitance on the applied potential E ⁸. When

⁷ The considerations relate to the electrochemical potential scale. They also apply complementarily to holes in the p-type semiconductor and a reversed polarity of the Fermi level difference ΔE .

⁸ E_F from the x-axis section and n_b from the gradient.

$E = E_F$ (also called "flat band potential" in this context) is reached, the band bending⁹ finally disappears, the effective thickness of the potential barrier approaches zero and the capacitance C_{SC} thus tends towards infinity.

$$\frac{1}{C_{SC}^2} = \frac{2}{\varepsilon \cdot \varepsilon_0 \cdot e_0 \cdot n_b} \cdot \left(E - E_F - \frac{kT}{e_0} \right) \quad (62)$$

Boltzmann constant k , absolute temperature T , material dielectric constant ε , vacuum dielectric constant ε_0 , elementary charge e_0 , majority charge carrier concentration n_b .

In practice, there are a number of possible errors that can call into question the usefulness of Mott-Schottky analysis. The method originates from research on classic, often monocrystalline semiconductors in contact with metals instead of electrolytes. A common procedure for determining the capacitance at the metal-semiconductor Schottky contact measures the imaginary part of the impedance - usually using an RCL measuring bridge set to a typical fixed frequency of 1 kHz - and assigns it to a capacitance C_{SC} . Even in such very clearly defined systems, errors can easily be made in this assignment due to the misinterpretation of the real part of the impedance. If one keeps Figure 43 and replaces the electrolyte side with a metal with corresponding work function, the measurable impedance is not determined by the space charge zone alone, but appears as a series connection with the impedance of the semiconductor bulk material (on the left in the figure). If the latter is approximated as an ohmic resistor, it forms a series RC element with the capacitance C_{SC} and the calculation of C_{SC} must be made from the imaginary part of the impedance. On the other hand, the approximation of considering the impedance of the depletion zone as a single capacitance is too simplistic in several respects. On the one hand, the majority carrier conductivity in the depletion zone does not decay to zero, but a finite residual conductivity (in this case of the electrons) remains, which becomes very high near the flat band potential. On the other hand, the Fermi level approaches the respective other band towards the phase boundary and the concentration of minority carriers (in this case the holes) can make a further significant contribution to the residual conductivity, whereby the relative proportions change with the applied potential E . If this parallel resistance component dominates the measured real component, the capacitance must be calculated from the imaginary component of the admittance (parallel capacitance) instead of the imaginary component of the impedance (series capacitance). The calculation method used should be specified in publications. If both parallel conductance and series resistance contribute to the real part, none of the specified approximations is permissible and the capacitance can only be determined by measuring the impedance at other frequencies, i.e., by impedance spectroscopy. This can be assumed if an electrolyte forms the partner in the Schottky contact instead of a negligibly low-resistance metal.

In this case, the total impedance of the Schottky contact is essentially¹⁰ determined by the series connection of the impedance of the field-free semiconductor body with the impedance of the depletion zone and the impedance of the electrolyte. The latter can generally be easily described as the electrolyte resistance.

The simplified modeling of the impedance of the depletion zone Z_{SC} as a parallel RC element must be viewed more critically. As can be seen from the discussion above, this is typically an impedance of a dielectric with a conductivity gradient, whose simplest approximation as a CPE has the serious disadvantage that the capacitance sought occurs as a function of frequency. As a way out, Z_{SC} can be approximated as a YG impedance, which can be connected in parallel with a resistor for potentials close to the flatband potential to allow for a tunnel current. The YG impedance is only defined for a single exponential conductivity profile. In the case of Z_{SC} , it can nevertheless be a useful approximation, as the minority carrier conductivity is negligible for small deviations of the potential from the flatband potential and the majority carrier conductivity is negligible for larger polarization.

In principle, the YG impedance model avoids the problems caused by frequency-dependent capacitances, as it is characterized by a physically clearly defined dielectric capacitance. As an

⁹ (apart from the small amount kT/e_0)

¹⁰ However, the contribution of the electrolytic double layer can only be neglected if the conductivity of the electrolyte is significantly higher than that of the semiconductor.

alternative to using the YG impedance model, the impedance behavior of the depletion layer can also be modeled directly numerically, as has recently been shown [59].

The impedance contribution of the field-free semiconductor body can be well represented for classical, homogeneous semiconductor materials by a parallel RC element whose capacitance is formed by the volume capacitance and whose conductivity is formed by the volume conductivity of the material. Plieth et al. showed for semiconducting polymers that the impedance of the semiconductor body for the Mott-Schottky analysis must be modeled as a layered structure with a porous phase [64]. Thus, flat band potentials and charge carrier concentrations of conducting polymers could be determined [62], [63]. The situation is different for oxide films on metals. As explained above, a stoichiometric gradient in the direction of the oxide depth leads to a conductivity gradient even without a space charge zone caused by electrolyte contact and thus to the occurrence of impedances that can be described directly or approximately by the YG impedance. Figure 44 shows schematically how such a passive layer could be modeled in order to obtain at least more meaningful Mott-Schottky characteristics than would be possible if only the imaginary part were recorded at a fixed frequency.

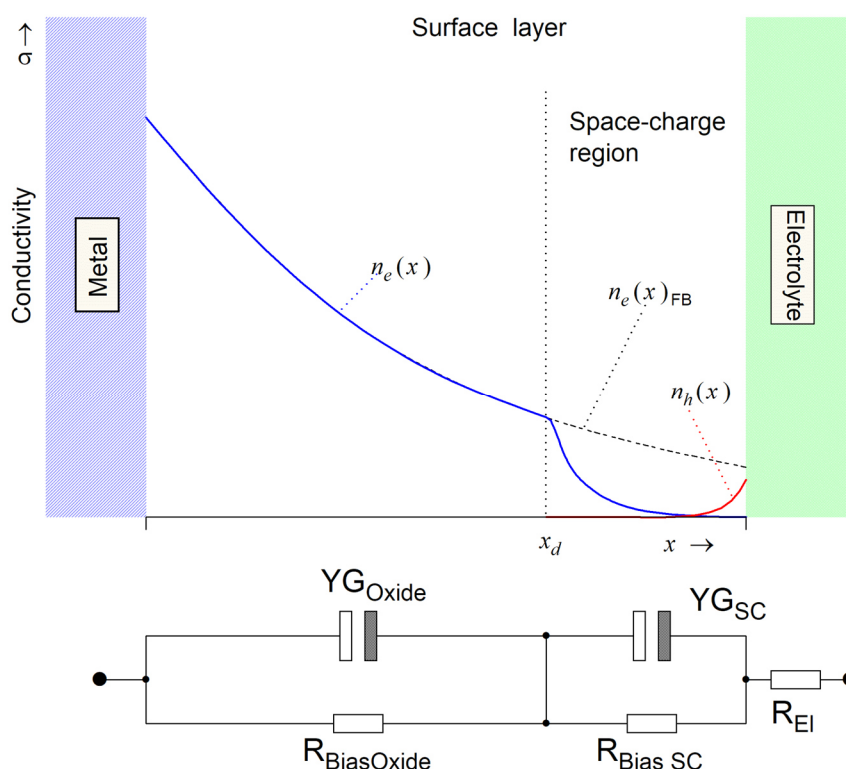


Figure 44: Top: Schematic conductivity curve σ within a cover layer with a conductivity gradient towards Young away from the flat band potential with the electron density n_e , the hole density n_h and the electron density $n_{e\text{FB}}$, which occurs at the flat band potential. Below: Electrical equivalent circuit diagram from the series connection of the impedance of the oxide main part, oxide depletion layer and electrolyte.

When using the Mott-Schottky analysis, it should be noted that the thickness of the space charge zone should remain small compared to the semiconductor material thickness. This is the case with high conductivity. In the case of thin or less conductive oxide films, the space charge zone can spread over the entire material thickness and the Mott-Schottky approximation fails even for moderate polarization. For applications with low polarization close to the flatband potential, the impedance model according to Figure 44 is too simplified due to the onset of cathodic reaction. In addition, the problem with the impedance evaluation is that the high admittance of the thin depletion zone in series with the low admittance of the residual film can only be determined inaccurately. With the expected conductivity gradient, the Mott-Schottky relationship Eq. 62 relevant charge carrier concentration n_b changes with the polarization. An experimental characteristic that comes close to the ideas of the Mott-Schottky theory can therefore only be expected if the semiconducting oxide behaves at least roughly like a homogeneously doped semiconductor. In addition, oxide films can exhibit many lattice defects, including an amorphous appearance, so that the density of states cannot be clearly divided into permitted and forbidden bands.

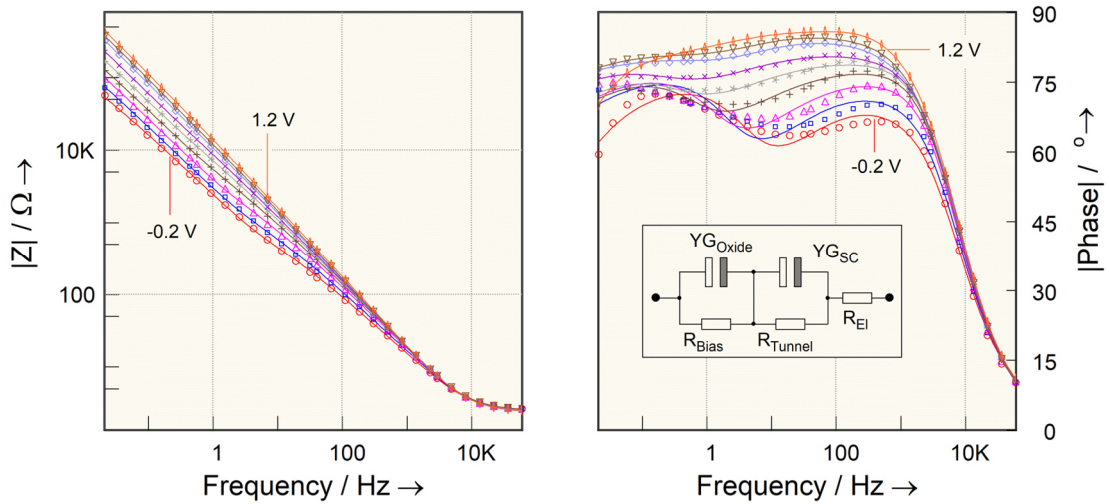


Figure 45: Impedance spectra series against potential (referred to Ag/AgCl in 3m-KCl) of an oxide layer on titanium in 0.5m aqueous K_2SO_4 solution (measured data: symbols) and the data fitted with the model shown in the inset on the right (simulation: solid curves). The oxide layer on the titanium sheet was generated by anodization in 1n- H_2SO_4 at 20V for 5 minutes and cured for 60 minutes at 450° C for annealing.

A great deal of experimental data on the Ti/TiO₂ system is already available in the literature. However, in order to verify the ideas discussed above, it is necessary to have impedance spectra available with high accuracy up to the highest possible frequencies. Therefore, the author himself carried out and evaluated impedance spectra series against potential on an oxide layer on titanium in a cell optimized for EIS (Figure 45). The samples were kindly prepared by the colleague Indhumati Paramasivam at the LKO. For this purpose, an oxide layer was generated on the titanium sheet by anodization in 1n- H_2SO_4 at 20V for 5 minutes and cured at 450° C for 60 minutes for annealing.

According to the model outlined above, the series capacitance of the components C_{Oxid} and C_{SC} , whose share changes with the potential, should be assigned to the dielectric capacitance of the entire layer and thus be independent of the potential. This could be confirmed with sufficient accuracy (Figure 46 left). The values given in the literature for the relative dielectric constant of anatase typically fluctuate between $\epsilon_{r(Anatas)} \approx 10$ [49] and $\epsilon_{r(Anatas)} \approx 41$ [50]. In this framework, the film thickness determined from the capacitance for an average $\epsilon_{r(Anatas)} = 20$ agrees with that of Indhumati Paramasivam and colleagues [51], [52], [52].

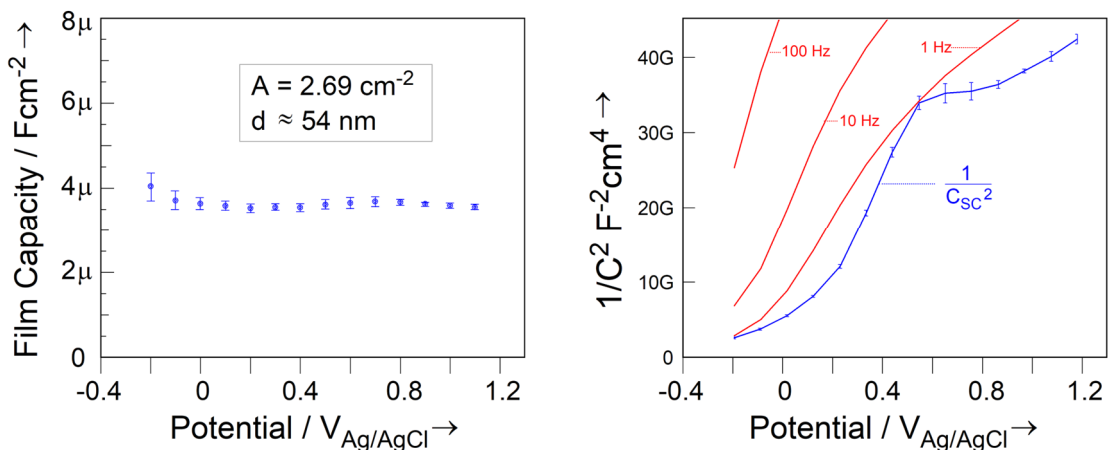


Figure 46: Left: Progression of the modeled dielectric capacitance $C_{Oxid} \sim C_{SC}$ of an oxide film on titanium in 0.5m aqueous K_2SO_4 solution over the potential from the experiment according to Figure 45. The total capacitance remains constant within the measurement accuracy. Right: Course of the modeled capacitance of the depletion layer in Mott-Schottky representation (blue). The Mott-Schottky plots determined from the imaginary part of the measured impedance at three different frequencies are shown in red.

From Figure 46 on the right, it is clear that the capacitance determination from the impedance measurement at a fixed frequency can lead to ambiguous Mott-Schottky plots (red curves). The

characteristic of the modeled capacitance C_{SC} of the depletion layer, on the other hand, is clear but not easy to interpret. The curve presumably reflects the varying electron density n_e over the changing penetration depth (Figure 44).

As shown in Figure 45 there are no areas in the measured impedance spectra that would allow assignment to a classic capacitance. Rather, all spectra are characterized by strong, changing dispersion of the capacitance and additional structure. Due to the ambiguity dependent on the evaluation frequency, this immediately rules out a classical Mott-Schottky evaluation.

Despite elaborate measurement technology, the author was unable to achieve the experimental goal of using the spectra to reach a frequency range in which the measured impedance is dominated by the high-frequency limit value of the dielectric capacitance. The constancy of the modeled dielectric capacitance $C_{Oxid} \sim C_{SC}$ predicted by the model nevertheless appears to be well fulfilled, which speaks for the applicability of the model. Unfortunately, even based on the YG model using the Mott-Schottky evaluation, it is not possible to clearly determine a charge carrier density n_e . The original model assumes that the charge carriers are present in a larger spatial area with a constant density n_e , so that no clear result can be expected for complex oxides of varying stoichiometry.

4.2.1.3 The impedance of dielectrics with power law conductivity curve based on A. I. Sotnikov

Other conductivity profiles for dielectrics are described in the literature, which can lead approximately to frequency dispersions of the capacitance that can be observed in practice, for example the model by Woods and Saxon, which assumes an S-shaped conductivity curve [118]. The model according to A. I. Sotnikov was included in the SIM simulation program. Sotnikov proposes a conductivity curve according to a power law. A closed solution exists for calculating this "Sotnikov impedance". However, it contains a principal value integral and is therefore not very suitable for numerical calculations. For this reason, the user element definition technique described in the appendix using an example was applied. It allows the dynamic definition of a calculation algorithm for impedance functions by the user, as already described in section 3.1.4.3 above. Hereby the numerical integration according to Eq. 56 of the layer impedance with a conductivity curve according to Eq. 63 was realized (Figure 47).

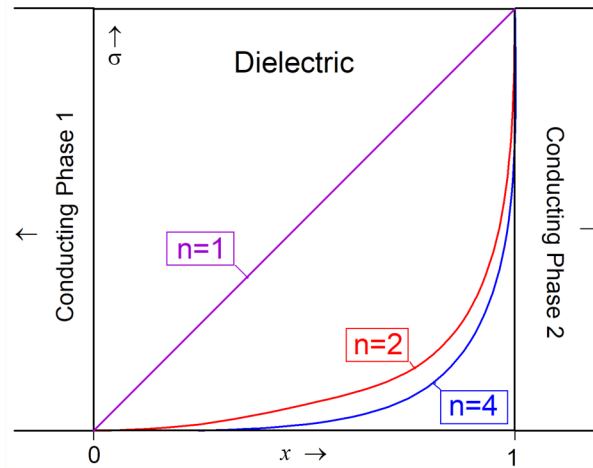


Figure 47: Power law conductivity curve in dielectrics based on A. I. Sotnikov. Shown are curves of orders n of 1, 2 and 4.

$$\sigma(x) = \sigma_1 \cdot x^n \tag{63}$$

x = (normalized) location in the dielectric with $0 \leq x \leq 1$, σ_1 = conductivity at $x = 1$, n = power order of the conductivity profile, $n \geq 1$.

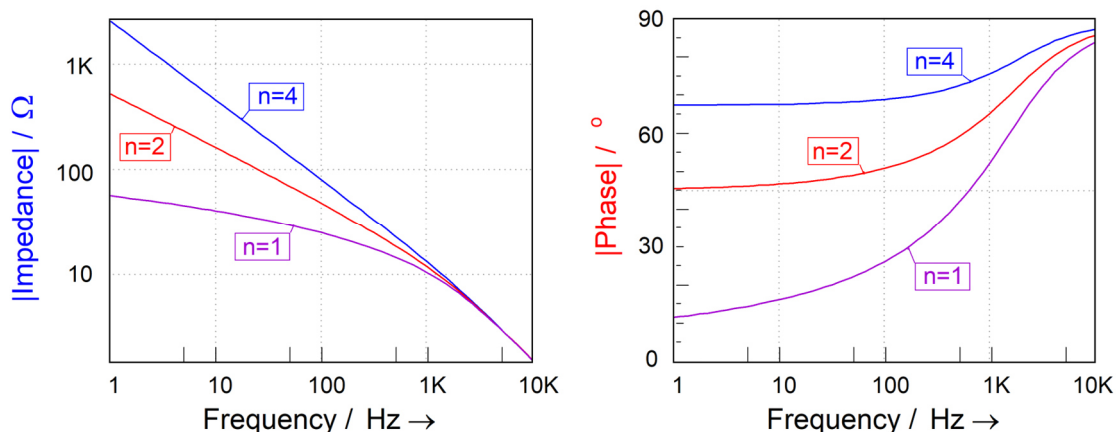


Figure 48: Bode diagram of the impedance curve of dielectrics with power-law conductivity curve according to A.I. Sotnikov. Shown are curves of orders n of 1, 2 and 4.

The implementation of the Sotnikov impedance was characterized more by academic than practical interest. The curve according to Eq. 63 is the only systematic¹¹ conductivity profile known to the author that shows perfect CPE behavior in the dielectric from an upper cut-off frequency ω_0 down to arbitrarily low frequencies (Figure 48). In the range for frequencies of around $\omega_0/10 < \omega < 10 \cdot \omega_0$ the frequency response at high n can hardly be distinguished from that of a YG impedance. This can also be seen from the approximations of Eq. 58 and Eq. 63 for $x \rightarrow 1$. The characteristic parameters α of CPE, δ of the YG impedance and order n of the Sotnikov impedance are compared in Eq. 64, where the range of validity for the last term with $n \gg 1$ is already known from the calculations of N. Müller [122].

$$\alpha \approx 1 - \delta \approx 1 - \frac{1}{n} \quad (64)$$

α = Exponent of the constant phase element, δ = Relative penetration depth of the conductivity in the YG model, n = Order of the conductivity profile according to Sotnikov

4.2.1.4 The PIN model

When applying the YG impedance model to the impedance of passive layers of some transition metal oxides in the electrolyte, certain deviations are sometimes noticeable. The shape of the phase angle curve is qualitatively similar to that of the YG impedance in Figure 42 - the same typical ranges are observed, from the approach to the dielectric capacitance at high frequencies to the approximately constant but somewhat "hanging phase" in a wide medium frequency range to the transition to ohmic behavior as the limit value for low frequencies. However, on closer analysis, e.g., after a fit of the measured data with the YG model, more or less significant deviations occur (Figure 49), as the author's measurement analyzed below shows:

¹¹ In addition to the continuous, monotonic conductivity profile, all arrangements created by permutation of the RC elements from the original profile show the same impedance, as the position within the series connection of the layers cannot be distinguished with regard to the impedance.

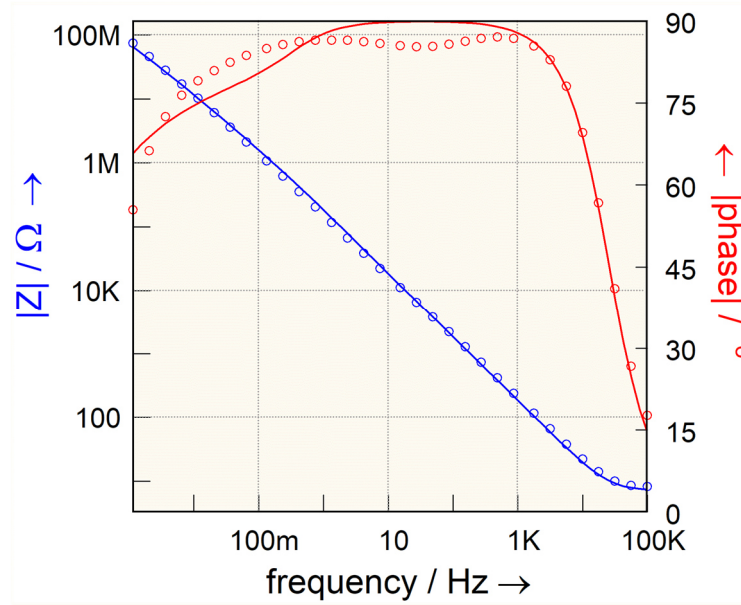


Figure 49: Bode diagram of an impedance spectrum (circles) recorded on the system Ta/Ta₂O₅/phosphate buffer after anodization at 45V at the rest potential of 1.5 V (against Ag/AgCl-3m NaCl) with the result fitted according to the YG model (solid line). Clear systematic deviations are recognizable in the medium frequency range.

The "hanging phase" region of the measured spectra usually shows a different magnitude of the phase angle than predicted by the YG model. As explained above, inhomogeneous distribution of conductivity in dielectrics generally leads to frequency dispersion of the capacitance and thus to similar appearances of the impedance. However, in many cases, such as with Ta₂O₅ as a dielectric, a systematic neglect of other conductivity components may underlie the observed deviations between the YG model and the measurement. As already mentioned, Scholte and Van Geel [120] and Sasaki [121] proposed a sequence of p-type conductivity due to excess oxygen on the electrolyte side, low intrinsic conductivity in the middle oxide with balanced stoichiometry and n-type conductivity due to excess metal in front of the electrode. The PIN conductivity profile in Figure 50 thus results according to Eq. 65.

$$\sigma(x) = \sigma_n \cdot e^{-\frac{x}{\delta_n}} + \sigma_p \cdot e^{-\frac{1-x}{1-\delta_p}} + \sigma_i \quad (65)$$

Here σ_n , σ_p are the maximum conductivities for electrons at location $x=0$ and for holes at location $x=1$, δ_n , δ_p are the relative penetration depths of electron or hole conductivity into the dielectric and σ_i is the contribution of the intrinsic conductivity independent of the normalized location x .

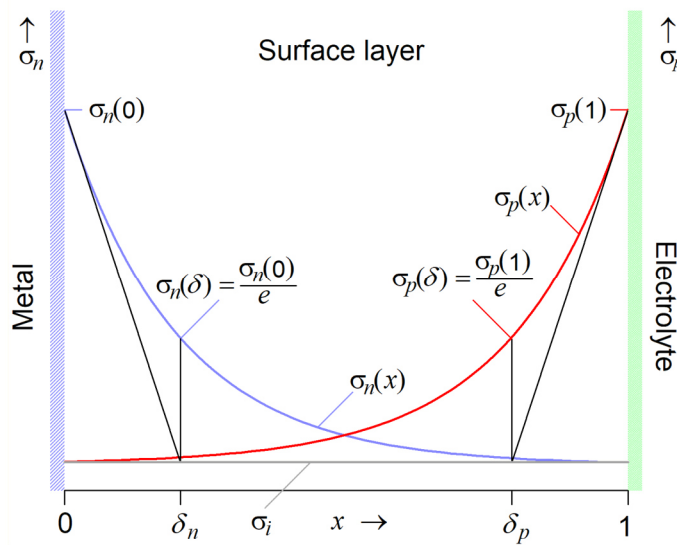


Figure 50: Ohmic conductivity curve inside a transition metal oxide electrode with changing stoichiometry. There is a lack of oxygen on the metal side and an excess of oxygen on the electrolyte side. This leads to the n-conductivity profile shown in blue and the p-conductivity profile shown in red. A (location-independent), intrinsic basic conductivity is shown in grey.

The result from Eq. 65 resulting from Eq. 66 for the impedance of a stack of RC elements according to Figure 40 cannot, to the author's knowledge, be represented in a closed mathematical form for the limiting value of vanishingly small partial layer thicknesses Δd . Therefore, Eq. 66 was transferred to the simulation program as an iterative approximation in a loop algorithm in the form of a user element.

$$Z_S = \frac{\Delta d}{A} \cdot \sum_{i=0}^N \frac{1}{\sigma_n \cdot e^{-\frac{x}{\delta_n}} + \sigma_p \cdot e^{-\frac{1-x}{1-\delta_p}} + \sigma_i + j\omega\epsilon_0\epsilon_r} \quad (66)$$

In Figure 51 it can be seen that the PIN model provides a much better description of the impedance behavior of the tantalum oxide electrode. Due to the ambiguity of statements based on transfer functions in general, and the basic interchangeability of the elements in the RC stack (see also footnote 11 in section 4.2.1.4) in particular, the good fit is not yet proof of the existence of the PIN structure. As shown later, the assumption of a PIN structure is supported by the depth profiles of the stoichiometry, obtained from Auger electron spectra under Ar-ion sputtering on anodically oxidized tantalum samples. The results of the dynamic photocurrent and photovoltage measurements on tantalum electrodes shown later are also consistent with the PIN model.

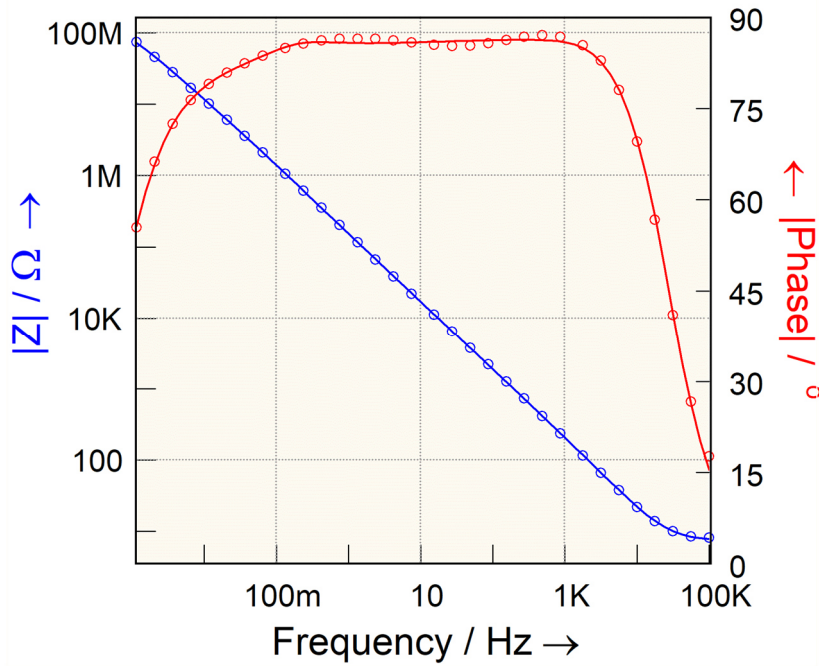


Figure 51: Bode diagram of an impedance spectrum (circles) recorded on the system Ta/Ta₂O₅/phosphate buffer after anodization at 45 V at the rest potential of 1.5 V with the result fitted according to the PIN model (solid line). In the medium-frequency range of the impedance, only very small deviations are recognizable compared with Figure 49.

4.3 The behavior of the impedance under the influence of the test variables voltage and current on the system parameters

It is generally desirable to analyze dynamic processes with a set of a few parameters ("kinetic parameters" according to [103], which are not subject to temporal modulation) and, in addition, only the necessary minimum of time-dependent variables ("state variables" according to [103], i.e. time-modulated variables). In the case of elementary impedances known from electrical engineering, such as resistance, capacitance or inductance, the kinetic parameters R , C and L are sufficient and can be limited to the test variables voltage \tilde{U} and current \tilde{I} as state variables (Eq. 67).

$$Z = \frac{\tilde{U}}{\tilde{I}}, \quad Z_{\Omega} = R, \quad Z_C = \frac{1}{i \cdot \omega \cdot C}, \quad Z_L = j \cdot \omega \cdot L \quad (67)$$

However, even in the impedance Z_F of a simple electrochemical charge transfer reaction, a whole series of kinetic parameters are hidden, such as the charge transfer number z , the stationary concentration C_{∞} far away from the electrode in the electrolyte, which also determines the modulated surface concentration $C_o(t)$, the symmetry coefficient α and the reaction rate constant k [1]. As the example $C_o(t)$ shows, the time-dependent test variables alone are no longer sufficient as state variables, but the modulation of the substance concentrations $C_o(t)$ in front of the electrode, which are relevant for the charge transfer reaction, must be taken into account (Eq. 68). The example of the stationary concentration far from the electrode C_{∞} also shows that the classification of a variable as a time-independent, kinetic parameter can sometimes only be approximately correct: With limited subsequent delivery, C_{∞} is only independent of $C_o(t)$ during rapid changes because of the large amount of substance between the electrode and the location belonging to C_{∞} and can therefore be regarded as time-independent. Long-lasting deviations of $C_o(t)$ from the mean value, as they occur at very low frequencies, can ultimately have an effect on C_{∞} . If there is a noticeable modulation of the concentration $C_{\infty}(t)$, this leads to the various known forms of diffusion impedance, depending on the diffusion boundary conditions.

In general, it can be concluded that impedance models may need to be extended if they are to describe the very low frequency range correctly.

In the practical application of impedance spectroscopy, weaknesses in modeling on such time scales are less noticeable, as measurements are rarely made down to very low frequencies for reasons of economy. On the other hand, valuable information can be obtained from the low-frequency spectrum of some systems. For example, the modulation of the effective electrode area by the effect of the test variables leads to a class of low-frequency impedance spectra that can be observed and evaluated, for example, in corroding systems with passive-active transitions, but also in fuel cells with partial poisoning of an electrode. In chapter 3.1.4 examples have already been shown in the discussion of transient systems. The following section presents a suitable model for the description, which was implemented in the simulation software in the course of the work.

In a generalized view, kinetic parameters that determine the effective conductivity of a test object can become state variables if they can be noticeably influenced by the test variables within the time frame of the test frequency. Temperature and humidity, for example, significantly influence the conductivity of the electrolyte in a solid oxide fuel cell SOFC or the conductivity of the membrane of a PEM fuel cell. If the test frequency comes into the range of the thermal time constant or the humidity time constant of a PEM, pseudo-capacitive or pseudo-inductive components appear in the impedance spectra. There are comparatively few precise studies on this. For example, H. Landes [105] and later A. Hahn in his dissertation [18] model the influence of current heat, heat transport and heat capacity on the low-frequency impedance of SOFCs. The role of temperature as a state variable is typical for the influence of a "mediating" parameter on the test variables and thus on the conductivity. On closer examination of the case that kinetic parameters at low frequencies can determine the effective conductivity of a test object and thus become state variables, a general rule for determining the associated impedance behavior could be found. In order to confirm this, measurements were carried out on easily understandable model systems. In the next but one section, the results are discussed and compared with the ideas of H. Landes and A. Hahn.

4.3.1 Faraday impedance of systems with temporal relaxation of the effective charge transfer reaction rate

The term "Faraday reaction" summarizes the most important processes involved in the material turnover of an electrode reaction. In the classical picture, the polarization that ultimately leads to a net conversion is divided between the overvoltage of the individual processes in the reaction sequence. The characteristic impedance of the Faraday reaction therefore essentially appears as a series connection of the impedance components assigned to the processes of the charge transfer reaction, mass transfer and possibly other steps in the reaction sequence. The transfer reaction can occur completely into the solid phase (charge number z integer) or partially (charge number z fractional) into an adsorption state, which may be followed by complete transfer. Diffusion, charge transfer and adsorption impedance are assigned to the individual overvoltage components. Depending on the chemical and geometric boundary conditions, the diffusion impedance can, as mentioned above, take on a variety of mathematical forms, the best known of which is the "special Warburg impedance". The frequency response of the various diffusion impedances differs only at low frequencies in a way that is characteristic of the boundary conditions, while the behavior at higher frequencies generally approximates the special Warburg impedance. The impedance of the transfer reaction itself occurs as a resistance independent of the frequency, since the electron transition takes place as an activated process without inertia measured on the time scale of the EIS. The impedance attributable to the adsorption overvoltage is usually dominated by the "adsorption capacitance", accompanied by an "adsorption resistance" associated with the partial charge transfer. For coupled adsorption with subsequent passage, a somewhat more complicated network results, whereby the schematic separation into diffusion, transfer and adsorption impedance can still be approximated in a series circuit. However, it is assumed that the rate constant k of the transfer reaction occurs as a stationary kinetic parameter that is independent of the modulation of the test variables (Eq. 68):

$$Z_F = \frac{\tilde{\varepsilon}}{\tilde{I}} = f(\tilde{c}_o, \tilde{\theta}; c_\infty, k, z, \alpha) \quad (68)$$

Here, the test variables $\tilde{\varepsilon}$ and \tilde{I} , the concentration \tilde{c}_o of the passing species in front of the electrode and, in the case of adsorption processes, the degree of coverage $\tilde{\theta}$ of the adsorbed species on the electrode are modulated, while the concentration of the passing species c_∞ far away in the medium, the symmetry coefficient α , the reaction rate k of the charge transfer (and of course the charge number z) are assumed to be time-independent. The Faraday impedance then results as the sum of the charge transfer resistance R_η , the diffusion impedance Z_c and the adsorption impedance Z_θ (Eq. 69).

$$Z_F = R_\eta + Z_c + Z_\theta \quad (69)$$

In fact, the charge transfer current ("Faraday current") I_F includes other variables proportional to the reaction rate constant k , such as the active area A . If A changes, as is the case in corroding systems with an active-passive transition, for example, this is equivalent to a change in the reaction rate constant k . The low-frequency influence of the test variable on k can be calculated according to [103], for example, as a potential dependence $dk/d\varepsilon$, which only occurs with a delay when $d\varepsilon/dt$ changes. This reflects the fact that a certain period of time is required to reach a new equilibrium state of k after a change in potential. During this time, for example, the chemical conversion necessary to establish a new equilibrium ratio between the active and passive surface can take place. In addition to the stationary potential dependence $dk/d\varepsilon$, the time law dk/dt is therefore characteristic. In the simplest case, the instantaneous value k_t relaxes to its equilibrium value k according to a first-order time law (Eq. 70) with the settling time τ .

$$-\frac{dk_t}{dt} = \frac{1}{\tau} \cdot (k_t - k) \quad (70)$$

The serial representation Eq. 69 of the Faraday impedance must then be corrected as in Eq. 71

$$Z_F = \frac{R_\eta + Z_c + Z_g}{1 + R_\eta / Z_k} \quad (71)$$

Instead of being connected simply in series, the values of charge transfer resistance, diffusion impedance and adsorption impedance appear in a fraction together with the term R_η/Z_k . If the relationship Eq. 70 is assumed as the time law, the "relaxation impedance" Z_k is calculated according to Eq. 72.

$$Z_k = \frac{1 + j\omega\tau}{I_F \cdot d \ln k / d\varepsilon} \quad (72)$$

It can be seen that Z_k becomes arbitrarily large when the average Faraday current I_F disappears at equilibrium, as well as when the potential dependence $d \ln k / d\varepsilon$ disappears. The denominator in Eq. 71 then tends towards one and the Faraday impedance is sufficiently described by Eq. 69. This is the reason why the relaxation impedance is only observed in non-equilibrium systems such as those that occur during corrosion or passivation.

The typical appearance of the relaxation impedance in spectra depends on the strength of the potential dependence $d \ln k / d\varepsilon$ and its sign in relation to the sign of the Faraday current, as shown in [103] in detail. However, as shown in the examples in section 2.1, a damped inductive component parallel to the expected Faraday impedance is usually observed at low frequencies. In these cases, the impedance does not tend monotonically to a maximum final value as the frequency approaches zero. Instead, it passes through a more or less pronounced maximum of the impedance magnitude depending on the magnitude of the potential dependence $d \ln k / d\varepsilon$. In the vicinity of this maximum, the sign of the phase angle changes from negative, characterized by double layer capacitance and diffusion impedance, to positive, i.e., inductive.

This is characteristic for the case that the potential dependence $d \ln k / d\varepsilon$ and the Faraday current I_F have the same sign, i.e., further (delayed) activation takes place in the direction of increasing conversion.

If significant contributions to the Faraday impedance occur due to diffusion or adsorption, the low-frequency spectra are complicated by the alternating predominance of inductive and capacitive influences. This can be seen in Figure 24. Similar spectra can be observed in other systems that are partially protected by passivation, such as aluminum in a chloride-containing solution and zirconium or zircaloy.

The relaxation impedance model offers the possibility of determining the direction, extent and time constant of activation and passivation.

The case displayed in Figure 26, measured under the influence of accumulating CO poisoning of the anode, shows particularly pronounced "pseudo-inductive"¹² low-frequency behavior over the course of the measurement time. A mechanism is postulated for this, similar to activation and passivation, which acts via the potential dependence of the electrode surface available for the transfer reaction: CO is very strongly bound to the platinum catalyst of the anode and occupies a large part of the activity centers available for hydrogen oxidation. As the positive polarization of the anode increases (which corresponds to a decrease in cell voltage under load), the equilibrium position for hydrogen oxidation is shifted towards higher conversion. In addition, the oxidation of adsorbed carbon monoxide takes place to a greater extent, so that the number of activity centers available for hydrogen oxidation also increases again with a time delay. The potential dependence of the effective reaction rate $d \ln k / d\varepsilon$ and the Faraday current I_F therefore have the same sign, which leads to the expected inductive expression of the relaxation impedance.

4.3.2 The influence of current heat on the impedance of systems with significantly temperature-dependent conductivity

A. Hahn investigated in his dissertation [18], the influence of the current heat of a high-temperature fuel cell under load on its impedance behavior. For the evaluation he used a model by H. Landes [105]. Landes first considers the "ideal case" in which the heat of the current has no noticeable influence on the cell voltage and establishes that a change in the current dI according to Ohm's law is accompanied by the change dU_{ideal} (Eq. 73) as a function of the cell impedance Z_{ideal} .

$$dU_{ideal} = -Z_{ideal} \cdot dI \quad [18] \quad (73)$$

In fact, the temperature also affects the cell voltage and dU_{real} is dependent on both the current and the temperature as in Eq. 74 so that the corrected impedance Z_{real} takes the form of Eq. 75.

$$dU_{real} = -Z_{ideal} \cdot dI + \frac{\partial U_{real}}{\partial T} \cdot dT \quad (74)$$

$$Z_{real} = -\frac{dU_{real}}{dI} = Z_{ideal} - \frac{\partial U_{real}}{\partial T} \frac{dT}{dI} \quad (75)$$

To calculate the contribution of the temperature dependence to the impedance, Landes and Hahn model the heat capacity and the one-dimensional heat flow in the cell analogously to diffusion processes. They arrive at the result - slightly modified here for clarity - of Eq. 76 with the stationary variables DC voltage U and DC current I and the temperature dependence of the potential Eq. 77, the thermal decay length d , the volume-related specific heat capacity c , the density ρ and the thermal conductivity λ are included in v .

$$Z_{real} = \frac{Z_{ideal} - v \cdot U}{1 + v \cdot I} \quad (76)$$

¹² The classification "pseudo-inductive" or "pseudo-capacitive" is used by the author to characterize inductive and capacitive contributions in impedance spectra whose occurrence is not directly linked to the effect of the magnetic or electric field. The term "chemical capacitance", which is occasionally used in semiconductor research, has a similar meaning.

¹³ The negative sign in front of Z is due to the "active" role of the fuel cell, in which, by convention, a positive calculated current under load is accompanied by a decrease in the cell voltage.

$$v = \frac{\tanh\left(d \cdot \sqrt{\frac{c \cdot \rho}{\lambda} j\omega}\right)}{2\lambda \cdot \sqrt{\frac{c \cdot \rho}{\lambda} j\omega}} \cdot \frac{dU}{dT} \quad (77)$$

Figure 52 is taken from parts of the original work. It clearly shows that the influence of the heat of the current on the spectra is a very small effect in the low-frequency range.

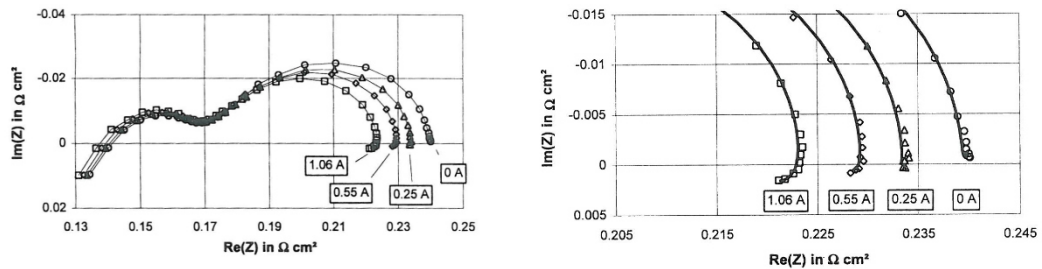


Figure 52: Impedance spectra array measured on a SOFC MEA at 950° C under different DC loads. Taken from the dissertation by A. Hahn [18], Figures 56 and 58.

It is therefore not surprising that the corresponding effects are often overlooked or perceived as artifacts, especially since drift can have a similar appearance on these time scales. By checking the spectra using ZHIT, it is generally possible to distinguish between "real" frequency response and drift contribution without any doubt. In fuel cell research, however, the linear Nyquist representation of the spectra in the complex plane is usually preferred to the logarithmic Bode diagram, which is more informative in this respect. Thus, an ad hoc distinction between frequency response and drift artifact is not possible by visual inspection alone.

Given the rather small effect on fuel cells, it is difficult to test experimentally whether the models developed are realistic, particularly with regard to the influence of heat transport. In the search for a more general description, various types of temperature-dependent resistances were experimentally investigated as model systems and interpreted using both the Landes-Hahn model and a simplified model with regard to heat transport. "Positive / Negative Temperature Coefficient" PTC and NTC resistors show the very simple impedance spectrum of ohmic resistors as long as the objects are not heated electrically or as long as the very low frequency range is ignored. It is therefore possible to study the current-heat influence on the spectra very precisely. In the series of measurements, an NTC optimized for temperature measurements and a PTC intended for overcurrent shutdown were examined. Various direct current and voltage loads were selected. For stability reasons, the measurements on the PTC must be carried out under potentiostatic control and the measurements on the NTC under galvanostatic control. Due to the strong non-linearity of the stationary characteristic curve, different temperature coefficients can be set for both objects by selecting the operating point. To protect against uncontrolled convection by the ambient air, the objects were enclosed in an insulated container. A uniform flow of nitrogen gas was used to set a defined short thermal compensation layer thickness so that the conditions at least reflected conditions comparable to those in Hahn's experiment. To further simplify the temperature transport conditions, a small incandescent lamp acting as a PTC was investigated. Incandescent lamps have a much smaller temperature coefficient of resistance and this can only be set within a relatively narrow range of values. However, due to the high filament temperature, the flow of the current heat is strongly dominated by the radiation into the much colder environment. The time law of temperature relaxation can therefore be based on a simple first-order decay behavior.

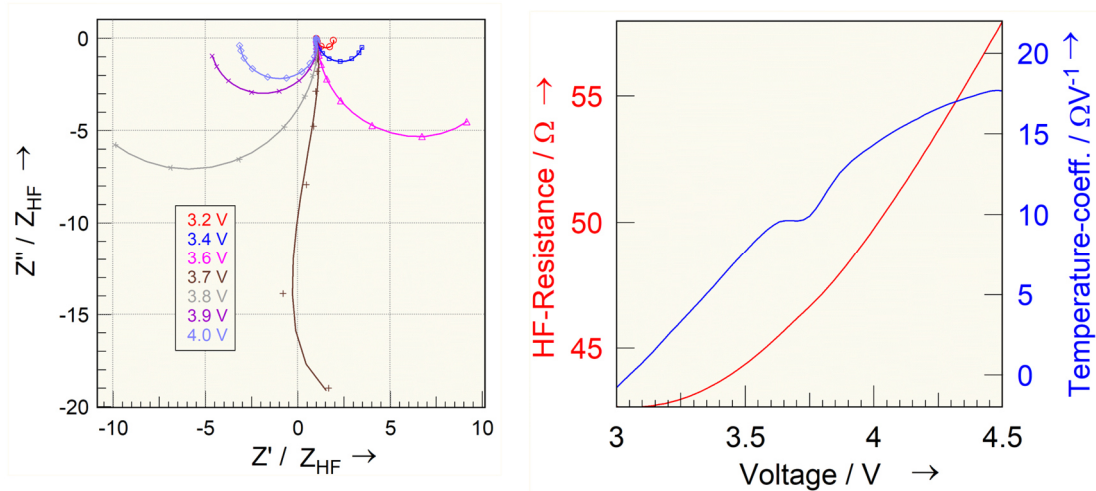


Figure 53: Nyquist diagrams of the impedance spectra series of a PTC resistor with different positive temperature coefficients (left). This is set via the strongly non-linear characteristic curve (right) by selecting the DC operating point (potentiostatic for stability reasons). For better comparability, the impedance scale is standardized to the value of the respective high-frequency limiting resistor. The original measurement data are shown as symbols, the approximation functions generated by polynomial smoothing as solid curves. The clearly negative real part contribution at higher voltages is striking.

Figure 53 summarizes the measurement results at the PTC. By selecting the temperature coefficient TC over the operating point, three characteristic frequency dependencies could generally be set. At $TC < TC_{crit}$, $TC_{crit} \approx 2 \text{ V}\Omega^{-1}$, damped, pseudo-capacitive behavior occurs below a cut-off frequency f_g , which can be estimated from the thermal time constant¹⁴ τ_g , which changes back to ohmic behavior after a corresponding increase in impedance at even lower frequencies.

$$f_g \approx \frac{1}{2 \cdot \pi \cdot \tau_g}$$

Although based purely on a temperature effect, the frequency response in this regime is strikingly similar to the spectrum of a Randles circuit consisting of charge transfer resistance, double layer capacitance and electrolyte resistance.

¹⁴ With the exception of the incandescent lamp, there is no "clear" thermal time constant (1st order) in the systems investigated, as the decay behavior is determined by a mixture of heat conduction, convection and radiation. The thermal time constant is qualitatively assigned to the time range in which the temperature response has the strongest effect on the frequency response ("transition frequency").

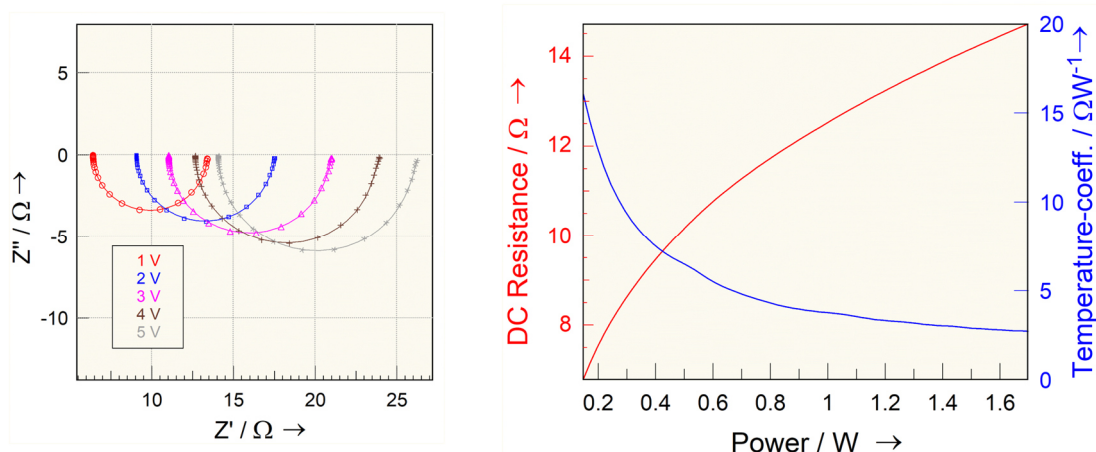


Figure 54: Impedance spectra of an incandescent lamp under different DC loads (left). As the temperature response does not change as dramatically over the load as with the PTC, the character of the spectra is retained. The original measurement data are shown as symbols, the approximation functions generated by polynomial smoothing as solid curves. The DC resistance and its temperature response as a function of power are shown on the right.

The impedance spectra measured on the incandescent lamp Figure 54 are similar to the PTC measurements for $TC < TC_{crit}$, but are characterized by a clear characteristic of the thermal time constant (semicircle in the Nyquist diagram). If the temperature response TC at the PTC reaches the value TC_{crit} , the lowest frequency transition back to the ohmic resistance as the limit value for frequency zero disappears - the system appears like an RC series circuit. However, this state is difficult to set, as the operating point for TC_{crit} reacts very sensitively to the smallest changes in convection.

With temperature coefficients $TC > TC_{crit}$, the system finally enters a (galvanostatically) unstable state in which, after passing through a damped pseudo-capacitive phase as in the case of $TC < TC_{crit}$, the lowest frequency limit value is again ohmic character, but here with a negative sign.

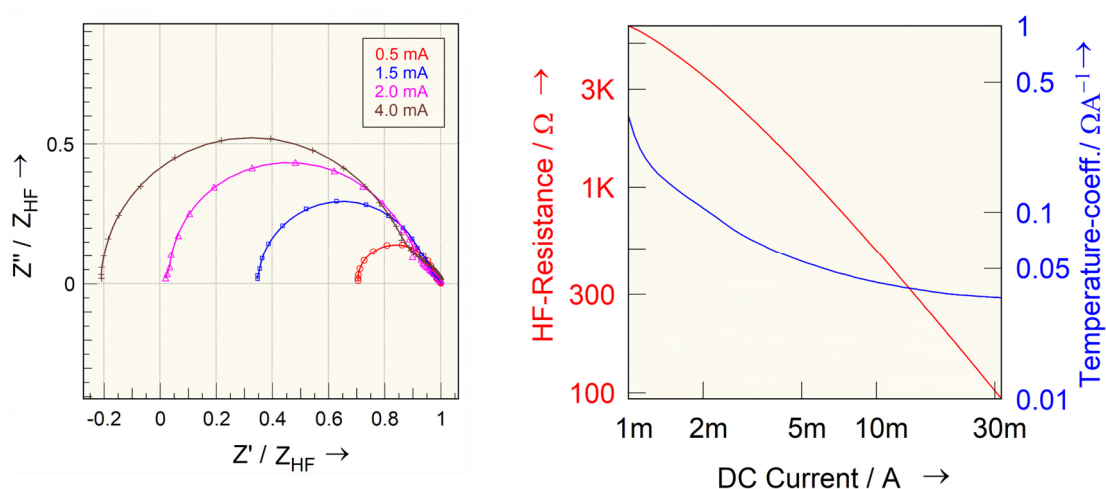


Figure 55: Series of impedance spectra of an NTC resistor with different negative temperature coefficients (left). This is set via the strongly non-linear characteristic curve (right) by selecting the DC operating point (galvanostatic for stability reasons). For better comparability, the impedance scale is standardized to the value of the respective high-frequency limiting resistor. Note the negative real part contribution at the highest current.

The NTC spectra show Figure 55. By selecting the negative temperature coefficient TC over the operating point, it was again possible to achieve different characteristics of the frequency response. With $TC > TC_{crit}$, damped, pseudo-inductive behavior occurs below the cut-off frequency f_g , which changes back to ohmic behavior after a corresponding increase in impedance at even lower frequencies.

The frequency response is similar to that of a circuit consisting of the high-frequency limiting resistor with a series RL element connected in parallel.

If the temperature response TC reaches the value TC_{crit} , the low-frequency transition back to the ohmic resistance as the limit value for frequency zero disappears - the system appears like an RL series circuit. Similar to the PTC, this state must be set very critically.

With temperature coefficients $TC < TC_{crit}$, the system finally enters a (potentiostatically) unstable state in which, after passing through a damped pseudo-inductive phase as in the case of $TC > TC_{crit}$, the lowest frequency limit value again becomes Ohmic, although here, as with the NTC, it is again characterized by a negative sign.

An attempt has now been made to calculate the PTC-NTC measurements using Landes-Hahn's Eq. 76 and 77 as interpretation. The moderate fit quality from the Figure 56ff shows that, as expected, the model concepts of one-dimensional heat conduction in a homogeneous medium are only very imperfectly fulfilled by these measurement objects.

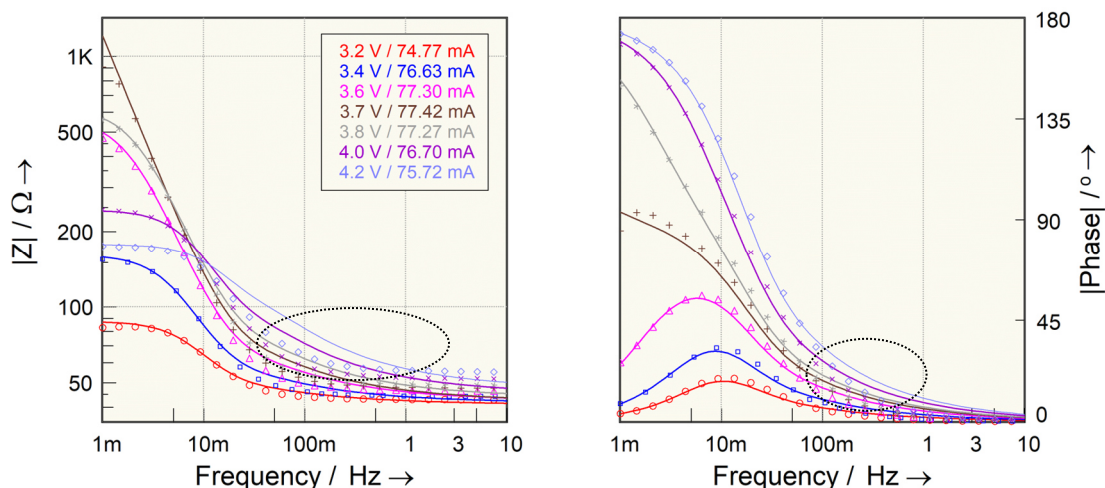


Figure 56: Fit of the PTC impedance spectra using the Landes-Hahn model Eq. 76 and 77. In the Bode diagram (left impedance magnitude, right phase), the residual deviations between the measured data (symbols) and the model calculation (solid curves) can be seen particularly clearly in the medium frequency range (ellipses).

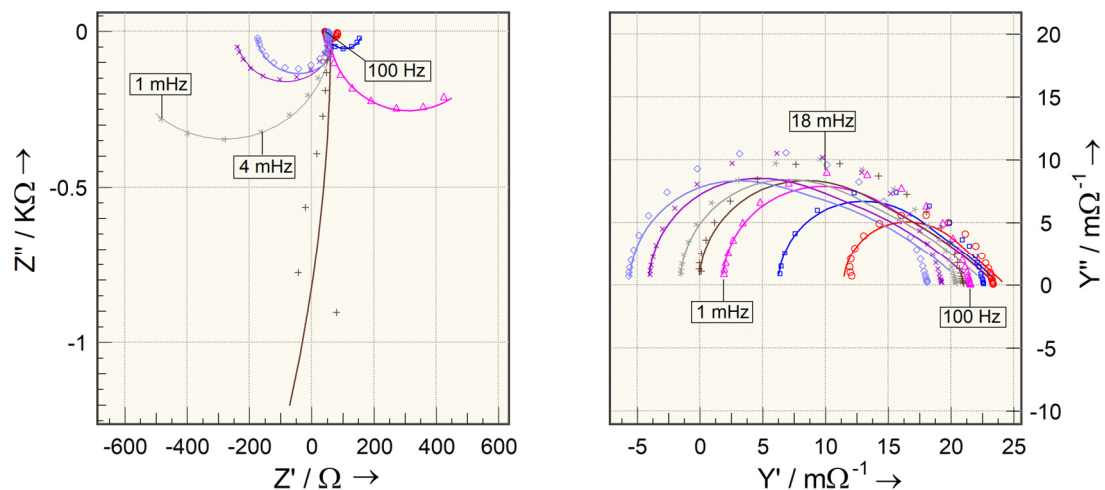


Figure 57: Fit of the PTC impedance spectra using the Landes-Hahn model Eq. 76 and 77. In the Nyquist diagram of the admittance (right), the residual deviations between the measured data (symbols) and the model calculation (solid curves) are easier to recognize than in the diagram of the impedance (left).

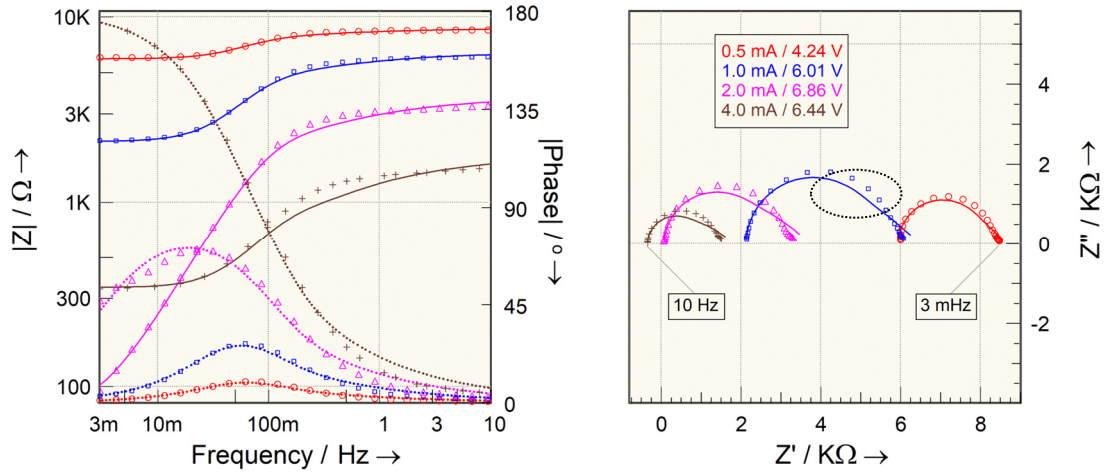


Figure 58: Fit of the NTC impedance spectra in the Bode diagram (left). In the Nyquist diagram (right) in particular, small but systematic deviations between the measured data (symbols) and the calculation using the Landes-Hahn model (solid curves) can be seen.

From the Nyquist diagrams in Figure 58 on the right, it is instead clear that the measured spectra rather indicate a decay behavior of the temperature with a dominant 1st order time constant (semicircle), together with a smaller contribution (root-law of time, -45° straight line at low frequencies), caused by heat conduction in the volume.

The impedance spectra of the incandescent lamp have now been used to check whether the even simpler mechanism to be expected there enables more accurate simulations. For this purpose, an alternative impedance model to the Landes-Hahn model was developed, which is based on a relaxation of the temperature according to a first-order time law (Eq. 78). The impedance Z_{bulb} of the light bulb is determined by the stationary values of the DC voltage U and the DC current I , from which the temperature dependence Eq. 79 caused by the temperature dependence v_{bulb} and the high-frequency limiting resistance of the light bulb $R_{HF} = U / I$. The temperature coefficient $\partial U / \partial T$ of the filament voltage at constant current, the dependence of the filament temperature on the power dT/dP , $P=U \cdot I$ and the thermal decay time τ_g are included in v_{bulb} . In a form more suitable for experimental testing, the frequency dependence with the temperature response of the limiting resistor R_{HF} as a function of the power P is as in Eq. 80. A detailed derivation can be found in the appendix, section 8.5.

$$Z_{bulb} = \frac{R_{HF} + v \cdot R_{HF}}{1 - v} \quad (78)$$

$$v_{bulb} = \left(\frac{\partial U}{\partial T} \right)_I \cdot \frac{I}{1 + j\omega \cdot \tau_g} \cdot \frac{dT}{dP} \quad (79)$$

$$v_{bulb} = \left(\frac{\partial R_{HF}}{\partial P} \right)_I \cdot \frac{P}{(1 + j\omega \cdot \tau_g) \cdot R_{HF}} \quad (80)$$

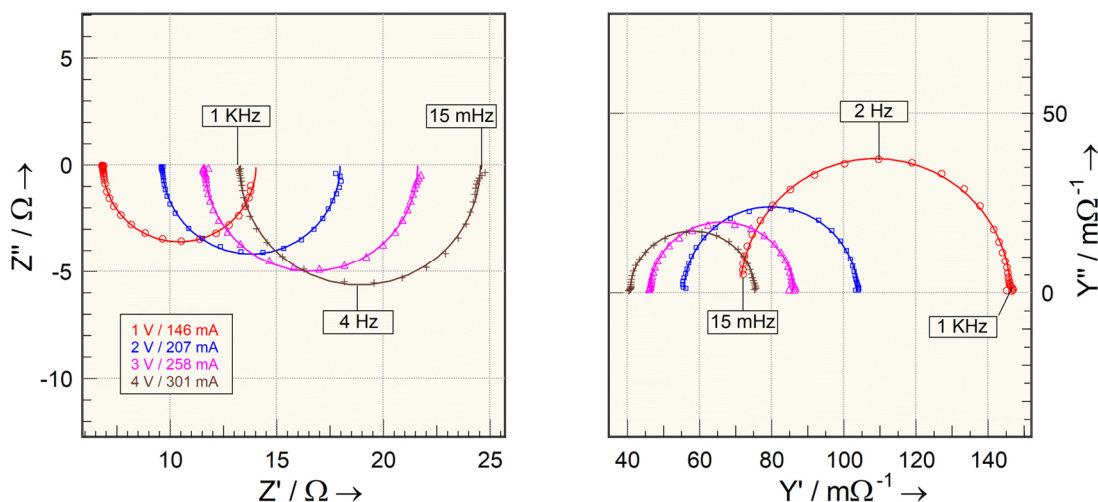


Figure 59: Application of the model for 1st order thermal decay behavior to the impedance spectra of the incandescent lamp. In the Nyquist diagram of the impedance (left), hardly any deviations between the model calculation (solid curves) and the measured data (symbols) are perceptible, except at the lowest frequency end. The Nyquist diagram of the admittance is shown on the right.

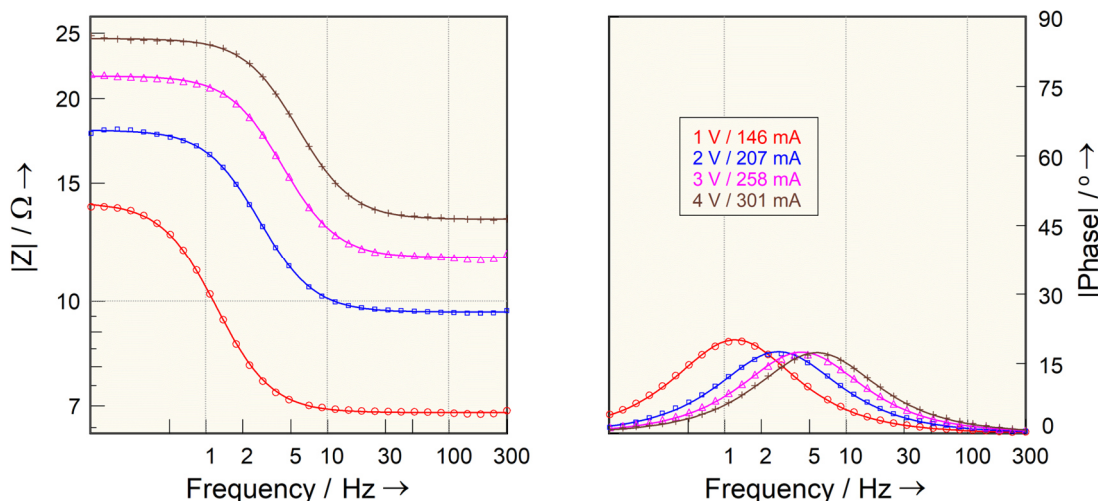


Figure 60: Application of the 1st order thermal decay model to the impedance spectra of an incandescent lamp. Both the impedance magnitude (left) and the phase angle diagram (right) confirm the model. The calculations (solid curves) correspond well with the measured data (symbols) for all operating points.

As hoped, the model for 1st order thermal decay behavior can explain the impedance spectra of the incandescent lamp well (Figure 59 and Figure 60). When the known values for DC voltage and current are entered into the model calculation, the fit values for the temperature coefficient agree well with the independently measured values in Figure 60 on the right. Both the Landes-Hahn model and the temperature relaxation model were not included directly in the standard library of the simulation program. However, they are available to potential users in the form of the user element source code and are listed in the appendix.

With regard to the measurements on NTC and PTC in the range of a large temperature coefficient amount, it must be added that the analysis of the measurement data using ZHIT also proves that these are unstable systems with potential contributions from negative real parts in the impedance. ZHIT (section 3.1.3.4) can therefore not be used to check drift or temporal stability.

4.3.3 The general relaxation impedance

The derivation of the incandescent lamp impedance can be generalized to systems of voltage- and current-dependent resistors that relax with time τ [106], Eq. 81 with the dimensionless voltage coefficient VC Eq. 82. VC results from the dependence of the voltage U on a mediating variable M_m , which in turn is dependent on U and I via the power P . In the case of the temperature-dependent resistors NTC and PTC, the incandescent lamp and the high-temperature fuel cell, the mediating variable is the temperature T . In corroding systems with active-passive transitions and in the above example of CO poisoning of a PEFC anode, the mediating variable is the active electrode area; in the modulation of the conductivity of a PEFC membrane by changing the water concentration, it is the humidity.

$$Z_\tau = \frac{R_{HF} + v \cdot R_{HF}}{1 - v}, \quad v = \frac{VC}{1 + j\omega \cdot \tau} \quad (81)$$

$$VC = \left(\frac{\partial U}{\partial M_m} \right)_I \cdot \frac{dM_m}{dP} \cdot I \quad \text{with } M_m = T \text{ for NTC, PTC and incandescent lamp.} \quad (82)$$

The following table lists the impedance behavior of general ohmic objects with relaxation (referred to as "general relaxation impedance") as a function of VC .

Coefficient VC	Resistor type	Low-frequency limit value $Z_0 = Z_R(\omega \rightarrow 0)$	Frequency response
$VC = 0$	Ohmic resistance	$Z_0 = Z_\infty = R_{HF}$	0
$1 > VC > 0$	PTC	$Z_0 > Z_\infty$	capacitive at $\omega \approx 1/\tau$
$-1 < VC < 0$	NTC	$Z_0 < Z_\infty$	inductive at $\omega \approx 1/\tau$
$VC > 1$	PTC	$Z_0 > Z_\infty, Z'_0 < 0$	capacitive at $\omega \approx 1/\tau$
$VC < -1$	NTC	$Z_0 < Z_\infty, Z'_0 < 0$	inductive at $\omega \approx 1/\tau$
$VC = 1$	PTC	$Z_0 \rightarrow \infty$	purely capacitive for $\omega \ll 1/\tau$
$VC = -1$	NTC	$Z_0 \rightarrow 0$	purely inductive for $\omega \ll 1/\tau$

It is noteworthy that the real part Z'_0 of the impedance becomes negative at low frequencies $\omega \ll 1/\tau$ for $|VC| > 1$ and even disappears for $|VC| = 1$.¹⁵

All listed frequency dependencies of the general relaxation impedance could be observed experimentally on NTC, PTC or incandescent lamps. As shown above in Figure 56ff above, the modeling of the impedance spectra of NTC and PTC using the Landes-Hahn model is only very imperfect due to the less realistic ideas of heat transport. The experimental data can be better reproduced with the model of a 1st order relaxation for the temperature assumed according to Eq. 81 (Figure 61 and 62).

¹⁵ $|VC| = 1$ corresponds to the case $TC = TC_{crit}$, which was discussed at the beginning of this section.

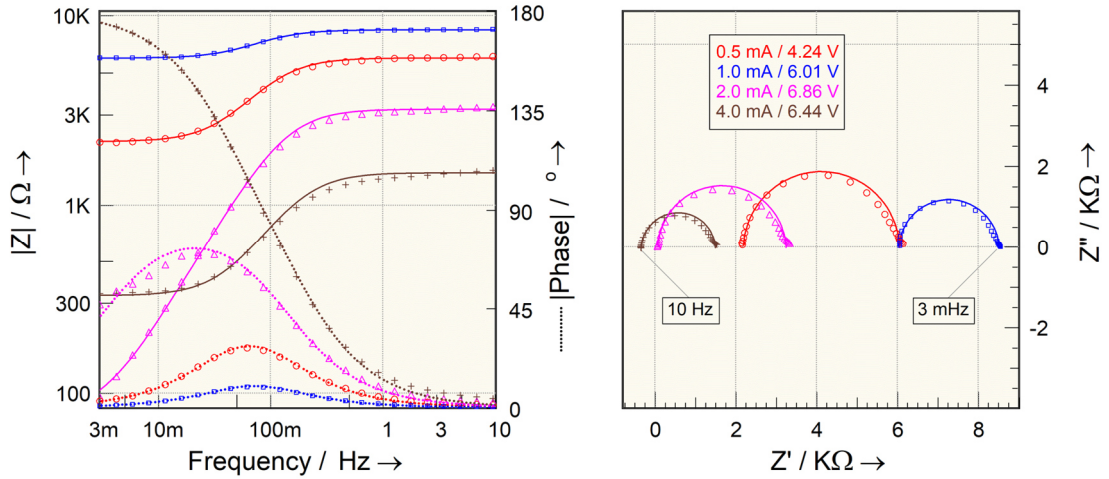


Figure 61: Fit of the impedance spectra (symbols) of NTC in the Bode diagram (left) and in the Nyquist diagram (right) using the model (solid curves) according to the relaxation model Eq. 81.

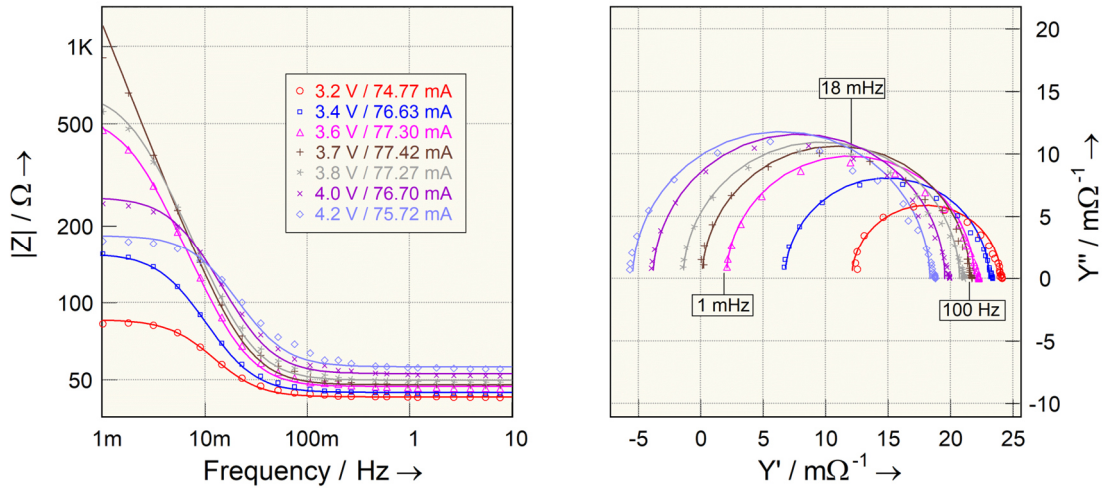


Figure 62: Fit of the impedance spectra (symbols) of the PTC in the Bode diagram of the impedance (left) and in the Nyquist diagram of the admittance (right) using the model (solid curves) according to the relaxation model Eq. 81. The better fit quality compared to the Landes-Hahn model is particularly evident in comparison with the marked points in Figure 56 and in Figure 58 on the right.

If the dependence of the resistance in the model is limited to the voltage instead of (via the power) to the voltage and current together, Eq. 81 becomes Eq. 83 and reflects the behavior of the Faraday impedance Z_D under temporal relaxation¹⁶ of the transfer reaction rate k , if only the charge transfer resistance R_η has to be taken into account, because diffusion and adsorption contributions to the overvoltage can be neglected.

$$Z_D = \frac{R_\eta}{1 - vc / (1 + j\omega \cdot \tau)}, \quad vc = R_\eta \cdot I_F \cdot d \ln k / d\varepsilon \quad (83)$$

The Faraday impedance discussed in section 4.3.1 can therefore be traced back to the general relaxation impedance.

¹⁶ See also chapter 3.2.1 with the equations 70 to 72.

5 The modeling of photo-electrochemical transfer functions

Photoelectric processes are of fundamental importance for the living world. One of the foundations of our biological life is photosynthesis and we are hoping that photovoltaics will be able to secure our energy supply in the long term. Here, the photo-electric effect within semiconductors is used to convert solar energy directly into electricity. As of 2011, the global installed capacity is estimated at around 25 GW. Almost 90% of this is achieved with monocrystalline and polycrystalline silicon (about half each) [25]. However, more than ten square kilometers of solar cells produced worldwide on the basis of monolithic silicon have not been enough to make production and energy costs¹⁷ competitive with traditional energy sources [26].

In the search for cheaper options for mass production, solar cell principles are being researched as an alternative to the monolithic type. Dye-sensitized solar cells (DSSCs) and organic polymer solar cells (OSCs) are being worked on intensively. Unfortunately, the same seems to apply to alternative solar cell concepts: The more attractive the production technology, the poorer the efficiency.

While the processes in monolithic solar cells have been studied and well understood for many decades, DSSC and OSC systems appear to be much more complex. On the one hand, they consist of more different active materials than monolithic solar cells. Secondly, the clear assignment of the processes to the material phases is problematic due to their often porous or mixed structures.

Dynamic transfer function analysis, which is used very successfully on fuel cells and batteries in the form of impedance spectroscopy (Eq. 17), is of course also suitable for the further development of alternative solar cells. In addition to impedance, the experimentally accessible measurements of dynamic photocurrent efficiency, Eq. 18 ("Intensity Modulated Photocurrent Spectroscopy" IMPS) and dynamic photovoltage efficiency, Eq. 19 ("Intensity Modulated Photo Voltage Spectroscopy" IMVS) can also be used to analyze photoelectrically active systems such as solar cells. The practical implementation of these measurement methods will be discussed in the experimental part of the thesis.

IMPS and IMVS have been used in research into DSSC for some time. The researchers are particularly interested in the cut-off frequency ω_{IMPS} of the cell current under short-circuit conditions and the cut-off frequency ω_{IMVS} of the open cell voltage.

According to the work of the DSSC pioneers [34], [35], [36], [37], it is expected that according to Eq. 84 and 85

$$\tau_d = \frac{1}{\omega_{IMPS}}, \quad \tau_l = \frac{1}{\omega_{IMVS}} \quad (84), (85)$$

the dominant IMPS time constant is assigned to the charge carrier diffusion time constant τ_d , and the dominant IMVS time constant τ_l is assigned to the charge carrier lifetime. Since for the photoelectrons, reaching the current collectors on the one hand and the loss due to premature recombination during migration on the other are in kinetic competition, the expression η_{dyn} Eq. 86 is a measure of the "dynamic" efficiency.

$$\eta_{dyn} = 1 - \frac{\tau_d}{\tau_l} \quad (86)$$

To determine τ_d and τ_l from the measured IMPS and IMVS transfer functions, an ad hoc graphical evaluation of the data is sufficient. No further modeling of the spectra is required. Although a more detailed analysis is often mentioned, this is ultimately also common practice for most groups working on DSSC. In fact, τ_d and τ_l , especially with alternative solar cell types, occur together with other frequency-dependent components that also determine the spectra. Without further analysis, the simplistic, popular approach therefore appears somewhat questionable, as the following consideration shows.

¹⁷ The installation costs for 1W of electrical energy are currently around €2 [25].

It is assumed that photoelectron generation on the one hand and recombination on the other determine the frequency behavior of the open cell voltage depending on the modulation of the light intensity. The photoelectrons inject a forward current in the sense of a semiconductor diode into the junction and polarize it to the extent that recombination current and generation current are in equilibrium. Electrically, this is equivalent (for an ideal solar cell in which all generated photocurrent must recombine in the junction in the electrically open state) to the polarization of the junction by a current of the same magnitude injected from outside without exposure. The resulting polarization resistance R_{pol} of the junction together with its effective capacitance C_{eff} determine the frequency response - quite analogous to the frequency response of the impedance of a charge transfer reaction: It is controlled by the polarization resistance set by the transfer current and the effective double layer capacitance. The following applies analogously:

$$\tau_l = R_{pol} \cdot C_{eff}$$

Polarization gives the differential resistance Eq. 87 of the solar cell at room temperature to

$$R_{pol} \approx \frac{U_g}{I_{pol}}, \text{ with } U_g = \frac{k \cdot T}{e_0} \approx 25.7 \text{ mV at } 298 \text{ K, } k: \text{ Boltzmann constant, } e_0: \text{ elementary charge (87)}$$

In a Si solar cell, the effective capacitance increases almost proportionally to the current at higher polarization due to the increase in the density of states for stored majority charge carriers. According to Eq. 87 the polarization resistance goes down in turn, so that τ_l is measured almost constantly over a larger range of light intensity. This is different with the Schottky contact of a dye-sensitized solar cell. Here, an inverse proportionality between τ_l and the light intensity is observed due to the only weakly polarization-dependent effective capacitance. At half the polarization or intensity, τ_l almost doubles.

A shunt can occur in a real solar cell. In organic solar cells, this appears, for example, through percolation of semiconductor material of the other conductivity type to the opposite electrode¹⁸. In dye solar cells, electrolyte can sometimes penetrate through defects in the photo-anode material to the contacts. As a result, part of the photocurrent is diverted and is no longer available for polarization when the cell voltage is open. If a significant part of the photocurrent flows through the leak, the resulting polarization voltage (the open cell voltage) changes only slightly (e.g., by $\Delta U \approx 25.7 \cdot \log_{10}(e) \approx 60 \text{ mV}$ with a polarization current change by a factor of 10). Conversely, reducing the polarization current by a certain factor increases the polarization resistance in almost the same way. The total resistance from the polarization resistance parallel to the shunt thus increases significantly: One would therefore observe a significantly larger recombination time constant τ_l without the kinetic conditions within the cell actually having changed. Since a shunt defect has practically no influence on the measurement result when measuring the diffusion time constant τ_d under short-circuit conditions, the quotient τ_d / τ_l is also determined significantly incorrectly with τ_l . This leads to the paradoxical result that a cell that works significantly worse due to the shunt defect appears to display a better "dynamic" efficiency.

Similar considerations about the role of the counter electrode in complete DSSCs when determining τ_d in short-circuit mode call into question the common simplifying practice for this parameter as well.

More precise models of the photoelectric response functions and the inclusion of the accompanying frequency-determining elements in an overall network model could alleviate the problem of determining τ_d and τ_l . In addition, the IMPS and IMVS transfer functions together with EIS offer a possibility that the individual functions lack: A fundamental problem that repeatedly arises when analyzing impedance spectra, e.g., in the field of electrochemical power generation, is the ambiguity of the spectra. While a certain mechanism only allows a specific type of transfer function, the reverse conclusion from the spectrum to the mechanism is in principle ambiguous. This can be illustrated by the equivalence of a simple network of two RC links, whose two representations stand for two different reaction sequences: Two series RC links connected in parallel can be converted directly into an equivalent network consisting of a

¹⁸ This is a common problem in organic solar cells of the so-called "bulk heterojunction type", where p-type and n-type polymers intentionally interpenetrate to increase the junction volume available for photon absorption.

series RC link in series with a parallel RC link (Figure 63). As a result, time constants can no longer be clearly assigned to specific processes without additional information.

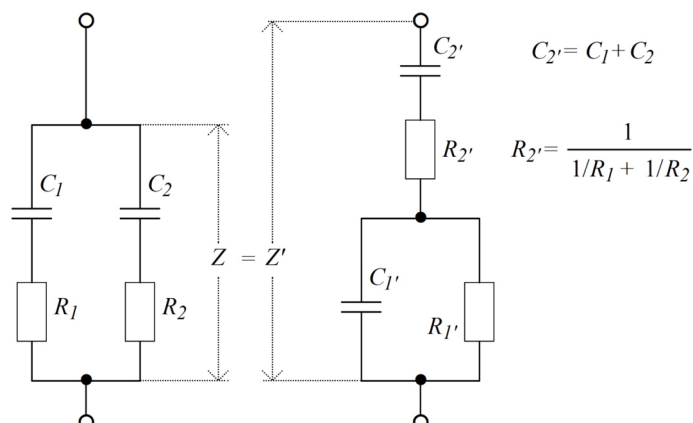


Figure 63: The two series RC elements on the left have the same impedance when connected in parallel as the series connection of the parallel and series RC elements on the right.

If, as in the field of fuel cells and batteries, only the impedance spectra are available as a dynamic transfer function, the modeling must be supported by sometimes complex variation of the stationary parameters such as temperature, fuel and oxidizer gas partial pressure, poisoning experiments, etc. in order to enable, for example, a clear assignment of the network components of the model to anode and cathode processes. Solar cells, on the other hand, benefit from the fortunate fact that the two photo-electric transfer functions can be analyzed in addition to the impedance. If all three functions are measured in the same state of the system, a model must therefore exist that simultaneously does justice to all three data sets together. EIS, IMPS and IMVS are differently "sensitive" to the contribution of certain processes to the respective transfer function. Impedance, for example, is "blind" to the actual photoelectric process. The¹⁹ IMVS measured under open cell voltage conditions is naturally insensitive to network components occurring in series, while the IMPS measured under short-circuit conditions is insensitive to network components occurring in parallel. The three transfer functions complement each other in such a way that ambiguities are at least eliminated with a high degree of probability: If a model has been developed that can actually reproduce all three data sets, it appears more reliable than if it is restricted to a single transfer function, as in the case of the EIS.

The preceding argumentation leads to the conclusion that a simulation program, similar to the programs for analyzing impedance spectra, can be a useful tool for understanding photo-electrochemical objects. In the following section, the realization of such a program is explained in the context of the present work.

¹⁹ The same system state when measuring EIS, IMPS and IMVS means that the steady-state values of voltage, current and lighting must match. This does not correspond to the procedure traditionally used to determine τ_d and τ_i . This will be discussed in more detail in the experimental part of the photoelectric measurements.

5.1 Program implementation

5.1.1 Stack-oriented calculation rule

In order to keep the amount of work involved in creating the program manageable, the implementation of the simulation and optimization program for photo-electric transfer functions was designed as an extension of the SIM impedance simulation program.

Here, the impedance is calculated algorithmically without different sets of calculation formulas being available for different networks. The user defines the impedance model ("equivalent circuit diagram") by entering a sequence of impedance elements, combined with the specification of their connection in the network. This dynamically creates a jump list, which can later be used to calculate the entered parameters in a stack-oriented manner. The most effective definition avoids unnecessary intermediate result calculations by defining the network "from the inside out". In the specification for calculating the impedance of a charge transfer reaction at an electrode in the form of the Randles circuit diagram Figure 13 you start with the definition of the charge transfer resistance R_{ct} and the linking rule "E: Enter - start new partial circuit diagram". In the next step, the diffusion impedance D_w is defined and the linking rule "S: Connect this element in series to the existing intermediate result" is used. The double layer capacitance C_{dl} can then be added directly with "P: Connect this element in parallel to the existing intermediate result". Finally, the electrolytic resistance R_{el} is defined and the linking rule "S: Connect this element in series to the existing intermediate result" is used for the second time to complete the definition. The table below shows the symbolic sequence and intermediate results with the most favorable input.

Impedance element	Symbol	Link	Interim result
Transfer resistance	R_{ct}	Enter	R_{ct}
Diffusion impedance	D_w	Series	$R_{ct} + D_w$
Double layer capacity	C_{dl}	Parallel	$(R_{ct} + D_w) // C_{dl}$
Electrolyte resistance	R_{el}	Series	$((R_{ct} + D_w) // C_{dl}) + R_{el}$

In the case of unfavorable input (from outside to inside), further intermediate results must be created (with the help of enter operations that place the previous intermediate results on the stack) in order to be linked later by operations without new input (null elements, they link the two intermediate results at the top stack level). The table below shows that significantly more operations are required to achieve the same final result.

Impedance element	Icon	Link	Interim results
Electrolyte resistance	R_{el}	Enter	R_{el}
Double layer capacity	C_{dl}	Enter	R_{el}, C_{dl}
Transfer resistance	R_{ct}	Enter	R_{el}, C_{dl}, R_{ct}
Diffusion impedance	D_w	Series	$R_{el}, C_{dl}, R_{ct} + D_w$
--	Zero	Parallel	$R_{el}, C_{dl} // (R_{ct} + D_w)$
--	Zero	Series	$R_{el} + (C_{dl} // (R_{ct} + D_w))$

Stacking intermediate results can sometimes be unavoidable, as the following example Figure 64 shows of two parallel adsorption processes (with neglected diffusion and double layer capacity).

Impedance element	Icon	Link	Interim results
Adsorption resistance 1	R_{ad1}	Enter	R_{ad1}
Adsorption capacity 1	C_{ad1}	Series	$R_{ad1} + C_{ad1}$
Adsorption resistance 2	R_{ad2}	Enter	$R_{ad1} + C_{ad1}, R_{ad2}$
Adsorption capacity 2	C_{ad2}	Series	$R_{ad1} + C_{ad1}, R_{ad2} + C_{ad2}$
--	Zero	Parallel	$(R_{ad1} + C_{ad1}) // (R_{ad2} + C_{ad2})$

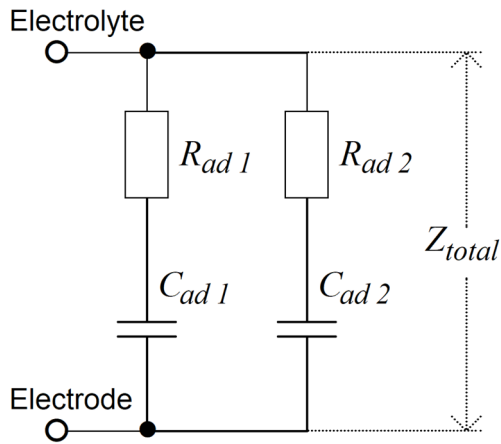


Figure 64: The impedance of two adsorption processes running in parallel cannot be calculated exclusively by directly successive parallel and series connections of impedance elements.

Overall, the stack-oriented structure results in a largely linear calculation processes, which pays off in high computing speed.

When calculating the impedance, only intermediate results with the dimension Ohm occur. If the principle is extended to other result variables from networks, additional stacks must be created for intermediate results with other dimensions. The realization of the successive principle can be illustrated by the rather simple calculation of impedance-voltage dividers. The simplest voltage divider, Figure 65 on the left consists of a "bottom impedance" Z_{bottom} and a "top impedance" Z_{top}

$$G = \frac{U_{out}}{U_{in}}$$

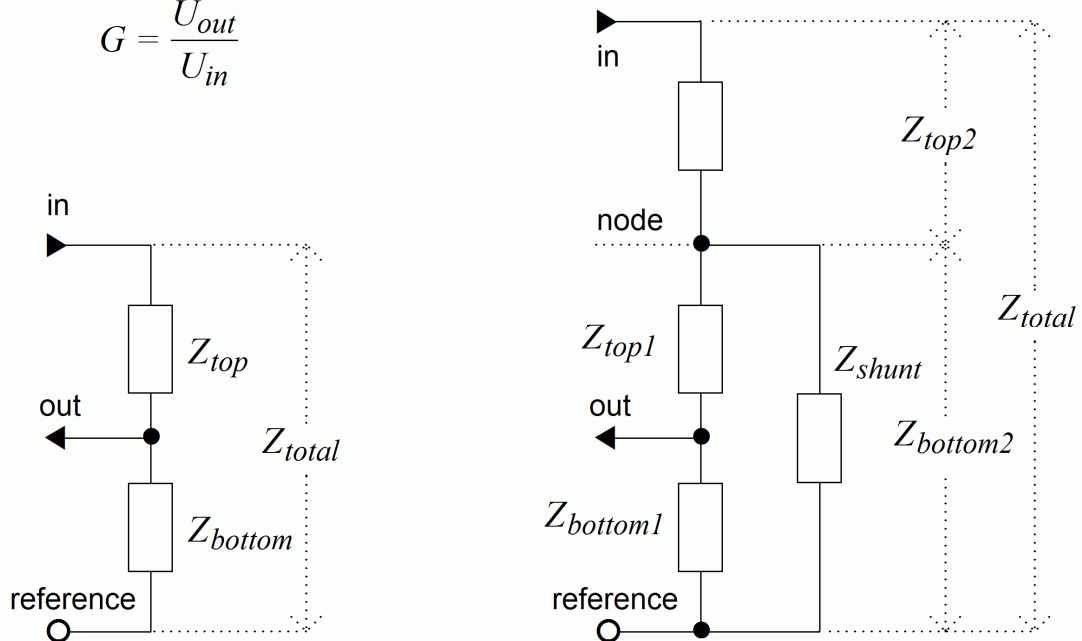


Figure 65: Single (left) and a multiple concatenated voltage divider consisting of partial impedances Z_{bottom} and Z_{top} (right). Several successive voltage divider sequences must be resolvable defined in partial impedances at the branching points ("nodes"), which are generated by additional parallel network components Z_{shunt} .

Although the partial impedances Z_{bottom} and Z_{top} could be connected directly in series to calculate the total impedance Z_{total} , the voltage divider ratio G (Eq. 88)

$$G = \frac{Z_{bottom}}{Z_{bottom} + Z_{top}} \quad (88)$$

needs separate intermediate results, which can be created using additional Enter operations. To iteratively continue the voltage divider algorithm, the series circuit $Z_{bottom} + Z_{top}$, together with impedance elements defining this node level ("node") and connected in parallel, must form the new base point impedance $Z_{bottom2}$, while the voltage divider ratio G determined first must be multiplied by the following divider ratios G_2 to G_n to determine the total divider ratio. The table below shows the input and calculation sequence as it appears when processing a chained voltage divider, Figure 65 on the right.

Impedance element	Icon	Link	Interim result Z	Interim result G
Base impedance 1	Z_{bottom}	Enter	Z_{bottom}	-
Top impedance 1	Z_{top}	Enter	Z_{bottom}, Z_{top}	-
--	Zero	Series, Divider	$Z_{bottom} + Z_{top}$	$G1 = Z_{bottom} / (Z_{bottom} + Z_{top})$
Parallel impedance 1	Z_{par}	Parallel	$(Z_{bottom} + Z_{top}) // Z_{par}$	$G1$
Top impedance 2	Z_{top}	Enter	$(Z_{bottom} + Z_{top}) // Z_{par}, Z_{top2}$	$G1$
--	Zero	Series, Divider	$((Z_{bottom} + Z_{top}) // Z_{par}) + Z_{top2}$	$G2 = G1 * ((Z_{bottom} + Z_{top}) // Z_{par}) / (((Z_{bottom} + Z_{top}) // Z_{par}) + Z_{top2})$

The calculation of voltage divider models is already provided for in the program and is used, for example, to simulate artifacts such as those frequently observed in three-electrode cell arrangements, [110].

Just as the divider ratios propagate in a chained voltage divider, the effect of the photocurrent in a solar cell moves from the inner network to the outside to the terminals. Since the effort required for a perfect specialized user interface for the simulation of photo-electrochemical models would have been considerable, the structure of the voltage divider development was used for simplification.

The program must also be informed that the impedance, dynamic photocurrent or dynamic photovoltage should be output instead of calculating the voltage divider ratio. A user element specially written for photo-electrochemical modeling is used for this purpose. The main task of this element is to introduce a current source that simulates the behavior of the photocurrent generation. The user communicates the level of the photocurrent to the program via the parameter input of the user element. A further input parameter serves as a signal ("flag") which dimension (V, A, Ω) should be output at the end of the calculation procedure.

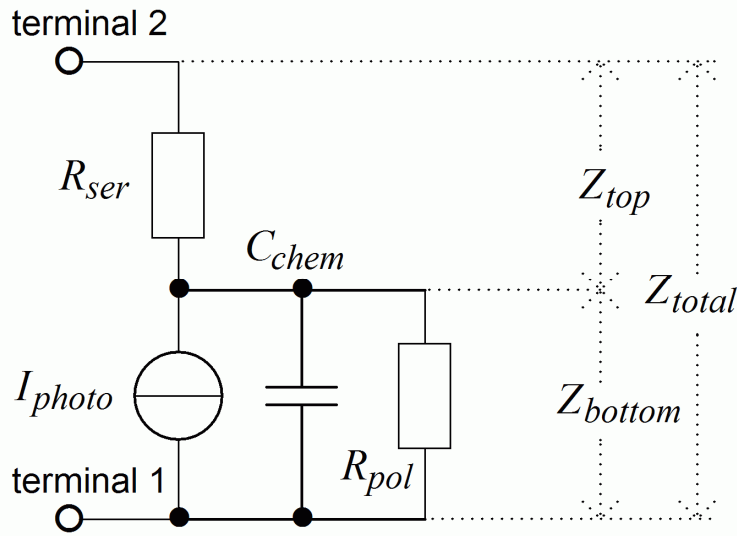


Figure 66: Symbol of the user element for photocurrent generation of the magnitude I_{photo} in a circuit diagram together with a shunt capacitance C_{chem} , a parallel resistor R_{pol} and the series resistor R_{ser} . The model shown can be used to simulate the dynamic behavior of an ideal photodiode or solar cell. The base impedance Z_{bottom} and the top impedance Z_{top} are optionally calculated with the photocurrent I_{photo} via the voltage divider algorithm to form the total impedance Z_{total} , the open cell voltage U_{ocv} or the short-circuit current I_{sc} .

The table below demonstrates the input and calculation sequence for the simplest case of simulating an ideal photodiode or solar cell, as shown in Figure 66.

Impedance element	Icon	Link	Interim result Z	Interim result V
User element	I_{photo}	Enter	∞	-
	<i>flag</i>	-	∞	-
Parallel impedance $C_{chem} // R_{pol}$	Z_{bottom}	Parallel	Z_{bottom}	$I_{photo} * Z_{bottom}$
Series impedance Tracking resistor R_{ser}	Z_{top}	Enter	Z_{bottom}, Z_{top}	$I_{photo} * Z_{bottom}$
--	Zero	Series,Divider	$Z_{bottom} + Z_{top}$	$I_{photo} * Z_{bottom}, I_{photo} * Z_{bottom} / (Z_{bottom} + Z_{top})$
Final result:				
$flag=0:$	Z_{total}	Total impedance	$Z_{total} = Z_{bottom} + Z_{top}$	
$flag=1:$	I_{sc}	Light-induced short-circuit photocurrent	$I_{sc} = I_{photo} * Z_{bottom} / (Z_{bottom} + Z_{top})$	
$flag=2:$	U_{ocv}	Light-induced open photocell voltage	$U_{ocv} = I_{photo} * Z_{bottom}$	

In the second term $I_{photo} * Z_{bottom} / (Z_{bottom} + Z_{top})$ in the column for the intermediate results V in the row after the series and divider operation, the same fraction G occurs as in the voltage divider calculation. Note that the cell voltage $I_{photo} * Z_{bottom}$ is independent of Z_{top} . If you were to end the definition after entering Z_{bottom} , the photocurrent would still be independent of Z_{bottom} . In contrast, all parameters except the generation current I_{photo} are included in the impedance. This illustrates the fact that different domains of the overall network are important for the three transfer function types.

The input value for the signal *flag* decides whether the total impedance, the short-circuit photoelectric current or the open photocell voltage should be calculated from the intermediate results Z and V and transferred at the end of the expression development. The *flag* signal is also used to communicate the current physical quantities and units to the further processing program parts for graphics and data export. For this purpose, separate input lines ("data" lines) are available in the user element definition to specify names and units. The data in these lines is read out depending on the value of *flag*.

5.2 Models

The previous section described ways of creating network models of photoelectrically active objects. Losses due to current branching can be simulated in the same way as the loss contributions due to series impedances, whereby interleaving is possible up to any depth. The modeling options thus appear to be sufficient for many applications. Spatially widely distributed photocurrent generation is, however, difficult to simulate using many "ideal" photocurrent sources integrated in chain conductors, as the program only allows the placement of one photocurrent-generating object in the network.

The final result as well as the intermediate results of the modeling of photoelectrically active objects can also be represented as source impedances combined with currents acting on them. Just like the source impedance, a (complex) photocurrent to be defined is also characterized by a characteristic frequency dependence. On the other hand, this makes it possible to simulate a distributed photocurrent generation by defining a characteristically frequency-dependent photocurrent source together with the associated source impedance instead of simulating an infinite number of ideal photocurrent sources distributed in the network, which is not supported by the program.

5.2.1 The extended photocurrent source

In many cases, the assumption of a frequency-independent photocurrent source localized in the network is sufficient to model solar cells with sufficient accuracy. In the case of dye-sensitized solar cells based on porous semiconductors, the quality of modelling using a localized photocurrent source can be inadequate. However, a photocurrent generation distributed over a chain conductor can be simulated using a localized but frequency-dependent photocurrent source with a chain conductor impedance connected in parallel. The user element provided by the simulation program for this purpose makes it possible to enter a frequency dependence of the photocurrent according to a first-order time constant and also according to a time constant of order $\frac{1}{2}$ ($\sqrt{\omega}$ dependence). Both time constants are set by their cut-off frequency. Since the effect of the frequency dependence can be suppressed by selecting a cut-off frequency far above the observation range, the user element defined in this way can be used both for frequency-independent photocurrent generation and as an approximation for distributed photocurrent generation. Figure 67 shows how the behavior of a Grätzel photoanode can be modeled with the simple (frequency-independent) photocurrent source. To do this, the photocurrent source must be embedded into a relatively complicated porous system (pore model according to H. Göhr, see chapter 4.1).

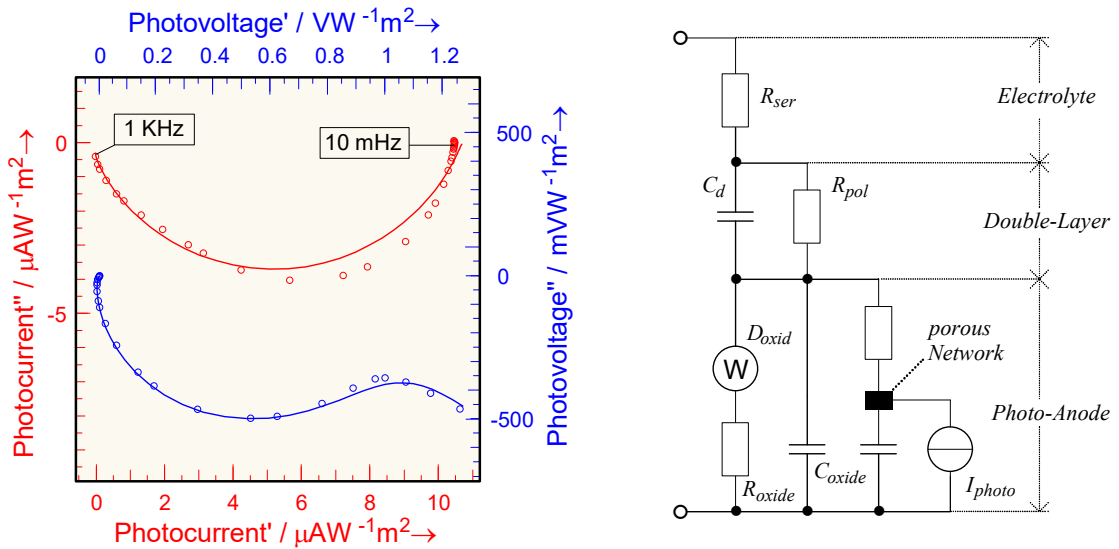


Figure 67: IMPS and IMVS spectra in the Nyquist diagram of a Grätzel dye-sensitized solar cell based on nano-porous TiO_2 . The measured values are shown as sample points, the simulation as a solid curve. The model calculation was based on the equivalent circuit diagram shown on the right. It is based on a frequency-independent photocurrent source embedded in a porous network.

The simulation of the same system using the extended (frequency-dependent) photocurrent source (Figure 68) succeeds in slightly better quality despite the use of a somewhat simpler network and directly provides the two time constants τ_1 and τ_2 that are effective in the photocurrent.

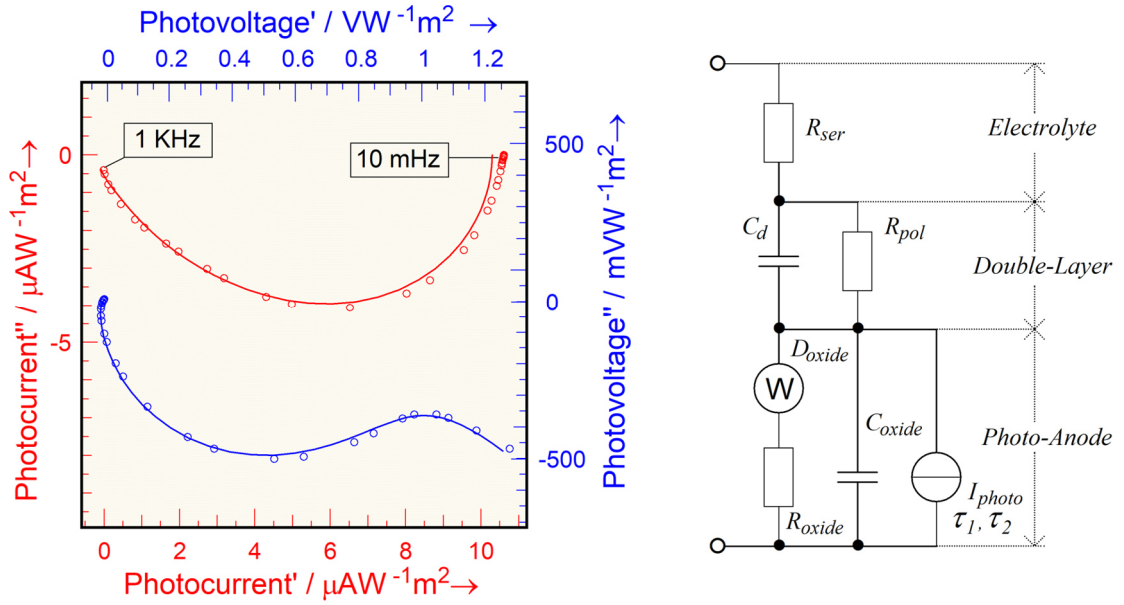


Figure 68: IMPS and IMVS spectra in the Nyquist diagram of the same system as described in Figure 67. The measured values are again shown as sample points, the simulation as a solid curve. The model calculation was based on the equivalent circuit diagram shown on the right. It differs from the model in Figure 67 by the use of the extended (frequency-dependent) photocurrent source.

The parameter numerical values of the parts of the network common to both models do not differ significantly after the fit (typically <3%).

The use of the extended (frequency-dependent) photocurrent source without explicit proof of its relevance in individual cases is certainly contestable. However, it is well suited for the quantitative determination of losses through the surrounding network. The next section deals with an analytical model developed for the Grätzel cell.

5.2.2 The porous dye-sensitized solar cell model according to L. Bay and K. West

The common models (hereinafter referred to as "continuum model") for the dynamic description of dye-sensitized solar cells [27], [28], [29], [30], [31] use an approach that is also partially used in the analysis of monolithic solar cells [32], [33]. As mentioned at the beginning, the kinetic competition between the migration of generated photo-electrons to the collector and their unwanted recombination on contact with the electrolyte plays a decisive role. The observable electron mobility is many orders of magnitude lower compared to the value of the silicon solar cell ($\approx 100\text{-}1000 \text{ cm}^2 / \text{Vs}$). This is explained by the fact that the electrons cannot move almost freely in the conduction band as in silicon (Figure 69), but are often briefly bound to impurities ("trapping") before they move on to the next (weak) binding site ("hopping").

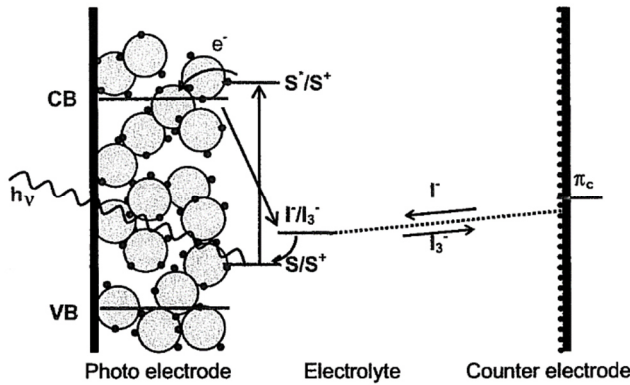


Fig. 1. Sketch of the geometry and energy levels in a DSSC.

Figure 69: Sketch of how a Grätzel-type dye-sensitized solar cell works. Taken from the original work [38] by Keld West and colleagues. Photo-electrons move from trap to trap or from grain to grain from the point of origin to the collector (left), while the holes reach the counter-electrode via the electrolyte by means of the redox system $I^- - I_3^-$.

To model the DSSC, photoelectron generation, diffusion and recombination are applied in the form of a continuity equation and the diffusion equations are solved taking into account the corresponding boundary conditions (see Eq. 1-3 [28]). Accordingly, one calculates with "effective" diffusion coefficients and mobilities without using an explicit model that takes into account the porous topology of the systems.

Keld West and colleagues [38] presented an alternative model based on the porous distributed components electrolyte, active interface and electron conductor. From the equivalent electrical network, they were able to calculate the impedance and, under the effect of photoelectron generation, the dynamic photovoltage and the dynamic photocurrent.

You place a chain ladder (Figure 70) whose bars are formed by the electron-conducting oxide on the one hand and the ion-conducting electrolyte on the other. The rungs correspond to the photon-absorbing and photoelectron-generating space elements. Photoelectrons can be stored inside these space elements and lost through recombination. Bay and West take this into account with a capacitance and an ohmic conductivity of each space element as the simplest approach.

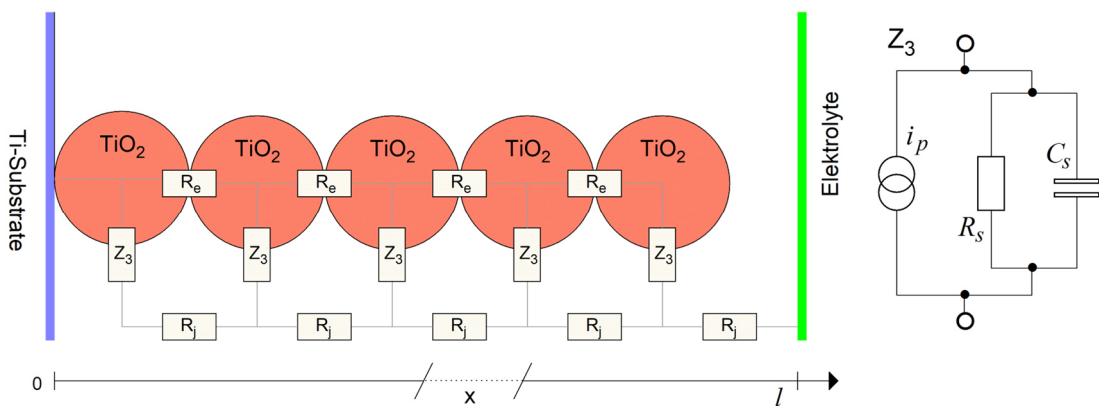


Figure 70 : Model of the porous dye solar cell of the Grätzel type according to Keld West and colleagues. The illustration is based on the original work, [38] Fig. 2. The chain conductor consists of the bars of electron-conducting TiO_2 phase (R_e , top) and ion-conducting electrolyte (R_i , bottom). The rungs Z_3 form the light-absorbing and photo-electron-storing spatial elements. Partial recombination also takes place in Z_3 , so that the circuit diagram shown on the right, consisting of photocurrent source i_p , loss resistance R_s and capacitance C_s , results as electrical equivalence for Z_3 .

Bay and West find the expression Z_{EC} for the impedance, Eq. 89, which, as shown briefly in the appendix, is equivalent to H. Göhr's result for the "homogeneous pore system".

Although Bay and West do not have a separate expression for the dynamic photocurrent, the IMPS function can easily be calculated using the definition from impedance and dynamic photovoltage, as also mentioned in relation 14 of their publication.

$$Z_{EC} = (R_e + R_i) \cdot l \cdot \frac{\coth(\alpha \cdot l)}{\alpha \cdot l} + \frac{R_e \cdot R_i}{R_e + R_i} \cdot l \cdot \left(1 - \frac{\tanh(\alpha \cdot l/2)}{\alpha \cdot l/2} \right) \quad (\text{according to Eq. 8 [38]} \quad (89)$$

$$Z_P(R_i, R_e) = \frac{B \cdot A \cdot R_i}{A^2 - \alpha^2} \left(e^{-A \cdot l} \left[1 + \frac{A}{\alpha} \coth(\alpha \cdot l) \right] - \frac{A}{\alpha \sinh(\alpha \cdot l)} \right) + \frac{B \cdot A \cdot R_i}{A^2 - \alpha^2} \left(\left[1 - \frac{A}{\alpha} \coth(\alpha \cdot l) \right] + \frac{A \cdot e^{-A \cdot l}}{\alpha \sinh(\alpha \cdot l)} \right) \quad (\text{according to Eq. 9 [38]} \quad (90)$$

(R_e , R_i : electronic oxide and electrolyte resistance [Ω -cm], B : quantum efficiency, A : absorption coefficient [cm^{-1}], l : depth of the pore system [cm], α : abbreviation with $\alpha^2 = (R_e + R_i)/Z_s$, [α] = cm^{-1}).

Their result for the dynamic photovoltage $V_p = -Z_p$ (IMVS), Eq. 90 is somewhat unusually normalized and all units of impedance elements are area-normalized or, like C_s , volume-normalized. In contrast, the simulation program of the present work prefers to calculate with measured Si units in order to facilitate direct application to measured data. Surface normalization can be activated independently of the model if required. In addition, following the tradition of H. Göhr, impedance elements are always defined in the program in such a way that only the minimum number of (independent) parameters is used. Therefore, in addition to the original formulation, the model of Bay and West was also implemented in the simulation program in a slightly modified form (see appendix) in the course of the present work and, as shown later, applied to experimental data.

The impedance Z_s of the rung elements is not assigned to the user element for the definition of the Bay-West function in the program, but is set up separately as a network in the usual program manner. This means that Z_s is not limited to the parallel connection of R_s and C_s and can be entered differently if necessary.

The strength of the model lies mainly in its derivation from the porous topology of the dye-sensitized solar cell. Photoelectron transport is understood as charge transfer between grain boundaries and the loss due to recombination can be described by the internal resistance of the particles. West and colleagues were able to show that their model produces the same results for a small electrolyte resistance R_i as those found using the continuity condition approach. The effective diffusion coefficient D_n usually given there becomes $D_n = [C_s \cdot (R_i + R_e)]^{-1}$ and the recombination time constant τ_n becomes $\tau_n = R_s \cdot C_s$ in Bay and West's model.

However, Bay and West do not mention that their approach also provides an unconstrained explanation for the mostly observed proportionality between the effective diffusion coefficient D_n and the intensity P of the illumination: If the charge transfer between the grain boundaries is attributed to an activated process (as is the case, for example, with the charge transfer reaction), the current is exponentially dependent on the difference between the effective potential and the activation energy. Since the effective potential²⁰ is proportional to the logarithm of the charge carrier concentration $D_n \propto P$, applies approximately if the electrolyte resistance can be neglected and C_s , as expected for Schottky barriers, is only slightly dependent on the potential.

²⁰ The "effective" potential is the sum of the electrical and chemical potential. D_n is generally determined in "short-circuit mode" so that only the chemical potential is effective.

6 Optimization and fit of transfer function triplets

As in the case of fuel cells or batteries, a great deal of knowledge can be gained about solar cells using impedance spectroscopy as a dynamic small-signal method. As photoelectrically active objects, they can also be characterized by measuring the dynamic photocurrent and voltage spectra (IMPS and IMVS).

As mentioned above, by combining the results from EIS, IMPS and IMVS measurements carried out on the same system, the fundamental ambiguity that must be accepted when interpreting the individual spectra can be partially eliminated.

When creating a model in the form of an electrical equivalence, the usual procedure is to start by incorporating the known properties of the structure of the object and the processes taking place into the definition of the electrical network. A simulation program calculates the transfer function of the network in the frequency range of the measured data and displays it graphically together with the measured data. The initial large discrepancy between the model calculation and the measured data can be attributed to various causes. The description using the network may be incomplete or incorrect because, for example, not all relevant processes are known, knowledge of the topology of the object is still incomplete or the contribution of systematic artifacts is neglected.

Even if the object is described completely in principle by the network, the model calculation and measurement data generally differ due to the remaining inaccuracy of the numerical values of the descriptive parameters. This fine-tuning of the model parameters for optimal adaptation to the measurement data is best left to an optimization program as described below. An incomplete or faulty model is revealed if the "fit", i.e., the final result of the automatic numerical value adjustment of the model parameters, still shows systematic deviations between the model calculation and the measurement data.

The process of successful modelling therefore usually consists of multiple sequences of manual correction of the model²¹ by the researcher and subsequent automatic optimization of the parameter numerical values. If this strategy is applied to a model that is intended to jointly explain impedance, photocurrent and photovoltage spectra, it is extremely tedious to apply the individual optimization steps sequentially to the different databases, as each optimization of a particular transfer function "neglects" the parameters that are less relevant for this function, while these are significant for the other transfer functions. As a result, the parameter sets drift apart. Synchronization to find a common optimum for all three types of spectra is therefore hardly feasible.

To solve this problem, the simulation and optimization program was extended so that the parameters of a common model can be fitted to the data of all three transfer function types simultaneously in the direction of a common error minimum ("TRIFIT" procedure).

The following section first describes how the Fit program works when traditionally applied to impedance spectra. This does not differ in principle from the application to IMPS or IMVS spectra.

²¹ Several attempts have been made to automate the model synthesis and correction step, always with dubious success. The model described in Chapter 4, (Figure 63) cannot in principle be solved automatically, as a calculation program lacks the necessary information about the system under investigation that goes beyond the frequency spectrum.

6.1 Fit procedure for impedance spectra (Complex Non Linear Least Squares "CNLS" fit)

In order to obtain a criterion for the deviation between model calculation and experimental data, the prediction of the model $Z_{mod}(\omega_i, P_1 \dots P_p)$ for the current parameter set $P_1 \dots P_p$ of the model is first calculated at all z frequency sample points ω_i of the measured impedances $Z_{exp}(\omega_i)$ of the spectrum to be taken into account. Since the impedances Z_{exp} and Z_{mod} are complex quantities, a real valued distance function $\Delta(Z_{exp}, Z_{mod})$ must be defined, which evaluates the difference between Z_{exp} and Z_{mod} . One might think that an evaluation is unnecessary, since the linear

distance definition $\Delta_{linZ} = \sqrt{\text{Re}\{Z_2 - Z_1\}^2 + \text{Im}\{Z_2 - Z_1\}^2}$ exists in the complex plane for two complex numbers Z_1 and Z_2 . Some impedance fit programs use this definition. However, apart from the fact that the distance definition Δ_{linZ} in the complex plane also represents an evaluation, it is usually poorly suited for the evaluation of EIS data: Deviations in frequency ranges of spectra with a large magnitude of the impedance are emphasized, while differences in frequency ranges with a small magnitude are neglected. Therefore, if the results of CNLS-Fit procedures based on the linear distance definition are presented exclusively as Nyquist diagrams in the complex plane, as is often practiced, the quality of the agreement appears convincing. A check of the results in the Nyquist diagram of admittance or in the Bode diagram, on the other hand, could in many cases reveal glaring weaknesses in the modeling.

The definition of distance used in this paper $\Delta_{\log Z}$, which evaluates the relative deviation based on the logarithm of the transfer function, appears to make more sense,

$\Delta_{\log Z} = \sqrt{\text{Re}\{\log(Z_2 / Z_1)\}^2 + w \cdot \text{Im}\{\log(Z_2 / Z_1)\}^2}$ with the logarithm of the magnitude of the impedance quotient $\text{Re}\{\log(Z_2 / Z_1)\} = \log|Z_2 / Z_1|$ and the phase angle φ of the impedance quotient $\text{Im}\{\log(Z_2 / Z_1)\} = \arg(Z_2 / Z_1)$. Weighting φ by w is recommended due to the limited value range of the phase angle.

When evaluating the deviations between two complete spectra, the program adds up all z real part and imaginary part squares of the impedance quotients $Q_i = Z_{exp}/Z_{mod}$ to calculate the standard Err .

This can be expressed as a relative total error according to Eq. 91

$$Err = \sqrt{\sum_{i=1}^z \{\log|Q_i|\}^2 + w \cdot \{\arg(Q_i)\}^2} \quad (91)$$

which is used to measure the quality of agreement between the experiment and the model.

The determination of Err according to Eq. 91 is also used to calculate error gradients G_i for each of the p parameters P_i of the model. With their help, the P_i are changed step by step as long as Err decreases. A new gradient set must then be calculated to match the changed parameter set. To calculate G_i , Err is first calculated for the initial parameter set. Then each parameter P_i is changed individually by a very small (relative) amount δ in order to calculate an individual Err_i before P_i is reset to the initial value. The error gradient G_i is calculated from the relative change of Err with the parameter P_i : $G_i = (Err - Err_i) / \delta$.

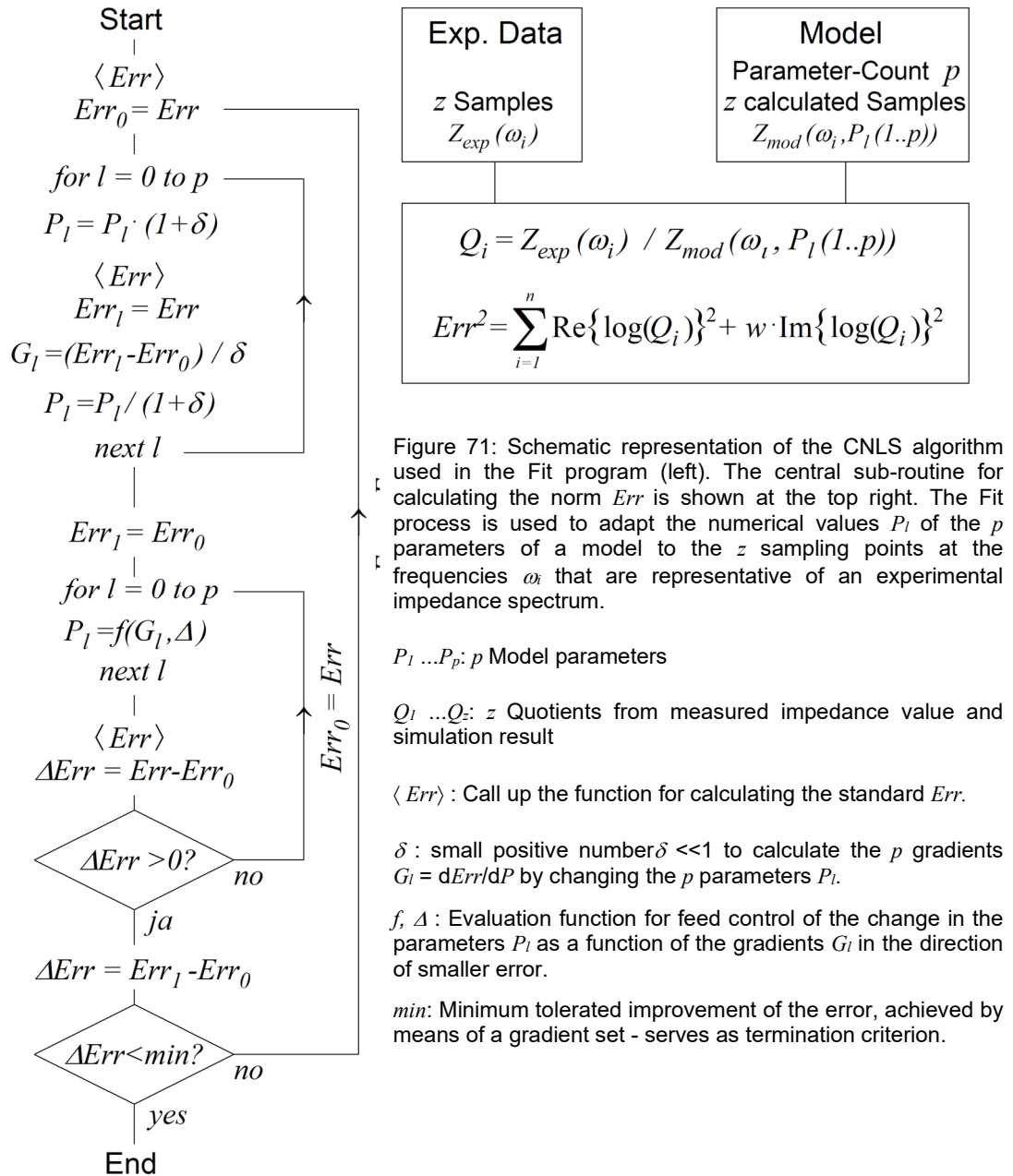


Figure 71 schematically shows the optimization process in which the calculation of the deviation Err , the calculation of the gradient set $G_1 \dots G_p$ and the step-by-step change of the parameters $P_1 \dots P_p$ is repeated cyclically until Err is minimal.

6.2 "TRIFIT" procedure

Even if they were measured in a common system state, EIS, IMPS and IMVS data are usually not available in the form of a common table column of z measurement frequencies ω_i . It does not make sense to determine the three transfer functions up to a common maximum frequency. Impedance spectra can often be measured close to the cut-off frequency of the instrument without any problems. Since both the electrical voltage and current response to changes in light intensity is close to zero at high frequencies due to the inertia of photoelectric systems, IMPS and IMVS measurements should only be carried out up to significantly lower maximum frequencies than is possible for EIS. Impedance spectra of complete solar cells can usually be measured up to the MHz range, half-cells in a three-electrode arrangement still up to around 100 KHz. The cut-off frequencies, above which the photoelectric spectra are only determined by artifacts due to the collapsing signal-to-noise ratio, are also in the MHz range for Si solar cells, but for organic polymer solar cells, for example, at 10-100 KHz, for ZnO-based dye solar cells at 1-10KHz and for TiO₂-based dye solar cells at only 100Hz-1KHz. The voltage response is usually slower than the current response. In addition, as described in section 3.1.2.3, Figure 16, the interpolation point selection and density for the Fitting process can also be selected differently from the original measurement data according to different strategies, the three experimental data sets appear separate. Generally, the three experimental data sets are available as separate tables of z impedance, c photocurrent and v photovoltage frequency pairs $Z_i; \omega_i$, $C_j; \omega_j$ and $V_k; \omega_k$.

To determine the total deviation $Err_{z,c,v}$, in addition to the n impedance quotients $QZ_i = Z_{exp_i} / Z_{mod_i}$, c photocurrent and v photovoltage quotients, $QC_j = C_{exp_j} / C_{mod_j}$ $QV_k = V_{exp_k} / V_{mod_k}$ must be determined from the respective sampling points and the values calculated by the model. $Err_{z,c,v}$ results in Eq. 92:

$$Err_{z,c,v} = \sqrt{\sum_{i=1}^z \{ \log|QZ_i| \}^2 + w \cdot \{ \arg(QZ_i) \}^2 + \sum_{j=1}^c \{ \log|QC_j| \}^2 + w \cdot \{ \arg(QC_j) \}^2 + \sum_{k=1}^v \{ \log|QV_k| \}^2 + w \cdot \{ \arg(QV_k) \}^2} \quad (92)$$

As with the fitting of impedance spectra, the error gradients $G_l = (Err_{z,c,v} - Err_{z,c,v_l}) \cdot P_l / \Delta P_l$ are again calculated from the dependence on $Err_{z,c,v}$ for each of the p parameters P_l of the model. In contrast to the separate procedure for optimization as described at the beginning of chapter 6 the Fitting process leads to a common error minimum for the different data types with the gradients determined in this way. The definition of Δ_{linZ} and $Err_{z,c,v}$ also shows that the linear distance definition Δ_{linZ} is unsuitable for determining a common error minimum for different data types because it is dimensionally dependent.

Figure 72 shows schematically how the error information Err is obtained according to Eq. 92 in the TRIFIT method. The optimization process itself hardly differs from the procedure for fitting impedance spectra.

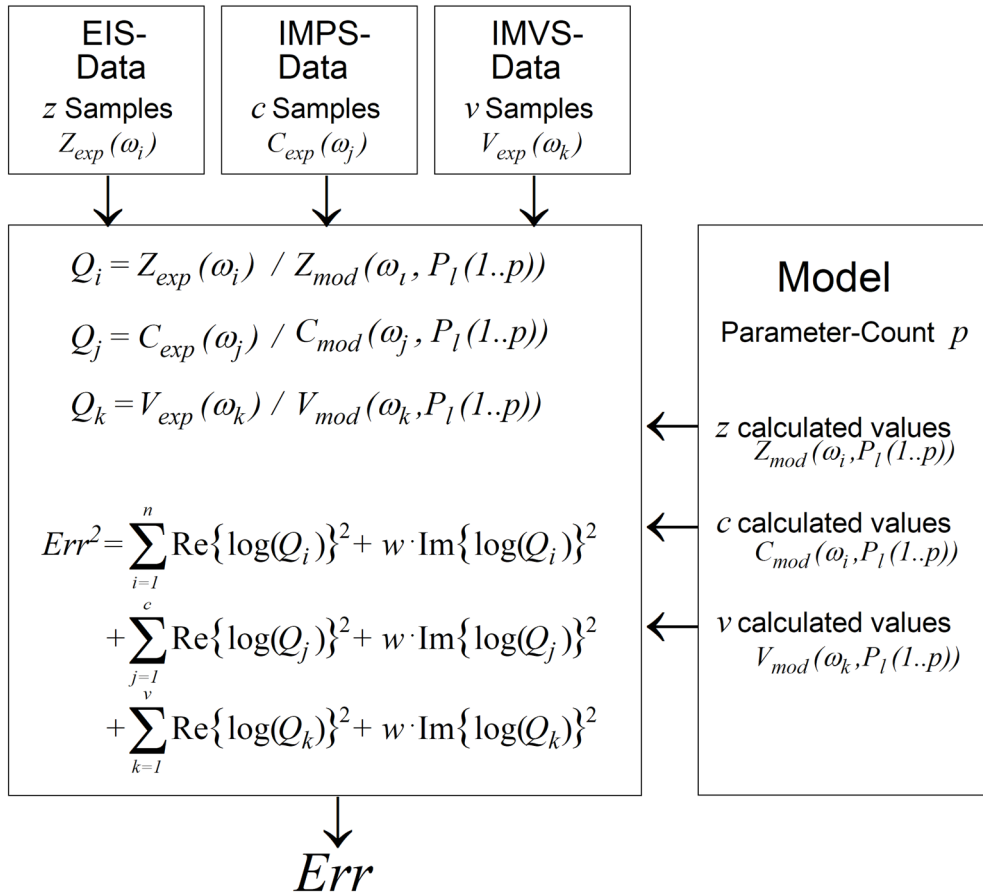


Figure 72: Schematic of the error calculation as the basis of the TRIFIT process for the simultaneous adjustment of the numerical values P_l of the p parameters of a model to the impedance points z measured at the frequencies ω_i , the IMPS points c measured at the frequencies ω_j and the IMVS points v measured at the frequencies ω_k .

7 Experimental applications of photo-electrochemical TFA

This chapter discusses the experimental principles of photoelectrochemical transfer function analysis, presents improvements achieved and demonstrates the application of the technique to the oxide film on tantalum and to titanium dioxide-based dye-sensitized solar cells.

7.1 Optimization of measurement technology for intensity-modulated photo spectroscopy

Impedance spectroscopy has been established for decades as a standard method in electrochemistry and in the broad field of related sciences, also thanks to a large number of functional and easy-to-use measuring instruments available on the market. However, the successful practical application of intensity-modulated photocurrent and photovoltage spectroscopy (IMPS and IMVS) still poses a certain challenge to researchers in the majority of laboratories. As no professional instrumentation optimized for IMPS / IMVS applications was available until the innovations developed in the course of this work were introduced, most working groups made do with provisional solutions based on the setups of pioneers such as Grätzel, Bisquert and Peters.

The following sections first discuss the known state of the art for carrying out IMPS and IMVS measurements. Then the further developments that have emerged in the course of the work are presented.

7.1.1 Principle of the traditional measurement technique for IMPS / IMVS known from the literature

As shown in the schematic drawing Figure 2, chapter 2, the instrumentation for IMPS / IMVS must be able to control the intensity P of the light source statically (bias) and dynamically (modulation). For IMVS it must be possible to measure the cell voltage at constant current (galvanostatic operation), for IMPS the cell current at constant voltage (potentiostatic operation). "Light Emitting Diodes" LEDs are predestined as a light source. With LEDs, the intensity P of the emitted light can be easily adjusted and modulated via the supply current I_{LED} , $P = \eta_{IP}(I_{LED})$. Compared to a laser, the light emission characteristics of LEDs are better suited to the wide-area illumination of photoactive test objects such as solar cells.

In traditional instrumentation, an LED light source is connected to the test current output of common frequency response analyzers "FRA". For the IMVS measurement with open cell voltage U , the DUT can be connected directly to the corresponding measurement voltage input of the FRA (Figure 73 left). For IMPS measurement under short-circuit conditions, the object must be connected to the input of a current to voltage converter ("Zero Resistance Amplifier" ZRA). Its output voltage, which is proportional to the cell current I , is in turn connected to the measurement voltage input of the FRA (Figure 73 right).

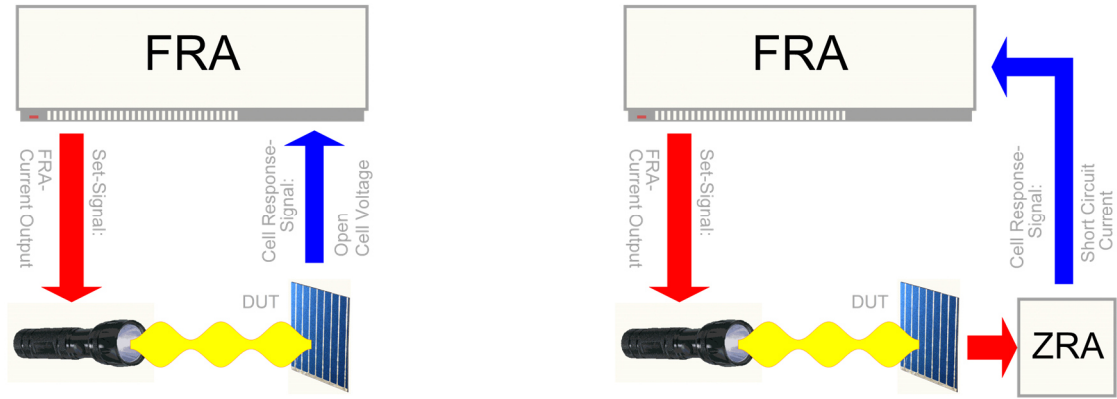


Figure 73: Traditional setup of a measuring device for IMVS (left) and IMPS (right). FRA: Frequency response analyzer. ZRA: Current to voltage converter.

The FRA correlates the dynamic component of the LED current \tilde{I}_{LED} with the dynamic component of the measured photovoltage \tilde{U} or the measured photocurrent \tilde{I} , so that the following transfer functions Eq. 93 are determined:

$$IMVS_{rad}(U, P) \approx \frac{\tilde{U}}{PF \cdot \tilde{I}_{LED}}, \quad IMPS_{rad}(I, P) \approx \frac{\tilde{I}}{PF \cdot \tilde{I}_{LED}} \quad (93)$$

The technique described involves a number of problems, which are discussed below.

Because the LED current is used as a proxy for the correlation instead of the measured intensity P , the above relationships are only approximations for the actual transfer functions. The relationship f_{IP} between P and I_{LED} is assumed to be linearly proportional, constant over time and independent of frequency - it is assumed that $P = PF \cdot I_{LED}$.

Direct-emitting, monochromatic LEDs have a low efficiency at low currents I_{LED} . Efficiency is optimal in the medium current range and decreases again up to the specified maximum current. With color conversion LEDs²² the saturation effect is even more pronounced at high currents. This makes the assumption $P = PF \cdot I_{LED}$ questionable. The actual bias intensity cannot be set reliably via I_{LED} and a sinusoidal modulation generates undesirable harmonics via the non-linear relationship f_{IP} . In addition, the scale factor for the modulation does not match the mean scale factor for the bias intensity.

It is possible to determine the bias intensity using an independent measurement. However, one serious problem is the lack of stability of the intensity over time.

As at the beginning of chapter 5 the important determination of the expression η_{dyn} , Eq. 86 for the dynamic efficiency depends on the - necessarily sequential - measurement of IMVS and IMPS. On the other hand, there is an approximate inverse proportionality between bias intensity and the characteristic time constants. If the intensity changes between the two measurements, the result for the dynamic efficiency is therefore directly falsified.

If one limits oneself solely to the determination of η_{dyn} , the stability and reproducibility problems of the traditional method can be overcome by careful independent intensity measurement and manual readjustment. Since the scale factor for the modulation can only be determined with great effort by independent measurements, the measurement data is still unsuitable for further quantitative evaluation. In addition, it can only be assumed for low modulation frequencies that the function $P = f_{IP}(I_{LED})$ is independent of the frequency. If the light from the LED can only follow the control current with a delay at higher modulation frequencies, this also affects the measured spectra as an unknown error contribution. Particularly with organic polymer solar cells, but also with ZnO-based dye solar cells, our own experiments have shown [41] with white light conversion LEDs, that the photocurrent spectrum in the cut-off frequency range (i.e. where the transport time constant τ_d is determined) already suffers detectable distortions.

A transfer function triplet of EIS, IMPS and IMVS in the same system state can only be determined with the traditional setup under open cell voltage conditions. In the equally important

²² Color conversion technology is used in particular to produce white LEDs. Here, an LED with high efficiency (usually in the blue range around 450 nm) emits light generated in fluorescent dyes, so that the sum of the original and fluorescent light results in the desired overall spectral curve.

complementary state at zero volts under short circuit, the IMVS measurement requires a galvanostat to apply exactly the amount of the short-circuit direct current that occurred during the IMPS measurement as a constant current so that the terminal voltage returns to zero volts. The cell states between these extreme values, e.g., at the point of maximum power, cannot be measured with the traditional setup either. This requires a separate potentiostat / galvanostat to supply the cell.

7.1.2 The principle of intensity control: "Controlled Intensity Modulated Photo Spectroscopy" CIMPS

In order to eliminate the weaknesses of the traditional measurement set-up for IMPS / IMVS measurements described above, a somewhat more complex test set-up was developed. In the CIMPS set-up, the LED light source is connected to a potentiostat specially reserved for this purpose (referred to as a "light potentiostat"). This means that the potentiostat of the basic system is available for unrestricted potentiostatic or galvanostatic control of the measuring cell. Transfer function triplets from EIS, IMPS and IMVS in the same system state can thus be carried out at all operating points of interest of a solar cell (Figure 74).

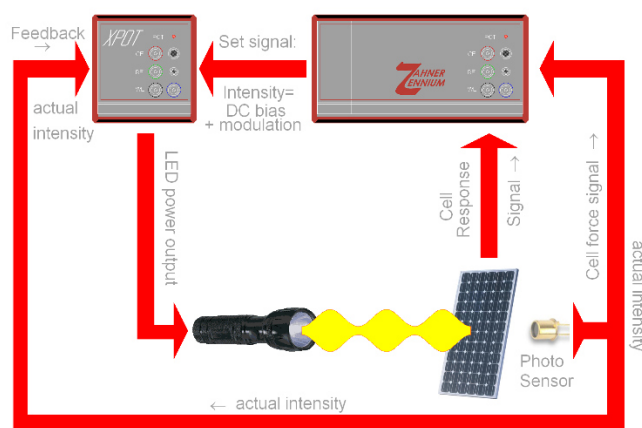


Figure 74: Setup of the measuring arrangement for photoelectric transfer function measurements with automatic intensity control.

The current intensity of the light is determined in the immediate vicinity of the object under investigation by a high-quality photodiode connected to a current-voltage converter. Good photodiodes show a linear, long-term stable relationship between illuminance and photocurrent over several orders of magnitude and are therefore also used in calibrated light meters. If the frequency bandwidth of the arrangement of current-to-voltage converter and photodiode is several orders of magnitude higher than the highest frequencies of interest for IMVS and IMPS, the output signal of the current-to-voltage converter represents an accurate, stable and frequency-independent, strictly proportional measure of the current intensity.

This signal (referred to as a "light signal") is fed to the light potentiostat at the feedback input. A potentiostat sets a predetermined potential by feeding back the voltage difference between the working and reference electrodes by means of the current through the counter electrode. In the same way, the light potentiostat can precisely set a light intensity specified in the form of a voltage by feeding back the light signal via the LED's supply current. The target light intensity can be precisely specified via the control voltage and modulation of the control voltage causes proportional modulation of the light intensity. The light signal is available for further processing alongside the LED supply current signal at the output of the light potentiostat.

A signal distributor in the frequency response analyzer of the basic device can be set up so that the excitation and response signals to be correlated can be recorded either by the potentiostat of the basic device (cell potentiostat) or by the connected sub-potentiostat (light potentiostat). It is also possible to calculate the transfer function between two signals mixed from both sources. The table below shows the results and applications for the various (useful) signal assignments.

Source	excitation signal	Source	response signal	TFA	Application
Cell potentiostat	Cell voltage	Cell potentiostat	Cell current	Cell impedance	EIS
Light potentiostat	LED current	Light potentiostat	Light intensity	Dynamic LED efficiency	for test purposes
Light potentiostat	Light intensity	Cell potentiostat	Cell current	dynamic photocurrent	CIMPS
Light potentiostat	Light intensity	Cell potentiostat	Cell voltage	dynamic photovoltage	CIMVS

By using the measured intensity P instead of the representative quantity I_{LED} to calculate the photoelectric transfer functions according to Eq. 94 eliminates some of the weaknesses of the traditional measurement set-up, as the following applies:

$$CIMVS(U, P) = \frac{\tilde{U}}{\tilde{P}}, \quad CIMPS(I, P) = \frac{\tilde{I}}{\tilde{P}} \quad (94)$$

CIMPS and CIMVS are true to scale and frequency-dependent amplitude and phase deviations between the setpoint and actual value of the intensity do not come into effect, as the actual value is directly incorporated into the TFA.

The use of a potentiostat to supply the light source offers further advantages. The feedback principle ensures that the non-linear characteristic curve $P = f_{IP}(I_{LED})$, drift and ageing of the LED are almost completely compensated for by the gain reserve of the potentiostat's operational amplifier. This ensures that successive measurements are carried out with stable intensity. In addition, the formation of harmonics during modulation is suppressed. Once the proportionality factor between intensity and light signal has been determined for a given geometry, calibrated intensities can be used from then on. This enables reproducibility and comparability with the results of other groups.

7.2 Dynamic measurements on a dye-sensitized solar cell based on TiO₂ nanotubes

Dye-sensitized solar cells DSSC based on semiconducting oxides of transition metals are seen as a potentially cost-effective alternative to monolithic solar cells. In addition to zinc oxide, titanium dioxide is being investigated as a promising starting material. Such oxides require a dye that ensures the absorption of photons in the visible light range, as the band gap of the materials themselves is too large for this. Effective absorption is achieved by fixing the largest possible amount of the dye, e.g., the ruthenium complex "N719", in the semiconductor. The colored oxide, together with a metallicly conductive carrier material (e.g., the metal substrate itself or TCO glass²³), forms the photo anode for collecting the photoelectrons. The holes that are also created during the dissociation of the photo-excitons are transported to the cathode in the DSSC by means of a transport redox system (e.g., iodine - iodide) in an electrolyte (e.g., acetonitrile with conducting salt) (where iodine is reduced back to iodide, for example).

In order to adsorb as much dye as possible in the oxide, a large surface area is required. If nano-porous material is used, however, the many grain boundaries make it more difficult for the electrons to travel and their recombination probability in contact with the electrolyte increases. Chapter 4 has already discussed the kinetic competition between photoelectron migration and recombination, which determines the "dynamic" efficiency (Eq. 86). To optimize this efficiency, a favorable compromise between maximum surface area and maximum electron mobility is sought. Nanotubes made of annealed titanium dioxide, which is predominantly present in the form of tetragonal anatase, are characterized on the one hand by a large surface area and on the other hand by good electron mobility and have therefore been the subject of intensive research in Prof. Schmuki's working group for some time now [42], [43], [44], [45]. In the following, the author reports on dynamic measurements of a dye-sensitized solar cell photoanode based on TiO₂ nanotubes and their results. The dynamic measurements were part of a broader investigation into the influence of various manufacturing parameters on the achievable efficiency.

²³ "Transparent Conducting Oxide" glass can be glass, coated with indium or fluorine-doped SnO₂, for example.

7.2.1 Experimental

In order to examine the photo anode specifically and to facilitate the interpretation of the dynamic measurements, a potentiostatic three-electrode arrangement with a reference electrode was used instead of a complete solar cell. The photo anode formed the working electrode. Figure 75 shows a sectional drawing of the cell structure. Further details on the measuring cell can be found in Figure 82. The system developed by the author was used as the photo-electrochemical measuring system.

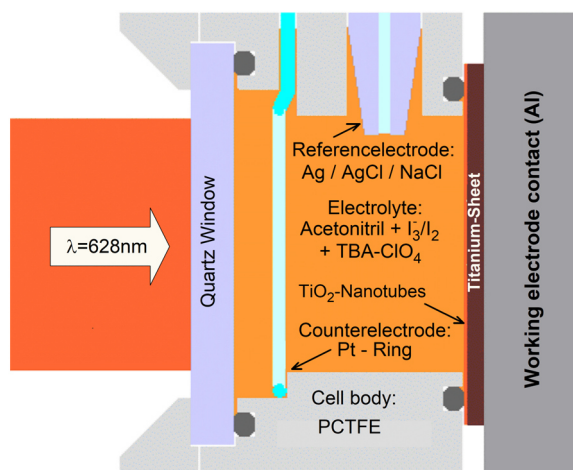


Figure 75: Cross-section of the photo-electrochemical cell "PECC" for dynamic measurements on a DSSC photo anode consisting of TiO_2 nanotubes on titanium sheet (after [39]). The light inlet is on the left.

The manufacturing process requires a titanium foil as the source and carrier of the resulting TiO_2 nanotubes. The electrode must therefore be illuminated through the counter electrode and the electrolyte column. In order to minimize losses due to light absorption in the electrolyte, complete solar cells of this type are manufactured using thin-film technology. This also minimizes the electrical losses in the electrolyte. At the light wavelength of 628 nm used in the experiment, the electrolyte (acetonitrile with I_3^-/I_2 -added and tert-butylammonium perchlorate as the conducting salt) in the PECC is still sufficiently translucent for the experiment with a transmission of approx. 20%.

The nanotubes are produced at the Institute in Prof. Schmuki's working group using a process described in [42], [43], [44], [45] by high-field anodization ("rapid anodization") of titanium sheet in fluoride-containing organic electrolytes. The titanium oxide tubes are formed under the competition of rapid anodic oxide formation and fluoride-induced oxide dissolution in a self-organization process in which the viscosity of the solvent probably also plays a certain role (Figure 76). However, according to the pH gradient model [48] the different dissolution rate of the oxide formed as a function of the local pH value, which differs at different locations. According to this model, a local decrease in the pH value (up to pH 2) takes place at the bottom of the nanotubes, while the solution becomes increasingly neutral closer to the electrolyte supply and thus the dissolution rate decreases.

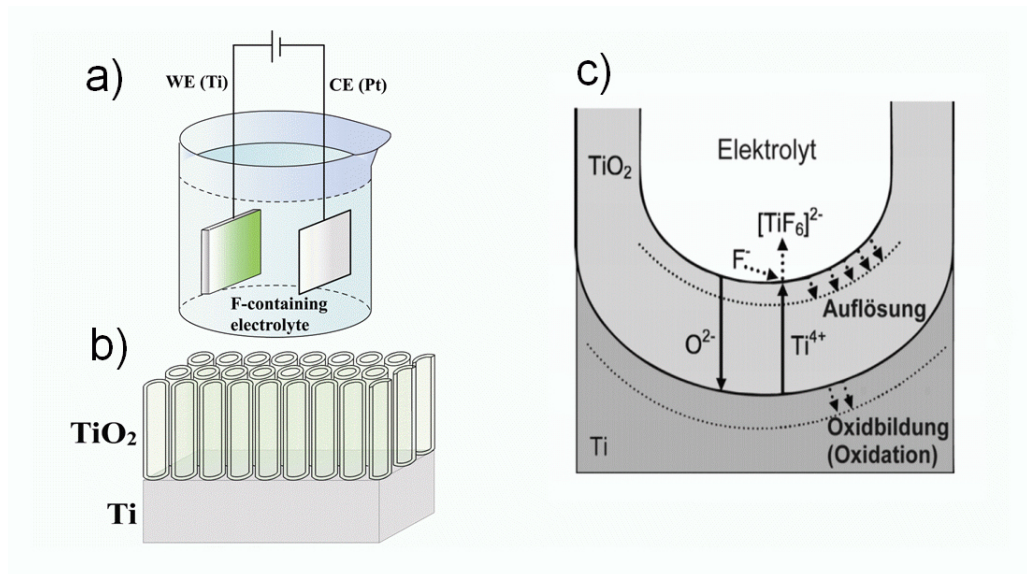


Figure 76: a) Schematic of anodization under high voltage ($\approx 100V$) in an electrolyte based on ethylene glycol and 0.5M HF. b) Sketch of a TiO_2 nanotube ensemble on a titanium substrate. c) Schematic of the self-organization process controlled by the competition of anodic oxide formation and fluoride-induced oxide dissolution (figures on the left from A. Ghicov and on the right from [47]).

This results in the electrolyte in an pH profile, approximately as shown in Figure 77.

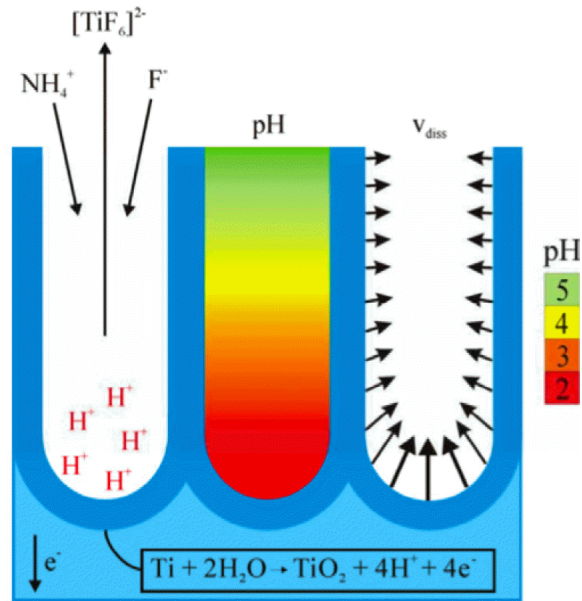


Figure 77: pH gradient model for the growth of TiO₂ nanotubes in fluoride-containing electrolytes (Fig. from [47]).

The tube length can be adjusted via the duration of the anodization. The freshly prepared samples are annealed in order to heal the initially amorphous structure of the oxide and to convert the majority into the tetragonal anatase modification. The length of the tubes, the annealing temperature and the annealing time (typically 10µm, 450°C and 60min) are decisive parameters for the photoelectric efficiency that can be achieved later.

The oxide can be colored by placing the samples in an alcoholic solution of the dye (typically 300µM / l) for a few hours.

Figure 78 shows the morphology of some samples in scanning electron microscopy (SEM) images (Fig. after [46]).

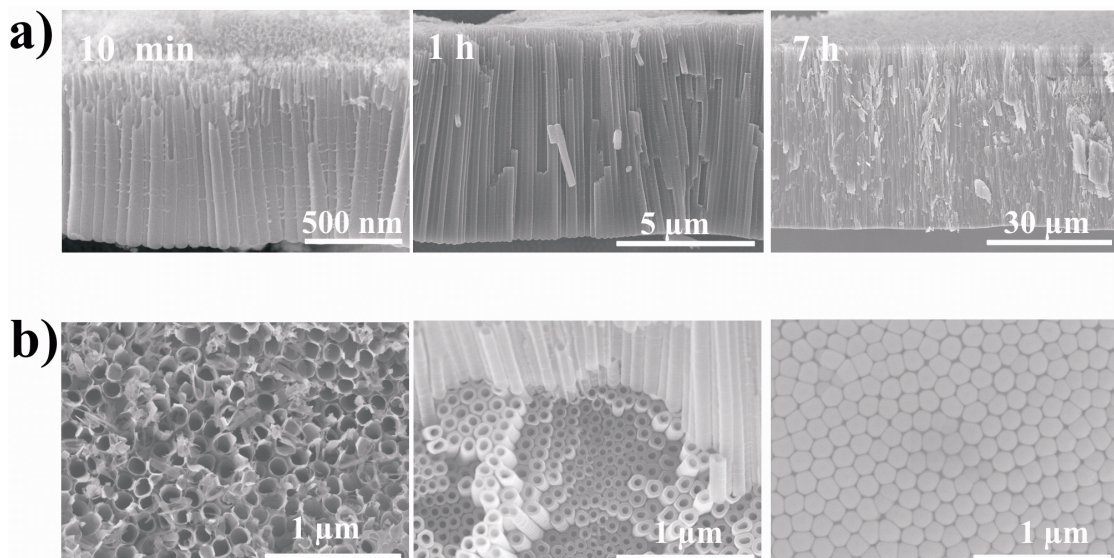


Figure 78: Scanning electron microscopy images SEM. a) Series of cross-sections of typical layers of TiO₂ nanotubes prepared by high-field anodization at 120V in ethylene glycol and HF for different lengths of time. b) Left: Top view, center: View of a deliberately broken layer, right: pore bottoms of detached tubes seen from below (images by A. Ghicov).

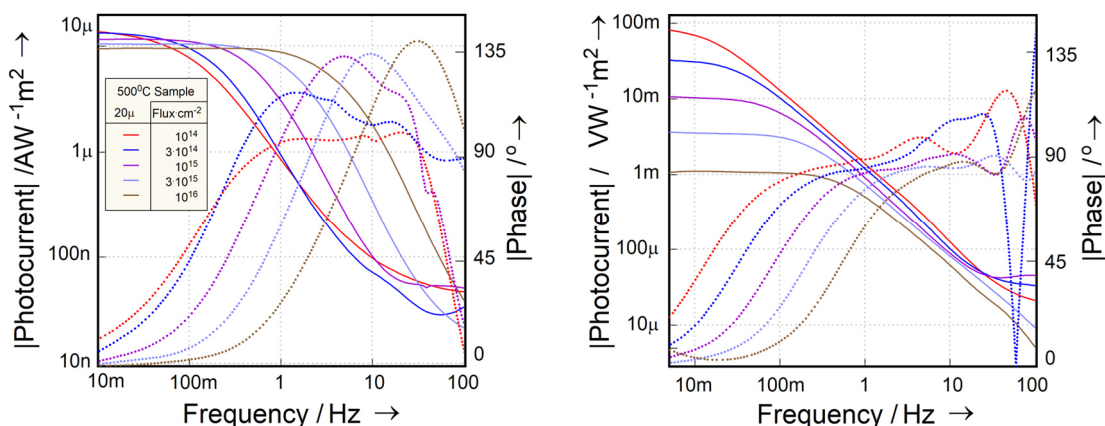


Figure 79: Typical CIMPS and CIMVS spectra series (Bode diagrams, dotted phase course) of the intensity (as photon flux) of a photo anode based on TiO₂ nanotubes measured under the experimental conditions of Figure 75. The tube length was approx. 20 μm. The sample was annealed for 1 hour at 500 C°.

In the experimental campaign, A. Ghicov and colleagues investigated many other samples in the form of thin-film cells both dynamically and in terms of the overall efficiency and the wavelength dependence of the photocurrent (normalized as "incident photon count efficiency" IPCE) [40]. The overall efficiency was found to improve with increasing tube length. This is not surprising because the light absorption path increases with increasing tube length.

Curing Temperature / C°	CIMPS τ_d / s	CIMVS τ_l / s	$1 - \tau_d / \tau_l$	$\eta / \%$	FF	Dye / nMcm ⁻²
350	0.018	0.6	0.95	1.1	0.45	47
450	0.027	0.29	0.91	1.6	0.50	103
500	0.077	0.25	0.69	1.6	0.50	100
550	0.12	0.25	0.52	1.2	0.51	(not available)

The table above shows the results for tubes with a typical length of 20 μm as a function of the annealing temperature. It is noteworthy that the total efficiency (η and fill factor FF) and the dynamic efficiency $1 - \tau_d / \tau_l$ appear to contradict each other: While η increases with the annealing temperature, the dynamic efficiency decreases. The investigation of the amount of adsorbed dye provided clarification. For this purpose, the dye was washed out of the samples in alkaline solution and determined by photometry. The more favorable ratio between electron migration and recombination time for lower annealing temperature is obviously overcompensated by the better dye adsorption after annealing at higher temperature.

7.2.2 Modeling of a TiO₂ nanotube photo anode according to L. Bay and K. West

Another sample was used to perform a combined impedance- CIMPS- and CIMVS measurement with the cell according to Figure 75 in (approximately) the same system state at the rest potential under light. The data triplet was analyzed using the Bay & West model (Chap. 5.2.2) and fitted. Figure 80 schematically shows the physical structure and the electrical equivalence model used.

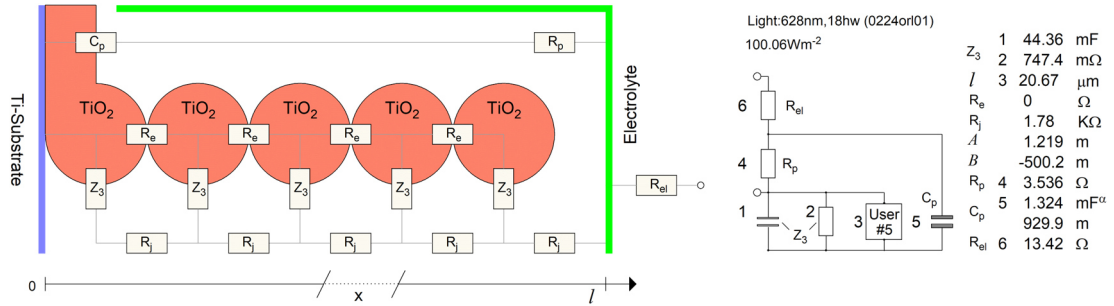


Figure 80: Left: Model of the photo anode made of TiO₂ nanotubes based on the model by Bay & West (see also Figure 70). The electrical equivalent circuit diagram is shown on the right. The resistance of the electron-conducting TiO₂ phase (R_e , top) appears to be negligible compared to the resistance of the electrolyte in the chain conductor (R_j , bottom). The rungs Z_3 (recombination impedance) are modeled as a parallel connection of resistance and capacitance. R_p and C_p form a shunt and correspond to the impedance of the bottom of the tube. B stands for the quantum efficiency, A for the absorption coefficient [cm^{-1}] and l for the depth of the pore system.

In Figure 81 the result of modeling and fitting using the TRIFIT algorithm (Chap. 6.2) is shown graphically. Considering that all three data types were approximated with the same model and the same set of parameters, it can be concluded that the Bay & West model is fundamentally suitable for analyzing dye-sensitized solar cell anodes. The parameter values determined for quantum efficiency, absorption coefficient and pore depth appear realistic.

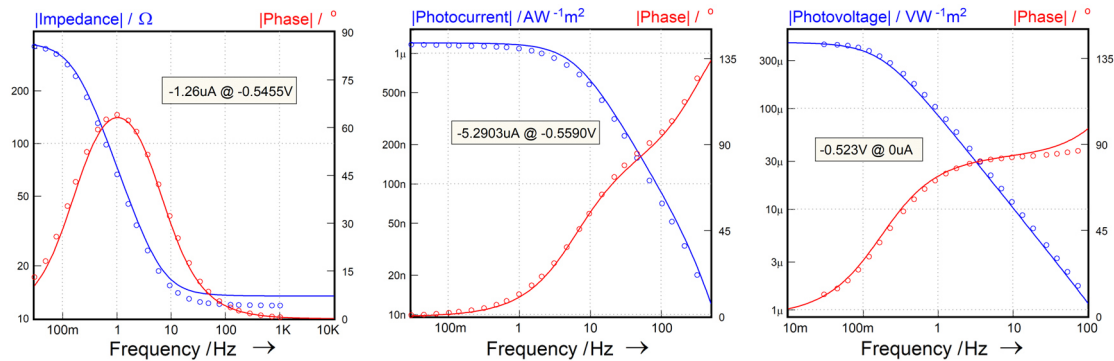


Figure 81: Bode diagrams of the three transfer functions impedance (left), CIMPS (center) and CIMVS (right) determined from measurement, modeling and fit of a TiO₂ nanotube photo anode. The sample points of the measurement data are shown as symbols, the curves calculated according to the Bay & West model as solid lines.

7.2.3 Discussion of the results achievable with the model according to L. Bay and K. West

Direct progress in the field of DSSC research could not yet be achieved by applying the Bay & West model in the course of this work. This raises the question of whether and why established model concepts (continuum model, cf. section 5.2.2) should be supplemented or even replaced in this area.

The following table compares the characteristics of the various models to aid discussion.

<u>Aspect</u>	<u>Continuum model</u>	<u>Model according to Bay & West</u>
Starting point of the model concept	Diffusion or migration of photoelectrons in the continuum to the electrode. No consideration of a distributed or porous structure (instead, use of "effective" diffusion coefficients)	Photoelectrons propagate in the inhomogeneous medium through the chain conductor formed by series and parallel resistors of the microstructure to the electrode
Transport mechanism	Diffusion and/or migration (controversial)	Longitudinal conduction across grain boundaries (chain ladder spars)
Loss mechanism	Photoelectron recombination at the electrolyte	Cross flow through the rungs of the chain ladder (equivalent to the continuum model)
Interpretation of the time constants from IMPS and IMVS	Diffusion or migration time constant (IMPS) and recombination time constant (IMVS)	No kinetic interpretation - the time constants result from the resistance-capacitor behavior of rung and tie bar resistances $R_i + R_e$ and R_s in interaction with the "double-layer capacitance" C_s of the rungs
Explanation for the intensity dependence of the time constants	–	The intensity dependence of the "recombination" time constant results directly from the proportionality between forward current and forward conductance of the semiconductor-electrolyte Schottky junction at the grain. If one also assumes an activated process for the charge transfer across the grain boundaries, this also applies to the "diffusion/migration" time constant.
Determined variables for use in DSSC optimization	Dynamic efficiency $\eta_{dyn} = 1 - \tau_d / \tau_l$	Equivalent values from: $\tau_d = [C_s \cdot (R_i + R_e)]^{-1}$, $\tau_l = R_s \cdot C_s$
Experimental measurement time expenditure	2 spectra (1 x IMVS, 1 x IMPS)	2 to 6 spectra (IMVS, IMPS, optionally EIS, optionally both under open cell voltage and under short circuit conditions)

The author draws the following conclusions from this:

Although the continuum model, in contrast to the Bay & West model, ignores the distributed nature of the dye solar cell and does not provide a conclusive explanation for the intensity dependence of τ_d and τ_l , the basic conclusion that the effectiveness of photoelectron forwarding in competition with loss can be derived from the time constants of the spectra is correct (cf. the introduction to chapter 5).

However, the author finds the common practice of extracting τ_d and τ_l from the geometric interpretation of the spectra without taking into account the fact that the time constants of other components or processes of the object are mixed into the spectra, such as the frequency response contribution of the counter electrode when measuring complete cells, to be questionable.

To determine the dynamic efficiency η_{dyn} , the data should instead be determined by fitting the IMPS and IMVS spectra using a model. If, for example, when testing many samples, it is only a matter of determining the numerical value of η_{dyn} and less a matter of understanding the underlying loss mechanisms, it is advisable to use the phenomenological model of the extended photocurrent source from section 5.2.1. Simplified in this way, the acquisition and evaluation of IMPS and IMVS spectra using a model can also be organized as an automated script with little effort.

More complex models, such as the Bay & West model, on the other hand, could be helpful in understanding and investigating the causes. In the author's opinion, this presupposes that the potential of joint measurement and analysis of EIS, IMPS and IMVS spectra in the same system state is used (cf. the introduction to Chapter 6).

The Bay & West model also stands out from the continuum model in that it offers the remarkable possibility of calculating a "transfer efficiency" for each system state along the DC load curve, which indicates the ratio of internal photocurrent (generation current determined by absorption and quantum efficiency) and externally measurable current (see also the end of section 8.7 in the appendix). This potential has not yet been utilized in the present work and will therefore be the subject of further research by the author.

7.3 Physical and dynamic measurements on tantalum oxide films

Oxide films on niobium, tantalum and aluminum are of great economic importance. In addition to the excellent stability and colorability of passivated aluminum, the use of oxide films as dielectrics in electrolytic capacitors is particularly in demand. The non-ideal dielectric behavior in this application limits the range of use of these materials in technology.

In the present work, tantalum oxide has been investigated as a model system for inhomogeneous dielectrics. In chapter 4.2 some aspects of such systems have already been dealt with from the point of view of impedance modeling. In the following, the experimental realization of a measurement campaign is discussed. Oxide films on tantalum were produced by anodic oxidation and investigated by means of combined physical, impedance and dynamic photocurrent measurements. The results are discussed.

7.3.1 Preparing the samples and setting up the electrochemical experiments

Square disks of 25x25x2 mm made of 99.9% pure tantalum were used for all measurements. The disks were mechanically polished down to a grain size of 2-4 μm with diamond paste. The appearance is then clear, reflective and under the microscope only a few grooves, but also a few small hole-like depressions are recognizable.

Immediately before assembly in the electrochemical cell and contact with the electrolyte, the oxide layer that formed spontaneously in the air was removed by briefly (approx. 10 s) swirling in 30% HF. A slightly longer treatment with HF already leads to a visible increase in the number of holes.

Aqueous phosphate buffer solution $\text{KH}_2\text{PO}_4 / \text{K}_2\text{HPO}_4$ with pH 7 was used as the electrolyte. A special photo-electrochemical cell "PECC" made it possible to mount the tantalum disk vertically as the end of a cylindrical electrolyte space. An O-ring limited the area wetted by the electrolyte to a diameter of 18 mm. On the opposite side, the electrolyte space could be exposed through a closing quartz window and through the ring-shaped counter electrode made of platinum wire. The thickness of the electrolyte space of 20 mm allowed the placement of a reference electrode made of Ag / AgCl in 3M-NaCl and holes to flush the cell with nitrogen. Details of the cell are shown in Figure 82.

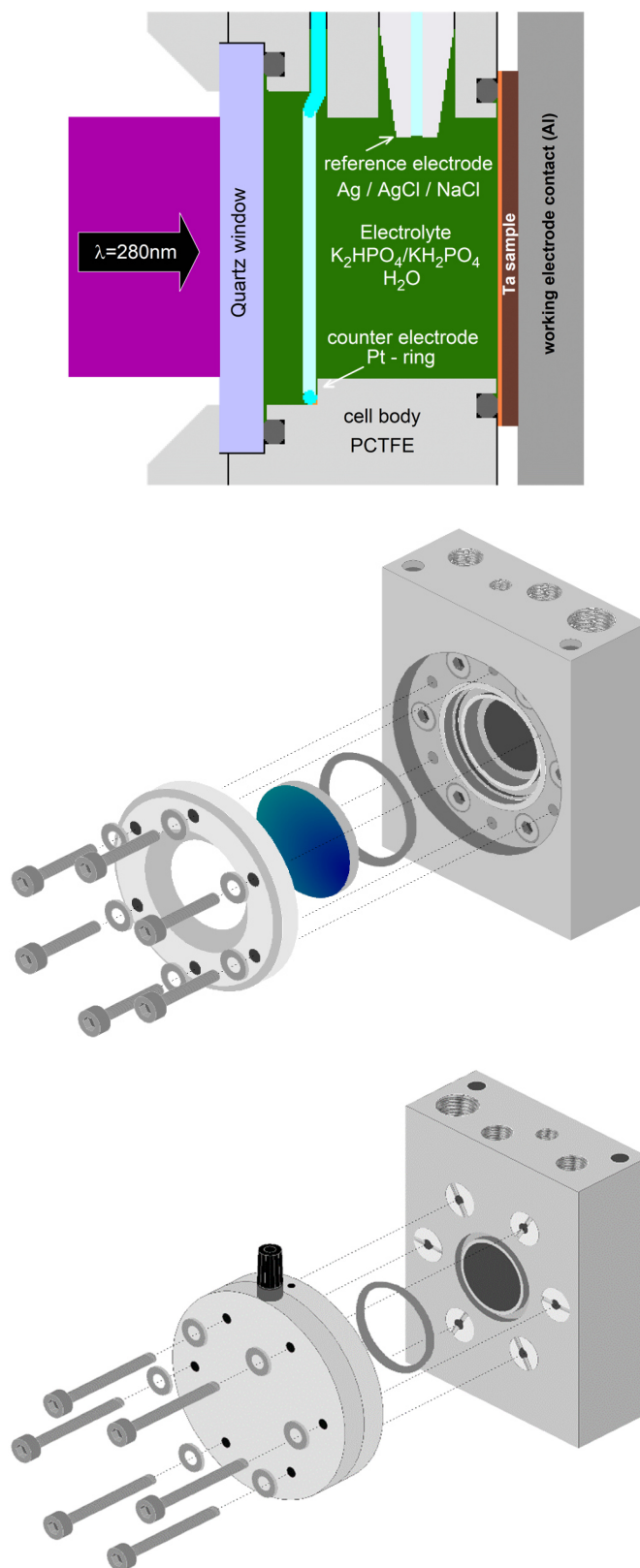


Figure 82: Photo-electrochemical cell "PECC". Sectional drawing of the electrolyte chamber (top) and exploded views of the light inlet side (center) and the back of the working electrode (bottom). The square tantalum working electrode is clamped between the O-ring and the Al back plate.

The photo-electrochemical measuring system used was the system developed by the author. The high polarization voltage required for the anodic oxidation of the samples was achieved, if necessary, by connecting a CVB120 buffer amplifier from the author's company upstream. The light source used was an array of nine 5 mm \varnothing LEDs with an aperture angle of around 15°, which was set up in such a way that a maximum light output of 7 W/m² was produced at the

light entry window of the PECC at a distance of 10 cm. The wavelength characteristic of the LED had a Gaussian distribution with a maximum emission at 280 nm and a half-width of about 10 nm. Due to the large band gap required for UV emission and the resulting high field strength in the crystal, UV LEDs age particularly quickly at maximum current. In order to be able to carry out the experiments with a set of these very expensive LEDs with uniform illumination, a reduced light output of 4 W/m² was usually adjusted.

To control the LED and to measure the transfer functions, the system described in section 7.1.2 and outlined in Figure 74 was used.

7.3.2 Electrochemical and photo-electrochemical measurement campaign on tantalum oxide film

The tantalum electrode was examined at various stages of electrochemical oxidation. The measurements began on the pristine electrode immediately after cleaning with HF and insertion into the PECC. This was followed by phases of anodic polarization with a gradual increase in potential until a forming voltage of 45 V was reached. During all anodization phases, the flowed charge was recorded. At the end of each phase, after the current had decayed from the beginning to less than 1%, the potential was slowly reduced and waited until the residual current had stabilized to less than 4 nA/cm².

At the beginning and after each new polarization phase, an impedance spectrum was first recorded without light exposure and the rest potential "DHP" was recorded in the dark. This was followed by exposure to 4 W/m² at 280 nm, an impedance spectrum under potentiostatic control at the DHP and a measurement of the dynamic photocurrent spectrum CIMPS. The (approximately stable) photocurrent at the end of the CIMPS measurement was automatically specified as the target current for setting the galvanostat for the final measurement of the dynamic photovoltage CIMVS. This allowed the potential to return to a value close to the DHP during the current-controlled phase. Accordingly, EIS measurement under exposure, CIMPS and CIMVS measurement were carried out as intended in almost the same system state of the electrode.

In order to investigate the influence of UV light on the stabilization of the oxide film, serial EIS measurements were also carried out on a freshly prepared electrode anodically oxidized to 45 V using different exposure intensities.

Impedance spectra were then recorded at this electrode over potentials between 45 V and -0.37 V.

7.3.3 Physical measurements on the tantalum oxide film

In the final state of the electrode after anodizing at 45 V, Mr. Steffen Berger at the LKO kindly contributed further physical measurements on the tantalum oxide film. These include scanning electron microscopy images "SEM", X-ray diffraction images "XRD" and X-ray atomic emission spectra "AES". The most informative way of investigating the postulated PIN structure of the tantalum oxide film was to determine the depth profile on the basis of AES in the argon plasma beam at an acceleration voltage of 3.5 KV and a current of 20 mA.

7.4 Discussion and evaluation of the measurement results on the tantalum oxide film

The total charge of 17.1 coulombs, which was applied to 2.54 cm² electrode surface in the first experiment (Figure 83) corresponds to 17.7 μmol Ta₂O₅. With a density of $\rho = 8.2 \text{ g/cm}^3$ and a molecular weight of 441.9 g/mol, this results in 7.82 mg of oxide in a volume of 954 μm³. This would correspond to an unrealistically large oxide film thickness of 3.76 μm. Using the impedance modeling shown below, the capacitance of the oxide film was found to be 859 nF. The literature data for the relative dielectric constant of Ta₂O₅ fluctuate around $\epsilon \approx 24-28$. With the mean value $\epsilon = 26$ and an ϵ_0 of $8.854 \cdot 10^{-12} \text{ As/Vm}$, an actual film thickness of around 70 nm is found if the oxide film is assumed to have an ϵ comparable to the bulk material. The AES depth profile measurement described below also provided a similar value of around 100 nm. This raised the question of the cause of the low charge yield. Two further charge balance control

experiments were therefore carried out under accelerated anodization but otherwise similar²⁴ experimental conditions. At around a third of the anodizing time of the initial experiment, only around 5.7 C was required, and at around a fifth of the anodizing time, more than 5.2 C charge was still required up to the final voltage of 45 V. Hydrogen developed at the counter electrode during anodization, which could theoretically reach the tantalum electrode in the PECC despite nitrogen purging. In order to minimize the influence of a possible H₂ reduction at the working electrode, a different reaction vessel with a graphite counter electrode separated by a frit was used for the fastest measurement.

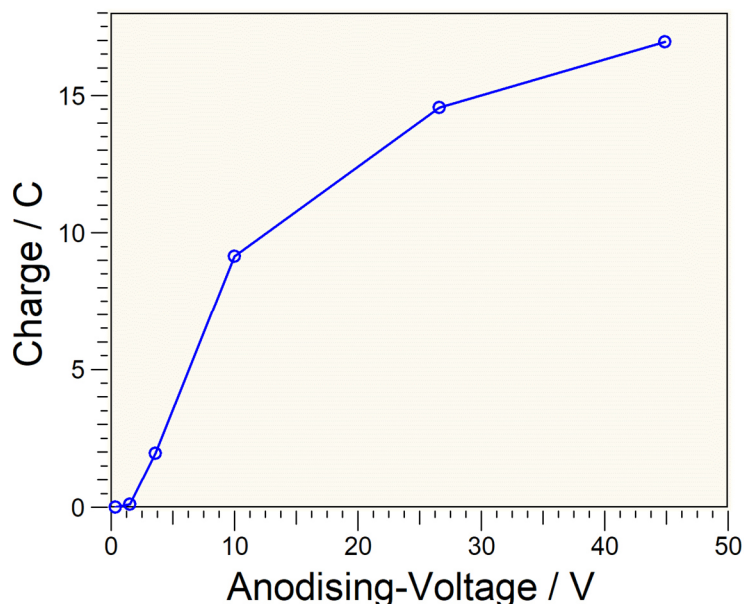


Figure 83: Charge balance during the anodic oxidation of the tantalum electrode of 2.54 cm² area with a polarization voltage curve over a longer period of time from 0 to 45 V.

Thermodynamically controlled, oxide formation on tantalum takes place at lower anodic overpotentials than oxygen evolution. However, the initially found charge yield of less than 2% indicates a kinetically strongly favored side reaction prior to oxide formation. Earlier experiments by D.A. Vermilyea [115] found a charge yield of almost 100%, albeit in an aqueous Na₂SO₄ solution with a different experimental control. At that time, galvanostatic polarization was carried out with about 8 mA/cm² for only about 5 minutes and a final voltage of more than 300 V was achieved. Vetter [116] justifies the high current yield with the electron conduction through the oxide layer, which is necessary for the competitive reaction $2 \text{H}_2\text{O} \rightarrow 4 \text{H}^+ + \text{O}_2 + 4 \text{e}^-$ and which is lacking in tantalum oxide. According to the author of the present work, the high current yield of the oxide formation in the historical experiment at high polarization is probably due to the strongly activation energy-dependent mobility of the tantalum ions. Thus, the ion current increases exponentially with the field strength via the defect hopping mechanism, while the electron current in the conduction band of the oxide only increases linearly. The series of experiments presented here with the lowest current yield was carried out over a period of many hours with much lower current densities and with long decay phases at low field strengths. The weak n-conduction described by many other authors, which decays over the layer thickness in the direction of the electrolyte, is thus favored relative to the Ta ion conduction. With little inhibition of the charge transfer reaction itself, this should allow moderate oxygen formation and could therefore be responsible for the poor current yield. The second competing reaction, the dissolution of the oxide in the electrolyte, appears to contribute little to the current loss. Further impedance measurements, not shown here, showed that the oxide layer thickness of the current-less electrode formed at 45 V in the electrolyte used did not change detectably within several days. To rule out any doubts, the electrolyte sample from the control experiment, in which a charge of 5.7 C was converted, was subjected to a quantitative analysis for tantalum. Given the electrolyte content of the PECC of approx. 6 ml, this amount of charge would correspond to a tantalum concentration of just under 1 mmol / l. However, less than 2 ppm / l

²⁴ The photo-electrochemical measurements on the holding potentials were omitted here.

was found, which meant that dissolution of the oxide in the phosphate-containing electrolyte could be ruled out as the cause of the low current yield.

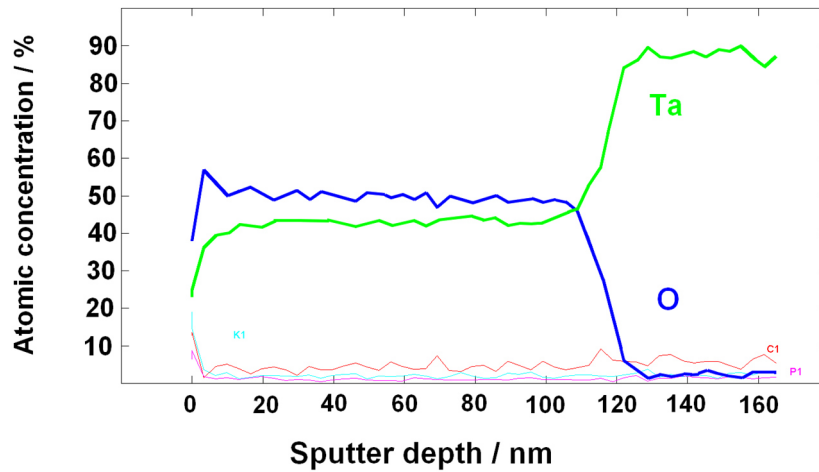


Figure 84: Depth profile of the element concentration distribution in the oxide film of the tantalum electrode anodically formed at 45 V. The AES measurement was carried out under argon sputtering at 3.5 KV acceleration voltage and 20 mA current. Calibration was performed with SiO₂ on a silicon wafer.

Figure 84 shows the depth profile of the sample anodized at 45 V as determined by AES. The layer thickness is determined at $\delta \approx 115$ nm. In the range between about 0.05δ below the oxide surface up to about 0.1δ in front of the metal electrode, an approximately stoichiometric composition of Ta₂O₅ results, with a slight increase in the O-Ta ratio towards the electrolyte. A clear excess of oxygen or metal can be seen between depth 0 to 0.05δ and depth $0.9-1 \delta$. This supports the assumption of a conductivity profile according to the PIN model with hole conduction to the electrolyte side, intrinsic conductivity in the oxide body and electron conduction in the area of the oxide directed towards the metal side.

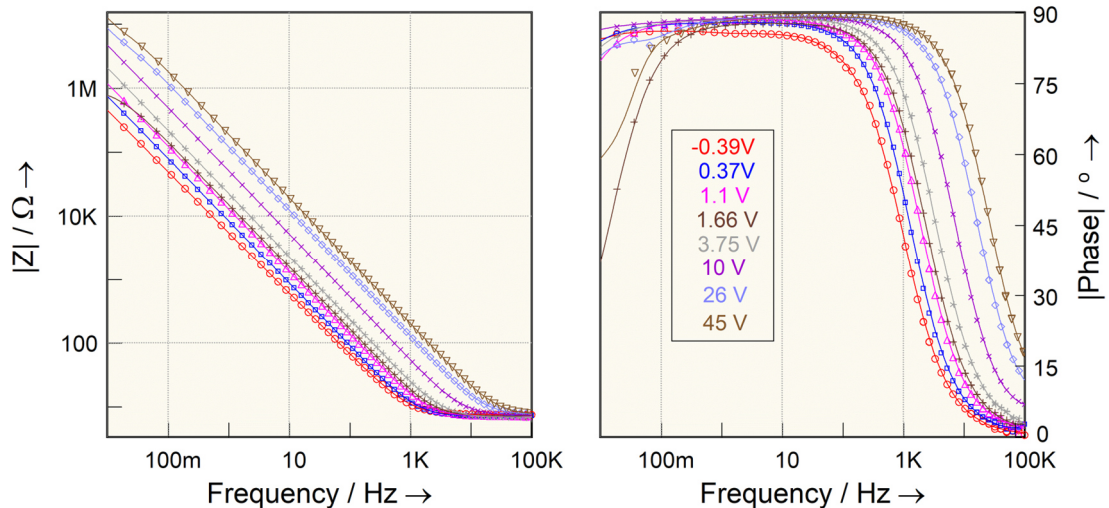


Figure 85: Impedance spectra series measured on the tantalum oxide electrode at different stages of anodic oxidation. The measurement at -0.39 V was carried out at the rest potential a few minutes after the freshly polished electrode etched in 30% HF was installed in the PECC. In the following measurements, the electrode was polarized at the specified holding potential until the current had decayed below 4 nA/cm^2 . The sample points show the measuring data, the solid curves the smoothed ones.

The courses in Figure 85 were measured at different stages of anodization after potentiostatic holding phase at the specified voltage without light exposure at the respective rest potential. The lower frequency measurement range was down to 3 mHz. Especially at higher forming voltages, reorganization processes still took place in the oxide film, which led to significant current fluctuations. The frequency range below 10 mHz was therefore so disturbed in some spectra that the lowest frequency sample points were not displayed.

The impedance modulus curves show the typical pattern of decreasing capacitance with increasing forming voltage and thus layer thickness. The phase angle diagram clearly shows that the quality of the film capacitance increases with increasing film thickness, as can be seen from the approach of the phase angle to the ideal value of -90° . This can be interpreted to mean that the relative proportion of the dielectric of stoichiometrically ideally composed, and therefore low conductive, oxide in the film increases. This interpretation is supported by the modeling described later using the PIN model.

The stabilization of the oxide layer could be forced by irradiation with UV light. For this purpose, an impedance spectra series was carried out on a sample formed at 45 V with an intensity decreasing from 4 W/m^2 to zero using 280 nm UV light. It is shown in Figure 86 shown. With an (almost) "ideal" photocurrent generator such as a photo diode, the exposure should have no noticeable influence on the impedance measured under short-circuit conditions.

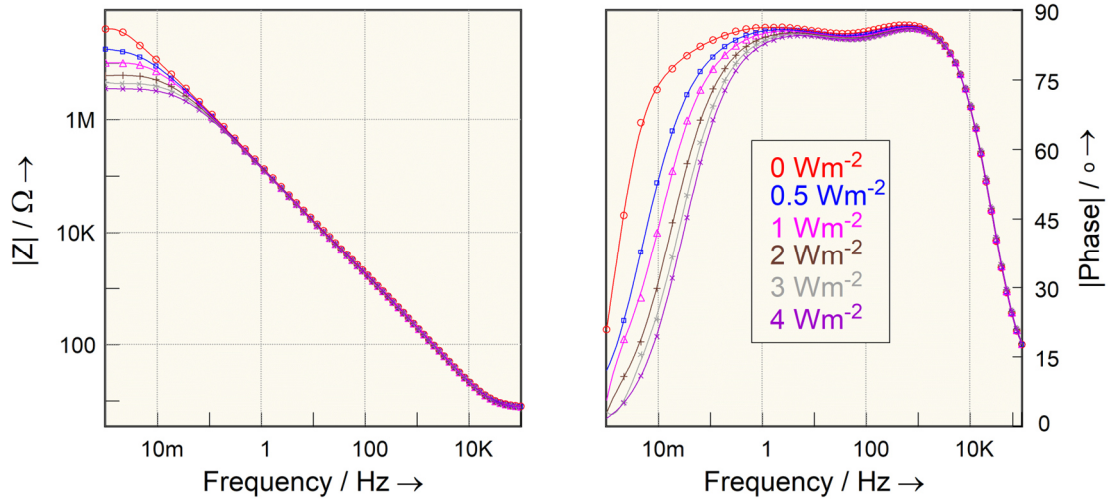


Figure 86: Impedance spectra series measured on the tantalum oxide electrode formed at 45 V with different UV exposure intensities. The sample points show the measurement data, the solid curves show the smoothed values.

From the significant decrease in impedance at low frequencies and higher light output on the system under investigation, it can therefore be concluded that a large proportion of the photoelectrons generated recombine inside the oxide. This process, which leads to photoconductivity, is presumably related to the "healing" of the oxide film under UV light. A long-term study of photocurrent activity under the influence of oxide film stabilization by UV light would have been desirable, but could no longer be carried out due to the increasing ageing of the light source.

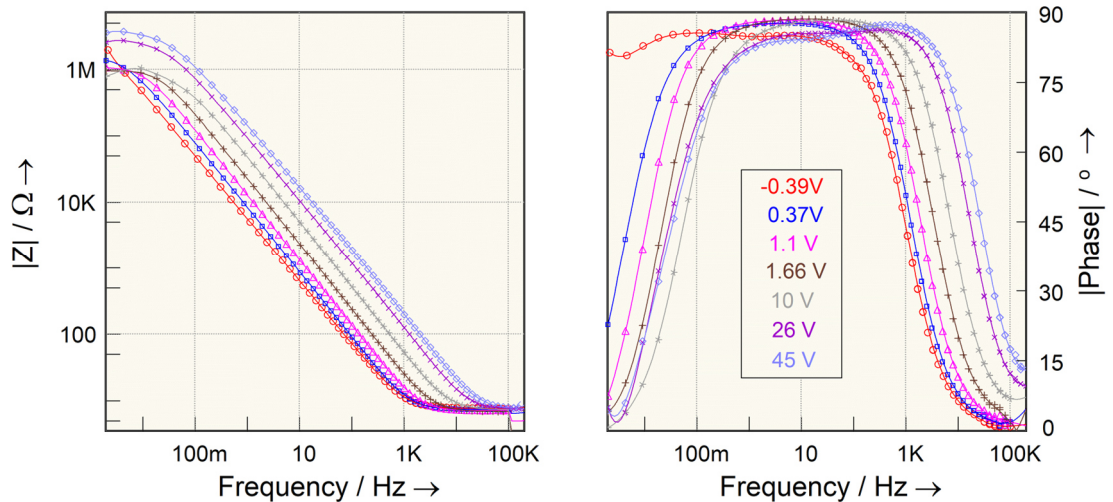


Figure 87: Impedance spectra series from the triplet measurement series of joint EIS, IMPS and IMVS measurements under UV illumination of 280 nm with 4 W / m². The tantalum oxide electrode was measured in various stages of anodic oxidation, in contrast to Figure 85 but under illumination. The measurement at +3.75 V forming voltage has been lost due to data loss. The sample points show the measuring data, the solid curves show the smoothed values.

Figure 87 shows the impedance result from the triplet measurement series of joint EIS, IMPS and IMVS measurements under light. In the spectrum of the pristine electrode (measured at the rest potential at -0.39 V), it is noticeable that there are no indications of larger internal recombination currents at the lower frequency end. This can be interpreted to mean that the spontaneously formed oxide film has fewer defects that could serve as recombination centers compared to the anodically formed film. If one compares the quality of the dielectric, estimated from the phase angle deviation of -90°, between the spectral series without light in Figure 85 and the one under irradiation in Figure 87 the irradiated electrode no longer shows the clear correlation of increasing dielectric quality with layer thickness. The supply of photoelectrons to the recombination centers, which occur more frequently in thicker layers, appears to reduce the quality.

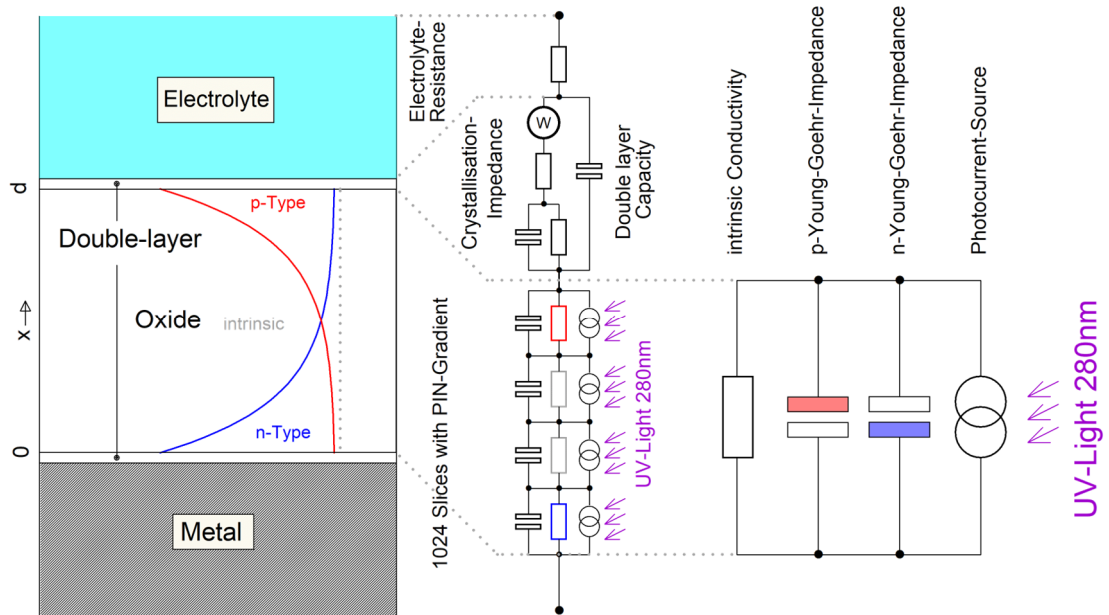


Figure 88: Physical model (left) and electrical equivalent circuit diagram (center iteratively algorithmic and right alternatively simplified mathematically closed) for the evaluation of the EIS, CIMPS and CIMVS measurements of the tantalum oxide electrode in different stages of anodic oxidation under UV illumination of 280 nm with $4 \text{ W} / \text{m}^2$.

Figure 88 outlines the model used to evaluate the triplet measurements. It is based on the model already described in section 4.2.1.4 about the impedance behavior of dielectrics with PIN conductivity distribution. The area of the oxide dielectric between the metal and the electrochemical double layer can be characterized by the area shown in Figure 88 bottom center as shown in chapter 4.1. The non-linear conductivity distribution is modeled by dividing it into thin slices with a homogeneous conductivity distribution. The calculation of a slice required to determine the impedance and photoelectric behavior must be run through about a thousand times in a program loop so that the calculation result is available with sufficient accuracy over the entire layer thickness of the oxide. With the joint fit of EIS, CIMPS and CIMVS measurements according to the TRIFIT principle, modeling based on iterative loops places high demands on the computing time. Tests have shown that, especially for small penetration depths of the p- and n-conductors into the dielectric compared to the proportion of intrinsic conductivity (i.e., thicker oxide), the values shown in Figure 88 on the right using two Young-Göhr impedances and an ohmic contribution provides a result that is hardly distinguishable from the result of the complex loop calculation. Therefore, this simplified but analytically closed model of the oxide film was used to evaluate the EIS, CIMPS and CIMVS measurements under the light of the differently oxidized tantalum electrodes.

In the upper part of Figure 88 the electrical equivalence model for the double-layer process is simplified at the electrolyte-oxide phase boundary.

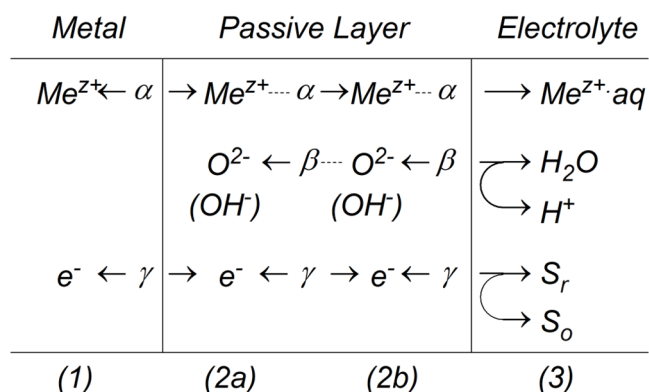


Figure 89: Phase diagram metal / passive layer / electrolyte with the various possible gross reactions according to K.J. Vetter [117]. The course of the redox reaction of the pair S_r - S_o in the path γ is dependent on electron conduction in the oxide, as is the case with oxygen evolution, for example.

The formation of new oxide probably takes place via the absorption of oxygen ions from the water [2] (path β in Figure 89), which diffuse with tantalum ions from the metal (path α in Figure 89) to form the oxide. Depending on the activation energy of the transition α -(1-2a) and β -(2b-3), both phase boundary layers can lead to relevant double layer impedance contributions²⁵. The total impedance is dominated by the surface layer component, especially for thicker layers. For this reason, these through-layer reactions, coupled with the diffusion of the ions through the oxide, are modeled in the circuit diagram in a simplified way by a single arrangement of a charge transfer resistance in series with a diffusion impedance ("W" in the circle symbol), which is similar to a Randles circuit diagram. In order to correctly represent the fine structure of the spectra, the simple Randles circuit was converted into a model of the crystallization impedance [8] model. This is taken into account by a parallel RC element appearing in series with the transfer impedance. The crystallization impedance describes the case in which the charge transfer reaction does not occur directly between the solid phase (with the defined activity of one) and the ion. The direct way can usually be assumed for simple metallic electrodes (1st type electrodes). Sometimes the atoms of the passing species must instead pass through a phase of less ordered intermediate state with concentration-dependent activity before they are incorporated into the crystal lattice in their final position. The introduction of crystallization impedance into the model is thus based on the assumption of reorganization processes in the freshly formed oxide.

²⁵ Whether a phase boundary is noticeable in the impedance depends essentially on whether a noticeable activation energy leads to a locally significantly reduced (effective, because possibly associated with a transfer reaction) conductivity. The (ubiquitous) capacitance of the medium then forms a time constant (possibly identifiable in the spectrum) together with the reduced conductivity of the phase transition.

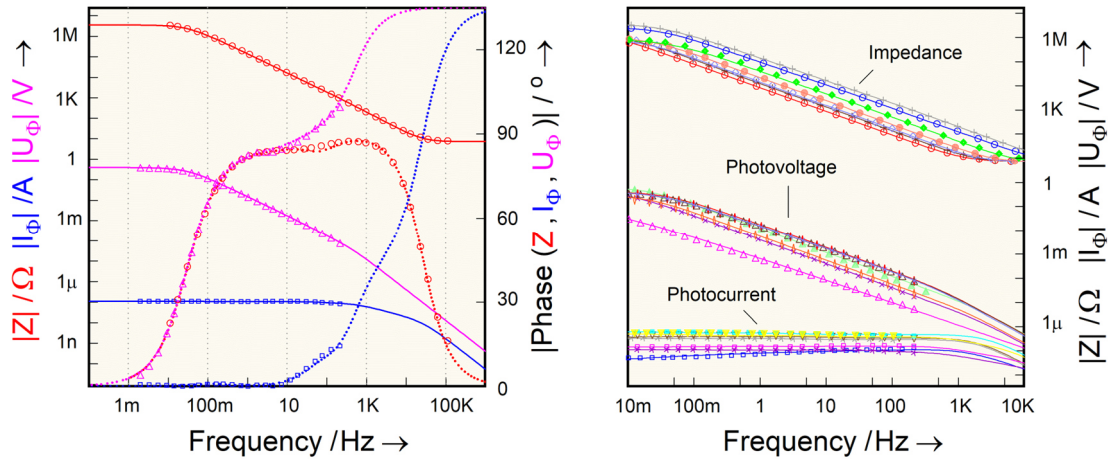


Figure 90: Bode diagram (left) of the EIS, CIMPS and CIMVS spectra measured together at the Ta electrode formed with 45V and fitted using the TRIFIT method. The symbols correspond to the experimental data, the solid curves (phase angles shown as dots) to the modeling with the help of the spectra shown in Figure 88 on the right. The fit results for all oxidation states are shown on the right in the Bode diagram of the modulus values.

From Figure 90 it can be seen that the Figure 88 can reproduce the measured curve of the three transfer functions at the oxide with the greatest layer thickness well. The overall curve of the fit result shown in the Figure on the right is also in good agreement with the model. The diagrams below were created by evaluating the parameter tables of the model created by the Fit process.

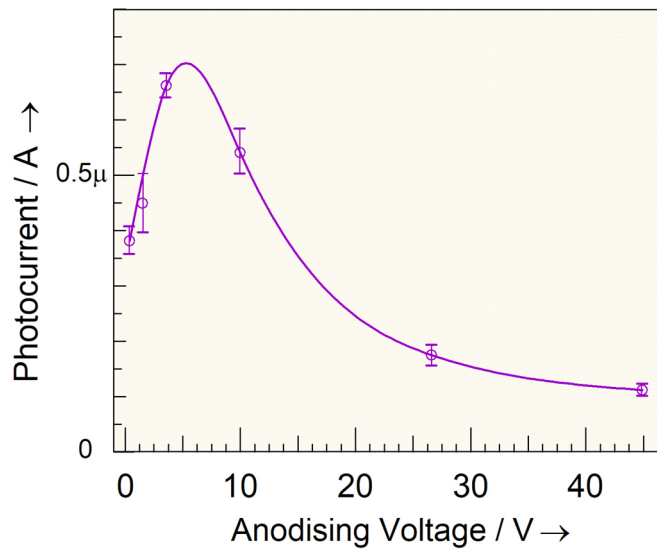


Figure 91: Photocurrent as a function of the forming voltage of the tantalum oxide electrode. The data values were obtained by serial evaluation of the EIS, CIMPS and CIMVS measurements optimized with the TRIFIT method. The parameter uncertainty (error bars) was calculated using the method described in section 3.1.2.

In Figure 91 the intrinsic photocurrent determined from the PIN model is plotted against the forming voltage. The initial photocurrent passes through a maximum at a forming voltage of around 5 V, which corresponds to a film thickness of around 12 nm. It decreases steadily with increasing thickness. The curve can be explained by the competition between increasing photon absorption with greater film thickness on the one hand and the increase in recombination probability on the other.

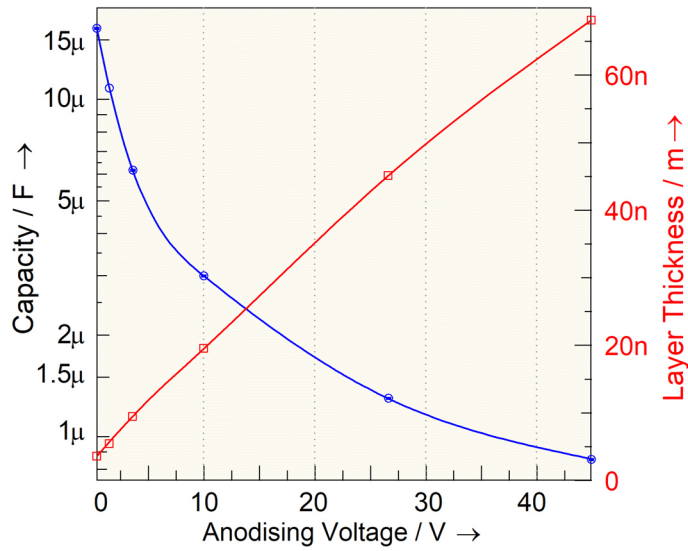


Figure 92: Course of the PIN capacitance (blue) of the oxide film on tantalum, obtained by serial evaluation of the EIS, CIMPS and CIMVS measurements optimized with the TRIFIT method. The calculated film thickness is shown in red. The parameter uncertainty for the capacitance, determined using the method described in section 3.1.2 was on average better than 0.7% (1.3% max.). The error bars were therefore not included in the layer thickness curve.

Figure 92 shows the course of the layer capacitance of the oxide film determined with the aid of the PIN model over the forming voltage. Also shown in the graph is the film thickness calculated from this, assuming a dielectric constant for Ta_2O_5 of $\epsilon \approx 26$. The relationship between forming voltage and oxide film thickness appears to be approximately linear at around 1.5 nm/V and is therefore close to the value calculated by L. Young [114] of 1.62 nm/V.

8 Appendix

8.1 List of frequently used formula symbols

a	Dependency between system parameters
A	Amplitude perturbation
α	Exponent of the "constant phase element"
α	Symmetry coefficient of the Butler-Volmer charge transfer reaction
\tilde{c}_o	Periodic modulation of the concentration of a species in front of the electrode
C	Capacity [Farad]
C	Concentration [mol/l]
C_{dl}	Double layer capacity [Farad]
C_{YG}	Dielectric capacitance in the Young-Göhr model [Farad]
D	Diffusion coefficient
D_w	Diffusion impedance parameter ("Warburg" parameter) [$\Omega \cdot s^{-1/2}$]
$\Delta\omega$	Frequency bandwidth [Hz]
δ	Relative penetration depth, relative location [1]
e	Base of the natural logarithm, 2.71828182845904
e_0	Elementary charge, $1.602\,176\,487 \cdot 10^{-19}$ [C]
$e^{j\omega t}$	Periodicity factor
E_{EE}	Redox potential, electrode potential [V, eV]
E_f	Excitation function
E_F	Fermi level [V, eV]
E_i	Physical system property
E_r	Response function
Err	Standard, normalized deviation between experimental sample points and model
ϵ_0	Dielectric constant of the vacuum, $8.854 \cdot 10^{-12}$ As/Vm
$\epsilon(x)$	Location-dependent, relative dielectric constant
$\tilde{\epsilon}$	Periodic modulation of the potential [V]
η	Efficiency of a photoelectric effect
η_{dyn}	Dynamic efficiency $1 - \tau_d / \tau_l$ of the photoelectric effect of a DSSC
f	Function
f	Frequency [Hz]
f_g	Cut-off frequency [Hz]
ϕ	Phase shift
G	Fitting error gradient in the direction of a parameter variation
G	Voltage divider ratio [1]
γ	Proportionality factor in the ZHIT relationship
Γ	Gamma function $\Gamma(s) = (s-1)!$
H	Transfer function, diction according to ZHIT proof
H^*	Dynamic transfer function, diction according to ZHIT proof
$ H $	Transfer function modulus, diction according to ZHIT proof
I	Electric current [A]
\tilde{I}	Periodic modulation of the current [A]
I_F	Charge transfer current ("Faraday current") [A]
$\text{Im}\{\}$	Imaginary component of a complex variable
I_P	Photocurrent [A]
j	Imaginary unit
k	Reaction rate constant [s^{-1}], Boltzmann constant, $1.3806488 \cdot 10^{-23}$ [J/K], $8.617332478 \cdot 10^{-5}$ [eV/K]
n	Count
n_b	Donor concentration or count
v	Frequency response $\partial/\partial\omega$
ω	Circular frequency [Hz $\cdot 2\pi$]
ω_{IMPS}	Cut-off frequency of the photocurrent under short-circuit conditions [Hz $\cdot 2\pi$]

ω_{IMVS}	Cut-off frequency of the open photocell voltage [Hz 2π]
P	Electrical power [W]
P	Light intensity [$W m^{-1}$]
P	Physical parameter
PV	Principal value integral labeling, "Principal Value"
π	Pi, 3.14156...
Q	Charge [Coulomb]
\underline{Q}	Loss capacity [Farad] ^{α}
R	Electrical resistance [Ω]
R_{ct}	Charge transfer resistance [Ω]
R_{diff}	Differential resistance [Ω]
R_{el}	Electrolyte resistance [Ω]
R_{η}	Charge transfer resistance (diction according to H. Göhr) [Ω]
R_{HF}	High-frequency limit resistance [Ω]
$Re\{\}$	Real component of a complex variable
R_p	Polarization resistance of an electrochemical transfer reaction
s	Operator $j\omega$
S	Physical system
S	Significance of a physical parameter in a model
$\sigma(x)$	Location-dependent conductivity [Ω^{-1}]
t	Time [s]
T	Absolute temperature [K]
TC	Temperature coefficient $\partial/\partial T$
τ	State lifetime [s]
τ	RC time constant [s]
τ_d	Charge carrier diffusion time constant [s]
τ_l	Charge carrier lifetime [s]
τ_n	Recombination time constant, charge carrier lifetime [s]
τ_{θ}	Thermal time constant [s]
$\tilde{\theta}$	Periodic modulation of the degree of coverage of an adsorbed species in front of the electrode [1]
U	Electrical voltage [V]
U_p	Photo voltage [V]
VC	Interaction coefficient between mediating variable and impedance [1]
x	Normalized location $x = X/d$, $0 \leq x \leq 1$
z	Charge number, number of elementary charges
Z^*	Complex impedance [Ω]
Z_c	Diffusion impedance (diction according to H. Göhr) [Ω]
Z_F	Faraday impedance (impedance of the electrochemical transfer reaction) [Ω]
Z_e	Face impedance in the homogeneous pore system according to H. Göhr [Ω]
Z_{EC}	Electrochemically active interfacial impedance in the photoelectric pore system according to Bay & West [Ωm^{-1}]
Z_m	Pore bottom impedance in the homogeneous pore system according to H. Göhr [Ω]
Z_q	Electrochemically active interfacial impedance in the homogeneous pore system [Ω]
Z_{θ}	Adsorption (coverage) impedance [Ω]

8.2 List of frequently used abbreviations

AC	Alternating current
AC-DC-AC method	Coating test by impedance measurement in combination with stress by DC polarization
AES	X-ray atomic emission spectrum, depth profile measurement in the argon plasma beam
CE	Counter electrode connection "Counter Electrode"
CIMPS	"Controlled Intensity Modulated Photo Spectroscopy"
CNLS	"Complex Non-linear Least Squares" Fit method
CPE	"Constant Phase Element"
DC	Direct current
DFT	Discrete Fourier transform
DHP	Rest potential in the dark
EIS	Electrochemical impedance spectroscopy
ESB	Equivalent circuit diagram, electrical model
FF	Fill factor $P_{max}/(U_{max} \cdot I_{max})$ of a solar cell
FRA	Frequency response analyzer
IMPS	Intensity-modulated photo spectroscopy in general, especially the dynamic transfer function between light intensity and current
IMVS	Dynamic transfer function between light intensity and voltage
IPCE	"Incident Photon Count Efficiency"
KKT	Kramers-Kronig transform
LED	"Light Emitting Diode"
LFS	Limited frequency selectivity
LHIT	Logarithmic Hilbert transform
LKK	Linear Kramers-Kronig transform
LKO	Chair of Corrosion and Surface Technology at the Institute of Materials Science IV at the University of Erlangen-Nuremberg
MOS	"Monochromatic Oversampling Method"
NTC	"Negative temperature coefficient"
OSC	Polymer solar cell "Organic Solar Cell"
PECC	Photo-electrochemical cell
PEM, PEFC	Polymer Electrolyte Membrane / Polymer Electrolyte Fuel Cell
PIN	Layer of p-, intrinsic- and n-conductive material
RC link	Combination of resistance and capacitance
PTC	"Positive temperature coefficient"
RCL measuring bridge	Measuring device for determining resistance, capacitance and inductance using the bridge method
RE	Reference electrode connection "Reference Electrode"
SEM	Scanning electron microscopy
SHE	Standard hydrogen reference electrode
SIM	Program for the simulation and analysis of dynamic transfer functions such as impedance spectra
S/N	Signal to noise ratio
SOFC	Solid Oxide Fuel Cell
TCO	"Transparent Conducting Oxide", e.g., on glass
TF	Transfer function
TFA	Dynamic transfer function analysis
TRIFIT	Triple transfer function fit algorithm
UV LED	Ultra Violet Light Emitting Diode
WE	Working electrode connection
WHA	Weighted Harmonics Autocorrelation
XRD	X-ray diffraction
YG	Dielectric with conductivity gradient according to L. Young & H. Göhr
ZHIT	Two-pole Hilbert transform

8.3 Linear Kramers-Kronig transform via FFT and IFFT in the s- plane

The Kramers-Konig transformation from real part to imaginary part of a causal transfer

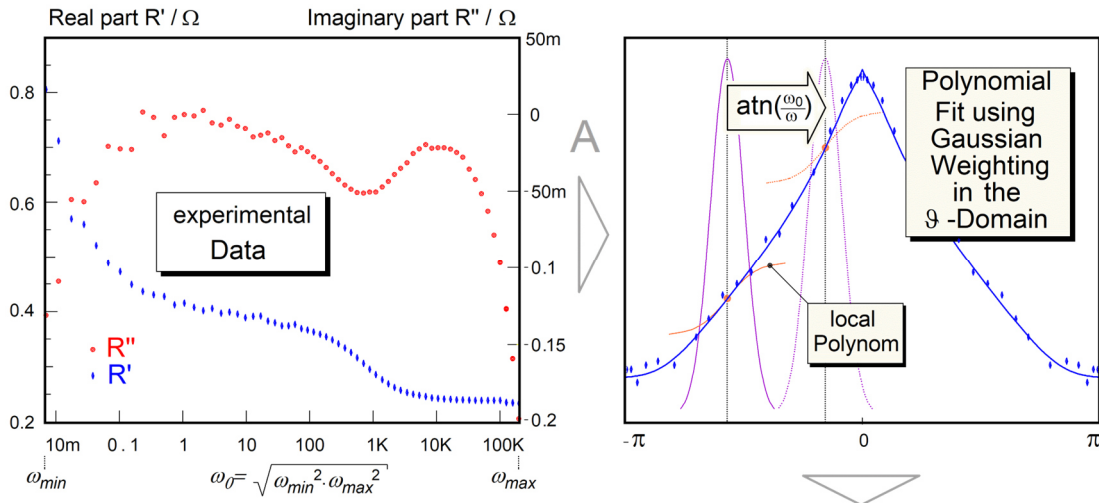
$$\text{Im}\{H(\omega_0)\} = \frac{2}{\pi} \omega_0 PV \int_0^{\infty} \frac{\text{Re}\{H(\omega)\}}{\omega^2 - \omega_0^2} d\omega$$

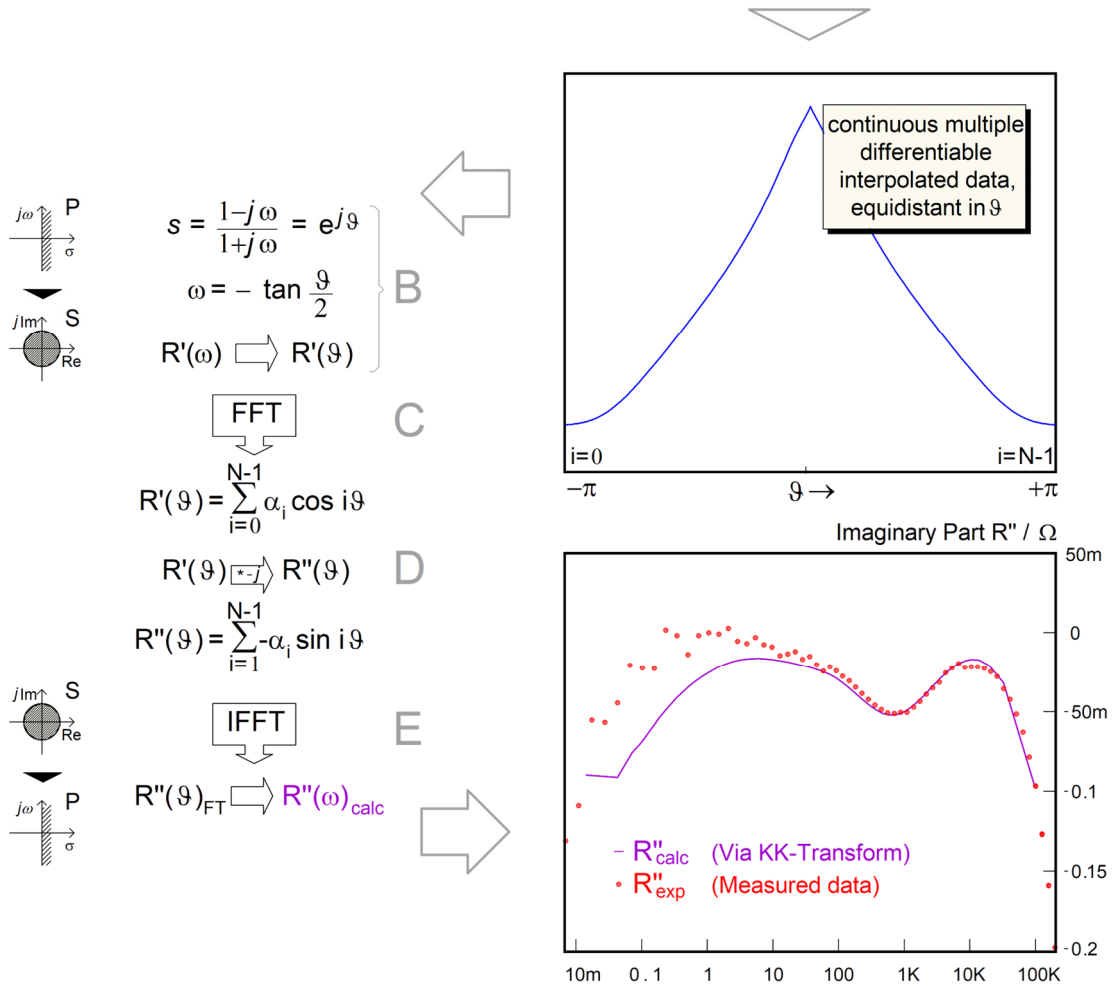
function can be performed by avoiding the numerical integration around the pole at $\omega = \omega_0$ according to [66] as shown below:

First (step A), $N = 2^n$ angular support points \mathcal{G} ($N = 2048$ is selected in the program) are calculated according to the measured frequency interval from ω_{min} to ω_{max} around the center frequency $\omega_0 = \sqrt{\omega_{min}^2 \cdot \omega_{max}^2}$ in accordance with $-\pi < \mathcal{G} < +\pi$.

The corresponding frequencies $\omega(\mathcal{G}) = \omega_0 \cdot \tan\left(\frac{\mathcal{G}}{2}\right)$ are used according to the procedure

described in section 3.1.2.2, $2^n - 2$ impedance sample points are calculated by interpolation. The real part curve $R'(\mathcal{G})$ is used to calculate the curve $R'(\omega)$ (step B). This corresponds to a Laplace transform from the P- to the S-plane. The interpolation points for $\mathcal{G} = -\pi$ and $\mathcal{G} = \pi$ are set to zero. In this way, no explicit extrapolation of the experimental data for $\omega = 0$ and $\omega = \infty$ is necessary.





Using the FFT (step C), the curve $R'(\vartheta)$ is discretely Fourier-transformed and the transformed $DFT(R'(\vartheta))$ is conjugated (i.e. the negative real part is transferred to the imaginary part, step D).

The conjugate curve $\text{conj}(DFT(R'(\vartheta)))$ is then discretely transformed back again using the inverse FFT (step E). The result is the KK transform $R''(\vartheta)_{calc}$ and thus also $R''(\omega)_{calc}$.

8.4 Examples of the user-defined calculation of an impedance element

The SIM simulation program naturally supports the basic impedance elements (resistance, capacitance, etc.) as well as many other specific electrochemical elements (such as various diffusion impedances, porous electrodes, etc.). In order to enable the user to integrate definitions and algorithms developed by himself into the simulation and fitting, a special compiler for so-called USER elements is included with the SIM, which translates the ASCII source text of a definition and mathematical description and integrates it into the program. The description is in a programming language based on the widely used "Basic" language. To ensure that the complex mathematics frequently required for impedance calculations can be programmed in a compact way, all calculation types and functions are supported in the complex number space in addition to integer and real.

For integration, the source text must be available in the editor of the program package as ASCII text. Once the translation has been completed, the extended SIM can be permanently saved as a program.

The following examples show some of the special impedance element definitions used in the work. In order to make the source text recognizable, a different character set is used in the following. Comments in the source text are highlighted in green and enclosed in '-characters. Keywords appear in red and data transferred in the source text appears in blue. Blank lines and characters are permitted outside of keywords and data.

The definition begins with a number that specifies the number of parameters describing the impedance element.

The next line contains the name to be managed by the SIM for the element, first in a language of your choice (here German), then, separated by a comma, in English.

This is followed by the definition block for the descriptive parameters (also bilingual). These are queried during input at runtime with the name specified here by SIM and (also during the run of the automatic fit routines) compared with the minimum and maximum permissible values specified in the same line.

Separated by a slash, you can define the physical units to be used at runtime. In order to be able to manage complicated names that contain superscripts and special characters in the ASCII text, it is possible to display character strings introduced by the \$ character in hexadecimal form.

The number of parameter definition lines must match the number of parameters specified above. The mathematical definition block is introduced with the keyword "formula". It begins after the keyword "local" with the names of the program variables of the parameters describing the impedance element, whereby the order of the variable names correlates with the order of the parameter names specified above them. To create additional auxiliary variables, e.g., for saving intermediate results, the local list can be extended accordingly. In the first example below, the name of the first descriptive parameter is "Voltage", the unit is "V" and the real variable used for this in the program text has the symbolic name "U". The variables s& and v& (defined as complex using the & terminator) are created for intermediate results.

The impedance calculation via a USER element is always performed individually for a specific frequency transmitted by SIM. It is implicitly included in the calculation as the reciprocal of the angular frequency ω with the reserved global variable "T". At the end of the impedance calculation, the complex numerical value of the impedance is returned to SIM as an output value using the "frend" function.

8.4.1 Source code of the Landes-Hahn temperature relaxation impedance

7 'parameter count'

Hahn-Impedanz, Hahn's impedance 'Element Name, element name'

```
Spannung/V, voltage/V, -100, 100 'parameter
Name/Einheit, name/unit, min, max'
Strom/A, current/A, -100, 100
Abklinglaenge/m, decline length/m, 1e-9, 1
Flaeche/m^2, area/$4d023202, 1e-12, 1
Waermeleitung/W, therm.conductivity/$774d022d31026b022d3102, 1e-12, 1e12
Waermekapazitaet/J, therm.capacity/$6a6b022d31024d022d3202, 1e-12, 1e12
TK/VK^-1, TC/$766b022d3102, -1, 1
```

```
formula: local U, I, d, a, Lambda, h, TC, s&, v&
s&=csqr(cmplx(0, h/T/Lambda)) 'T: global variable 1/2πf'
v&=ctanh(d*s&)/(2*a*Lambda*s&)*TC
s&=Z&:ZG&=0
fnend(s&-v&*U)/(1-v&*I) 'complex impedance result'
```

8.4.2 Source code of the 1st order temperature relaxation impedance

3 'parameter count'

```
TC-Impedanz, Thermal impedance
Rhf/Ohm, Rhf/Ohm, -1e39, 1e39
Zeitkonstante/s, timeconstant/s, 1e-12, 1e12
TK/ , TC/ , -1e9, 1e9
```

```
formula: local Rhf, Th, TC, s&, v&
v&=TC/cmplx(1, Th/T)
fnend(Rhf+v&*Rhf)/(1-v&)
```

8.4.3 Source code of the general relaxation impedance

2 'parameter count'

```
Relaxations-Impedanz, relaxation impedance
Rnf/Ohm, Rnf/Ohm, 0, 1e39
Zeitkonstante/s, timeconstant/s, 1e-12, 1e12
```

```
formula: local Rnf, Th, s&, v&
v&=1/cmplx(1, Th/T)
s&=ZG&:ZG&=0
fnend(s&+v&*Rnf)/(1+v&)
```

8.5 Derivation of the general relaxation impedance

The following derivation was formulated by F. Richter. The basic ideas on relaxation impedance were developed by H. Göhr and published in 1986 together with C. A. Schiller [103]. The occurrence of the relaxation impedance is based on the following idea:

A kinetically effective parameter T has the value \bar{T} in the steady state. \bar{T} is influenced by another parameter P and for small deviations ΔP the following applies according to a Taylor expansion

$$\bar{T} = \bar{T}_0 + \frac{d\bar{T}}{d\bar{P}} \Delta P, \text{ with } \bar{P}_0 = \bar{T}(\Delta P = 0) \text{ and } \bar{P} \text{ as the stationary value of } P. \quad (95)$$

A time-varying value T_t at time t can also be formulated using a small deviation ΔT :

$$T_t = \bar{T}_0 + \Delta T \quad (96)$$

This gives you

$$T_t - \bar{T} = \Delta T - \frac{d\bar{T}}{d\bar{P}} \Delta P. \quad (97)$$

For the relaxation of the parameter T , a first-order time law with the relaxation time constant τ applies for sufficiently small deviations:

$$-\frac{dT_t}{dt} = \frac{1}{\tau} \cdot (T_t - \bar{T}) = \frac{1}{\tau} \cdot \left(\Delta T - \frac{d\bar{T}}{d\bar{P}} \Delta P \right) \quad (98)$$

The restoring force according to Eq. 98(4), the deviation from the *current* steady-state value is decisive, as the associated steady-state value \bar{T} also changes with a different parameter P . It is plausible that a "correction" $\frac{d\bar{T}}{d\bar{P}} \Delta P$ must be applied for this.

The following therefore applies to small periodic deviations $\Delta T, \Delta P$ ²⁶

$$j\omega \Delta T = \frac{1}{\tau} \cdot \left(\Delta T - \frac{d\bar{T}}{d\bar{P}} \Delta P \right). \quad (99)$$

In Example I and Example II below, T can be modeled as a temperature or a rate constant. With "direct" coupling, the parameter P can be the current I or the voltage U itself. With "indirect" coupling, P must depend on U, I or both variables through a mediating process (e.g., via the mediating variable "temperature" as a function of the power $P = U \cdot I$ so that the phenomenon of relaxation impedance occurs.

Example I: Indirect coupling to U and I .

Here, the comparatively complicated but more general approach is dealt with using the example of temperature relaxation in the energy-open system. T then stands for the temperature and P for the electrical power introduced into the system $P = U \cdot I$.

It applies to $P = P(U, I)$:

$$\Delta P = \left(\frac{\partial P}{\partial I} \right)_U \cdot \Delta I + \left(\frac{\partial P}{\partial U} \right)_I \cdot \Delta U. \quad (100)$$

²⁶ In the following part of this derivation, the index t and the overlines at T and P are not used to indicate stationary values.

In the case of temperature relaxation, the partial differential quotients are simply determined by the thermally effective voltage

$$U_T = \left(\frac{\partial P}{\partial I} \right)_U \quad (101)$$

or by the direct current

$$I = \left(\frac{\partial P}{\partial U} \right)_I \quad (102)$$

to replace them. However, they should be retained in order to be able to use the derivation for other physical variables such as temperature and power. From Eq. 99 and 100 follows

$$j\omega\Delta T = -\frac{1}{\tau} \cdot \Delta T + \frac{1}{\tau} \cdot \left(\frac{\partial P}{\partial I} \right)_U \cdot \left(\frac{dT}{dP} \right) \cdot \Delta I + \frac{1}{\tau} \cdot \left(\frac{\partial P}{\partial U} \right)_I \cdot \left(\frac{dT}{dP} \right) \cdot \Delta U \quad (103)$$

and thus

$$\Delta T = \frac{\left(\frac{\partial P}{\partial I} \right)_U \cdot \left(\frac{dT}{dP} \right) \cdot \Delta I + \left(\frac{\partial P}{\partial U} \right)_I \cdot \left(\frac{dT}{dP} \right) \cdot \Delta U}{1 + j\omega\tau} \quad (104)$$

With the current I as the dependent variable (potentiostatic case), the following applies for $I = I(U, T)$

$$\Delta I = \left(\frac{\partial I}{\partial U} \right)_T \cdot \Delta U + \left(\frac{\partial I}{\partial T} \right)_U \cdot \Delta T \quad (105)$$

and using the abbreviations from Eq. 106

$$R = \left(\frac{\partial U}{\partial I} \right)_T \text{ and } \nu = \frac{1}{1 + j\omega\tau} \quad (106)$$

from Eq. 104 for the relaxation impedance Z_R

$$Z_R = \frac{\Delta U}{\Delta I} = \frac{R - R \cdot \left(\frac{\partial P}{\partial I} \right)_U \cdot \left(\frac{\partial I}{\partial T} \right)_U \cdot \left(\frac{dT}{dP} \right) \cdot \nu}{1 + R \cdot \left(\frac{\partial P}{\partial U} \right)_I \cdot \left(\frac{\partial I}{\partial T} \right)_U \cdot \left(\frac{dT}{dP} \right) \cdot \nu} \quad (107)$$

If the voltage U is set as the dependent variable (galvanostatic case) analogous to Eq. 105 then instead of Eq. 107 for the relaxation impedance Z_R follows

$$Z_R = \frac{\Delta U}{\Delta I} = \frac{R + R \cdot \left(\frac{\partial P}{\partial I} \right)_U \cdot \left(\frac{\partial U}{\partial T} \right)_I \cdot \left(\frac{dT}{dP} \right) \cdot \nu}{1 - \left(\frac{\partial P}{\partial U} \right)_I \cdot \left(\frac{\partial U}{\partial T} \right)_I \cdot \left(\frac{dT}{dP} \right) \cdot \nu} \quad (108)$$

The equations 107 and 108 can be converted into one another using the implicit derivative $\left(\frac{\partial U}{\partial T} \right)_I$ of the function $I = I(U, T) = \text{const.}$ (stationarity condition).

The following applies to the conversion of Eq. 108 into Eq. 107

$$\left(\frac{\partial U}{\partial T}\right)_I = -\frac{\left(\frac{\partial I}{\partial T}\right)_U}{\left(\frac{\partial I}{\partial U}\right)_T} = \left(\frac{\partial I}{\partial T}\right)_U \cdot R. \quad (109)$$

Depending on the experimental conditions (potentiostatic or galvanostatic), formula 107 or 108 can be used.

In abbreviated form, instead of Eq. 108 using the dimensionless number T_C

$$T_C = \left(\frac{\partial P}{\partial U}\right)_I \cdot \left(\frac{\partial U}{\partial T}\right)_I \cdot \left(\frac{dT}{dP}\right) = I \cdot \left(\frac{\partial U}{\partial T}\right)_I \cdot \left(\frac{dT}{dP}\right) \quad (110)$$

write

$$Z_R = \frac{R + U_T \cdot \left(\frac{\partial U}{\partial T}\right)_I \cdot \left(\frac{dT}{dP}\right) \cdot \nu}{1 - \left(\frac{\partial P}{\partial U}\right)_I \cdot \left(\frac{\partial U}{\partial T}\right)_I \cdot \left(\frac{dT}{dP}\right) \cdot \nu} = \frac{R + U_T \cdot \frac{T_C}{I} \cdot \nu}{1 - T_C \cdot \nu}. \quad (111)$$

With Eq. 106, $R = \left(\frac{\partial U}{\partial I}\right)_T = U_T / I$ follows

$$Z_R = \frac{R + R \cdot T_C \cdot \nu}{1 - T_C \cdot \nu}. \quad (112)$$

The relationship 112 was tested experimentally in the present study (section 4.3.2).

Case II: Direct coupling to the voltage U .

Case II can be regarded as a simplification of case I. The parameter T is here only a function of the voltage U , so that in Eq. 98 the voltage U is directly effective as parameter P and thus P can be replaced by U . Relationship 97 thus takes the form

$$\Delta T = \frac{dT}{dU} \cdot \Delta U \quad (113)$$

Due to $\left(\frac{\partial P}{\partial U}\right)_I = 1$ and $\left(\frac{\partial P}{\partial I}\right)_U \cdot \left(\frac{\partial I}{\partial T}\right)_U \cdot \left(\frac{dT}{dP}\right) = 0$, Eq. 107 as the current dependence

$\left(\frac{\partial I}{\partial T}\right)_U$ disappears. With $P \equiv U$ instead of Eq. 107 for Z_R

$$Z_R = \frac{R}{1 + R \cdot \left(\frac{\partial I}{\partial T}\right)_U \cdot \left(\frac{\partial T}{\partial P}\right) \cdot \nu}. \quad (114)$$

If the parameter T is interpreted, for example, as the rate constant k of an electrochemical transfer reaction, the result for Z_R is

$$Z_R = \frac{R}{1 + R \cdot \left(\frac{\partial I}{\partial k}\right)_U \cdot \left(\frac{dk}{dU}\right) \cdot \nu} = \frac{R}{\frac{1}{R} + \left(\frac{\partial I}{\partial k}\right)_U \cdot \left(\frac{dk}{dU}\right) \cdot \nu}. \quad (115)$$

Eq. 115 corresponds to that in chapter 4.3.1 discussed by H. Göhr and C. A. Schiller [103], which can be derived from the general case I, as shown here.

8.6 The equivalence between the impedance of a porous electrode according to L. Bay and K. West and according to H. Göhr

Impedance formula according to H. Göhr, Eq. 45:

$$Z = Z_{||} + Z^* \cdot \frac{1 + 2p \cdot s \left(\sqrt{1 - T^2} - 1 \right) + T(p^2 q_m + s^2 q_e)}{T(1 + q_e q_m) + q_e + q_m}$$

Neglecting the end face impedance $Z_{e \rightarrow \infty}$ and the impedance of the pore base $Z_{m \rightarrow \infty}$ simplifies Eq. 45:

$$\begin{aligned} Z &= Z_{||} + Z^* \cdot \frac{1 + 2p \cdot s \left(\sqrt{1 - T^2} - 1 \right)}{T} \\ &= Z_{||} + Z^* \cdot \coth(v) + \frac{Z^* \cdot 2p \cdot s \left(\sqrt{1 - T^2} - 1 \right)}{T} \end{aligned} \quad (116)$$

Impedance formula according to Bay & West Eq. 8 [38]:

(R_e, R_i here means specific resistances ρ , according to the definition equation $R = \rho \cdot l / q$).

$$Z_{EC} = (R_e + R_i) \cdot l \cdot \frac{\coth(\alpha \cdot l)}{\alpha \cdot l} + \frac{R_e \cdot R_i}{R_e + R_i} \cdot l \cdot \left(1 - \frac{\tanh(\alpha \cdot l / 2)}{\alpha \cdot l / 2} \right) \quad (117)$$

Shorten l in the 1st summand:

$$Z_{EC} = \frac{R_e + R_i}{\alpha} \coth(\alpha \cdot l) + \frac{R_e \cdot R_i}{R_e + R_i} \cdot l \cdot \left(1 - \frac{\tanh(\alpha \cdot l / 2)}{\alpha \cdot l / 2} \right) \quad (118)$$

Inserting $\alpha = \sqrt{(R_e + R_i) / Z_s}$ into the 1st summand and multiplying out the 2nd summand results in a sum of the terms 1 to 3

$$\begin{aligned} Z_{EC} &= \\ &\sqrt{(R_e + R_i)} \cdot \sqrt{Z_s} \cdot \coth(\alpha \cdot l) && \text{Term 1} \\ &+ \frac{R_e \cdot R_i}{R_e + R_i} \cdot l && \text{Term 2} \\ &- \frac{R_e \cdot R_i}{R_e + R_i} \cdot \frac{2}{\alpha} \tanh(\alpha \cdot l / 2) && \text{Term 3} \end{aligned}$$

Conversion of the specific impedances [$\Omega \cdot \text{cm}^{-1}$] into [Ω] by multiplying by the parameter l and the relationships

$$Z_s^G = R_e \cdot l \quad (Z_s^G \text{ to Göhr and } Z_s \text{ to Bay \& West have different meanings!})$$

$$Z_p^G = R_i \cdot l$$

$$Z_q^G = Z_s / l$$

$$\nu^G = \sqrt{(Z_s^G + Z_p^G) / Z_q^G} = \alpha \cdot l \quad (119)$$

converts term 1 and term 2 to the notation of H. Göhr (indicated by the superscript G).

In principle, the variables obtained in this way using the above relationships are Z_s^G, Z_p^G, Z_q^G according to the definition equation

$$R \cdot q = \rho \cdot l \quad (120)$$

"area resistances" $R \cdot q$. For the "area impedances", $Z^G = Z$ (measured) $\cdot q$ (area). However, this is only important for the conversion or direct comparison of the values of L. Bay with those of H. Göhr. In the practical coding in the calculation program, the quantities Z_s^G, Z_p^G, Z_q^G and ν^G can also be understood without restrictions as non-specific quantities with the dimension [Ω] or as dimensionless (ν^G).

It applies to term 1 and term 2:

$$\text{Term1} = (Z_s^G + Z_p^G)^{1/2} \cdot (Z_q^G)^{1/2} \cdot \coth(\nu^G) = Z^* \cdot \coth(\nu^G) \quad (121)$$

$$\text{Term2} = \frac{Z_s^G \cdot Z_p^G}{Z_s^G + Z_p^G} = Z_{II}^G \quad (122)$$

Insert $\alpha = \sqrt{(R_e + R_i) / Z_s}$ into term3:

$$\begin{aligned} \text{Term3} &= -2 \frac{R_e \cdot R_i}{R_e + R_i} \cdot \frac{Z_s^{1/2}}{(R_e + R_i)^{1/2}} \tanh\left(\frac{l}{2} \left(\frac{R_e + R_i}{Z_s}\right)^{1/2}\right) \\ &= -2 \frac{R_e \cdot R_i}{(R_e + R_i)^2} (R_e + R_i)^{1/2} Z_s^{1/2} \tanh\left(\frac{l}{2} \left(\frac{R_e + R_i}{Z_s}\right)^{1/2}\right) \\ &= -2 \frac{R_e}{(R_e + R_i)} \frac{R_i}{(R_e + R_i)} (R_e + R_i)^{1/2} Z_s^{1/2} \tanh\left(\frac{l}{2} \left(\frac{R_e + R_i}{Z_s}\right)^{1/2}\right) \end{aligned}$$

Conversion of the specific impedances [$\Omega \cdot \text{cm}^{-1}$] into [Ω] by multiplying by l brings term 3 into the notation of H. Göhr with the abbreviation

$$p \cdot s = \frac{Z_p^G \cdot Z_s^G}{(Z_p^G + Z_s^G)^2}$$

This gives you the following for term 3:

$$\text{Term3} = -2p \cdot s \cdot (Z_s^G + Z_p^G)^{1/2} (Z_q^G)^{1/2} \tanh\left(\frac{1}{2} \left(\frac{Z_s^G + Z_p^G}{Z_q^G}\right)^{1/2}\right)$$

Insert further abbreviation according to H. Göhr after Eq. 119 and $T = \tanh(\nu^G)$ results:

$$Term3 = (Z_s^G + Z_p^G)^{1/2} \cdot (Z_q^G)^{1/2} \cdot 2p \cdot s \cdot \tanh\left(\frac{\nu^G}{2}\right).$$

With the angle theorems $\cosh(x) = \frac{1}{\sqrt{1 - \tanh(x)^2}}$ and $\tanh\left(\frac{x}{2}\right) = \frac{\cosh(x) - 1}{\sinh(x)}$ you get for term 3

$$Term3 = \sqrt{(Z_p^G + Z_s^G) \cdot Z_q} \cdot 2p \cdot s \cdot \frac{(\sqrt{(1 - T^2)} - 1)}{T}. \quad (123)$$

With the abbreviation Eq. 46, $Z^* = \sqrt{(Z_p^G + Z_s^G) \cdot Z_q}$, the sum of term 2 (Eq. 122), term 1 (Eq. 121), and term 3 (Eq. 123) the simplified Eq. 45 is found (like Eq. 116 without the contribution of the top and bottom impedances):

$$Z = Z_{||} + Z^* \cdot \coth(\nu) + \frac{Z^* \cdot 2p \cdot s (\sqrt{(1 - T^2)} - 1)}{T}$$

The impedance formulas are therefore physically equivalent.

8.7 Conversion of the specific photoelectric transfer function according to L. Bay and K. West for non-specific quantities with elimination of linearly dependent, redundant parameters

According to L. Bay and K. West [38], the following applies to the dynamic photovoltage

$$V_p = -Z_p :$$

$$Z_p(R_i, R_e) = \frac{B \cdot A \cdot R_i}{A^2 - \alpha^2} \left(e^{-A \cdot l} \left[1 + \frac{A}{\alpha} \coth(\alpha \cdot l) \right] - \frac{A}{\alpha \sinh(\alpha \cdot l)} \right) + \frac{B \cdot A \cdot R_e}{A^2 - \alpha^2} \left(\left[1 - \frac{A}{\alpha} \coth(\alpha \cdot l) \right] + \frac{A \cdot e^{-A \cdot l}}{\alpha \sinh(\alpha \cdot l)} \right)$$

The variables R_i , R_e , α and l have the values described in the previous section 8.6 above. The absorption coefficient A and the quantum yield B are added. The product $A \cdot l$ is abbreviated as C .

By introducing the variables from H. Göhr, section 8.6, $Z_s^G = R_e \cdot l$, $Z_p^G = R_i \cdot l$, $Z_q^G = Z_s / l$ and

$$\nu = \sqrt{(Z_s^G + Z_p^G) / Z_q^G} = \alpha \cdot l :$$

$$\frac{B \cdot A \cdot R_i}{A^2 - \alpha^2} = \frac{B \cdot Z_p^G}{A \cdot l - \alpha^2 \cdot l / A} = \frac{B \cdot Z_p^G}{C - \frac{\nu^2 \cdot l}{l^2 \cdot A}} = \frac{B \cdot Z_p^G}{C - \nu^2 / C}$$

and finally, in the Göhr spelling

$$Z_p = \frac{B \cdot Z_p^G}{C - \nu^2 / C} \cdot \left(\exp(-C) \cdot \left[1 + \frac{C}{\nu} \cdot \coth(\nu) \right] - \frac{C}{\nu} \cdot \frac{1}{\sinh(\nu)} \right) + \frac{B \cdot Z_p^G}{C - \nu^2 / C} \cdot \left(\left[1 - \frac{C}{\nu} \cdot \frac{\exp(-C)}{\sinh(\nu)} \right] \right)$$

(In both formulas above, ν can be read as ν^G , the superscript has been omitted for technical reasons)

with the 5 parameters Z_s^G , Z_p^G , ν^G , C and B . In the program, instead of ν^G , the parameter from Eq. 119 the electrochemical interfacial impedance to be calculated from Eq. 124 is used:

$$Z_q^G = \frac{Z_p^G + Z_s^G}{(\nu^G)^2} \quad (124)$$

For the application of the Göhr parameters of the porous electrode Z_s^G , Z_p^G , ν^G , the same applies as described in section 8.6 with regard to their use as non-specific quantities.

For the different types of lighting SE illumination and EE illumination (see page 619 of the original paper [38]), Z_s^G and Z_p^G must be interchanged in the last formula for Z_p . The derivation was given for the SE illumination. It still contains the non-integrally defined quantity $C = A \cdot l$. This can be replaced by the integral photoelectric current \bar{i}_p .

(Starting point are Eqs. 4 and 5 of the original paper [38]) The derivation of the integral photoelectric current \bar{i}_p is given below.

Derivation of the integral photoelectric current \bar{i}_p :

$$\bar{i}_p = \int_{x=0}^{x=l} i_0 \cdot B \cdot A \cdot \exp(-A \cdot x) \cdot dx$$

$$\bar{i}_p = i_0 \cdot B \cdot A \cdot \int_{x=0}^{x=l} \exp(-A \cdot x) \cdot dx$$

(Note: i_0 = light intensity according to the diction of Bay & West !)

$$\begin{aligned} \int \exp(-A \cdot x) dx &= -\frac{1}{A} \cdot \exp(-A \cdot x) + IC \quad (\text{with } IC = \text{integration constant}) \\ &= -i_0 \cdot B \cdot A \cdot \exp(-A \cdot x) + IC \end{aligned}$$

$$\bar{i}_p = -i_0 \cdot B \cdot A \cdot \exp(-A \cdot l) + i_0 \cdot B \cdot A = i_0 \cdot B \cdot (1 - \exp(-A \cdot l)) \quad (125)$$

The result for C is obtained:

$$C = A \cdot l = \ln \frac{i_0 \cdot B}{i_0 \cdot B - \bar{i}_p}$$

From the simulation and fit of impedance and photoelectric spectra (section 6.2) using the model according to L. Bay & K. West, B and C can be determined.

With the help of Eq. 125 it is possible to compare the photocurrent \bar{i}_p generated inside the solar cell with a current i_{outer} flowing in the external circuit and to calculate a transfer efficiency

$$\eta_{transfer} = i_{outer} / \bar{i}_p$$

9 Bibliography

- [1] H. Göhr, *Über Beiträge einzelner Elektrodenprozesse zur Impedanz*, Ber. Bunsenges. Phys. Chem. 85 (1981) 274-280.
- [2] P. Schmuki, M.J. Graham, *Corrosion, Encyclopedia of Chemical Physics and Physical Chemistry, Volume III: Applications*, Eds. J.H. Moore, N.D. Spencer, Institute of Physics Publishing, Bristol and Philadelphia (2001) 2415-2436.
- [3] M. Stern, A. L. Geary, *Electrochemical Polarization: I. A Theoretical Analysis of the Shape of Polarization Curves*, J. Electrochem. Soc. 104 (1957) 56-63.
- [4] R. Grauer, P. R. Moreland, G. Pini, *A Literature Review of Polarization Resistance Constant (B) Values for the Measurement of Corrosion Rate*, Publication No. 52405, NACE, Houston (1982).
- [5] F. Mansfeld, *The polarization resistance technique for measuring corrosion currents*, Advances in Corrosion Science and Technology, M. G. Fontana and R. W. Stachle eds., Plenum Press, New York (1976) 163-262.
- [6] I. Epelboin, C. Gabrielli, M. Keddam, *Non-steady state techniques*, in *Comprehensive Treatise of Electrochemistry*, Vol. 9, Plenum Press, New York (1984) 62.
- [7] W. J. Lorenz, F. Mansfeld, *Determination of corrosion rates by electrochemical DC and AC methods*, Corros. Sci. 21 (1981) 647-672.
- [8] H. Gerischer, K. J. Vetter, *Elektrodenpolarisation bei Überlagerung von Wechselstrom und Gleichstrom*, Z. phys. Chem. 197 (1951) 92.
- [9] W. Schmickler, *Grundlagen der Elektrochemie*, Verlag Vieweg, Wiesbaden, Deutschland (1996) 86-91, ISBN 3-540-67045-9.
- [10] R. de Levie, *On porous electrodes in electrolyte solutions, Capacitance effects*, Electrochim. Acta 8 (1963) 751-780.
- [11] K. Mund, G. Richter, F. v. Sturm, *Titanium-Containing Raney Nickel Catalyst for Hydrogen Electrodes in Alkaline Fuel Cell Systems*, J. Electrochem. Soc. 124, 1 (1977) 1-6.
- [12] M. Edeling, K. Mund, W. Naschwitz, *Impedance measurements on inert porous electrodes*, Siemens Forschungs- und Entwicklungsberichte Bd. 12 (1983) 85.
- [13] H. Göhr, J. Söllner, H. Weinzierl, *Kinetic Properties of Smooth and Porous Lead/Lead Sulfate Electrodes*, Extended Abstracts, 34. I.S.E. Meeting (1983) Poster 0715.
- [14] A. Hahn, H. Landes, *Investigations into the Kinetics of SOFC Cathodes*, Proc. Of 5th Int. Symp. On SOFC, Electrochem. Soc., Vol. 97-40 (1997).
- [15] K. J. Euler, *Die Verteilung der Stromdichte über die Dicke von ebenen porösen Gas-Elektroden in elektrochemischen Stromquellen*, Ann. D. Physik, 7. Folge, Bd. 26, Heft 4 (1971) 257.
- [16] K. Mund, *Impedanzmessungen an porösen gestützten Raney-Nickel-Elektroden für alkalische Brennstoffzellen*, Siemens Forschungs- und Entwicklungsberichte Bd. 4 (1975) 68.
- [17] H. Göhr, *Impedance Modelling of Porous Electrodes*, Electrochemical Applications, ZAHNER-elektrik, 1, 7-9 (1997), https://zahner.de/media-files/support_downloads/files/ea1997.pdf.
- [18] A. Hahn, *Analyse und Optimierung von Zirkoniumoxid-Lanthan-Manganit-Mischgefügen als Kathode in Hochtemperatur-Brennstoffzellen (SOFC)*, Dissertation Techn. Fak. der Univ. Erlangen-Nürnberg (1998).
- [19] F. Richter, persönliche Mitteilung (1997).
- [20] G. Paasch, P. H. Nguyen, *Impedance of Inhomogeneous Porous Electrodes*, Electrochemical Applications, ZAHNER-elektrik, 1, 7-9 (1997), https://zahner.de/media-files/support_downloads/files/ea1997.pdf.

- [21] N. Wagner, "Electrochemical Power Sources – Fuel Cells" in *Impedance Spectroscopy: Theory, Experiment, and Applications*, 2nd Edition, Edited by Evgenij Barsoukov and J. Ross Macdonald, John Wiley & Sons, Inc. (2005) 497-537, ISBN: 0-471-64749-7.
- [22] I. D. Raistrick, *Impedance Studies of Porous Electrodes*, *Electrochim. Acta*, 35 (1990) 1579.
- [23] F. Richter, *Impedance Measurements under High Current for Development and Quality Control of Solid Oxide Fuel Cells (SOFC)*, *Electrochemical Applications*, ZAHNER-elektrik, 1 (1997) 3-7, https://zahner.de/media-files/support_downloads/files/ea1997.pdf.
- [24] C. A. Schiller, *Basics and Applications*, Kronach Impedance Days 2011 at Kloster Banz, Vortrag und Skript (2011). ZAHNER-elektrik, www.zahner.de/downloads/pdf/Basics_And_Applications.pdf.
- [25] S. Glunz, Fraunhofer ISE, Freiburg, Vortrag (2011), Quellenangabe: EPIA, Global Market Outlook for Photovoltaics until 2015.
- [26] McEvoy, T. Markvart, L. Castaner, *Practical Handbook of Photovoltaics: Fundamentals and Applications*, 2nd edition, Academic Press, 13.10 (2011), ISBN 978-0-12-385934-1.
- [27] Q. Wang, J.-E. Moser, M. Grätzel, *Electrochemical Impedance Spectroscopic Analysis of Dye-Sensitized Solar Cells*, *J. Phys. Chem. B* 109 (2005) 14945-14953.
- [28] J. Krüger, R. Plass, M. Grätzel, P. J. Cameron, L. M. Peter, *Charge Transport and Back Reaction in Solid-State Dye-Sensitized Solar Cells: A Study Using Intensity-Modulated Photovoltage and Photocurrent Spectroscopy*, *J. Phys. Chem. B* 107 (2003) 7536-7539.
- [29] J. Bisquert, V.S. Vikhrenko, *Interpretations of the Time Constants Measured by Kinetic Techniques in Nanostructured Semiconductor Electrodes and Dye-Sensitized Solar Cells*, *J. Phys. Chem. B* 108 (2004) 2313-2322.
- [30] L.M. Peter, N.W. Duffy, R.L. Wang, K.G.U. Wijayanta, *Transport and interfacial transfer of electrons in dye-sensitized nanocrystalline solar cells*, *J. Electroanal. Chem.*, 524-525 (2002) 127-136.
- [31] T. Oekermann, T. Yoshida, H. Minoura, K.G.U. Wijayanta, L.M. Peter, *Electron Transport and Back Reaction in Electrochemically Self-Assembled Nanoporous ZnO/Dye Hybrid Films*, *J. Phys. Chem. B* 108 (2004) 8364-8370.
- [32] J. O. Schuhmacher, W. Wuttling, *Device Physics of Solar Cells, Photoconversion of Solar Energy*, edited by M. Archer, Imperial College Press, London (2001), ISBN 1-86094-161-3.
- [33] M. Di Giulio, S. Galassini, G. Micocci, A. Tepore, C. Manfredotti, *Determination of minority-carrier lifetime in silicon solar cells from laser-transient photovoltaic effect*, *J. Appl. Phys.* 52 (1981) 7219.
- [34] B. O'Regan, M. Grätzel, *A low-cost, high-efficiency solar cell based on dye-sensitized colloidal TiO₂ films*, *Nature* 353 (1991) 737-740.
- [35] M. Grätzel, K. Brooks, A. J. McEvoy, *Dye-sensitized nanocrystalline semiconductor photovoltaic devices*, *Adv. Sci. Technol.* 24 (1999) 577-584.
- [36] M. Grätzel, *Perspectives for dye-sensitized nanocrystalline solar cells*, *Prog. Photovoltaic Res. Applic.* 8 (2000) 171-185.
- [37] A. Hagfeldt, M. Grätzel, *Molecular Photovoltaics*, *Acc. Chem. Res.*, 33 (5), (2000) pp 269–277.
- [38] L. Bay, K. West, *An equivalent circuit approach to the modelling of the dynamics of dye sensitized solar cells*, *Solar Energy materials and Solar Cells*, 87 (2005) 613.
- [39] P. Schmuki, A. Ghicov, S. Berger, C. A. Schiller, M. Multerer, *EIS- and Controlled Intensity Dynamic Photo-Electrochemical Measurements on TiO₂-Nanotube Photo-Anodes for Dye Sensitized Solar Cells and an Alternative Model for the Data Interpretation*, Session B7, Lecture 734, 216th ECS meeting, Wien, (2009).
- [40] A. Ghicov, S. P. Albu, R. Hahn, D. Kim, T. Stergiopoulos, J. Kunze, C. A. Schiller, P. Falaras, P. Schmuki *TiO₂ Nanotubes in Dye-Sensitized Solar Cells: Critical Factors for the Conversion Efficiency*, *Chem. Asian J.*, 4 (2009) 520-525.

- [41] C. A. Schiller, M. Multerer, W. Strunz; *Characterization of solar cells by means of improved frequency resolved techniques – CIMPS*, ZAHNER-elektrik (2009), https://zahner.de/media-files/support_downloads/files/poster_zahner_ecs_2009.pdf.
- [42] R. Beranek, H. Hildebrand, P. Schmuki, *Self-organized porous titanium oxide prepared in H₂SO₄ / HF electrolytes*, *Electrochem. Sol. State Lett.* 6 (3), B12 (2003).
- [43] J. M. Macak, K. Sirotna, P. Schmuki, *Self-organized porous titanium oxide prepared in Na₂SO₄ / NaF electrolytes*, *Electrochim. Acta* 50 (18), (2005) 3679.
- [44] J. M. Macak, H. Tsuchiya, L. Taveira, S. Aldabergenova, P. Schmuki, *Smooth anodic TiO₂ nanotubes*, *Angew. Chem. Int. Ed.* 44 (45), (2005) 7463.
- [45] J. M. Macak, H. Tsuchiya, A. Ghicov, K. Yasuda, R. Hahn, S. Bauer, P. Schmuki, *TiO₂ nanotubes: Self-organized electrochemical formation, properties and applications*, *Curr. Op. Sol. State Mater. Sci.* 11 (1-2), (2007) 3.
- [46] A. Ghicov, P. Schmuki, *Self-ordering electrochemistry: a review on growth and functionality of TiO₂ nanotubes and other self-aligned MO_x structures*, *Chem. Commun.* 20 (2009) 2791.
- [47] S. Berger, *Selbstorganisierte nanostrukturierte anodische Oxidschichten auf Titan und TiAl-Legierungen: Morphologie, Wachstum und Dünnschichtanodisation*, Dissertation, Erlangen (2009).
- [48] J. M. Macak, H. Tsuchiya, P. Schmuki, *High-aspect-ratio TiO₂ nanotubes by anodisation of titanium*, *Angew. Chem. Int. Ed.* 44 (14), (2005) 2100.
- [49] P. Barquinha, L. Pereira, H. Aguas, E. Fortunato, R. Martins, *Influence of the deposition conditions on the properties of titanium oxide produced by r.f. magnetron sputtering*, *Mater. Sci. Semicond. Process.* 7 (4–6), (2004) 243–247.
- [50] Jin Young Kim, Dong-Wan Kim, Hyun Suk Jung, Kug Sun Hong, *Influence of Anatase–Rutile Phase Transformation on Dielectric Properties of Sol–Gel Derived TiO₂ Thin Films*, *Jpn. J. Appl. Phys.* 44 (2005) 6148-6151.
- [51] A. Ghicov, H. Tsuchiya, R. Hahn, J.M. Macak, A. G. Muñoz and P. Schmuki, *TiO₂ nanotubes: H⁺ insertion and strong electrochromic effects*, *Electrochemistry Communications* 8 (4), (2006) 528-532
- [52] I. Paramasivam, S. Singh, M. Moll, C. Hauser, K. Meyer, P. Schmuki, *Photocatalysis vs. anodic - breakdown catalysis on TiO₂ layers*, *Electrochimica Acta* 2010, doi:10.1016/j.electacta.2011.12.113.
- [53] F. Cardon, W. P. Gomes, *On the determination of the flat-band potential of a semiconductor in contact with a metal or an electrolyte from the Mott-Schottky plot*, *J. Phys. D: Appl. Phys.* 11 (1978).
- [54] A. J. Bard and L. R. Faulkner, *Electrochemical Methods*, Chap. 14, Wiley (1980).
- [55] P. Schmuki, H. Böhni and J. A. Bardwell, *In Situ Characterization of Anodic Silicon Oxide Films by AC Impedance Measurements*, *Electrochem. Soc.*, Volume 142, 5 (1995) 1705-1712.
- [56] A. Le Mehaute, *Transfer Processes in Fractal Media*, *J. Statistical Physics* 36, 665-667.
- [57] A. Le Mehaute, *Fractal electrodes and constant phase angle response*, *Electrochim. Acta* 34, 4 (1989) 591–592.
- [58] W. H. Mulder, J. H. Sluyters, *The admittance of smooth electrodes with a fractal carpet structure*, *Electroanal. Chem. Interfacial*, 282, 1–2 (1991) 27–32.
- [59] F. La Mantia, H. Habazaki, M. Santamaria, F. Di. Quarto, *Use of Mott-Schottky Plots to Characterise the Amorphous Passive Film/Electrolyte Junction*, Lecture, 8. International Symposium on Electrochemical Impedance Spectroscopy, Portugal (2010).
- [60] T. Pajkossy, D. M. Kolb, *Anion-adsorption-related frequency-dependent double layer capacitance of the platinum-group metals in the double layer region*, *Electrochim. Acta* 53 (2008) 7403-7409.
- [61] T. Pajkossy, D. M. Kolb, *The interfacial capacitance of Rh(111) in HCl solutions*, *Electrochim. Acta* 54 (2009) 3594–3599.

- [62] U. Rammelt, S. Bischoff, M. El-Dessouki, R. Schulze, W. Plieth, L. Dunsch, *Semiconducting properties of polypyrrole films in aqueous solution*, J. Solid State Electrochem. 3 (1999) 406.
- [63] A. Fikus, U. Rammelt, W. Plieth, *Characterization of semiconductor properties of polybithiophene film electrodes in contact with aqueous electrolytes. A combination of electrochemical impedance spectroscopy and photocurrent measurements*, Electrochim. Acta 44 (1999) 2025-2035.
- [64] U. Rammelt, N. Hebestreit, A. Fikus, W. Plieth, *Investigation of polybithiophene: n-TiO₂ bilayers by electrochemical impedance spectroscopy and photoelectrochemistry*, Electrochim. Acta. 46 (2001) 2363-2371.
- [65] CPE-Kritik an Mehaute, Diskussionen auf dem EIS-meeting, Portugal (2010).
- [66] R. Unbehauen, *Systemtheorie*, R. Oldenbourg Verlag, München (1972).
- [67] H. A. Kramers, *La diffusion de la lumiere par les atomes*, Atti Cong. Intern. Fisica, Trans. Volta Cent. Congr. Como, 2 (1927) 545-557.
- [68] H. A. Kramers, *Die Dispersion und Absorption von Röntgenstrahlen*, Z. Phys. 30 (1929) 521-523.
- [69] R. L. de Kronig, *On the theory of the dispersion of X-rays*, J. Opt. Soc. Am. 12 (1926) 547-557.
- [70] R. L. van Meirhaeghe, E. C. Dutoit, F. Cardon, W. P. Gomes, *On the application of the Kramers-Kronig relations to problems concerning the frequency dependence of electrode impedance*, Electrochim. Acta. 21, 1 (1976) 39-43.
- [71] H. W. Bode, *Network Analysis and Feedback Amplifier Design*, Van Nostrand, New York (1945).
- [72] H. Göhr, *Kramers-Kronig-Beziehungen*, Seminar-Manuskript (1977), https://zahner.de/media-files/support_downloads/files/seminar-electrochemie_en_de.pdf.
- [73] M. Urquidi-Macdonald, S. Real and D. D. Macdonald, *Review of mechanistic analysis by electrochemical impedance spectroscopy*, Electrochim. Acta. 35 (1990) 1559.
- [74] P. Agarwal, M. E. Orazem, L. H. García-Rubio, *Measurement Models for Electrochemical Impedance spectroscopy: 3. Evaluation of Consistency with the Kramers-Kronig Relations*, J. Electrochem. Soc. 142 (1995) 4159-4168.
- [75] Claude Elwood Shannon, *Communication in the Presence of Noise*, Proc. IRE, Vol. 37, No. 1, (1949), Nachdruck in: *Proc. IEEE*, Vol. 86, No. 2 (1998) .
- [76] A. Papoulis, *The Fourier Integral and Its Applications*, McGraw-Hill (1962).
- [77] W. Ehm, *Expansions for the Logarithmic Kramers-Kronig Relations* (1998), https://zahner.de/media-files/support_downloads/files/zhitehm.pdf.
- [78] W. Ehm, persönliche Mitteilung (1998).
- [79] W. Ehm, H. Kaus, R. Göhr, C. A. Schiller, *The Evaluation of Electrochemical Impedance Spectra Using a Modified Logarithmic Hilbert Transform*, *Acta Chimica Hungarica*, 137, 2-3 (2000) 145.
- [80] W. Ehm, H. Kaus, C. A. Schiller, W. Strunz, *ZHIT - A Simple Relation between Impedance Modulus and Phase Angle, Providing a New Way to the Validation of Electrochemical Impedance Spectra*, Proceedings Proceedings of the ECS, New Trends in Electrochemical Impedance Spectroscopy (EIS) and Electrochemical Noise Analysis (ENA), eds. F. Mansfeld, F. Huet. O.R. Mattos, Electrochemical Society, Pennington, NJ, vol. 2000-24 (2001) 1.
- [81] H. Göhr, B. Röseler, C. A. Schiller, *Advantages of Hilbert transform compared with Kramers-Kronig Rule when examining the causality of experimental impedance spectra*, ISE, 46th Meeting, Xiamen China, Extended Abstract 3.05 (1995).
- [82] H. Göhr und F. Richter, *Einfluß löslicher oxidischer Produkte vorausgehender Oxidation von Platin-Oberflächen auf die Elektrosorption von Wasserstoff*, Z.Phys.Chem. NF Bd. 115 (1979) 69-88.

- [83] Z. Stoynov, *Impedance modelling and data processing: structural and parametrical estimation*, *Electrochim. Acta* 35, 10 (1990) 1493–1499.
- [84] Z. B. Stoynov und B. S. Savova-Stoynov, *Impedance study of non-stationary systems: four-dimensional analysis*, *J. Electroanal. Chem.* 183, 1-2 (1985) 133–144.
- [85] H. Göhr, H. Bode, A. Burghart, and C. A. Schiller, *Impedance Measurement at Electrodes of Continuously Changing State*, 2nd International Symposium on EIS, Santa Barbara, CA, USA (1992), www.zahner.de/downloads/interpol.pdf.
- [86] N. Wagner, “*Electrochemical power sources – Fuel cells*” in *Impedance Spectroscopy: Theory, Experiment, and Applications*, 2nd Edition, Edited by Evgenij Barsoukov and J. Ross Macdonald, John Wiley & Sons, Inc., ISBN: 0-471-64749-7 (2005) 497-537
- [87] A. J. Appleby and F. R. Foulkes, *Fuel Cell Handbook*, Krieger Publishing Comp., Malabar FL, USA (1993).
- [88] N. Wagner, *Handbook of PEM Fuel Cell Durability*, Volume 2: PEM Fuel Cell Diagnostic Tools, Chapter 3: *Electrochemical Impedance Spectroscopy (EIS)*, Eds. H. Wang, X.-Z. Yuan and H. Li, CRC Press, Taylor & Francis Group, London, UK, ISBN: 078-1-4398-3919-5 (2011) 37-70.
- [89] B. Andreaus, A. J. McEvoy and G. G. Scherer, *Analysis of Performance Losses in Polymer Electrolyte Fuel Cells at high Current Densities by Impedance Spectroscopy*, *Electrochim. Acta*, 47 (2002) 2223-2229.
- [90] M. Ciureanu and H. Wang, *Electrochemical impedance study of anode CO-poisoning in PEM fuel cells*, *J. New Mat. Electrochem. Systems*, 3 (2000) 107-119.
- [91] K. Kochloefl, *Water Gas Shift and COS Removal*, *Handbook of Heterogeneous Catalysis*, Herausgeber: Ertl, G.; Knözinger, H.; Weitkamp, J.; Wiley-VCH, Weinheim, Vol. 2 (1997) 1831-1842.
- [92] C. A. Schiller, F. Richter, E. Gülzow 3, N. Wagner, *Validation and Evaluation of Electrochemical Impedance Spectra of Systems with States that change with time*, *J. Phys. Chem. Chem. Phys.* 3 (2001) 374.
- [93] C. A. Schiller, F. Richter, E. Gülzow, N. Wagner, *Relaxation Impedance as a Model for the Deactivation Mechanism of Fuel Cells Due to Carbon Monoxide Poisoning*, *J. Phys. Chem. Chem. Phys.* 3 (2001) 2113.
- [94] Z. Stoynov, *Nonstationary Impedance Spectrometry*, *Electrochim. Acta* 38, 14 (1993) 1919-1922.
- [95] R. H. Milocco, *Minimal Measurement Time in Electrochemical Impedance Identification*, *Electrochim. Acta* 39, 10 (1994) 1433-1439.
- [96] Y. Van Ingelgem, E. Tourwé, O. Blajiev, R. Pintelon, A. Hubin, *Advantages of odd random phase multisine electrochemical impedance measurements*, *Electroanalysis* 21(6) (2009) 730-739.
- [97] A. Pilla, *A transient impedance technique for study of electrode kinetics - Application to potentiostatic methods*, *J. Electrochem. Soc.* 117 (1970) 467-477.
- [98] W. H. Smyrl, *Digital impedance for faradaic analysis. 1: Introduction to digital signal analysis and impedance measurements for electrochemical and corrosion systems*, *J. Electrochem. Soc.* 132 (7), (1985) 1551-1555.
- [99] G. S. Popkirov, R. N. Schindler, *In-Situ Time Resolved Impedance Spectroscopy of Processes in the Solid/Liquid Interface: Electropolymerization of Bithiophene*. *Ber. Bunsenges. Phys. Chem.* 97, 3 (1993) 479–482.
- [100] E. Barsoukov, S. Ryu, H. Lee, *A novel impedance spectrometer based on carrier function Laplace-transform of the response to arbitrary excitation*, *J. Electroanal. Chem.* 536 (2002) 109-122.
- [101] Y. Vaningelgem, E. Tourwé, J. Vereecken, A Hubin, *Application of multisine impedance spectroscopy, FE-AES and FE-SEM to study the early stages of copper corrosion*, *Electrochim. Acta*, 53, 25 (2008) 7523-7530.

- [102] C. A. Schiller, *Electrochemical Noise, fundamentals and methods*, Electrochemical Applications 1/96, ZAHNER-elektrik (1996), 1-3, https://zahner.de/media-files/support_downloads/files/ea1996.pdf.
- [103] H. Göhr, C. A. Schiller, *Faraday-Impedanz als Verknüpfung von Impedanzelementen*, Z. Phys. Chem. Neue Folge 93 (1986) 105-124.
- [104] U. Ruhrberg, *Untersuchungen zum Phasengrenzverhalten von grenzflächenaktiven Wirkstoffen bei der Bekämpfung der Stahlkorrosion in Erdgasförder sonden*, Diss. Univ. Bochum (1992).
- [105] A. Landes, *Einfluss der Zellabwärme und der Wärmeleitung auf das Impedanzspektrum einer SOFC-Einzelzelle*, Laborbericht Siemens AG, ZT EN 1, EN1/DA/8919, 7.5. (1998).
- [106] C. A. Schiller, F. Richter, N. Wagner, *The Appearance of Unexpected Reactance Contributions in Systems Dominated by Resistance – The Nature of Inductive and Capacitive Behaviour in Low Frequency Impedance Spectra of Corroding Electrodes, Batteries and Fuel Cells*, 62th Annual Meeting of ISE, Niigata, Japan, September 11-16 (2011).
- [107] C. A. Schiller, *Frequenzanalyse ohne Spezialgeräte*, Markt & Technik, Nr. 11/52, März 13 (1981) 57.
- [108] C. A. Schiller, *Main Error Sources at AC Measurements on Low Impedance Objects*, Electrochemical Applications 1/97, ZAHNER-elektrik (1997), 10-11, https://zahner.de/media-files/support_downloads/files/ea1997.pdf.
- [109] C. A. Schiller, *Introduction into Electrochemical Instrumentation*, Analytical Methods in Corrosion Science and Engineering, Eds. P. Marcus, F. Mansfeld, Taylor & Francis, York, Penn. (2006) 361-434, ISBN-10: 0-8247-5952-4.
- [110] H. Göhr, M. Mirnik, C. A. Schiller, *Distortions of High Frequency Electrode Impedance, Their Causes and How to Avoid Them*, J. Electroanal. Chem., K 180 (1984) 273-285.
- [111] C. A. Schiller, R. Kaus, *On-line error determination and processing for electrochemical impedance spectroscopy measurement data based on weighted harmonics autocorrelation*, Bulgarian Chemical Communications, Vol. 41, 2 (2009) 192-198.
- [112] C. A. Schiller, R. Kaus, *Consistent Discussion of the Uncertainty of Physical Parameters Evaluated by EIS, Based on an Automatic Measurement Error Determination*, ECS Transactions, 25, (32), (2010) 49-62.
- [113] L. Young, *The interpretation of impedance measurements on oxide coated electrodes on niobium, Anodic oxide films*. Part 4, Trans. Faraday Soc., 51 (1955) 1250-1260.
- [114] L. Young, *Steady-State Kinetics of Formation of Anodic Oxide Films on Tantalum in Sulphuric Acid*, Proc. R. Soc. London, Ser. A 258 (1295), (1960) 496.
- [115] D. A. Vermilyea, *The Kinetics of Formation and Structure of Anodic Oxide Films on Tantalum*, Acta met. 1 (1953) 282.
- [116] K. J. Vetter, *Elektrochemische Kinetik*, Springer-Verlag Berlin, Göttingen, Heidelberg (1961) 618-620.
- [117] K. J. Vetter, *Zur Potentialdifferenz innerhalb der Passivschicht des Eisens*, Z. Phys. Chem. Neue Folge 4 (1955) 165-174.
- [118] T. Mayer-Kuckuck, *Physik der Atomkerne*, B. G. Teubner, Stuttgart (1970).
- [119] A.I. Sotnikov, G.I. Savina, N.K. Dehemilev, N.S. Smirnov, *Impedance of Fe, Co, Ni and Pt in a Sodium Borosilicate Melt*, Elektrokimiya 9, Jan. (1973) 121.
- [120] J. W. A. Scholte und W. Ch. Van Geel, *Impedances of the electrolytical rectifier*, Philips Res. Rep. 8 (1953) 47.
- [121] T. Sasaki, *p-i-n junction in the anodic oxide film of tantalum*, J. Phys. Chem. Solids 13, 3-4 (1960) 177-186.
- [122] N. Müller, *Impedanz von Deckschichten mit Leitfähigkeitsgradient - Theorie und Anwendung auf die passive und aktive Titan-Elektrode*, Dissertation, Erlangen (1980).
- [123] U. Rammelt, C. A. Schiller, *Impedance studies of layers with vertical decay of conductivity or permittivity*, Acta Chim. Hung. 137 (2000) 199.

- [124] H. Göhr, J. Schaller, C. A. Schiller, *Impedance Studies of the Oxide Layer on Zircaloy After Previous Oxidation in Water Vapour at 400 °C*, *Electrochim. Acta* 38 (1993) 1961-1964.
- [125] H. Göhr, H.-J. Oh, C. A. Schiller, *Impedanz von Deckschichten mit Leitfähigkeitsgradienten*, GDCh-Monographien, Bd. 2, S. Verlag Chemie, Weinheim (1994) 341-348.
- [126] C. A. Schiller, W. Strunz, N. Wagner, F. Richter; *Current Interrupt Techniques as a completion of EIS: Struggling against Mutual Induction in Fuel Cells Research and Time Saving in Barrier Coatings Characterization*, *Bulgarian Chemical Communications*, Volume 39, Number 3 (2007) 211-223.
- [127] N. Wagner, *Application of Impedance Spectroscopy in Fuel Cell Research*, Technische Mitteilung tm 1/2011, DLR-Institut für Technische Thermodynamik, Stuttgart (2011).
- [128] J. Hollaender, *Rapid Assessment of food/package interactions by electrochemical impedance spectroscopy (EIS)*, *Food Additives and Contaminants* 14, No. 6-7 (1997) 617-626.
- [129] K. N. Allahar, V. Upadhyay, G. P. Bierwagen, *Characterizing the Relaxation of the Open-Circuit Potential during an AC-DC-AC Accelerated Test*, *CORROSION* 66, 095001 (2010), DOI:10.5006/1.3490306.
- [130] K. N. Allahar, Q. Su, G. P. Bierwagen, D.-H. Lee, *Monitoring of the AC-DC-AC Degradation of Organic Coatings Using Embedded Electrodes*, *CORROSION* 64 (2008) 773, DOI:10.5006/1.3278445.
- [131] W. Strunz, C. A. Schiller, J. Vogelsang, *The change of dielectric properties of barrier coatings during the initial state of immersion*, *Materials and Corrosion* 59, No. 2 (2008) 159-166.
- [132] S. H. Glarum, *Dielectric Relaxation of Isoamyl Bromide*, *J. Chem. Phys.* 33 (1960) 639.
- [133] P. Bordewijk, *Defect-diffusion models of dielectric relaxation*, *Chem. Phys. Lett.* 32 (1975) 592.
- [134] M. F. Schlesinger, E. W. Montroll, *On the Williams-Watts Function of Dielectric Relaxation*, *Proc. Natl. Acad. Sci.* 81 (1984) 1280.
- [135] G. Williams, D. C. Watts, *Non-Symmetrical Dielectric Relaxation Behaviour Arising from a Simple Empirical Decay Function*, *Trans. Faraday Soc.* 66 (1970) 80.
- [136] G. Williams, D. C. Watts, S. B. Dev, A. M. North, *Further Considerations of Non-Symmetrical Dielectric Relaxation Behaviour Arising from a Simple Empirical Decay Function*, *Trans. Faraday Soc.* 67 (1970) 1323.
- [137] C. A. Schiller, W. Strunz, *The evaluation of experimental dielectric data of barrier coatings by means of different models*, *Electrochim. Acta* 46 (2001) 3619.
- [138] C. A. Schiller, W. Strunz, *The validation of experimental impedance data of barrier coatings by means of the Z-HIT algorithm*, Lecture, Electrochemical methods in corrosion research. International symposium EMCR N°9, Dourdan , France, June (2006).
- [139] C. A. Schiller, W. Strunz, J. Vogelsang, *The change of the coating capacity of barrier coatings during water uptake - an oversimplification ?*, Lecture, Electrochemical methods in corrosion research. International symposium EMCR N°9, Dourdan , France, June (2006).
- [140] W. Strunz, C. A. Schiller, J. Vogelsang, *The evaluation of experimental dielectric data of barrier coatings in frequency and time domain*, *Electrochim. Acta* 51 (2006) 1437.

Acknowledgments

I must especially thank my doctoral supervisor, Prof. Dr. Patrik Schmuki, who was willing to supervise this work, which was not very compact in terms of time or subject matter, as well as for the trouble I caused Prof. Dr. Günter Grampp with my request for a second opinion.

I was kindly supported at the LKO by Dr. Steffen Berger, Dipl. Ing. Robert Hahn, Dr. Andrei Ghicov, PhD student Indhumati Paramasivam, Dr. Florian Kellner, Dr. Doohun Kim, Ms. Barbara Scholz and Ms. Helga Hildebrand, with logistical help, with the provision of literature, samples, reagents, help with physical measurements, microscopy and sample preparation.

I have to thank my colleagues from the former working group of Prof. Hermann Göhr, above all Dr. Franz Richter, Prof. Rüdiger Kaus, Dr. Norbert Wagner, Dr. Jürgen Söllner and many scientists from cooperating institutes such as Dr. Jochen Hollaender from the Fraunhofer Institute IVV, Prof. Waldfried Plieth and Dr. Ursula Rammelt from the University of Dresden, Dr. Jörg Vogelsang from the SIKA Zurich and Dr. Würfel from the ISE Freiburg. I would like to thank Dr. Werner Ehm for solving a particularly stubborn mathematical problem and Ms. Charlotte Beck for photo-electrochemical measurements on the tantalum sheet. I would also like to thank my colleagues at Zahner Dr. Werner Strunz, Dr. Burkhard Röseler, Dr. Michael Multerer, my brother Wolfgang and my son Ralf, who have supported me with many lectures, posters and publications.

I would like to dedicate this work to my wife Monika with a particularly heartfelt thank you.

Publication list

1. C. A. Schiller, *Analoges und Digitales über PET*, Markt & Technik, Nr. 51/52, Dezember 21 (1979) 34.
2. C. A. Schiller, *Frequenzanalyse ohne Spezialgeräte*, Markt & Technik, Nr. 11/52, März 13 (1981) 57.
3. G. Grampp, C. A. Schiller, *Microcomputer Interface for Calculation of Autocorrelation Functions of Electron Spin Resonance Spectra*, Anal. Chem., 53 (1981) 560-561.
4. F. L. Dickert, S. W. Hellmann, C. A. Schiller, *Data System for Nuclear Magnetic Resonance Spectrometry*, Anal. Chem., 53 (1981) 558-560.
5. H. Göhr, M. Mirnik and C. A. Schiller, *Distortions of High Frequency Electrode Impedance, Their Causes and How To Avoid Them*, J. Electroanal. Chem., K 180 (1984) 273-285.
6. H. Göhr and C. A. Schiller, *Faraday-Impedanz als Verknüpfung von Impedanzelementen*, Z. Phys. Chem. Neue Folge 93 (1986) 105-124.
7. C. A. Schiller, *Impedanzspektroskopie auf der Basis eines universellen Messsystems*, Markt & Technik, Nr. 1 (1988) 30-34.
8. A. Baurichter, W. Eylich, M. Frank, H. Göhr, W. Kreische, H. Ortner, B. Röseler, C. A. Schiller, G. Weeske, W. Witthun, *Search for Cold Fusion in Palladium*, Zeitschrift für Physik B, Condensed Matter, vol. 76, issue 1 (1989) 1-2.
9. B. Iglar, H. Bode, C. A. Schiller, *Kalte Kernfusion und Elektrochemische Messtechnik – das Erlanger Parallel-Experiment*, Markt & Technik, Nr. 3 (1989) 8-12.
10. T. Fehn, C. A. Schiller, *Kalte Kernfusion und Elektrochemische Messtechnik*, Chem.-Tech. (Heidelberg), 18 (1989) 72, 75, 77.
11. H. Göhr, J. Schaller, C. A. Schiller, *Impedance Studies of the Oxide Layer on Zircaloy After Previous Oxidation in Water Vapour at 400 °C*, Electrochim. Acta 38 (1993) 1961-1964.
12. H. Göhr, H.-J. Oh, C. A. Schiller, *Impedanz von Deckschichten mit Leitfähigkeitsgradienten*, GDCh-Monographien, Bd. 2, S. Verlag Chemie, Weinheim (1994) 341-348.
13. C. A. Schiller, *Electrochemical Noise, fundamentals and methods*, Electrochemical Applications 1/96, ZAHNER-elektrik, 1996, 1-3, www.zahner.de/downloads/ea1996.pdf.
14. C. A. Schiller, *Main Error Sources at AC Measurements on Low Impedance Objects*, Electrochemical Applications 1/97, ZAHNER-elektrik (1997) 10-11, www.zahner.de/downloads/ea1997.pdf.
15. U. Rammelt, C. A. Schiller, *Impedance studies of layers with vertical decay of conductivity or permittivity*, Acta Chim. Hung. 137 (2000) 199.
16. W. Ehm, H. Kaus, R. Göhr, C. A. Schiller, *The Evaluation of Electrochemical Impedance Spectra Using a Modified Logarithmic Hilbert Transform*, Acta Chimica Hungarica, 137, 2-3 (2000) 145.
17. B. Röseler, C. A. Schiller, *Strom - Potential korrelierte Rauschmessung (CorrEINoise) - Ein neues Verfahren zur elektrochemischen Rauschanalyse*, Materials and Corrosion, 52, 6 (2001) 413-417.

18. W. Ehm, H. Kaus, C. A. Schiller, W. Strunz, *ZHIT - A Simple Relation Between Impedance Modulus and Phase Angle, Providing a New Way to the Validation of Electrochemical Impedance Spectra*, Proceedings of the ECS, New Trends in Electrochemical Impedance Spectroscopy (EIS) and Electrochemical Noise Analysis (ENA), eds. F. Mansfeld, F. Huet. O.R. Mattos, Electrochemical Society, Pennington, NJ, vol. 2000-24 (2001) 1.
19. C. A. Schiller, F. Richter, E. Gülzow, N. Wagner, *Validation and Evaluation of Electrochemical Impedance Spectra of Systems with States that change with time*, J. Phys. Chem. Chem. Phys. 3 (2001) 374.
20. C. A. Schiller, F. Richter, E. Gülzow, N. Wagner, *Relaxation Impedance as a Model for the Deactivation Mechanism of Fuel Cells Due to Carbon Monoxide Poisoning*, J. Phys. Chem. Chem. Phys. 3 (2001) 2113.
21. C. A. Schiller, W. Strunz, *The evaluation of experimental dielectric data of barrier coatings by means of different models*, Electrochim. Acta 46 (2001) 3619.
22. F. Richter, C. A. Schiller, N. Wagner, *Current Interrupt Technique-Measuring low impedances at high frequencies*, Electrochemical Applications, 1/2002, 1-6, Ed. Zahner-elektrik, Kronach (2002).
23. C. A. Schiller, W. Strunz, *Impedanzmessungen – Sein oder Schein*, Technische Mitteilungen, (Eds. U. Brill, D. U. Sauer), Heft 1/2 06, ISSN 0040-1439, Essen (2006) 14–18.
24. C. A. Schiller, W. Strunz, *Impedanzmessungen an Systemen mit merklicher zeitliche Drift*, Technische Mitteilungen, HDT Essen, ISSN 0040-1439, Essen (2006) 12-13.
25. W. Strunz, C. A. Schiller, J. Vogelsang, *The evaluation of experimental dielectric data of barrier coatings in frequency and time domain*, Electrochim. Acta 51 (2006) 1437.
26. C. A. Schiller, *Introduction into Electrochemical Instrumentation*, Analytical Methods in Corrosion Science and Engineering, Eds. P. Marcus, F. Mansfeld, Taylor & Francis, York, Penn. (2006) 361-434, ISBN-10: 0-8247-5952-4.
27. C. A. Schiller, W. Strunz, N. Wagner, F. Richter; *Current Interrupt Techniques as a completion of EIS: Struggling against Mutual Induction in Fuel Cells Research and Time Saving in Barrier Coatings Characterization*, Bulgarian Chemical Communications, Volume 39, Number 3 (2007) 211-223.
28. W. Strunz, C. A. Schiller, J. Vogelsang, *The change of dielectric properties of barrier coatings during the initial state of immersion*, Materials and Corrosion 59, No. 2 (2008) 159-166.
29. C. A. Schiller, R. Kaus, *On-line error determination and processing for electrochemical impedance spectroscopy measurement data based on weighted harmonics autocorrelation*, Bulgarian Chemical Communications, Vol. 41, 2 (2009) 192-198.
30. Ghicov, S. P. Albu, R. Hahn, D. Kim, T. Stergiopoulos, J. Kunze, C. A. Schiller, P. Falaras, P. Schmuki *TiO₂ Nanotubes in Dye-Sensitized Solar Cells: Critical Factors for the Conversion Efficiency*, Chem. Asian J., 4 (2009) 520-525.
31. C. A. Schiller, R. Kaus, *Consistent Discussion of the Uncertainty of Physical Parameters Evaluated by EIS, Based on an Automatic Measurement Error Determination*, ECS Transactions, 25 (32), (2010) 49-62.
32. C. A. Schiller, *Basics and Applications, Kronach Impedance Days 2011 at Kloster Banz*, Vortrag und Skript, ZAHNER-elektrik (2011), www.zahner.de/downloads/pdf/Basics_And_Applications.pdf.

Conference contributions

1. H. Göhr, C. A. Schiller, *Impedance Spectra of Electrodes - A Technique of Measurement and Evaluation*, ISE Meeting 1983, Poster 0528, Extended Abstract, Erlangen (1983).
2. H. Göhr, H. Bode, A. Burghart, and C. A. Schiller, *Impedance Measurement at Electrodes of Continuously Changing State*, 2nd International Symposium on Electrochemical Impedance Spectroscopy, Santa Barbara, CA, USA (1992). www.zahner.de/downloads/interpol.pdf.
3. H. Göhr, B. Röseler u. C. A. Schiller, *Impedance of Surface Layers with Conductance Gradients*, Poster, 3rd International Symposium on Electrochemical Impedance Spectroscopy, Ysermonde, Nieuwport, Belgium (1995).
4. H. Göhr, F. Richter, B. Röseler, C. A. Schiller, E. Wessel, *Investigation of Solid Oxide Fuel Cells (SOFC) by In-Situ Impedance Spectroscopy and Determination of the Cathodes Electrochemical Parameters by the Model of a Porous Electrode*, Lecture 5-42 46th Meeting of International Society of Electrochemistry, Xiamen China (1995).
5. H. Göhr, B. Röseler, C. A. Schiller, *Advantages of Hilbert transform Compared with Kramers-Kronig Rule when Examining the Causality of Experimental Impedance Spectra*, Poster 3.05, 46th Meeting of International Society of Electrochemistry, Xiamen China (1995).
6. K. Liefelth, H. Göhr, C. A. Schiller, *Electrochemical Corrosion Tests on Metallic Biomaterials*, Lecture 8a-3, 47th Annual Meeting of International Society of Electrochemistry, Veszprém, Hungary, September 1-6 (1996).
7. B. Röseler, C. A. Schiller, *A New Method to Measure Correlated Noise Signals in Comparison with Impedance Measurements at Corroding Aluminium and Steel*, Lecture 7b-6, 47th Annual Meeting of International Society of Electrochemistry, Veszprém, Hungary, September 1-6 (1996).
8. H. Göhr, C. Günther, F. Richter, B. Röseler, C. A. Schiller, *Investigation of Solid Oxide Fuel Cells (SOFC) and Qualification of the Cell's Components by In-Situ Impedance Spectroscopy*, Poster 5b-20, 47th Annual Meeting of International Society of Electrochemistry, Veszprém, Hungary, September 1-6 (1996).
9. W. Ehm, H. Göhr, B. Röseler, R. Kaus, C. A. Schiller, *Validating Electrochemical Impedance Spectra - The Advantages of the Logarithmic Hilbert Transform Compared With the Linear Kramers-Kronig Rule*, Lecture, 4th International Symposium on Electrochemical Impedance Spectroscopy, Angra dos Reis, Brazil (1998).
10. H. Göhr, F. Richter, B. Röseler, C. A. Schiller, *Impedance Measurements up to High Current Densities for Development and Quality Control of Solid Oxide Fuel Cells*, Poster 10-14-35, 49th Annual Meeting of International Society of Electrochemistry, Kitakyushu, Japan, September 13-18 (1998).
11. C. A. Schiller, F. Richter, E. Gülzow, N. Wagner, *Validation and Evaluation of Electrochemical Impedance Spectra (EIS) of Systems with Time Changing States*, Poster S2-548, 50th Annual Meeting of International Society of Electrochemistry, Pavia, Italy, September 5-10 (1999).
12. N. Wagner, B. Müller, C. A. Schiller, F. Richter, *Appearance of Relaxation Impedance in the Electrochemical Impedance Spectra (EIS) During Carbon Monoxide-Poisoning of the Pt Anode in a Membrane Fuel Cell*, Lecture S2-582, 50th Annual Meeting of International Society of Electrochemistry, Pavia, Italy, September 5-10 (1999).

13. C. A. Schiller, E. Gülzow, N. Wagner, F. Richter, *Relaxationsimpedanz als Modell für den Deaktivierungsmechanismus von Brennstoffzellenanoden durch Kohlenmonoxid*, Tagung der Deutschen Bunsengesellschaft, Würzburg 1.-3.06 (2000).
14. C. A. Schiller, E. Gülzow, N. Wagner, F. Richter, *Validierung von Impedanzspektren instationärer, stromerzeugender elektrochemischer Systeme*, Tagung der Deutschen Bunsengesellschaft, Würzburg 1.-3.06 (2000).
15. C. A. Schiller, W. Strunz, *The evaluation of experimental dielectric data of barrier coatings by means of different models*, Lecture, 7th International Symposium on Electrochemical Methods in Corrosion Research, EMCR2000, Budapest, Hungary – May 28 – 1 June (2000).
16. N. Wagner, E. Gülzow, B. Müller, C. A. Schiller, *Temperature Dependency of Electrochemical Impedance Spectra (EIS) during Carbon Monoxide –Poisoning of the Pt-Anode in a Membrane Fuel Cell*, 51th Meeting of International Society of Electrochemistry, Warszawa, Poland, 3-8 September (2000).
17. N. Wagner, E. Gülzow, B. Müller, C. A. Schiller, *Comparison of Electrochemical Impedance Spectra (EIS) during Carbon Monoxide –Poisoning of the Pt and Pt/Ru-Anodes in a Membrane Fuel Cell*, 51th Meeting of International Society of Electrochemistry, Warszawa, Poland, 3-8 September (2000).
18. R. Kaus, B. Röseler, C. A. Schiller, „Correlnoise“ – *A Novel Data Acquisition Method Enhances Electrochemical Noise Analysis, First Results and Experiences*, Lecture, 198th Meeting of the Electrochemical Society, Phoenix, USA, October 22-27 (2000).
19. W. Ehm, H. Kaus, C. A. Schiller, W. Strunz, *ZHIT - A Simple Relation between Impedance Modulus and Phase Angle, Providing a New Way to the Validation of Electrochemical Impedance Spectra*, Lecture, 198th Meeting of the Electrochemical Society, Phoenix, USA, October 22-27 (2000).
20. F. Richter, C. A. Schiller, N. Wagner, *High Current Interrupt Technique – A New Analysis Approach Complements Impedance Measurements for Low Ohmic Objects at High Frequencies*, Lecture, 5th International Symposium on Electrochemical Impedance Spectroscopy, Marilleva (Tn), Italy (2001).
21. J. Hollaender, C. A. Schiller, W. Strunz, *Accelerating the Time Scale of Coating Tests - Can the Combination of Linear Small Signal Methods with Electrochemical Stress Improve the Coating Lifetime Prediction?* Poster, 5th International Symposium on Electrochemical Impedance Spectroscopy, Marilleva (Tn), Italy (2001).
22. J. Hollaender, C. A. Schiller, W. Strunz, *Electrochemically Forced Local Coating Degradation and Detection*, Poster, S5, 53th Annual Meeting of International Society of Electrochemistry, Düsseldorf, Germany, September 15-20 (2002).
23. N. Wagner, T. Knöri, E. Gülzow, C. A. Schiller, *Local Current and Impedance Distribution in Polymer Electrolyte Fuel Cells (PEFC)*, Poster, S8, 53th Annual Meeting of International Society of Electrochemistry, Düsseldorf, Germany, September 15-20 (2002).
24. J. Xu, W. Olberding, R. Kaus, C. A. Schiller, *Electrochemical impedance spectrometry - a well-suited tool for the development of alkaline batteries*, Lecture, 54th Annual Meeting of International Society of Electrochemistry, Sao Pedro, Brazil, August 31 - September 5 (2003).
25. W. Strunz, C. A. Schiller, J. Vogelsang, *The evaluation of experimental dielectric data of barrier coatings in the frequency and time domain*, Lecture, 6th International Symposium on Electrochemical Impedance Spectroscopy, Cocoa Beach, Florida, May 16-21 (2004).

26. W. Plieth, C. A. Schiller, U. Rammelt, N. Hebestreit, *Intensity Modulated Photo Spectroscopy on Conducting Polymers - Examination of Poly-Bi-Thiophene in the Reduced State*, Lecture 6-020, 56th Annual Meeting of International Society of Electrochemistry - Busan, Korea, September 25-30 (2005).
27. W. Plieth, C. A. Schiller, U. Rammelt, *Controlled Intensity Modulated Photo- and Impedance Spectroscopy on Conducting Polymers*, Poster S7-P-70, 57th Annual Meeting of International Society of Electrochemistry, Edinburgh, UK (2006).
28. C. A. Schiller, W. Strunz, *The validation of experimental impedance data of barrier coatings by means of the Z-HIT algorithm*, Lecture, S: Electrochemical methods in corrosion research, International symposium EMCR N°9, Dourdan, France, June (2006).
29. C. A. Schiller, W. Strunz, J. Vogelsang, *The change of the coating capacity of barrier coatings during water uptake - an oversimplification ?* Lecture, S: Electrochemical methods in corrosion research, International symposium EMCR N°9, Dourdan, France, June (2006).
30. C. A. Schiller, W. Strunz, *Impedanzmessungen – Sein oder Schein*, Vortrag, EIS-Tagung, RWTH Aachen, Haus der Technik Essen, 16-17. Mai (2006).
31. C. A. Schiller, W. Strunz, *Impedanzmessungen an Systemen mit merklicher zeitliche Drift*, Vortrag, EIS-Tagung, RWTH Aachen, Haus der Technik Essen, 16-17. Mai (2006).
32. F. Richter, C. A. Schiller, R. Kaus, *Online Error Determination and Processing for EIS Measurement Data Based on Harmonic Analysis*, Lecture, 7th International Meeting on Electrochemical Impedance Spectroscopy, Argelès-sur-Mer, France (2007).
33. W. Plieth, C. A. Schiller, U. Rammelt, *Impedance Spectroscopy Combined with Intensity Modulated Photo-Spectroscopy IMPS, Applied to TiO₂-Based Solar Cell Components*, Lecture, 7th International Meeting on Electrochemical Impedance Spectroscopy, Argelès-sur-Mer, France (2007).
34. N. Wagner, R. Reissner, C. A. Schiller, *Surface Science and Electrochemical Study of Interaction of Nickel and Alkaline Solutions*, Poster S5-P-41, 58th Annual Meeting of International Society of Electrochemistry – Banff, Canada (2007).
35. C. A. Schiller, *The Importance of Dynamic Analysis Methods in Electrochemical Power Generation: EIS- and Photo-electrochemical Transfer Functions Applied on Alternative Solar Cell Concepts. Results from TiO₂-Nanotube Based Photo-anodes for Dye Sensitized Solar Cells*, Lecture, CNMS Meeting on Sustainable Energy Future, September 24-26, Oak Ridge National Laboratory, USA (2008).
36. C. A. Schiller, P. Schmuki, *Dynamic EIS- and Photo-Electrochemical Measurements on TiO₂-Nanotube Based Photo-Anodes for Dye Sensitized Solar Cells - the Influence of the Annealing Temperature*, Lecture S5: Electrochemistry of New Materials and Novel Microstructures for Sustainable Development, 59th Meeting of International Society of Electrochemistry, Sevilla, Spain (2008).
37. C. A. Schiller, U. Würfel, B. Zimmermann, S. Berger, *Spectroscopic Methods in Dye Sensitized and Organic Solar Cell Research*, Lecture, CNMS Meeting on Sustainable Energy Future, September, Oak Ridge National Laboratory, USA (2009).
38. P. Schmuki, A. Ghicov, S. Berger, C. A. Schiller, M. Multerer, *EIS- and Controlled Intensity Dynamic Photo-Electrochemical Measurements on TiO₂-Nanotube Photo-Anodes for Dye Sensitized Solar Cells and an Alternative Model for the Data Interpretation*, Session B7, Lecture 734, 216th Meeting of the Electrochemical Society, Vienna, October 4-9 (2009).

39. C. A. Schiller, R. Kaus, *A Consistent Uncertainty Discussion of Physical Parameters Evaluated by EIS, Based on Automatic Measurement Error Determination*, Lecture 3171, S.J2, Impedance Techniques: Diagnostics and Sensing, 216th Meeting of the Electrochemical Society, Vienna, October 4-9 (2009).
40. C. A. Schiller, P. Schmuki, *The Oxide Layer on Tantalum Metal - a Model System for the Investigation of Dielectric Behaviour and Semiconductor Properties of Non-Uniform Passive Films. EIS and Dynamic Photo-Electrochemical Measurements*, Lecture, S9: Interfacial Electrochemistry, 60th Meeting of International Society of Electrochemistry, Beijing (2009).
41. C. A. Schiller, W. Strunz, J. Vogelsang, *The Dielectric Properties of Barrier Coatings - a Superposition of Coating Material and Pores*, Poster s02-P-017, Corrosion Science and Technology, 60th Meeting of International Society of Electrochemistry, Beijing (2009).
42. C. A. Schiller, S. Berger, *Spectroscopic Techniques in Solar Cell Research*, Lecture, Symposium Photovoltaic, International Conference on Functional Nanocoatings, Dresden, Germany, March 28-31 (2010).
43. C. A. Schiller, N. Wagner, *Analysis of the Local Dependency vs. Time in a PEM Fuel Cell Stack after Process Parameter Transients by Means of Multi-Channel Synchronous Impedance Measurements*, Lecture, S4, Advances in Fuel Cells, 61th Meeting of International Society of Electrochemistry, Nice, France (2010).
44. C. A. Schiller, U. Würfel, M. Multerer, *Impedance and Spectro-Electrochemical Measurements on Organic LED and Solar Cell Materials: The Potential Dependent Properties of the Bi-Layer PEDOT:PSS-P3HT*, Lecture O-083-G, International Meeting on Electrochemical Impedance Spectroscopy, Portugal (2010).
45. C. A. Schiller, W. Strunz, J. Vogelsang, *The Dielectric Properties of Barrier Coatings - a Superposition of Coating Material and Pores*, Poster P-122-A, International Meeting on Electrochemical Impedance Spectroscopy, Portugal (2010).
46. P. Schmuki, A. Ghicov, S. Berger, C. A. Schiller, M. Multerer, *EIS- and Controlled Intensity Dynamic Photo-Electrochemical Measurements on TiO₂-Nanotube Photo-Anodes for Dye Sensitised Solar Cells and an Alternative Model for the Data Interpretation*, Poster P-117-G, International Meeting on Electrochemical Impedance Spectroscopy, Portugal (2010).
47. C. A. Schiller, P. Schmuki, S. Berger, *The Oxide Layer on Tantalum Metal - a Model System for the Investigation of Dielectric Behavior and the Semiconductor Properties of Non-Uniform Passive Films*, Poster P-104-D, International Meeting on Electrochemical Impedance Spectroscopy, Portugal (2010).
48. C. A. Schiller, R. Kaus, *Consistent Discussion of the Uncertainty of Physical Parameters Evaluated by EIS Based on an Automatic Measurement Error Determination*, Poster P-115-D, International Meeting on Electrochemical Impedance Spectroscopy, Portugal (2010).
49. C. A. Schiller, *Impedance and Photo-Electrochemical Techniques in Renewable Energy Research*, Lecture, CNMS Meeting on Sustainable Energy Future, Oak Ridge National Laboratory, USA, September (2010).
50. C. A. Schiller, F. Richter, N. Wagner, *The Appearance of Unexpected Reactance Contributions in Systems Dominated by Resistance – The Nature of Inductive and Capacitive Behaviour in Low Frequency Impedance Spectra of Corroding Electrodes, Batteries and Fuel Cells*, Poster, 62th Meeting of International Society of Electrochemistry, Niigata, Japan, September 11-6 (2011).

51. C. A. Schiller, *Impedance Spectroscopy on Photovoltaics*, CNMS Meeting on Sustainable Energy Future, Lecture, September, Oak Ridge National Laboratory, USA, September 22 (2011).